ELECTRIC DIMENSIONAL TREATMENT OF MATERIALS

Evaluation of the Protective Properties of Multilayer Coatings for Steam Turbine Blades

E. K. Sevidova[a], V. M. Matsevityi[b], I. B. Kazak[b], and K. V. Vakulenko[b]

[a] National Technical University, Khar'kov Polytechnic Institute,
ul. Frunze 21, Khar'kov, 61002 Ukraine
[b] Podgornyi Institute of Mechanical Engineering Problems,
ul. Dmitriya Pozharskogo 2/10, Khar'kov, 61046 Ukraine

Received July 7, 2007

Abstract—The results of investigation of the protective properties of multilayer ion-plasma coatings relative to the conditions of their exploitation on steam turbines are described. It was established that the protection properties of coatings on 20X13 steel in an aggressive NaCl environment of various concentrations increase according to the sequence $[Cr + (Cr,Ti)N]_{10} < (Ti + TiN)_{10} < (Cr + CrN)_{10}$. It was also found that a breach in the coating integrity can lead to the appearance of macrogalvanic couples. Their activity considerably increases (by 4–5 times) during the mechanical passivation of the surface under the conditions of drop-collision erosive wear. The greatest values of the EMF in stationary conditions are generated between the 20X13 steel and Ti + TiN coating.

INTRODUCTION

The main reason for surface damage of the last stage blades of wet-steam turbines is their erosive and corrosive wear [1–3].

In the working state, the first component prevails—the wear-out due to the drop collision, which is the most characteristic for the entering edges along the blade periphery [3]. After the turbine stops, the corrosion processes intensifies significantly, which is connected with the local concentration of aggressive corrosive admixtures, air access, and the after effects of the substances used for conservation. At that, the damage has, as a rule, a patchy, pitting character.

One of the ways to improve the erosive and corrosive resistance of the blade construction materials is deposition of protective coatings on them, which are characterized by high resistance both to the mechanical wear-out and corrosion in the aggressive environment of the turbine exploitation.

Nitrides of the transition metals, which have proven their worth in other branches of the machine industry, are among the prospective materials for such coatings.

The purpose of this paper is to compare the corrosion-protective properties of three variants of multilayer durable nitride-based coatings relative to the conditions of their exploitation on steam turbine blades.

EXPERIMENTAL PROCEDURE

In the research of corrosion-protective properties of the coatings, we used cylindrical specimens with $\varnothing$16mm and h = 20mm, made of 20X13 steel, on the front surface of which coatings were deposited according to various technological schemes; in particular: (a) $(Ti + TiN)_{10}$, $h \sim 10$ µm; (b) $(Cr + CrN)_{10}$, $h \sim 10$ µm; (c) $(Cr + (Cr, Ti) N)_{10}$, $h \sim 7$ µm. The standard for comparison in the tests was the surface of the original (without coatings) specimens made of 20X13 steel, the blade construction material.

The coatings were deposited by the CIB (condensation with ion bombardment) method on a Bulat-6 installation. The specimen surface was preliminary treated to yield R_a 0.16 µm.

The coatings' protective properties were evaluated by electrochemical methods and corrosion tests. The value of the corrosion potential, E_{cor}; the characteristics of the anode polarization dependences, $j–E_a$; and the currents of the contact galvanic couples were taken as basic electrochemical criteria. Relative to the research object, various versions of galvanic couples between the materials of the base plate and the metal-like coatings (CrN, TiN, (Cr,Ti)N) may realize in the condition of an integrity breach and also in the penetrating voids and defects. The electrochemical measurements were taken under stationary conditions and under mechanical depassivation of the surface, which imitated the process of erosion wear of the surface by condensate drops. The mechanical depassivation was conducted on the experimental system according to the previously developed technique [4]. The currents of the contact galvanic couples were measured by the compensation method.

The corrosion-active medium was natrium chloride solution of various concentrations, whose presence in

Table 1. The values* of the corrosion potential E_{cor} (in V) under the exposition in 0.9% NaCl solution

Specimen number	Specimen type	After the exposition for τ h					Under the surface depassivation
		1	2	5	24	72	
1	Original (without coating)	−0.05	−0.03	−0.04	−0.16	−0.17	−0.32
2	With $(Ti + TiN)_{10}$ coating	+0.04	−0.12	−0.09	+0.05	+0.044	−0.19
3	With $(Cr + CrN)_{10}$ coating	−0.21	−0.27	−0.27	−0.22	−0.18	−0.19
4	$[Cr + (Cr,Ti)N]_{10}$	−0.22	−0.26	−0.29	−0.20	−0.27	−0.21

* The values of the potentials are given relative to the chloride silver electrode.

the feed water most significantly influences corrosion of the constructive materials of the steam turbines [2].

In the procedures of the corrosion tests, the specificities of the turbine blade corrosion in the exploitation conditions were taken into account; in particular:

—a relatively wide range of possible concentrations of aggressive reagent (NaCl) on the surface (from 0.3% to saturated);

—the film-type corrosion;

—the temperature factor (the temperature of the water-steam mixture in the region of the turbine last stages may reach 90–95°C) [3].

In the tests, a fixed volume ($V = 100 \mu l$) of the aggressive solution was deposited on the specimen surface: 3% solution for one set and a solution saturated under room temperature for another. The first specimen set was incubated in a desiccator with the salt solution in a dry heat oven at 95°C for 20 h. The second set was kept in the open air under room temperatures for three days and nights. After each 24-h period, 100 μl of distilled water was deposited on the surface to initiate the corrosion processes.

The corrosive damage was evaluated visually.

DISCUSSION OF THE RESULTS

It follows from the analysis of the E_{cor} values (Table 1) that the surface of the base plate material, 20X13 steel, activates while being kept in a 0.9% solution of NaCl, which is indicated by the relatively monotonous denobling of E_{cor}: from −0.05 to −0.17 V.

The system of the 20X13 base plate with a (Ti + TiN)$_{10}$ coating is characterized by the most positive value of E_{cor} among the investigated variants of protective coatings, and the system with the (Cr + (Cr, Ti)N)$_{10}$ coating, by the most negative one. In general, this may demonstrate the highest thermodynamic resistance of the specimens with the titan nitride protective coatings and, presumably, the better corrosion protection properties of them in comparison with the chromium steel.

A nonmonotonous change of E_{cor} for the specimens with coatings (denobling $\rightleftarrows$ nobling) give indirect evidence of the coating defects and the development of

the processes there connected with the origination and healing (passivation) of the corrosion centers.

The mechanical depassivation of the surface results in significant denobling of E_{cor} for the 20X13 steel specimens and the ones with (Ti + TiN)$_{10}$ coatings. The ΔE_{cor} shift for them amounted to 0.15 and 0.23 V, correspondingly. This confirms the presence of passivating oxide layers on the specimen surfaces, whose removal may intensify the overall corrosion. In the activated state, the base plate material is characterized by the most negative value of E_{cor}; so, this material is the anode in the galvanic couples with all the variants of the coatings.

The mechanical depassivation of the surface virtually does not change the E_{cor} value for the specimen with the (Cr + CrN)$_{10}$ coating, whereas it even "improves" this characteristic for the specimen with the nitrides (Cr, Ti)N mixture moving it into the positive values region.

The inadequate reaction of the surface to the removal of the passivating films can be explained by the compromise nature of the registered corrosion potential of the system with the coating, whose value is an integral quantity:

$$E_{cor} = E_n + \sum \Delta E_i,$$

where E_n is the stationary potential of the coating, and $\sum \Delta E_i$ is the average shift of the stationary potential of the entire specimen caused by the presence of voids.

At that, as was shown in [5], the E_{cor} value may be much more negative than the potential of the anodal base plate itself in the voids. The author of that research explains this by the presence of a mechanochemical effect in the voids caused by the tensions of various nature in the coating and the base; this effect especially often takes place in the case of ion-plasma deposition of coatings.

The character of the polarization dependencies (Fig. 1) confirms that deposition of all the kinds of coatings has a protective effect, but of various degrees. The best result in the polarization research was shown by the specimen with the multilayer Ti + TiN coating (curve number *4*). Activation of the anode processes,
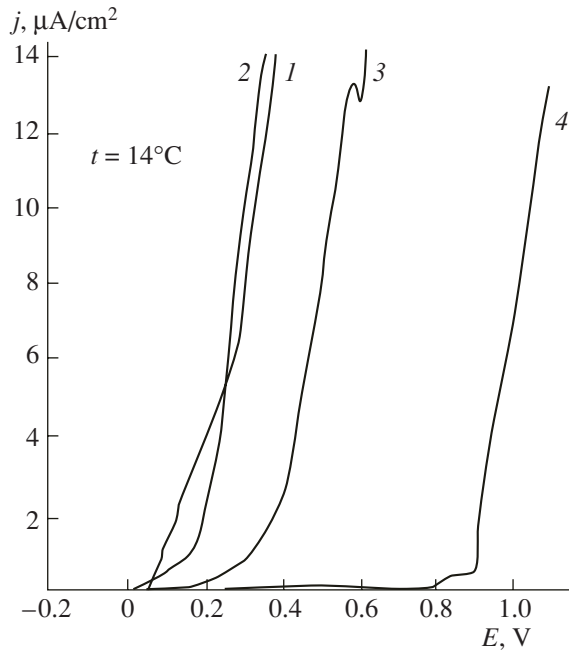
Fig. 1. Anodal polarization curves of the specimens with coatings in 0.9% NaCl solution. (*1*) 20X13 (without coating); (*2*) 20X13 + [Cr + (Cr,Ti)N]$_{10}$; (*3*) 20X13 + (Cr + CrN)$_{10}$; (*4*) 20X13 + (Ti + TiN)$_{10}$.

connected most probably with oxidation of TiN [6], starts on it at relatively high positive potentials (~0.8 V), whereas the region of relative passivity amounts to ~750 mV. A sharp current increase in the region of $E \sim 0.9$ V bears evidence of a change of the anode process nature, whereas a characteristic current oscillation in the time development of the anode poten-

tial indicates a pitting formed in the voids (defect) on the base plate material.

The (Cr + CrN) coatings activate at less positive potentials; the passivity region is 180–200 mV, whereas a pitting formation reaction starts at $E \sim 0.42$ V. This coating is inferior in all the characteristics of the polarization dependence to the (Ti + TiN) coating.

The mixed nitride coatings are characterized by the weakest protective effect in the anode polarization. They, as well as the initial specimen, virtually lack a passivity zone (the reactions start directly from the established value of E_{cor}), whereas the breakdown or pitting formation potential lies within the range of 0.16–0.18 V.

One of the obvious reasons for the corrosion protection properties of this kind of coatings being worse in comparison with the (Cr + CrN)$_{10}$ coating may be its lesser thickness (7 and 10 μm, respectively), the value of which correlates, as a rule, with the number of penetrating voids and defects.

The measurement of the electrochemical characteristics of the contact galvanic couples (Table 2) has shown that the most efficient of them is the first one with the (Ti + TiN) coating being the cathode.

If the material of the base plate is 20X13, then this contact is the least favorable, because it may strengthen (intensify) the pitting corrosion.

The best coating material in terms of the galvanic couples functioning is (Cr + CrN)$_{10}$.

Due to the relatively greater negative potential E_{cor}, this system provides cathode protection for the unprotected 20X13 base plate while remaining inert as an anode ($I = 0$).
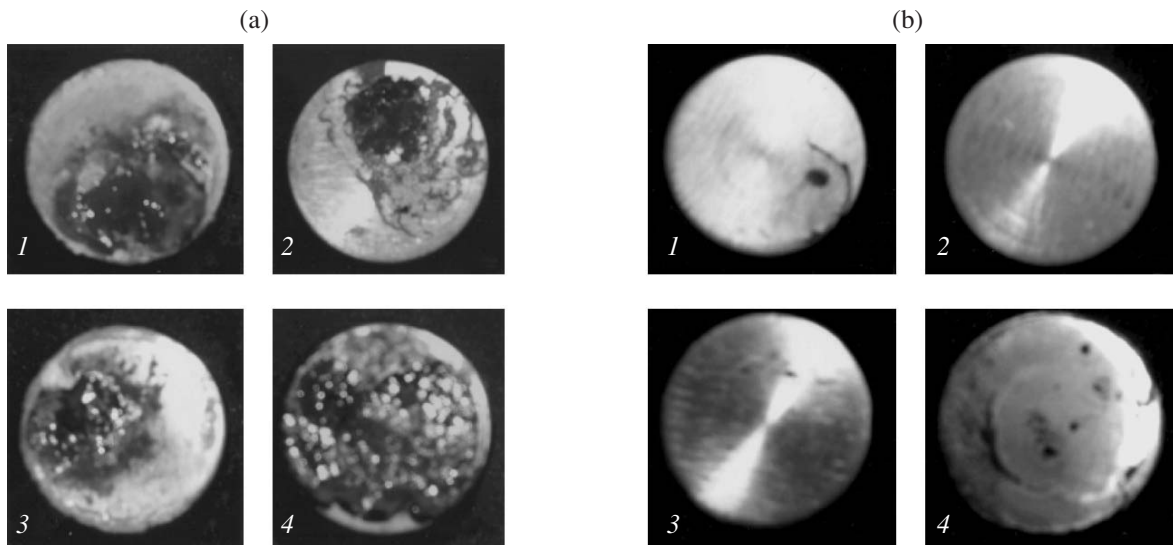

Fig. 2. The surface of the specimens after the corrosion tests in 3% NaCl solution ($t = 95°C$, $\tau = 20$ h). (*1*) (Ti + TiN)$_{10}$; (*2*) (Cr + CrN)$_{10}$; (*3*) [Cr + (Cr,Ti)N]$_7$; (*4*) 20X13. (a) Original state; (b) after removal of the corrosion products.
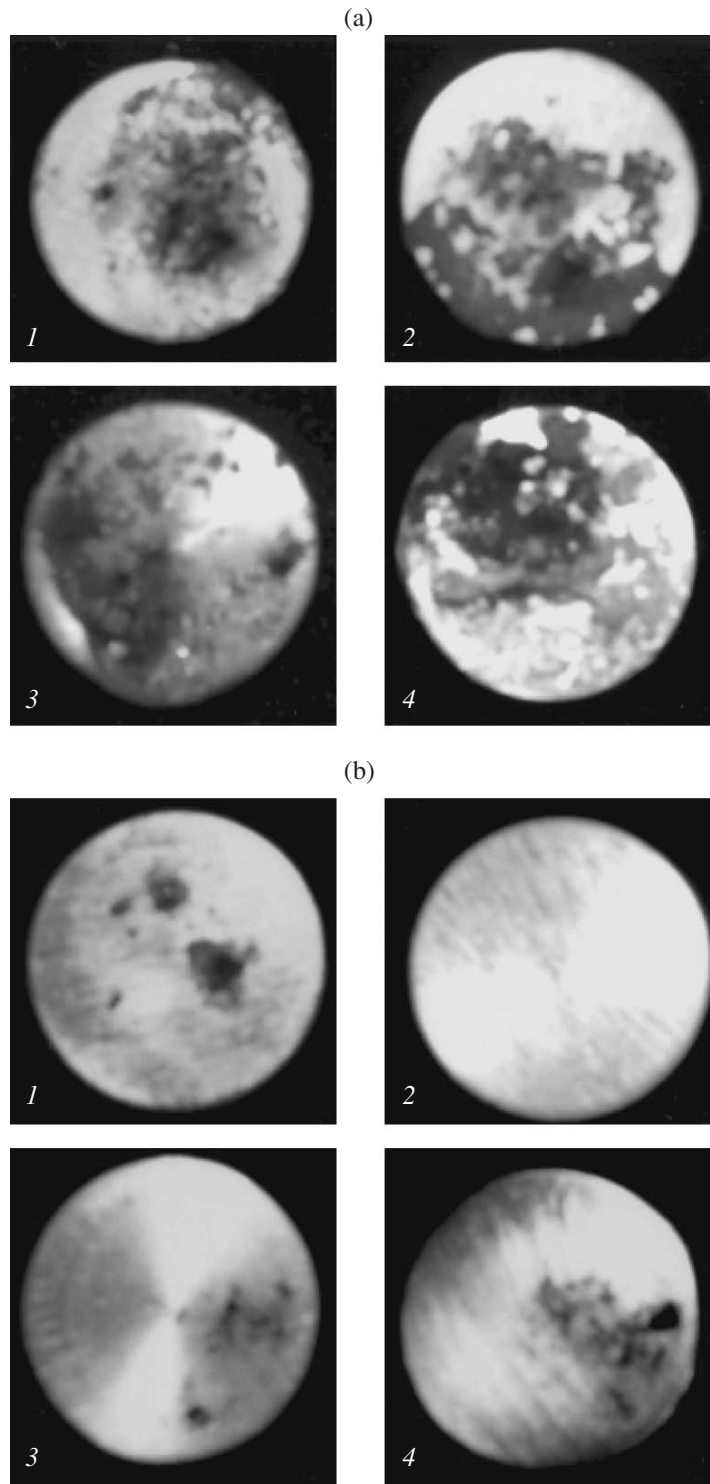
(a)

(b)

Fig. 3. The specimen surface after the corrosion tests in saturated (~28%) NaCl solution ($t = 14°C$, $\tau = 72$ h). (*1*) $(Ti + TiN)_{10}$; (*2*) $(Cr + CrN)_{10}$; (*3*) $[Cr + (Cr,Ti)N]_7$; (*4*) 20X13. (a) Original state; (b) after removal of the corrosion products.

The variant of the steel contact with the mixed nitride coating is rather dangerous for the system with a coating, since it becomes an anode and an active one. The current value of 5 μA is rather large for the surface $S = 2$ cm^2, but it is especially dangerous for the pitting corrosion, which may be significantly intensified under the EMF action.

The mechanical depassivation, simultaneous for two electrodes or just the 20X13 surface, results in an increase of the current for all the variants of the gal-

Table 2. Electrochemical characteristics of short-circuited galvanic couples

Variants of galvanic couples	Material		Stationary conditions		Simultaneous depassivation of electrodes		Depassivation of anode	
	Anode	Cathode	EMF, V	I, μA	EMF, V	I, μA	EMF, V	I, μA
1	20X13	$(Ti + TiN)_{10}$	0.27	8	0.07	11	0.23	31
2	20X13	$(Cr + CrN)_{10}$	−0.06*	0	0.10	12	0.19	28
3	20X13	$[Cr + (CrTi)N]_{10}$	−0.06*	5	0.11	21	0.18	27

* In the galvanic couples, the 20X13 is the cathode.

vanic couples, especially in the second case. Activated steel is a stable anode with respect to all kinds of coatings regardless of the condition of the counter electrode surface. A defining factor for the current increase in the chain is the decrease of the polarization resistance of the anode reaction, which can be observed in the example of the 20X13–(Ti + TiN) couple. Greater values of the generated currents correspond to lesser values of the EMF appearing under the activation of surfaces (one of two simultaneously).

It should be indicated that the mechanical depassivation, while increasing the total current, does intensify the uniform corrosion, and, at that, the pitting formation is suppressed. Therefore, in the presence of erosion processes, the patchy damage of the surface that is under the anode potential is unlikely to be observed. Most probably, some "troubles" from the galvanic couples functioning should be expected in a calm, stationary state (after the turbine stopping, for example).

The results of the corrosion tests of the specimens correlate with the electrochemical investigations of the protective capacity of the coatings.

In the initial observation immediately after the tests (Figs. 2, 3), it was noticed that the specimens suffered the most aggressive impact in 3% NaCl solution under the temperature of 95°C and 20 h long exposure in a humid atmosphere. Relative to the initial 20X13 surface, all the investigated surfaces manifested protective properties but with different effect. According to its increase (correspondingly, the decrease of the visible corrosion products and the damaged area), the coatings may be placed in the following order: Cr + (CrTi)N < Ti + TiN < Cr + CrN.

After removal of the rust, one could see, using 10-fold magnification, some patchy defects of the coatings on the surface having various shapes and sizes. According to the number of visible damages, the specimens can be arranged in a sequence analogous to the one above. The initial surface of the steel, besides local ulceration, suffered general etching.

The corrosion damages on the specimens under the film of saturated NaCl solution were almost identical, at least, in terms of the number of visible patchy damages. The sequence, given above according to the cor-

rosive damages decrease, also remained. The Cr + CrN coating had the best result; the Cr + (Cr,Ti)N coating, the worst one (Fig. 3).

In the general case, it is justifiable to make a conclusion that the results of the various corrosion tests correlate with each other. All the investigated coatings provide a protective effect with respect to the base plate material, 20X13 steel. In the conditions of stationary (without a mechanical impact) corrosion, relatively reliable protection can be expected from the Cr + CrN coating.

CONCLUSIONS

(1) The investigated coating systems $(Ti + TiN)_{10}$, $(Cr + CrN)_{10}$, and $[Cr + (Cr,Ti)N]_{10}$, being cathodal with respect to 20X13 steel, protect it from the electrochemical corrosion in the natrium chloride medium only mechanically. In the considered thickness ranges, all the researched coatings are porous; their protective properties increase in the following sequence: $[Cr + (Cr,Ti)N]_{10} < (Ti + TiN)_{10} < (Cr + CrN)_{10}$.

(2) The coating deposition is conductive to the appearing of microgalvanic couples between them and the base plate material, which may strengthen the pitting corrosion of steel. The (Ti + TiN) coatings are relatively unfavorable: the maximum value of the EMF is generated in the contact with these coatings.

(3) During the mechanical depassivation of the surface taking place in the erosive wear conditions, the galvanic couple intensity increases, especially under the integrity failure of the coatings and the functioning of 20X13 steel as an active anode.

REFERENCES

1. Tomarov, G.V., The Physico-Chemical Processes and Regularities of Erosion–Corrosion of the Metal of the Power Equipment in Two-phase Flow, *Teploenergetika*, 2001, no. 9, pp. 59–67 [*Therm. Engineering* (Engl. Transl.), vol. 48, no. 9, pp. 761–770].

2. Bogachev, A.F., Preventing Corrosive and Other Kinds of Damage to the Equipment of the Steam-Water Path of Thermal Power Stations, *Teploenergetika*, 2001, no. 7,

pp. 65–71 [*Therm. Engineering* (Engl. Transl.), vol. 48, no. 7, pp. 588–594].

3. Rezinskikh, V.F., Bogachev, A.F., Lebedeva, A.I., Ryzhenkov, V.A., and Bodrov, A.A., An Investigation of Promising Protective Coatings for the Exhaust Blades of Steam Turbines, *Teploenergetika*, 1996, no. 12, pp. 28–31 [*Therm. Engineering* (Engl. Transl.), vol. 43, no. 12, pp. 990–993].

4. Kotyar, A.M., Sevidova, E.K., and Steglik, T.V., On the Current Measurement in the Corrosive Elements of Con-structions under their Mechanical Depassivation, *Fiz.-khim. Mekh. Materialov*, 1991, no.1, pp. 103–105.

5. Kostrzhitskii, A.I., On the Stationary Potentials of the "Porous Coating–Base Plate" Complex Electrodes, *Zashchita Metallov*, 1986, vol. 22, no. 6, pp. 960–964.

6. Shvets, V.A., Talash, V.N., Lavrenko, V.A., and Fren-kel', O.A., Specificity of the Corrosion-Electrochemical Behavior of Titan Nitride with Various Nitrogen Contents in 3% NaCl Solution, *Sverkhtverdye Materialy*, 2005, no. 5, pp. 58–64.

Spark Alloying Using Metals and ZrB$_2$-Based Ceramics of Tungsten-Containing Hard Alloys for Increasing Serviceability

A. D. Verkhoturov[a], I. A. Podchernyaeva[b], and L. A. Konevtsov[a]

[a] Institute of Material Science, Khabarovsk Branch, Far East Division, Russian Academy of Sciences,
ul. Tikhookeanskaya 153, Khabarovsk, 680042 Russia

[b] Institute of Problems of Material Sciences, National Academy of Sciences of Ukraine,
ul. Krzhizhanovskogo 3, Kiev, 3680 Ukraine

Received April 10, 2007

Abstract—The possible use of electric-spark alloying using metals and ZrB$_2$-based ceramics for tungsten-containing hard alloys is shown to provide layers on the operating surface of cutting tools with the purpose of increasing their serviceability.

INTRODUCTION

At the present time, more than 80% of the cutting tools (CT) made from tungsten-containing hard alloys (THA) are produced with protective coatings deposited mainly by various methods of thermal-diffusion saturation or by vapor phase deposition (PVD, PCVD). The main disadvantages of these methods are the difficulties of fabrication of composite ceramic coatings with a complex composition and the environmental safety of the technological process, as well as the high cost of the equipment. This investigation is devoted to the development of works on spark hardening of tool materials: structural alloys [1, 2], stamping tools [3], and tungsten-containing hard alloys [4]. To provide the carrying capacity of the CT and resistance to shock loads, coatings are designed with a definite structure (layered gradient or matrix) by means of alternation of hard and solid components [5, 6]. From this viewpoint, the method of electric spark alloying (ESA) is of interest. Along with its low power intensity, this method is characterized by simple and low-cost equipment (2–3 orders of magnitude lower cost), environmental purity, and the possibility to deposit any current-carrying materials including layer-by-layer treatment, especially under conditions of small-lot production [2, 7]. In the literature, data on formation of coatings by the ESA method on THA and their effect on the final parameters of the quality of the parts after cutting are virtually absent.

Refractory titanium compounds were most often selected as the material of the alloying electrode for THA. This is explained by the fact that, due to peculiarities of structural transformations in the surface layers of titanium alloys during ESA and interatomic interactions in the crystal lattice, compounds of Ti with B, C, and N possess a higher level of the properties responsible for the wear resistance of CTs (melting point, hardness, corrosion resistance) compared with tungsten carbide [7, 8]. However, titanium is prone to the formation of loose polyoxide Ti$_y$O$_x$ layers during oxidation. This can exert a negative effect on the continuity and strength of secondary films forming during wet friction in the region of tribocontact during tribooxidation of Ti-containing materials. For this reason, it is necessary to investigate the effect on the properties of CT of coatings from refractory compounds of zirconium. In contrast with Ti, the latter forms a dense layer of ZrO$_2$ scale during oxidation. It is noteworthy that Ti and Zr are isoelectronic and isostructural elements, which should provide the similarity of the physicochemical and physicomechanical properties of their compounds with B, C, and N. The availability of the use of ZrB$_2$-based composite materials for obtaining coatings with increased wear resistance during layer-by-layer ESA of steels is shown in [2, 9]. Studying ESA of THA by carbide-forming elements (Ti/Zr, C) and aluminum attracts our attention. Aluminum can be partially oxidized in an interelectrode spacing with the formation of aluminum oxide and oxynitrides promoting the improvement of the working characteristics of the CT surface [10].

Nickel and chromium from solid solutions with Co and wet zirconium diboride providing adhesion both with the WC–Co basis and with a refractory component of the composite. Starting from the above, the purpose of this work was to investigate the possibilities of increasing the resistance of THA by means of ESA of the cutting edge by aluminum and composite ZrB$_2$-based ceramics with an Ni–Cr–Al binder.
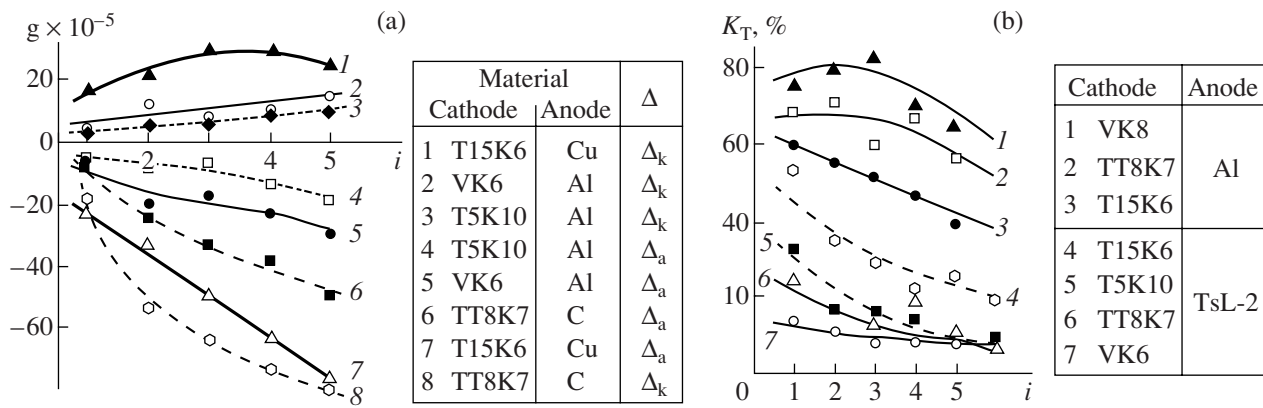
Fig. 1. (a) Variation of the weight of the anode and cathode depending on the number of passages i during ESA using the ELFA-541 setup by metals and graphite and (b) the effect of the number of passages on the variation of K_T. ESA by TsL-2 ceramics was carried out using an Elitron-22 setup.

EXPERIMENTAL

To study the effect of the substrate on the formation of coatings and the cutting properties of the system coating–THA, the basis was a wide spectrum of the most widely used tungsten hard alloys of types VK (WC–Co), TK (WC–TiC–Co), and TT (WC–TiC–TaC–Co) of grades VK6, VK8, TT8K7, T5K10, and T15K6.

As the material of alloying the electrodes, we used metals (Al, Ti, Cu), colloid graphite (C), and composition ceramics TsLAB-2 based on ZrB_2 of the system ZrB_2–$ZrSi_2$–LaB_6 with the binder Ni–Cr–Al (30 mol %). Electrodes in the form of rods $3 \times 4 \times 35$ mm in size from ThLAB-2 were obtained by hot pressing under pressure at ~1900°C.

To test the resistance of the THA, we used pentahedral quick-changing plates of industrial samples for lathe tools with mechanical fastening. The CT wear was measured over the rear face h and front cutting edge l at the cutting tool top. The mentioned parameters of the wear were compared with the parameters of the serviceability of the CT taking into account the qualitative final characteristics of the surfaces of the treated material. As is known from the technology of mechanical engineering [11], these are the parameters of the size accuracy (SA), relative turn (T), and shape (S) obtained due to the cutting treatment. Studies of THA resistance were carried out in the course of turning rods of steel 45 with a diameter of 55–30 mm and a length of 450 mm at finish modes of cutting: rotation frequency of the spindle $n = 1000$ rpm, feed of the longitudinal support $s = 0.07$ mm/rev, cutting depth $t = 0.2$–0.3 mm.

The ESA process was performed using an ELFA-541 setup with the rotation frequency of the spindle $n = 700$–850 rpm, the moving velocity of the longitudinal table $v = 20$–40 mm/min, the transverse feed $s = 0.5$–0.9 mm/passage, the current $I = 0.8$–3.6 A, the voltage

$U = 65$–90 V, the pulse frequency $f = 3$–4 kHz, the pulse duration $\tau = 8$–12 μs, and the capacity of the discharge capacitor $C = 0.68$ mF. To compare the results in a series of modes (obtaining of a liquid phase, ESA TSLAB-2/THA), we used Korona-1101 and Elitron-22A setups. On the ELFA-541 setup, we used electrodes with a diameter of $\varnothing = 1$ mm from aluminum A5, copper M1, titanium VT1-0, and colloid graphite. On the Korona-1101 and Elitron-22A setups, the electrodes had the form of rods with a size of $3 \times 4 \times 35$ mm. To investigate the microstructure of the materials of the anode, cathode, and erosion products, we used MIM-10 and Axiosplan-2 (Carl Zeiss) microscopes, and, to measure the microhardness, we used a PMT-3M device. The element distribution was investigated using a WDS/EDX JXA-8100 combined electron probe microanalyzer with secondary and reflected electrons in various modes (LDF and MDF) with varying the focal distance to obtain the topography of the sample surface. The analysis was carried out under an accelerating voltage of 20 kV and a probe current of 1×10^{-8} A (the beam diameter was 1 μm). The methods of X-ray diffractometry were realized with the use of DRON-3M and ADVANCE diffractometers with monochromated CuK_α radiation at $U = 35$ kV, $I = 40$ mA.

RESULTS AND DISCUSSION

The results analyzed below were obtained using the ELFA-541 setup in the previously mentioned modes. Figure 1 shows the variation of the parameters of the mass transfer with the number of passages of the electrode i during ESA of THA by metals, graphite, and ZrB_2-based composite. Interpreting the obtained results, the dependence of these parameters on the wettability and adhesion interaction between the materials of the anode and cathode should be taken into account.
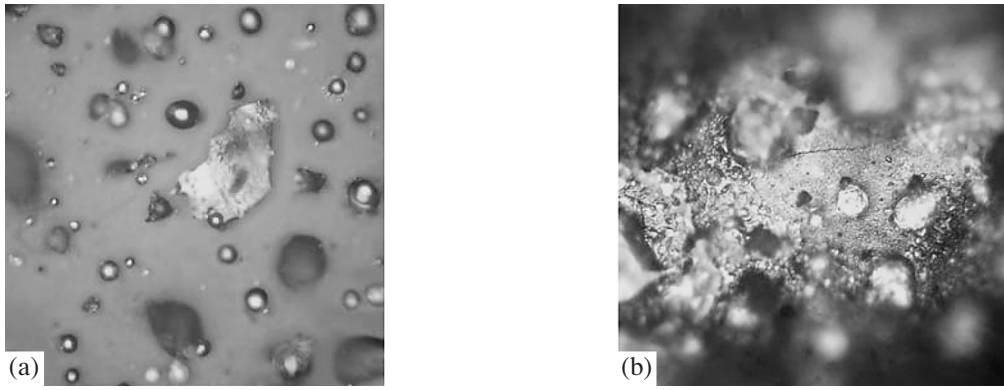
Fig. 2. (a) Erosion products and (b) formation of the secondary structure on the anode during ESA in the TsLAB-2/VK6 × 800 system. The results are obtained using an Elitron-22A setup.

During ESA by Al and Cu metal, the cathode weight continuously increases (Fig. 1a), which points to favorable conditions of formation of the alloyed layer conditioned by the solubility of Al and Cu in the Co-binder of THA. However, during ESA by colloid graphite, loss of the cathode weight over the entire range of i takes place due to intense oxidation of graphite with the formation of volatile CO and CO_2 oxides, which makes its use problematic for accepted modes. It should be noted that, in the previously fulfilled works by Gitlevich, the results of increasing the weight of the T15K6 cathode with the use of an anode from graphite MPG-6 and MG-2 grades were demonstrated, which confirms the necessity to continue investigations on the use of graphite in the processes of ESA for THA. The mass-transfer coefficient $K_T = |\Delta_C|/|\Delta_a| \times 100\%$ (cathode weight increment Δ_C with respect to the anode decrement Δ_a) for all the investigated systems decreases as the number of passages of the electrode i increases (Fig. 1b). During ESA by aluminum, the largest value of K_{WI} is reached for the substrate from VK8 alloy. For the binary and ternary carbide alloys WC–TiC and WC–TiC–TaC, the value of K_{WI} decreases as the TiC content in the alloy increases. This can indicate that the limiting wetting angles by aluminum for titanium carbide are larger than for tungsten carbide.

The mass-transfer coefficient K_T, in contrast with the ESA by aluminum, for the TsLAB-2 material increases as the fraction of TiC in the THA increases reaching the highest value (~35%, the number of passages i = 2) for THA T15K6. This is the result of the adhesion interaction in the ZrB_2–TiC system being stronger than in the ZrB_2–WC system. In general, for all THA, the coefficient K_T during ESA by Al is larger than during ESA by the composite TsLAB-2–(Ni–Cr–Al), apparently due to the stronger wettability of W and WC by aluminum.

The composition of the products of erosion and the secondary structure of the anode exert a substantial effect on the formation of a varied surface layer including K_T (Fig. 2). Under the mentioned technological modes of ESA of THA using the ELFA-541 setup, both globular particles of the liquid phase 0.5–4 μm in size and solid-phase particles ~3–35 μm in size are formed in the products of the erosion. During ESA by aluminum, both transparent particles of γ-Al_2O_3 (leucosapphire) and rare blue azure colored (sapphires) are met [12] formed due to partial oxidation of aluminum in the interelectrode gap.

The results of the metallographic and elemental analyses of the surfaces of the cathode, anode, and erosion products confirm the presence of these phases, including amorphous ones. Due to brittle destruction of the secondary structure of the anode material and the alloyed layer on the anode, the amount of solid-phase particles in the erosion products increases as the number of passages i increases.

In the surface layer of the cathode for the system TsLAB-2/VK6 at $i \geq 5$ passages, gray and brownish gray phases similar to those forming on the anode are formed (Fig. 3). Metallographic analysis shows that, at large values of the working current in the interelectrode gap I = 2.8–3.4 A, a grid of smooth grooves—stress concentrators—is formed on the cathode, and microcracks are formed in the course of prolonged ESA. ESA with the use of the Elitron-22A and Korona-1101 setups, which give a rougher coating, causes the appearance of such grooves and cracks for a duration of 3–4 min/cm^2 and with the use of the ELFA-541 setup for a duration of more than 5–7 min/cm^2. The best conditions for the formation of the surface layer during ESA of THA by aluminum are observed for the number of passages i = 3–6 with allowance made for the K_T, coating thickness h, and roughness Ra.

The flowing micrometallurgical process, depending on the ESA modes, can build up various conditions of formation of the surface layer according to the coating depth and, consequently, its properties with the corre-
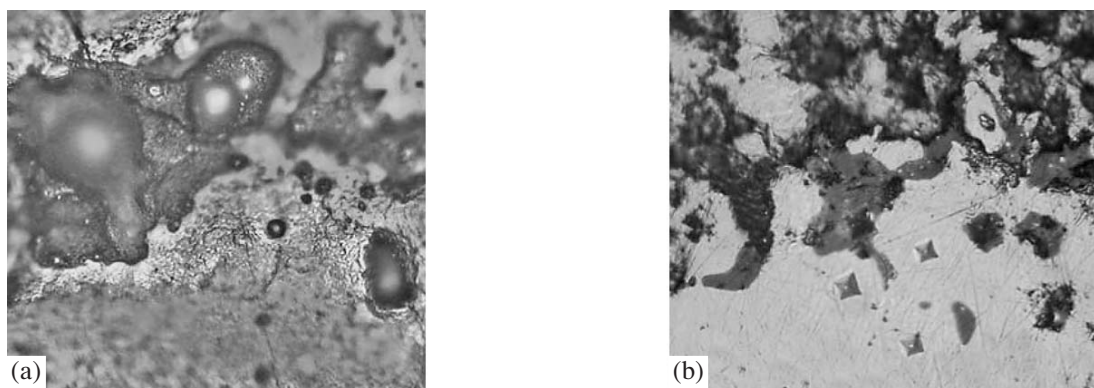
Fig. 3. (a) Microstructure of the coating of the TsLAB-2/VK6 system and (b) diagonal cut. ESA using an Elitron-22A setup: working current $I = 0.8$ A $\pm$ 30%; number of passages $i = 4$; $\times 800$.
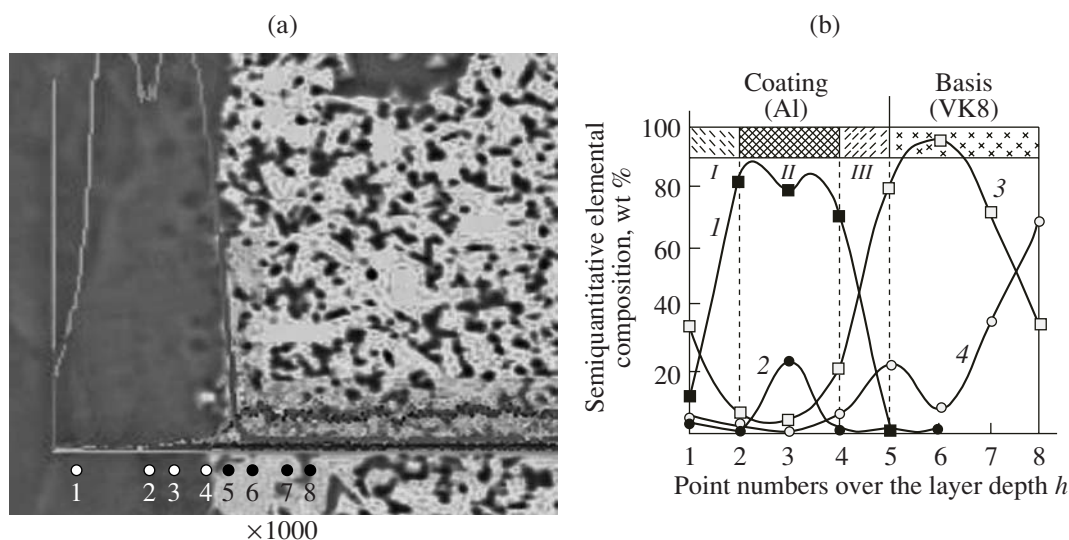

Fig. 4. (a) Microphotographs of the diagonal cut (45°) of the Al/VK8 sample with indication of the points for semiquantitative analysis and (b) variation in the semiquantitative composition (wt %) of the diagonal cut in the direction normal to the basis.

sponding variation in the elemental composition and various phase distribution over the thickness in the direction normal to the basis.

Figure 4 shows the microstructure of a transverse cut of the sample of the system Al/VK8 (a) and variation in the semiquantitative elemental composition (wt %) at points 1–8 in the direction normal to the basis (b). ESA was carried out using the ELFA-541 setup.

Comparing the phase composition of the coating with its elemental distribution over the thickness, we can establish the phase distribution over the layer depth. The obtained X-ray diffraction patterns of the surface of the coating of the Al/VK8 system (appendix, Fig. 1) indicate the presence of tungsten carbide WC, Al, β-W, α-Al$_2$O$_3$, and small amounts of γ-Al$_2$O$_3$ and η-Al$_2$O$_3$. These data indicate partial oxidation of alumi-

num during ESA and dissociation of WC with the formation of β-WC.

The character of the spectra of the energy dispersive X-ray analysis (Fig. 4) allows us to separate three regions with various phase compositions in the alloyed layer: the transient region (III) adjoining the basis, which consists of a mixture of three phases, namely, WC, Co, and Al, provides the adhesion bonding of the coating with the substrate. The widest intermediate region (II) is two-phase. Judging from the Al and O contents in it, as well as by the coincidence of the concentration peaks of Al and O, this region contains a mixture of Al$_2$O$_3$ and Al of equimolar composition (1 : 1). The narrow outer region (I) involves mainly Al and W, probably in the form of a mixture of the phases of tungsten aluminide (WAl$_2$), W, and Al.
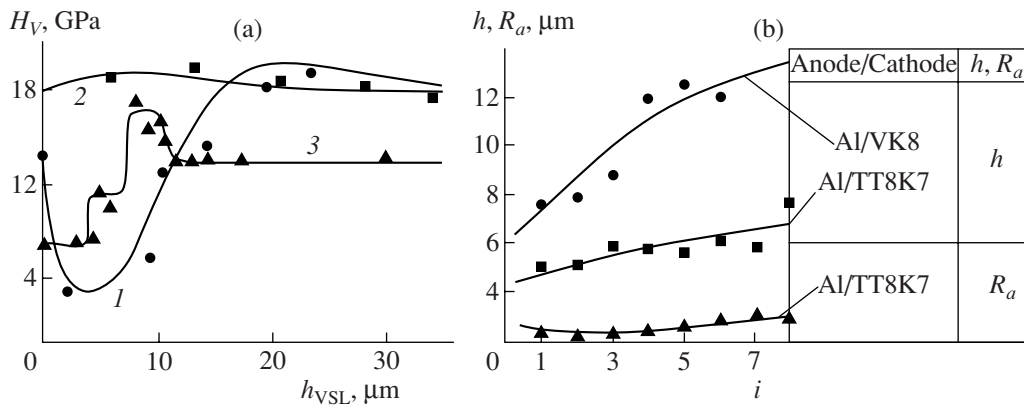
Fig. 5. Variation of micromechanical characteristics of ESA coatings: (a) the microhardness H_V over the thickness h; (b) the thickness h and roughness parameter Ra over the number of passages i for the THA/Al system.

This region immediately contacts with the treated surface and is responsible for the formation of a secondary polyoxide film in the tribocontact region preventing seizure of the working surfaces and playing the role of a solid lubricant under the conditions of dry friction. Aluminum, which is present in all three regions, forms low limiting wetting angles with the main phases of the coating ($\ll 90°$) [13] increasing its adhesion strength.

Figure 5 presents the dependences of the micromechanical characteristics of the ESA coatings of THA on the layer thickness h (a) and on the number of electrode passages i (b). It is evident that the microhardness H_V increases with increasing h reaching the peak value 17 GPa (3–4 GPa higher than the H_V of the VK6 basis) near the boundary with the substrate, which can indicate an increase in the ZrB_2 concentration in this region.

For the Al/TT8K7 system, an abrupt decrease in the microhardness to a depth of ≥ 5 μm in the outer layer precedes an increase in H_V with increasing h (≥ 5 μm). This can be explained both by an abrupt increase in the amount of Al towards the basis in the outer layer and by an increase in the content of the alloy components with increasing the depth h in the inner layer of the coating (Fig. 4).

The layer thickness h and roughness Ra increase as the passage number i increases (Fig. 5b). It is noteworthy that, for ESA by aluminum, the value of h of the coating is higher for the VK8 alloy than for the TT8K7 alloy. This agrees with the maximum value of the mass transfer for the Al/VK8 system (Fig. 1b) and reflects the larger strength of the adhesion force in the Al–WC system compared with the Al–TiC system.

Taking into account the phase distribution in the alloyed layer (Fig. 4) and the reference data for them, by the elasticity modulus E, linear thermal expansion coefficient α, and thermal conductivity λ, we can schematically represent the variation of these parameters

over the coating thickness (Fig. 6a). Intermediate region II is characterized by extreme values of the parameters: minimal E and maximal α and λ. At the coating–basis interface, the difference in the value of α can be compensated for by sufficiently close values of E for the coating and the basis providing the strength of the composite as a whole. The thermal conductivity λ increases over the thickness towards the basis, which builds up favorable conditions of a heat sink from the cutting edge.

The experimentally obtained three-region scheme (Fig. 6a) as a whole agrees with the calculated multistep scheme (Fig. 6b) of the carrying capacity of the coating with optimal distributions of E and α providing both the gradual variation of these properties over the coating depth and their approach to the corresponding magnitudes of the base [6, 7, 9].

The high-temperature oxidation resistance of the cutting edge exerts a large effect on the serviceability of CTs made from THA. In the range of working temperatures of cutting of 650–1000°C in an air medium, the THA samples without a coating are intensely oxidized with the formation of volatile oxides WO_3 with a dominant arrangement near the basis and $CoWO_4$, which is formed preferentially in the upper layer (Fig. 7b). They are easily removed from the friction region along with shavings during the cutting treatment.

The X-ray diffraction patterns of the oxidized surface (Appendix, Fig. 2) confirm the formation of the mentioned oxides. The low corrosion resistance of the THA manifests itself in the large value of the weight increment of the starting samples (without coating) during oxidation (Fig. 8a). Deposition of the ESA coating decreases the weight increment of the THA sample at elevated temperatures by a factor of 4–10 (Fig. 8b).

In this case, the highest corrosion corresponds to the systems Al(Ti)/VK8 and TsLAB-2/TT(TK) with high values of the mass-transfer coefficient (Fig. 1b), i.e., with coatings of high continuity.
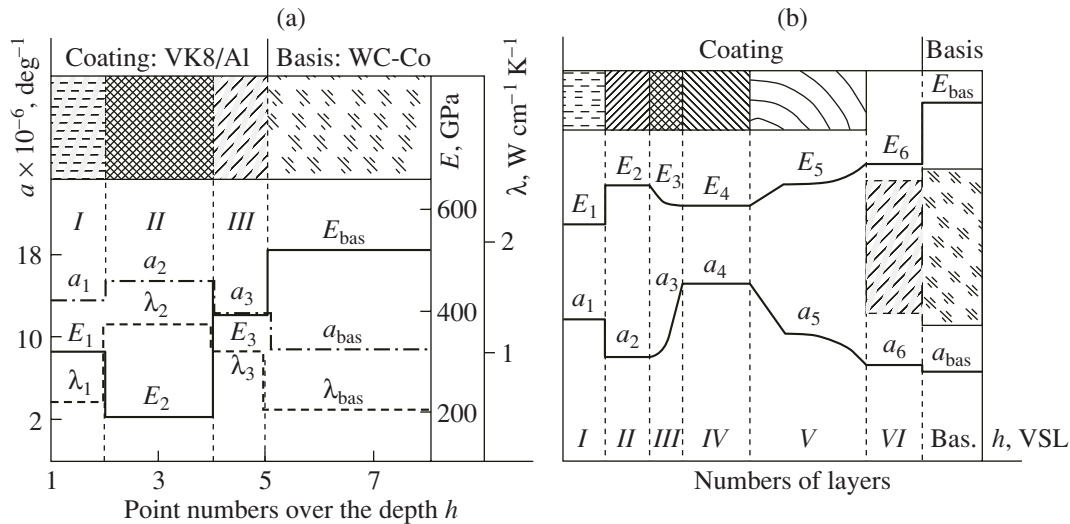
Fig. 6. Distribution of properties (E, α, λ) over the coating depth: (a) experimental scheme for the VK8/Al system; (b) calculated scheme of the carrying capacity of the CT with the optimal distribution of properties in the coating.
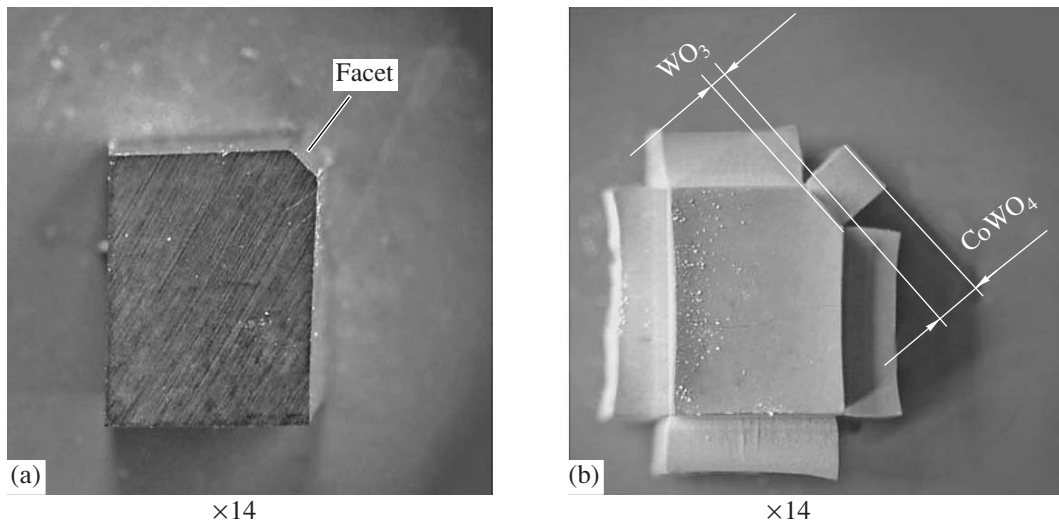

Fig. 7. View of the VK8 sample without coating (a) prior to and (b) after oxidation in air under heating with a rate of 20°C/min to 1000°C and cooling for 1 h.

The formation of corrosion-resistant high-temperature phases both under the steady-state conditions in the scale and in the processes of tribooxidation in the region of the tribocontact is associated with the fact of the corrosion protection of ESA coatings. In the tribooxidation process, the outer layer of the coating, which interacts with the treated part, is responsible for the formation of a polyoxide film in the friction region, which plays the role of a solid lubricant during wet friction. The most probable phases of the secondary film can be tungsten aluminates of the W–Al–O system and Al_2O_3 in the case of the Al/VK8 coating and ZrO_2, SiO_2, and La_2O_3 in the case of the coating from the TsLAB-2 material. Under the enhanced cutting modes, such films, which are strongly bound with the coating material, are difficult to remove from the tribocontact region and are responsible for increasing the level of tribotechnical characteristics.

Tests using parameters characterizing the stability of the CT of the TsLAB-2/VK6 system were performed for the wear of the rear facet h and front cutting edge l (Fig. 9).
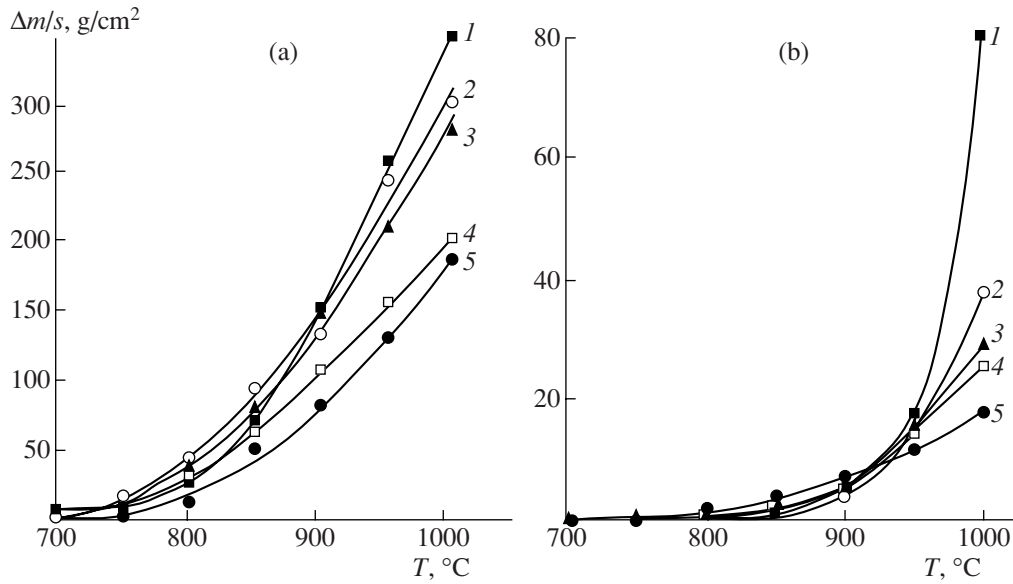
Fig. 8. Specific weight increment of THA in the range of working temperatures on heating with a rate of 20°C/min to 1000°C and cooling for 1 h (a) without a coating and (b) with the ESA coating.
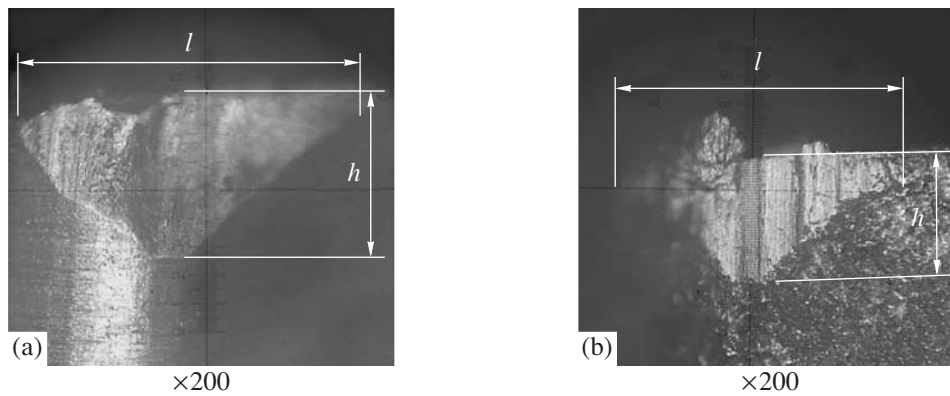

Fig. 9. Wear at the top of the VK6 cutting tool over the rare facet h and front cutting edge l for the cutting way $L = 42$ km ($i = 52$): (a) CT without coating and (b) CT with the TsLAB-2/VK6 coating.

During testing of the dimensional stability of quick-change pentahedral plates from THA without coatings and with ESA coatings of Ti, Zr, Al, and TsLAB-2, it is revealed that the mentioned coatings vary the character of the CT stability during the finish treatment of shafts by the parameters of its final quality during cutting (SA, T, S). For example, during ESA of Al/T15K6 for 4 passages, the error in SA, T, and S depending on the cutting way L after the finish treatment of the shafts (rotation frequency of the spindle $n = 1000$ min^{-1}, feed of the longitudinal support $s = 0.07$ mm/rev, cutting depth $t = 0.25$ mm, shaft length $l = 450$ mm, treated material steel 45) is less than without the coating according to the shape error by a factor of ~1.5 not exceeding 20–25 μm

at the cutting length $L = 1.91–2.09$ km and, by the conicity (relative to the turn of the shaft generatrix to the axis), by a factor of 1.6–1.7 not exceeding 35/300 μm/mm at $L = 1.87–2.28$ km. Similarly, the error in the diameter decreases by a factor of ~1.3 and equals 30 μm at $L = 2.09$ km. The error over the parameters SA, T, and S with the TsLAB-2/VK6 coating at $L = 57$ km is smaller by 20–40% than without the coating.

The variation of the CT wear over the rear facet h_{RF} and cutting edge l_{CE} at the cutting tool top depending on the cutting edge is shown in Fig. 10a. Using the regression analysis, we plotted the trend lines characterizing the variation of the wear at the cutting tool top over the
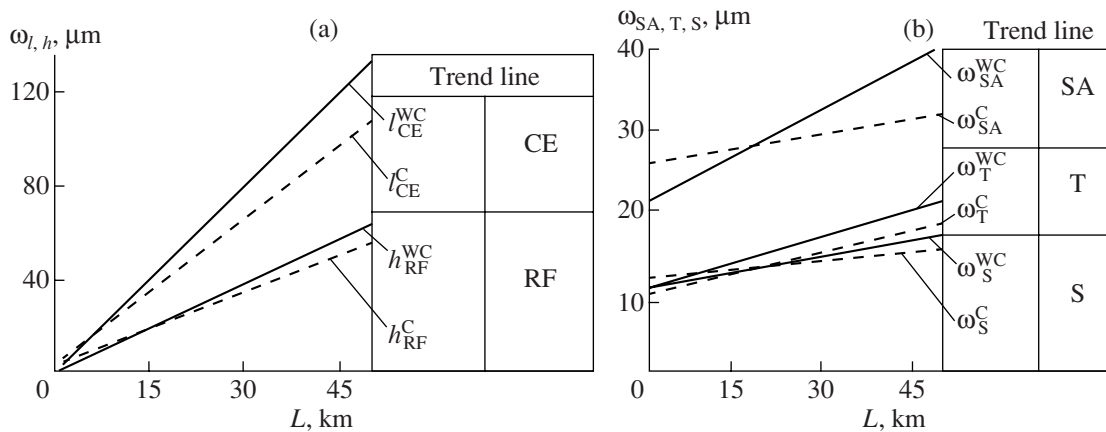
Fig. 10. Trend lines (a) of the wear at the cutting tool top of the rear facet h_{RF}, cutting edge l_{CE}, and (b) for dimensional stability by the error parameters SA, T, and S depending on the cutting way L without a coating (WC) VK6 and with the coating (C) TsLAB-2/VK6.

rear facet and front edge. It is evident that the trend lines reflect the larger wear resistance during cutting of THA with a coating (C) than without it (WC). The equations of the trend lines are as follows:

$$l_{CE}^{WC} = 2.9L + 0.77; \quad h_{RF}^{WC} = 1.3L + 0.37;$$

$$l_{CE}^{C} = 2.3L + 3.4; \quad h_{RF}^{C} = 1.06L + 4.1.$$

The slope tangent of straight lines for the CT without a coating is larger by a factor of ≈ 2.2 than with a coating. Therefore, the wear at the cutting tool top over h_{RF} and l_{CE} has an increased rate larger for the CT without a coating than with a coating. The CT with a coating has a tendency to higher resistance at identical cutting conditions and larger stability to conservation of the equilibrium state of the cutting process without reset.

The trend lines reflecting the tendencies in varying the accuracy parameters of the size, relative turn, and shape during the treatment by the CT without a coating and with the TsLAB-2 coating (Fig. 10b) are described by the following approximation equations for the CT without a coating (WC) and with a coating (C):

$$\omega_{SA}^{WC} = 0.26L + 23.1; \quad \omega_{SA}^{C} = 0.11L + 27.2;$$

$$\omega_{T}^{WC} = 0.16L + 11.3; \quad \omega_{T}^{C} = 0.12L + 12.4;$$

$$\omega_{S}^{WC} = 0.11L + 10.1; \quad \omega_{S}^{C} = 0.08L + 8.92.$$

The general tendency of varying of the accuracy parameters, as it is evident from the obtained equations that characterize the quality of the treated details, also reflects the higher stability to the cutting process of the CT with a coating than without a coating. The slope tangent has values larger by a factor of 2.4, 1.3, and 1.4,

correspondingly, for the straight lines over the parameters SA, T, and S for the CT without a coating than with the TsLAB-2 coating. In this case, for the TsLAB-2 material, the largest wear resistance of the coating on the CT from THA with the highest content of TiC (T15K6) should be expected. This coating provides the largest mass-transfer coefficient (Fig. 1b) forming the maximum coating continuity and, correspondingly, the highest stability to oxidation. The positive effect of the ESA by the aluminum and ZrB_2-based composite on the tribological characteristics of the THA indicates that the ESA is the structure-forming and phase-forming technology due to high-temperature oxidation of products of electroerosion in the interelectrode gap, their interaction, and convective stirring in the melt pool.

A correlation of the data is observed both over the rate of the processes (wear and formation of the error of the cutting treatment) and over their magnitude. A correlation of the obtained results is noticeable according to the parameters of the serviceability of the THA according to the wear h_{RF}, l_{CE} with the results of the error of the SA, T, and S, which, to a large extent, characterize the final parameters of the quality of the cutting process. Consequently, the latter results can be used for evaluation of the dimensional stability of the CT under the conditions when the CT wear is the dominant factor of formation of the treatment error.

CONCLUSIONS

(i) The dependence of the mass-transfer coefficient on the composition of the tungsten-containing hard alloy, which is determined by the adhesion interaction of the alloying components with the refractory components, is established.

(ii) The oxidation resistance of the hard alloy at temperatures of ~1000°C is increased by a factor of four and more during ESA by the metals (Al, Ti) and ZrB_2-based composite, which is explained by the formation of high-temperature corrosion-resistant oxides in a protective scale. The latter are the most probable phases of the secondary film in the region of the tribocontact playing the role of a solid lubricant during the cutting treatment of metals.

(iii) The method of electric-spark alloying provides an increase in the THA resistance by 20–40% over the wear parameters of the rear facet, the cutting edge at the cutting tool top, and the dimensional stability (SA, T, S) during the final treatment of turning the shafts made from steel 45.

(iv) The possibility of formation of a layered structure on THA by the ESA method is shown due to the convection and temperature gradient in the melt pool, the high-temperature oxidation, and the interaction and selectivity of the wetting of the alloying components by the substrate material. Using the ESA method, coatings with various phase compositions of the three-layered structure determining the scheme of the carrying capacity of the CT and variation in the microhardness can be formed, which is shown by the example of the Al/VK8 system.
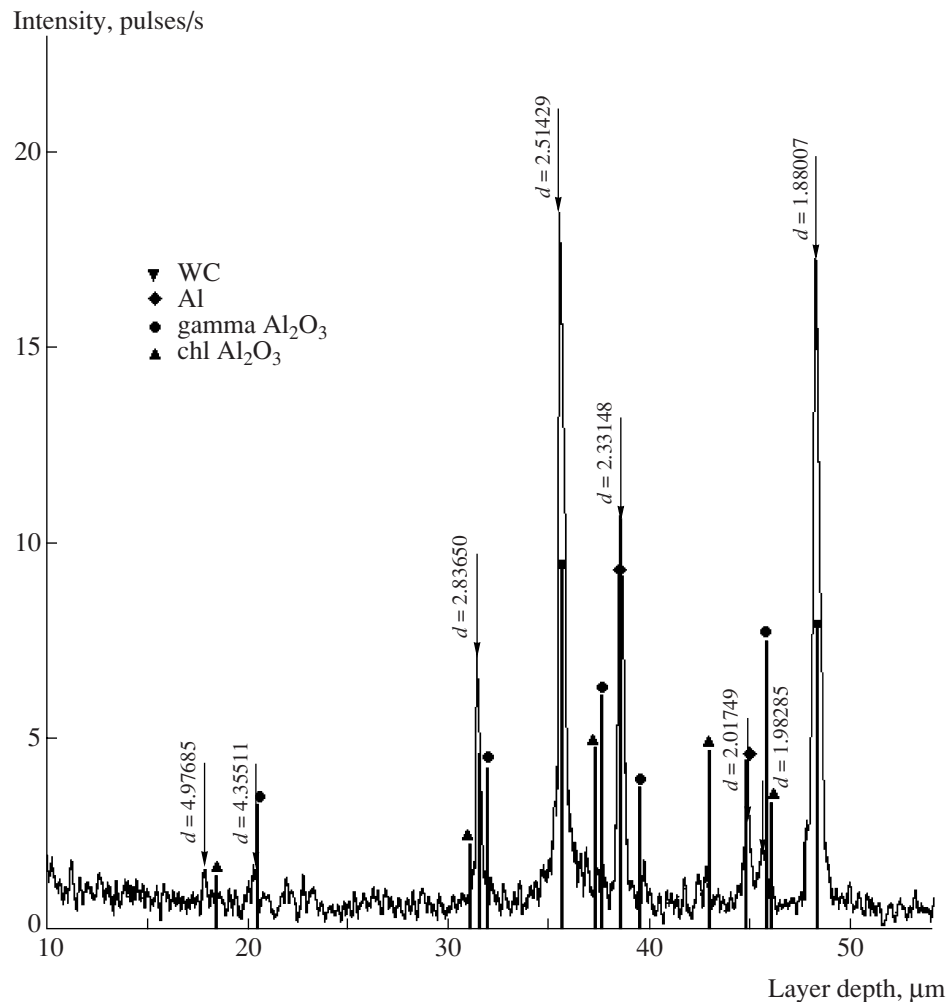
ACKNOWLEDGMENTS

APPENDIX

Fig. 11. X-ray diffraction pattern of the surface layer of the Al/VK8 sample after ESA using the ELFA-541 setup.
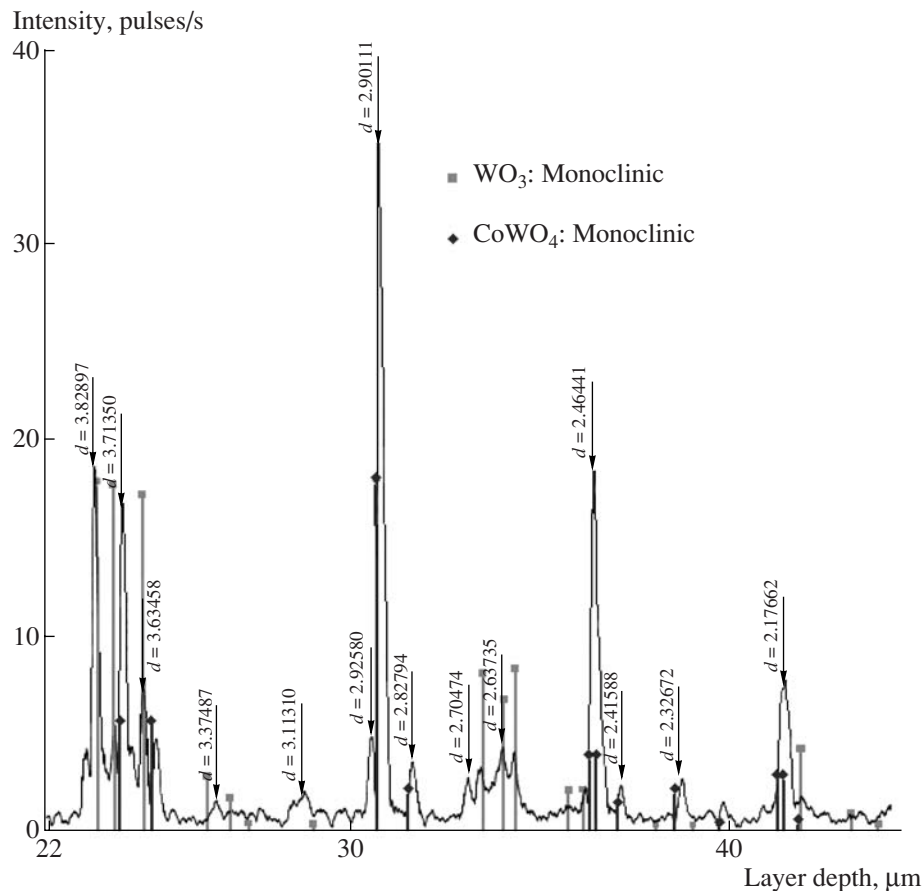
Fig. 12. X-ray diffraction pattern of the VK8 sample without coating after oxidation in air on heating with a rate of 20°C/min to 1000°C and cooling for 1 h.

REFERENCES

1. Podchernyaeva, I.A., Panasyuk, A.D., et al., Electric-Spark Alloying of Construction Alloys by the TiCN–AlN-Based Composite Material, *Poroshk. Metallurg.*, 2000, no. 5/6, pp. 21–29.

2. Podchernyaeva, I.A., Teplenko, M.A., Kostenko, A.D., et al., Effect of Layer-by-Layer Electric-Spark Alloying on the Properties of Composition Electrolytic Coating of the Ni–B System, *Poroshk. Metallurg.*, 2004, no. 1/2, pp. 42–46.

3. Verkhoturov, A.D., Mulin, Yu.I., and Vishnevskii, A.N., Reduction and Strengthening of Matrices for Pressing of Aluminum Profiles by Electric-Spark Alloying, *Fiz. Khim. Obrab. Mater.*, 2002, no. 4, pp. 82–89.

4. Podchernyaeva, I.A., Panasyuk, A.D., Lavrenko, V.A., et al., Effect of Electric-Spark Alloying of Tungsten Hard Alloy on Its Resistance to Wear and Corrosion, *Poroshk. Metallurg.*, 1999, no. 5/6, pp. 42–47.

5. Matthews, A. and Zeyland, A., Developments in Vapour Deposited Ceramic Coatings for Tribological Applications, *Key Eng. Mater.*, vols. 206–213 (2001), pp. 459–466.

6. Verkhoturov, A.D. and Emel'yanov, E.N., Effect of a Surface Gradient of Elastic Properties on the Strength of the Coated Material: TiN Coatings on Hard Alloys with a Transient Region, in *Issledovaniya instituta materialovedeniya v oblasti sozdaniya materialov i pokrytii* (Investigations of the Institute of Material Science in the Field of Development of Materials and Coatings), Vladivostok: Dal'nauka, 2001, pp. 68–74.

7. Fadeev, V.S., Verkhoturov, A.D., Paladin, N.M., and Chigrin, Yu.L., Development and Fabrication of Layered Materials of Tool Destination with a Specified Gradient of Properties, *Perspekt. Mater.*, 2004, no. 5, pp. 45–52.

8. Gitlevich, A.E., Mikhailov, V.V., Taran, G.F., et al., Features of Structural Transformations in Surface Layers of Titanium Alloys during Electric-Spark Alloying, *Electron. Obrab. Mater.*, 1987, pp. 19–22.

9. Podchernyaeva, I.A., Grigor'ev, O.G., Subbotin, V.I., et al., Wear-Resistant Layered Electric-Spark ZrB₂-Based Coatings, *Poroshk. Metallurg.*, 2004, no. 7/8, pp. 77–81.

10. Frantsevich, I.N., Gnesin, G.G., Kurdyumov, A.V., et al., *Sverkhtverdye materialy* (Superhard Materials), Kiev: Naukova Dumka, 1980.

11. Kolesov, I.M., *Osnovy tekhnologii mashinostroeniya. Ucheb. dlya mashinostroit. spets. vuzov. 3-e izd., ster.* (Foundartions of Technology of Mechanical Engineering. Handbook for Mechanical Engineering Specialties of Higher Schools, 3rd Edition, Reprint), Moscow: Vyssh. Shkola, 2001.

12. *Mineralogicheskaya entsiklopediya* (Mineralogical Encyclopedia), Fray, K., Ed., Leningrad: Nedra, 1985.

13. Panasyuk, A.D., Fomenko, V.S., and Glebova, G.G., *Stoikost' nemetallicheskikh materialov v rasplavakh* (Resistance of Non-Metallic Materials in Melts. Reference Book), Kiev: Naukova Dumka, 1986.

Electrochemical Obtaining of Co–Mo Coatings from Citrate Solutions Containing EDTA: Composition, Structure, and Micromechanical Properties

S. P. Sidel'nikova, G. F. Volodina, D. Z. Grabko, and A. I. Dikusar

Institute of Applied Physics of the Academy of Sciences of Moldova,
ul. Academiei 5, Chisinau, MD-2028 Republic of Moldova

Received July 6, 2007

Abstract—The preparation conditions, structure, rate of deposition, and microhardness of electrochemical cobalt–molybdenum coatings from citrate electrolyte containing sodium salt of ethylene diamine tetraacetic acid (EDTA) at pH = 4 in the range of current density of 2–10 A/dm^2 at room temperature are studied. It is shown that, under the investigated conditions, a falling dependence of the current efficiency on the current density and an increase of the Mo concentration in the coatings are observed with the current density increasing. Textured coatings and the increase of the molybdenum concentration at high current density lead to an increase of the microhardness of the coatings. The correlation between the molybdenum concentration in the coatings and their quasi-static and sclerometric microhardness is shown.

DOI: 10.3103/S1068375507060038

INTRODUCTION

In the last years, methods for electrodeposition of cobalt alloys have been intensively developed due to the corrosion, strength, catalytic, and magnetic properties of these coatings [1–5]. Introduction of 5 to 11 wt % molybdenum into cobalt electrodeposits leads to obtaining of materials with good low-coercitivity properties [6–14]. As the molybdenum amount in the alloy grows, its hardness, corrosion stability, and wear resistance increase. The magnetic and strength properties of cobalt–molybdenum alloys make them promising for application in microelectronics.

It is impossible to obtain functional coatings of molybdenum from water solutions; however, when the bath contains the iron group metals, its induced codeposition with obtaining of corresponding alloys occurs. The electrolytic bath composition and electrolysis conditions allow control of the composition and properties of the coatings [1–14]. Co–Mo alloys characterized by magnetic properties are deposited from citrate and citrate–ammonium electrolytes [1, 3, 6–14].

For obtaining alloys with a higher content of molybdenum (up to 50 wt % and more), pyrophosphate and mixed pyrophosphate–citrate solutions are applied [2, 16]. One of the conditions for the induced codeposition is the necessity to introduce complexing agents into the bath composition; usually, they are either citric acid or pyrophosphate or both. In [15], there was shown the efficiency of the additional introduction into the composition of a sodium salt bath of such a widespread complexing agent as ethylene diamine tetraacetic acid (Na$_2$EDTA). The goal of the present work is to study the composition, structure, and micromechanical properties of cobalt–molybdenum coatings obtained from this electrolyte.

EXPERIMENTAL

Electrodeposition was carried out from the electrolyte of the following composition: 100 g/l CoSO$_4$ · 7H$_2$O; 20 g/l Na$_2$MoO$_4$ · 2H$_2$O; 35 g/l H$_3$C$_6$H$_5$O$_7$ (citric acid); 35 g/l Na$_2$EDTA; pH = 3.8 ± 0.3. The deposition occurred in the interval of bulk temperatures of 20–60°C and in the range of current densities of 1–10 A/dm^2. The electrolyte was prepared of chemical agents of the "chemically pure" grade. Coatings were deposited on the samples prepared of St.3 in the form of flags (on an area of 1 cm^2) and disks (2.5 cm^2). Steel disks were placed into a specially prepared frame of organic glass with current lead. The deposition time favored the constancy of the passed charge value. The thickness of the deposited coatings varied within 14–23 μm. The coatings were deposited in the galvanostatic mode with application of the potentiostats PI-50.1 or P-5827M. The samples were preliminarily polished, degreased with Vienna lime, washed, and then treated in dilute hydrochloric acid (1:1) with subsequent washing with distilled water. Graphite served an anode.

The morphology and composition of the coatings were studied by virtue of a scanning electron microscope (TESCAN) with a roentgen system for local chemical analysis (INCA Energy EDX). The analysis was carried out at at least three points of the samples.
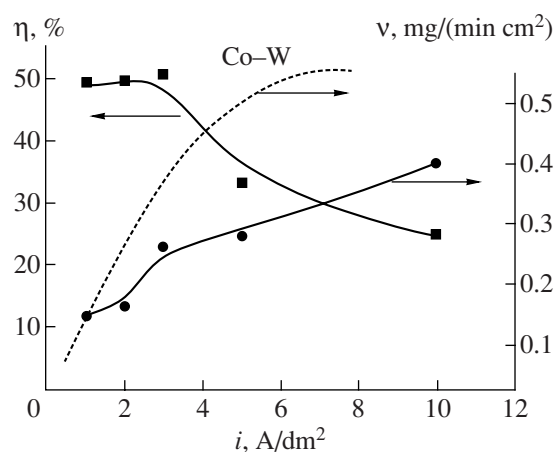
Fig. 1. Current density influence on the current efficiency and rate of cobalt–molybdenum coating deposition.

The results given below are an average of three measurements with root-mean-square deviations.

The structure of the electrodeposits was studied by X-ray phase analysis with application of a diffractometer (ДРОН-3): Co K_α-radiation, Fe-filter, $2\theta/\theta$ method.

The microhardness was measured by two methods: static and dynamic. In the first case, a 50-g load on the indenter was used, and the dimensions of the indentations were registered with application of a microhardness tester (ПМТ-3). The microhardness was calculated by the empiric formula $H_v = 1854\ P/d^2$ [17], where P is the load value, and d is the indentation diagonal (μm). The scratch width with a 20-g load on the indenter was measured by the dynamic method (scratching method, scleroscopy), and the microhardness was calculated by the formula $H_s = 1000\ P/a^2$, where a is the scratch width (μm) [17]. One of the goals of the work was to find the relation between the composition of the coatings and their microhardness and to determine the correlation between various types of

measurable values of the microhardness. The values of the dynamic microhardness (the scratch dimensions give a semiquantitative characteristic of the phenomena of wear, because they are a reflection of the elementary act of abrasive wear of the surface at friction) and their dependence on the coating composition were compared with analogous dependences for the quasi-static microhardness. It is obvious that, when there is an interaction between different types of microhardness measurements, the method for determination of the quasi-static microhardness may be a rapid-test method for estimation of the tribological behavior of the surface for coatings of this kind; this seems to be extremely important for development of new electrolytes and modes of treatment favoring high tribological characteristics of the surface.

RESULTS AND DISCUSSION

In all the cases, in the mentioned range of densities at a temperature of 20°C, from the electrolyte of the given composition, light lustrous coatings were obtained; sometimes they were covered by insignificant dark films. At temperatures of 40 and 60°C, dark thin coatings are deposited. Therefore, the coatings obtained at 20°C were taken for further quantitative measurements.

Current Efficiency and Deposition Rate

Figure 1 shows the dependences of the current efficiency and the deposition rate on the current density. For comparison, the dotted line shows the dependence of the deposition rate of cobalt–tungsten coatings from citrate electrolyte at the same current densities [18]. One can see that the deposition rates for cobalt–molybdenum coatings are lower; this is chiefly due to the lower values of the current efficiency. It is also obvious that the given electrolyte must be characterized by high scattering ability, because, in a wide range of current
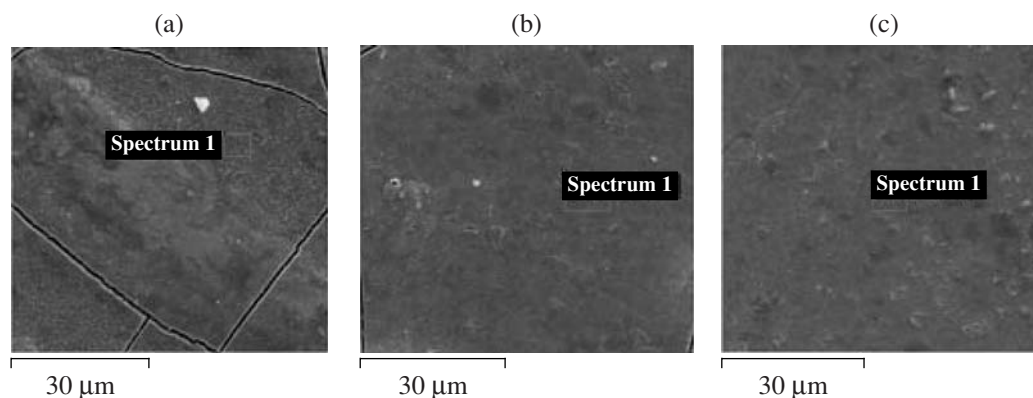

Fig. 2. Morphology of the surface of cobalt–molybdenum coatings deposited at the following current densities, A/dm^2: 2 (a); 5 (b); 10 (c).

(a)

Element	wt %	at %
C K	6.93	21.46
O K	10.51	24.45
Na K	4.50	7.27
Co K	67.96	42.90
Mo L	10.10	3.92
Totals	100.00	

Full Scale 964 cts Cursor: 0.000 keV

(b)

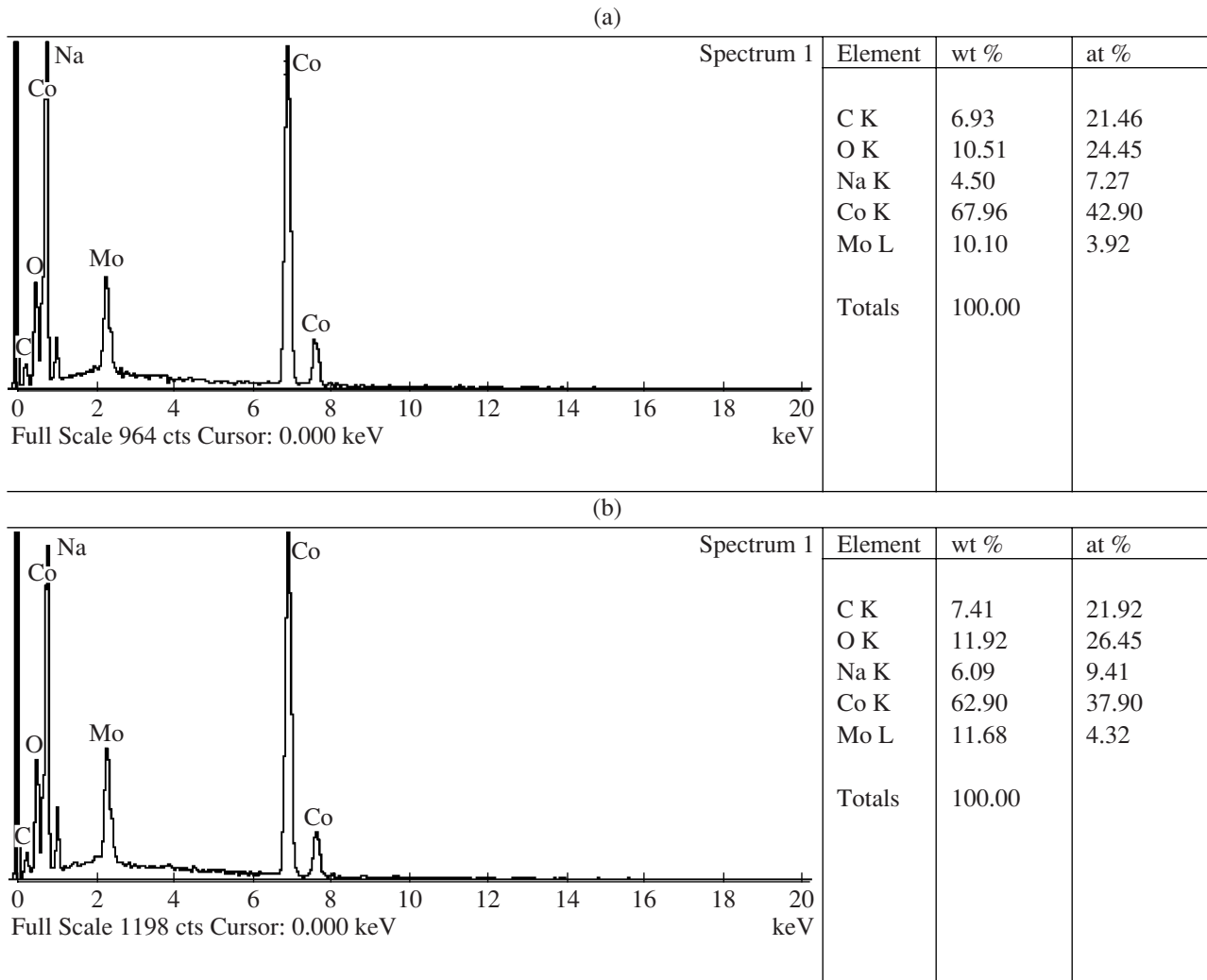| Element	wt %	at %
C K	7.41	21.92
O K	11.92	26.45
Na K	6.09	9.41
Co K	62.90	37.90
Mo L	11.68	4.32
Totals	100.00	

Full Scale 1198 cts Cursor: 0.000 keV

Fig. 3. EDX-spectra and chemical composition of the coatings deposited at the following current densities, A/dm^2: 5 (a); 10 (b).

densities, a falling dependence of the current efficiency on the current density is observed.

Morphology, Composition, and Structure of the Coatings

Figure 2 shows the morphology of the obtained coatings and Figure 3 illustrates the spectra of the EDX analysis and chemical composition of the coatings obtained at current densities of 5 and 10 A/dm^2. One can see that the sample surface is sufficiently uniform though covered by a net of cracks; this is obviously seen on the coatings deposited al low current densities. Earlier, it was mentioned that alloys of cobalt and molybdenum are characterized by cracking [3, 13] and that the density and cracking of the formed coatings depend on the ratio of the concentrations of cobalt salt and citrate. If this ratio is less than one, compact homogeneous films are obtained. At a high ratio (more than
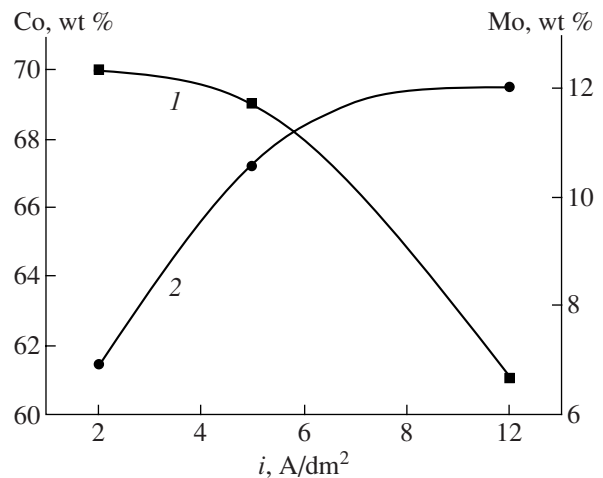
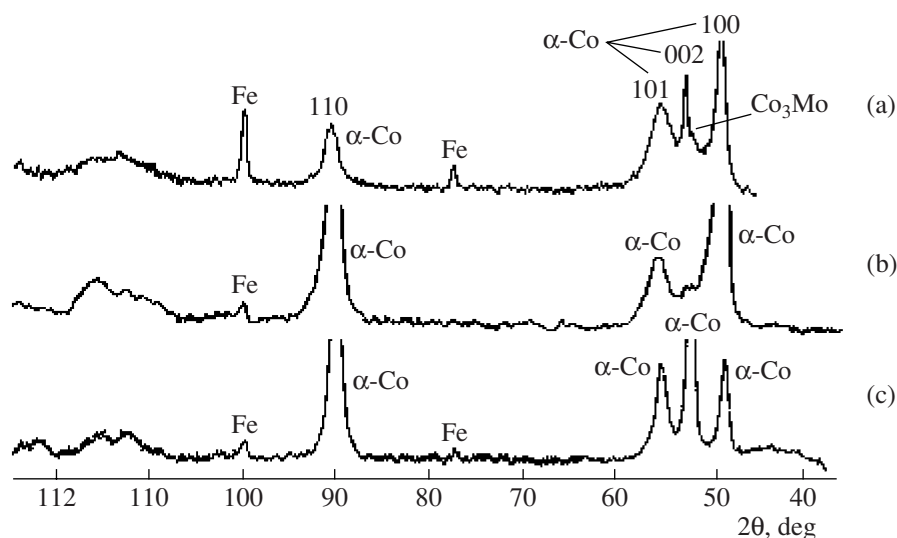**Fig. 4.** The current density influence on the content of cobalt and molybdenum in the coatings: (*1*) Co; (*2*) Mo.

Fig. 5. X–ray spectra of the coatings obtained at the following current densities, A/dm^2: 2 (a); 5 (b); 10 (c).

two), cracked films are formed [13]. In our case (at the ratio of cobalt salt and citrate less than 1), cracking of the deposits may be due to the second complexing agent in the bath composition (Na$_2$EDTA) and due to the sufficiently great thickness of the coatings.

Data of the chemical composition of the coatings count in favor of the fact that, in addition to cobalt and molybdenum, they contain sodium, carbon, and oxygen in appreciable amounts (Fig. 3). As a matter of fact, components of the organic phase (citrate, EDTA sodium salt) may be "trapped" by the deposit and, therefore, enter into its composition. Considerably high measurable concentrations of light elements may be due to peculiarities of the EDX analysis. In the applied variant, a layer of 2-μm depth was analyzed; it is natural that the role of the elements constituting the surface layer (including the adsorbed one) was appreciable, thus affecting the surface analysis results. It should be also noted that the error of the EDX analysis is 3–5% [16].

The influence of the electrodeposition current density is shown by a decrease of the cobalt concentration in the coating and an increase of the molybdenum content with this density increasing (Fig. 4), the molybdenum concentration being relatively low (12 wt %). At this concentration, cobalt–molybdenum coatings behave as good magnetic materials [6, 9, 11, 14] and the deposition rate is a method for control of the molybdenum content in the coating.

Results of the X-ray diffractometry are shown in Fig. 5. The diffractograms contain, in addition to the lines α-Fe (substrate), the lines corresponding to the diffraction spectra of polycrystalline hexagonal α-Co. A small shift of the lines towards lesser angles is due to probable implantation of molybdenum atoms into the cobalt structure. The spectra contain the line with $d = 2.05$ Å ($2\theta = 51.9°$), which may belong to the Co$_3$Mo structure. For the sample obtained at a current density of 2 A/dm^2, the relative intensities of the spectrum lines practically correspond to filed data (Fig. 5a); i.e., this is a polycrystalline residue with an arbitrary position of its crystallites. Sharply increased intensities of reflections 100, 110, and 002 on diffractograms of the samples obtained at current densities of 5 and 10 A/dm^2 (Figs. 5b and 5c) signify their being textured. The spectrum of the sample obtained at 5 A/dm^2 (Fig. 5b, lines 100 and 110 are intensified) counts in favor of the fact that crystallites are deposited on the substrate surface mainly by faces 1010 and 1120, and, in the spectrum of the sample obtained at a current density of 10 A/dm^2 (Fig. 5c), lines 110 and 002 are intensified. In this case, crystallites are deposited on the substrate surface by lateral faces of the hexagonal prism 1120 and its basal plane 0001.

The different nature of the texturing of the studied deposits and their different chemical composition must influence the functional properties of the surface.

Microhardness of the Deposits

The data given in Fig. 6 show that an increase of the electrodeposition current density leads to a significant increase of the coating microhardness. It is noteworthy that, despite the relatively low concentration of molybdenum in the coating (slightly higher than 4 at %), the quasi-static microhardness is considerably high (750 kg/mm^2). A correlation is observed between the static and dynamic microhardness, and a clearly defined dependence is observed between both types of the measured microhardness and the molybdenum concentration in the coating (Fig. 7). It should be emphasized that the high values of the microhardness are apparently affected by both the increase of the molyb-
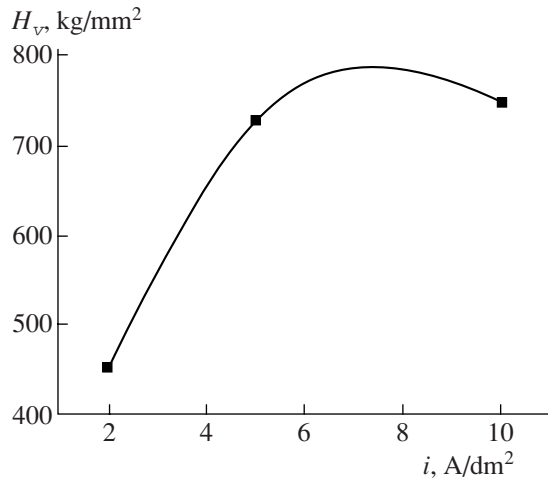
H_v, kg/mm^2

Fig. 6. Static microhardness dependence on the coating electrodeposition current density.
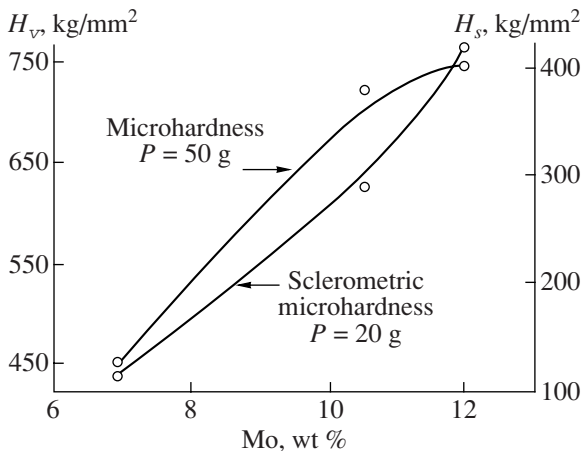
H_v, kg/mm^2 H_s, kg/mm^2

Fig. 7. Influence of the molybdenum content in the coatings on their quasi-static and sclerometric microhardness.

denum concentration in the coating and the texture of the deposit; in totality, this leads to achievement of high microhardness values.

It was noted in works [13, 14] that induced codeposition of molybdenum and cobalt at low concentrations of the former in the coatings allows preservation of satisfactory magnetic properties derived from cobalt (in particular, the high level of magnetic saturation at low coercive force; this allows their consideration as promising low-coercitivity materials). The results of the work show that coatings of the kind obtained from citrate electrolyte containing EDTA must be characterized by satisfactory tribological behavior, i.e., high wear resistance at friction.

CONCLUSIONS

There emerged a possibility to obtain qualitative cobalt–molybdenum coatings at room temperature from the citrate electrolyte containing an additional complexing agent—EDTA sodium salt. The deposition rate and current efficiency dependence on the current density, as well as the morphology, structure, and composition of the obtained coatings, are determined. It is shown that, as the current density increases (5–10 A/dm^2), the molybdenum content in the coatings and their texture increase; as a result, the microhardness of the coatings is improved (750 kg/mm^2). It is shown that these coatings are promising for their application in microelectronics as low-coercitivity materials.

ACKNOWLEDGMENTS

REFERENCES

1. Brenner, A., *Electrodeposition of Alloys*, New York: Academic Press, 1963, vols. 1–2.

2. Krohn, A. and Brown, T.M., Electrodeposition of Cobalt–Molybdenum Alloys, *J. Electrochem. Soc.*, 1961, vol. 108, no. 1, pp. 60–70.

3. Vyacheslavov, P.M., *Elektroliticheskoe osazhdenie splavov* (Electrolytic Deposition of Alloys), Leningrad, 1971.

4. Vas'ko, A.T., *Eektrokhimiya molibdena i vol'frama* (Electrochemistry of Molybdenum and Tungsten), Kiev, 1977.

5. Podlaha, E. J. and Landolt, D., Induced Codeposition III. Molybdenum Alloys with Nickel, Cobalt, and Iron, *J. Electrochem. Soc.*, 1997, vol. 144, no. 5, pp. 1672–1680.

6. Gomez, E., Pellicer, E., and Valles, E., Electrodeposited Cobalt–Molybdenum Magnetic Materials, *J. Electroanal. Chem.*, 2001, vol. 517, pp. 109–116.

7. Gomez, E., Pellicer, E., and Valles, E., Influence of the Bath Composition and the pH on the Induced Cobalt–Molybdenum Electrodeposition, *J. Electroanal. Chem.*, 2003, vol. 556, pp. 137–145.

8. Gomez, E., Pellicer, E., and Valles, E., Detection and Characterization of Molybdenum Oxides Formed During the Initial Stages of Cobalt–Molybdenum Electrodeposition, *J. Appl. Electrochem.*, 2003, vol. 33, pp. 245–252.

9. Gomez, E., Pellicer, E., and Valles, E., Microstructures of Soft–Magnetic Cobalt–Molybdenum Alloy Obtained by Electrodeposition Seed Layer/Silicon Substrates, *Electrochem. Comm.*, 2004 vol. 6, pp. 853–859.

10. Gomez, E., Pellicer, E., and Valles, E., Intermediate Molybdenum Oxides Involved in Binary and Ternary

Induced Electrodeposition, *J. Electroanal. Chem.*, 2005, vol. 580, pp. 238–244.

11. Gomez, E., Pellicer, E., and Valles, E., Electrodeposition of Soft–Magnetic Cobalt–Molybdenum Coatings Containing Low Molybdenum Percentages, *J. Electroanal. Chem.,* 2004, vol. 568, pp. 29–36.

12. Gomez, E., Pellicer, E., and Alcobe, X., Properties of Co–Mo Coatings Obtained by Electrodeposition at pH 6.6, *J. Solid State Electrochem.*, 2004, vol. 8, pp. 497–504.

13. Gomez, E., Pellicer, E., and Valles, E., Developing Plating Bath for the Production of Cobalt–Molybdenum Films, *Surface Coatings Technology*, 2005 vol. 197, pp. 238–246.

14. Gomez, E., Pellicer, E., Duch, M., Esteve, J., and Valles, E., Molybdenum Alloy Electrodeposits for Magnetic Actuation, *Electrochim. Acta,* 2006, vol. 51, pp. 3214–3222.

15. Socha, J. and Zak, T., Poland Patent 70948, 1974.

16. Martin–Gonzales, M., Prieto, A.L., Gronsky, R., Sands, T., and Stacy, A.M., High Density 40 nm Diameter Sb–Rich $Bi_{2-x}Sb_xTe_3$ Nanowire Arrays, *Adv. Mater.*, 2003, vol. 15, no. 12, pp. 1003–1006.

17. Boyarskaya, Yu. S., Grabko, D.Z., and Kats, M.S., *Fizika protsessov microindentirovaniya* (Physics of Microindentation Processes), Chisinau, 1986.

18. Tsyntsaru, N.I., Belevskii, S.S., Volodina, G.F., Kublanovskii, V.S., Bersirova, O.L., Yapontseva, Yu.S., and Dikusar, A.I., Composition, Structure and Corrosion Properties of Coatings of Co–W Alloys Electrodeposited at Direct Current, *Elektron. Obrab. Mater.*, 2007, no. 5, pp. 9–15.

Promotion of Steel Corrosion Resistance by Chemical-Thermal Treatment in Electrolytes

V. V. Parshutin and E. A. Pasinkovskii

Institute of Applied Physics, Academy of Sciences of Moldova, ul. Akademiei 5, Chisinau, MD-2028 Moldova
Received June 13, 2007

Abstract—A method of promotion of steel corrosion resistance by 2.6–7.4 times by steel working in a 10–30 g/l water solution of sodium nitrite after electrolytic heating-oxidation is proposed. It can be used for treatment of machine parts, tools, and production accessories and for an essential increase in their working lives without application of expensive coatings.

In the usual metallurgical doping technique to produce an alloy with enhanced anticorrosion and mechanical properties, as a rule, expensive rare alloying ingredients are applied. However, since the corrosion resistance of parts is determined in general by the properties of the surface and nearby layers, the usual metallurgical doping is very prodigal. Therefore, it is economically feasible and promising to apply surface treatment, for example, nitration with the use of electrolytic plasma [1].

A chemical-thermal metal processing technique under electrolytic heating is known. It is produced using an anodic process in an aqueous solution of an electrolyte containing nitric acid, sal ammonia, and glycerin [2]. A limitation of this technique is the presence of a toxic agent (nitric acid) and the weak formation of the oxide film on the processed surface, which enhances the corrosion resistance of steel parts.

Also, nitration in an electrolyte is used [3], in which the process is performed with anodic heating in an electrolyte containing nitrogen compounds: (1) 10% NH_4Cl and 5% NH_4OH; (2) 11% NH_4Cl and 11% NH_4NO_3. Cooling of the parts is carried out either in the electrolyte after turning off the current or in air. In this case, the part's surface layer becomes saturated with nitrogen with the formation of nitrides, and an oxide film is formed on them owing to the high-temperature oxidation of the surface in vapors of the aqueous solution of the electrolyte. However, the film formed has a small thickness and insufficient continuity, which decreases the corrosion resistance of the parts.

The objective of this work is to enhance the corrosion resistance of the surface of parts subjected to chemical-thermal processing due to additional oxidation.

EXPERIMENTAL

The chemical-thermal processing is fulfilled for specimens of 45 steel with a diameter of 30 mm and a height of 25 mm in the electrolytes: (1) 11% NH_4Cl and 11% NH_4NO_3 (11/11 electrolyte); (2) 10% NH_4Cl and 5% NH_4OH (10/5 electrolyte). The part was connected to the anode, the electrode voltage was 150–220 V, the current density was 1–2.5 A/cm^2, and the treatment temperature was 750°C. The handling time was 3–5 min. Then, the specimen under current was taken out of the bath; the current was switched off; and, immediately afterwards, it was put into a quenching medium (a 20–30 g/l sodium nitrite solution) for temperature equalizing with the cooling medium.

The corrosive effect was estimated by the corrosion rate, the potential-dynamic polarization curves (4 mV/s), and the values of the anodic dissolution currents measured using a P-5827M potentiostate in a 0.05 M solution of Na_2SO_4.

RESULTS AND DISCUSSION

The technique of the thermal and chemical-thermal processing of steel products is developed, in particular, for processing in the anodic process of electrolytic heating. It involves initial heating of the part; the simultaneous surface saturation of the part by nitrogen; the high-temperature oxidation of its surface in vapors of the electrolyte aqueous solution; and, after chemical-thermal processing, additional oxidation in the 10–30 g/l sodium nitrite aqueous solution.

Not only does the thickness of the anodic coating increase by 2–3 times but its continuity is also enhanced, which results in the significant enhancement of the anticorrosion properties of the finished part.

The work part serves as the anode in an electrolyzer containing an aqueous solution of nitrogen compounds. At voltages of 100–200 V and current densities of tens of A/dm^2, the electrolyte in the anode region boils up and separates from the part as a continuous vapor film, through which the current flows by electric discharges. The source energy liberation is localized in the vapor

Table 1. Effect of a type of processing on currents of anodic dissolution in a 0.05 M solution of Na_2SO_4 (the numerator is the 11/11 electrolyte and the denominator is the 10/5 one)

| Processing	i_a, A/m² at −0.1 V	i_a, A/m² at 0.1 V
Without processing	168	308
Without additional oxidation	59.1/62.4	285/293
With additional oxidation in 20 g/l $NaNO_2$ solution	10.2/11.05	15.4/16.3
With additional oxidation in 10 g/l $NaNO_2$ solution	19.2/20.79	22.3/23.6
With additional oxidation in 30 g/l $NaNO_2$ solution	8.4/9.05	11.6/12.26

Table 2. Effect of the type of processing and the processing time on the rate of the specimen corrosion (the numerator is a 10 g/l $NaNO_2$ solution and the denominator is a 30 g/l $NaNO_2$ solution)

Electrolyte	Method of cooling	Corrosion rate c, g/(m² day)		
		8 h	24 h	72 h
10/5	In electrolyte	24.35	8.64	5.76
	In $NaNO_2$ solution	8.05/7.5	2.15/2.05	1.1/1.01
11/11	In Electrolyte	16.45	7.72	6.3
	In $NaNO_2$ solution	6.41/5.95	1.9/1.76	0.9/0.85

film, and part of it is consumed on heating the anode, whose temperature can be adjusted smoothly by changing the voltage in the range of 400–950°C. The presence of the nitrogen compound in the solution causes a necessary concentration of the saturating component in the covering, its adsorption on the anode surface, and diffusion into the metal. However, the presence of water vapor in the anode region results in the high-temperature oxidation of the steel surface and the formation of an initial oxide film on it.

After taking the part under current out of the solution, switching off the current, and moving the red-hot part into the $NaNO_2$ solution, its oxidation (quenching) and the additional growth and compression of the oxide film at the part surface occur by the oxidizing ability of the NO_2^- ion:

$$2Fe + NaNO_2 + 2H_2O \longrightarrow \gamma\text{-}Fe_2O_2 + NaOH.$$
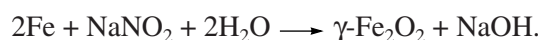
From the experiment, it is seen (Tables 1 and 2) that additional quenching (oxidation) of the specimen in the sodium nitrite solution (for two selected electrolytes) decreases the currents of the anodic dissolution at the potential $\varphi = -0.1$ V (for example, at an $NaNO_2$ concentration of 20 g/l) by more than 5.6 times and by more than 18 times at $\varphi = 0.1$ V. In this case, after additional oxidation in the 30 g/l $NaNO_2$ solution, the corrosion rate decreases after 8 h of tests by 3.0–3.2 times (processing in the 10/5 electrolyte) and by 2.6–2.8 times (11/11 electrolyte); after 24 h, by 4.0–4.2 times (10/5 electrolyte) and 4.1–4.4 times (11/11 electrolyte); and, after 72 h, by 5.2–5.7 times (10/5 electrolyte) and 7–7.4 times (11/11 electrolyte). It is clear that the maximum increase in the corrosion rate takes place on oxidation in the $NaNO_2$ solution of a more high concentration. However, the use of the concentration below 10 g/l gives an unexpected result, and, at the $NaNO_2$ concentration of more than 30 g/l, the oxidation mechanism changes and the corrosion resistance increases insignificantly.

From a study of the potential-dynamic polarization curves (see figure), it is evident that the maximum difference is observed between the behaviors of steel 45 unprocessed and chemical-thermally processed (curves *1* and *2*); i.e., the currents after processing decrease by almost three orders. The additional oxidation leaves the
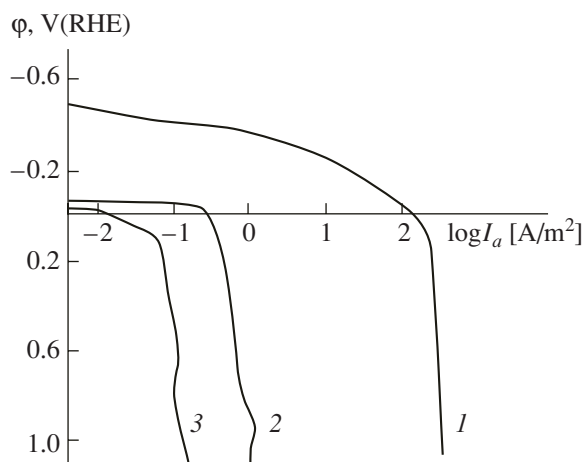
Polarization curves of 45 steel unprocessed (*1*), processed (*2*) in the 10/5 electrolyte, and additionally quenched in the 20 g/l $NaNO_2$ electrolite (*3*).

pattern of the curves unchanged but, in addition, decreases the current by almost an order of magnitude in comparison with the steel processed in the 10/5 electrolite. After chemical-thermal processing, the active dissolution potential of the steel is shifted in the positive direction by 400 mV in comparison with the unprocessed steel. The additional oxidation of the surface in the 20 g/l $NaNO_2$ electrolite shifts this by ~70 mV. A similar phenomena is observed on processing the steel in the 11/11 electrolyte.

Thus, the technique of the thermal and chemical-thermal processing of steel products is developed, in particular, for processing in the anodic process of electrolytic heating, which allows one to significantly enhance the corrosion resistance of machine parts, tools, and production accessories and their working lifetime without application of expensive coatings.

REFERENCES

1. Parshutin, V.V., Revenko, V.G., Pasinkovskii, et al., Effect of the Method of Introduction of Nitrogen on Electrochemical, Corrosion Behavior and Physicomechanical Properties of Modified Surfaces of Steels, *Elektron. Obrab. Mater.*, 2004, no. 4, p. 14.

2. Zemskii, S.V., Faktorovich, A.A., Belkin, P.N., et al., USSR Inventor's Certificate no. 969 761, *Byull. Izobret.*, 1982, no. 40.

3. Revenko, V.G., Chernova, G.P., Parshutin, V.V., et al., Effect of Parameters of Nitridation in Electrolyte on the Protective Properties of Conversion Coatings, *Zashch. Met.*, 1988, no. 2, p. 204.

4. Parshutin, V.V. and Pasinkovskii, E.A., Moldova Patent 2959, *Byull. Izobret.*, 2006, no. 1.

ELECTRICAL PROCESSES
IN ENGINEERING AND CHEMISTRY

Features of Electrohydrodynamic Flows
in a Multielectrode System

M. K. Bologa[a], F. P. Grosu[b], and I. V. Kozhevnikov[a]

[a] Institute of Applied Physics, Academy of Sciences of Moldova,
ul. Academiei 5, Kishinev, MD-2028 Republic of Moldova
[b] State Agrarian University of Moldova,
ul. Mirchesht' 44, Kishinev, MD-2049 Republic of Moldova
Received August 14, 2007

Abstract—The electrohydrodynamic flow in the system "needle–two wires" has been investigated using the Shadow method with simultaneous recording of the transversal pumping intensity. An unstable electrohydrodynamic flow appears as a fluctuation of the central jet (flow from the blade) between the electrodes, which results in decreasing of the efficiency of the three-electrode system. The possibility of electrohydrodynamic flow stabilization by means of decreasing the interelectrode gap and using an additional, fourth electrode, which is situated behind the first two electrodes, is shown. A theoretical model of the pumping process considering the flow as a diffuser flow from the blade limited by two lateral eddies near the upper electrode collectors is proposed. As the electrohydrodynamic flow develops, the average speed of the diffuser flow, as well as the eddy dimensions, is increasing. These two factors influence the maximum flow rate of the electrohydrodynamic pump. The maximum flow rate was found theoretically, and the optimum parameters of the electrohydrodynamic pump were established.

INTRODUCTION

Electrohydrodynamic (EHD) flows are the most interesting manifestations of interaction of electric fields with dielectric media from the viewpoint of their investigation and practical application. Their control and optimization involves many difficulties, and it is very important to overcome them. In this work, there are presented the results of experimental and theoretical research of EHD flows in three- and four-electrode systems as applied to the realization of dielectric liquid EHD pumps.

1. FINDINGS OF THE EXPERIMENTAL RESEARCH

The investigation of electrohydrodynamic flows in narrow channels at small spacing between electrodes providing reasonable voltages is of prime interest for practical implementation, namely, the creation of a dielectric liquid through pumping. Under such conditions, the usage of air bubbles [1] to visualize the flows is impossible because of their effect on the distribution of the electric field and the space charge in the interelectrode space (IES).

EHD flow structures were studied with the help of a shadow method; the experimental plant and research procedure are described in [2]. A blade (e—emitter) and two wires with diameter of 1 mm (c—collector) placed parallel to each other (Fig. 1) at the same distance and symmetric about the blade edge, similarly to the needle–ring system, served as the electrodes. The electrodes were seated in a channel of width $\delta_1 = 6.6$ mm (a section of a closed pipeline). Photocinecamera recording of the EHD flow structure visualized with the help of the shadow method was carried out simultaneously with the measurement of the maximum velocity of the fluid flow through the pipeline out of the field. As a working medium, purified transformer oil was used.

Shadow pictures of the EHD flow structure at the symmetric location of the central jet about the collector wires with the geometrical parameters being $S = 5$ mm (the gap between the generants of the wires), $d = 1.5$ mm (the distance between the emitter and collector) are presented in Figs. 1, 2. As the voltage between the electrodes rises up to 20 kV, the maximum flow speed in the pipeline first grows from 0.5 cm/s (at $U = -15$ kV) up to 0.7 cm/s (at $U = -20$ kV) and then decreases virtually to 0 (at $U = -25$ kV). There is observed the growth of the central jet fluctuation between the collector wires. Apparently, it is one of the causes of the through pumping intensity reduction. Another cause lies in the fact that the dielectric fluid charged by the emitter doesn't manage to discharge completely on the collector (for reasons the surface is limited). As a result, behind the IES, there originates the force of Coulomb interaction between the charged medium and collector electrodes directed opposition to the liquid flow and growing with the voltage increase;
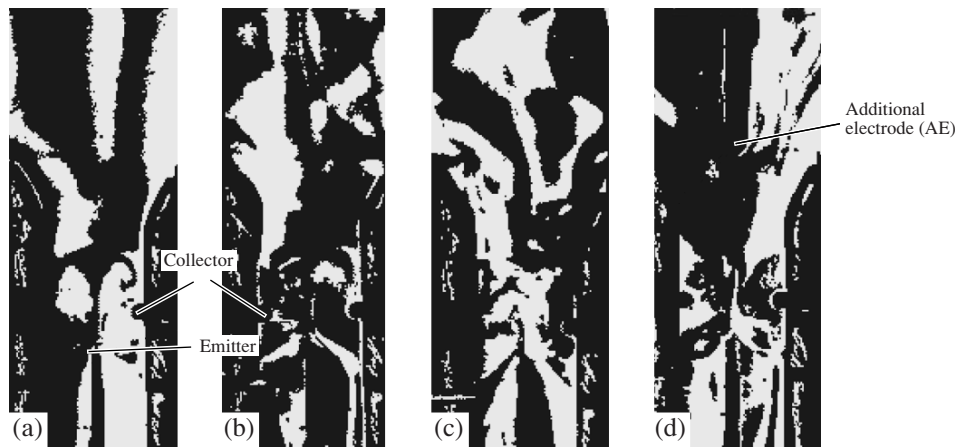
Fig. 1. EHD flow structures at different voltages, kV: (a) 10, (b) 15, (c) 20, (d) 20 (d_1 = 9.5 mm). Working medium—transformer oil.
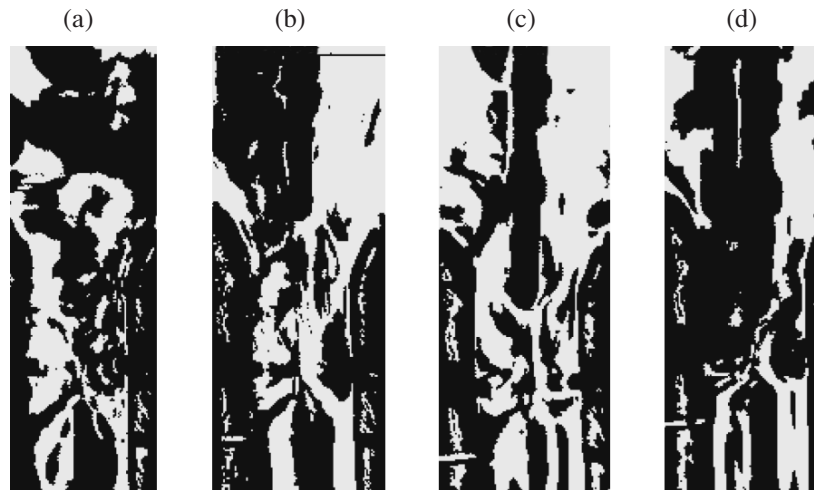

Fig. 2. EHD flow structures at different distances d_1 between the fourth electrode and collectors, mm: (a) ∞; (b) 9.5; (c) 4.5; (d) 1.5; U = –25 kV.

as a consequence, there develops backward flows in the form of eddies directed to the collector (Figs. 1a–1c).

The same is witnessed by the experiments with the additional grounded electrode of ∅1 mm (AE, Fig. 1d) seated symmetrically and at the distance d_1 from the collector wires, which influences both the EHD flow structure (Figs. 1c, 1d) and the through pumping intensity. The additional electrode favors the "drawing" of the charged medium from the near-collector region; it is easily noticeable when the EHD flow structures are compared (Figs. 1b and 1d). As the central additional electrode approaches the lateral ones (distance d_1 decreasing), there is observed the central jet stabilization (Fig. 2), the degeneracy of the eddies behind the collector (Fig. 2c), and the maximum flow speed grows (Fig. 3, curves *2–4*).

The narrowing δ_1 of the channel and simultaneously of the gap S between the collector wires in the absence of the additional electrode causes the reduction of the central jet oscillation amplitude and backward flow intensity both in the IES and behind it, thus positively effecting the medium flow speed (Fig. 3, curves *1* and *6*). At the same time, there doesn't occur the complete neutralization of the charged medium on the collectors. This fact is confirmed by the data on the action of the fourth electrode on the through pumping intensity (Fig. 3, curve *7*), which remains practically constant when the distance between the collectors and additional electrode changes in the range of 0.8–2.5 mm (Fig. 3, curve *8*). Apparently, as the fourth electrode approaches the collectors ($d_1 \leq 2.5$ mm), its resistance to the fluid flow increases, thus compensating for the pumping rate growth.
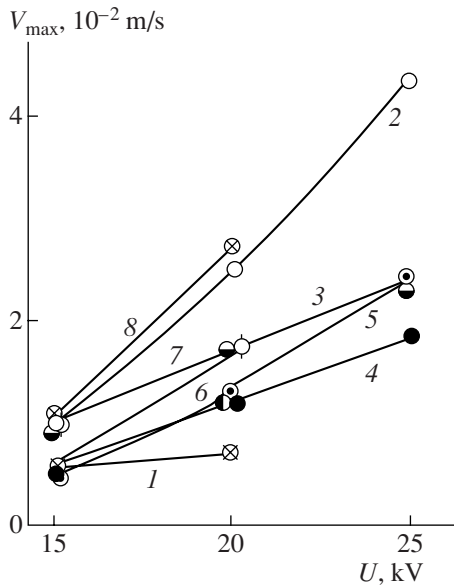
V_{max}, 10^{-2} m/s

Fig. 3. Maximum flow velocity in the piping versus the voltage characteristic at different distances between the electrodes, mm. 1—$d = 1.7$, $S = 5.0$; d_1: 1—without additional electrode, 2—1.5, 3—4.5, 4—9.5; 5—$d = 3$, $S_1 = 5.0$, $d_1 = 1.5$; $d = 1.7$, $S = 1.8$, d_1: 6—without additional electrode, 7—6.9, 8—2.5, 0.8; $\sigma = 3.9 \times 10^{-12}$ Cm m^{-1}.

Fig. 4. Pattern of the flow in the EHD pump.

2. THEORETICAL INTERPRETATION OF THE EXPERIMENTAL RESULTS

Two mathematical models seem to be adequate to describe the experimentally observed EHD flow. One of them is the model of Galley type diffuser flow [3], and the other is the model of a submersed slot jet, which is analogous to the one examined by Landau [3]. Though the mathematical difficulties on the way to the solution of both problems can be overcome, the outcome appears to be rather cumbersome, so, in the initial stage, we shall restrict our consideration to a more transparent, from the physical point of view, model.

In accordance with the presented experimental picture of the EHD flow in the system of electrodes O, O_1, O_2, O_3 (Fig. 4), the slot jet from blade O forces its way upward through the liquid thickness with the Coulomb force being the moving one with the volume density

$$\vec{f} = \rho \vec{E}. \qquad (1)$$

In the vicinity of the grounded collectors O_1 and O_2, there are generated two very symmetric eddies (Figs. 1, 2).

In the initial stages of the flow, that is, at small voltages, the eddy size is negligible and the flow is radial across the whole circular arc with radius R measured by the central angle 2α (see Fig. 4). As the flow develops, that is, the voltage rises, the sizes of eddies "O_1," "O_2" increase, thus shutting the clear opening for liquid pumping through.

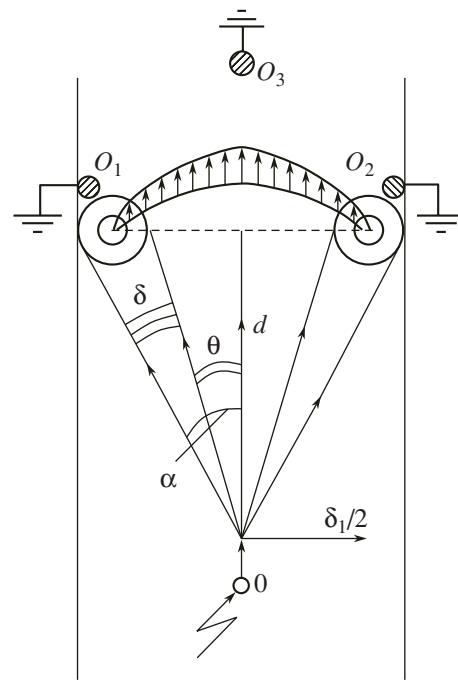Consequently, the reinforcement of the liquid electric pumping leads to antagonistic tendencies: growth of the flow rate owing to the speed rising and a simultaneous decrease of the flow rate because of the reduction of the clear channel opening, which is measured by the central angle 2θ (Fig. 4). As at the initial voltages, the flow rate is zero, and, at bigger ones, it tends to zero for reasons of the complete shutting of the through passage of the liquid by the grown eddies. It is clear that there must exist an optimal (maximum) flow rate under some intermediate operating conditions (voltage) of the EHD pump. From simple physical considerations, we'll try to give a quantitative explanation of these notions, while initially determining the flow rate by the formula

$$Q = \gamma \int_0^b dz \int_{-\theta}^{\theta} \upsilon(R) R d\theta = 2\gamma b R \bar{\upsilon} \theta, \qquad (2)$$

where γ is the medium density, b is the blade edge length, and $\bar{\upsilon}$ is the average speed in the arc 2θ. To determine it, let's remember that "the electric wind" from the points in gases (at a good discharge) and in liquids has, in essence, the same nature and moving force [4–6] defined by the formulas

$$\vec{j} = \kappa \rho \vec{E} \Rightarrow \vec{f} = \bar{j}/\kappa, \qquad (3)$$

where κ is the mobility of the charge carriers with the sign of the electrode blade, and $\vec{j}$ is the electric current density, which is defined by the equality

$$j = \frac{I}{3\pi db}. \qquad (4)$$

Here, the total current I corresponds to the areas of three conductors–collectors with diameter d_0 and length b. We have previously shown [5] that the average rate of the electric wind can be defined by the formula

$$\bar{\upsilon} = C\left(\frac{\Gamma_1}{\Gamma_2}\right)\left(\frac{jl^3}{\kappa\gamma\nu^2}\right)^m\frac{\nu}{l}, \qquad (5)$$

where l is the typical size, as which $l = d_0$ should be accepted; ν is the kinematic viscosity, $1 > m > 1/2$ and reduces as the laminar flow transforms into a turbulent one [5]; and $C(\Gamma_1/\Gamma_2)$ is the proportionality factor depending on similarity simplexes caused by the boundary conditions.

The angle θ can be defined by the formula

$$\theta = \alpha - \delta = \alpha - 2r_0/R, \qquad (6)$$

where r_0 is the radius of the lateral eddies according to Fig. 4. To estimate it, we assume the eddy to be circular and the particles participating in the vortical motion are under the influence of only centripetal forces being simultaneously Coulomb ones, so we presume a priori these forces to be equal:

$$\frac{\gamma\bar{\upsilon}^2}{r_0} \cong \rho E = j/\kappa, \qquad (7)$$

whence

$$2r_0 = \frac{2\kappa\gamma\bar{\upsilon}^2}{j}. \qquad (8)$$

Substitute (4) into (5), then (5) and (6) into (2) we get

$$Q = 2\gamma bR\left(\frac{\nu}{d}\right)C\left(\frac{\Gamma_1}{\Gamma_2}\right)\left(\frac{I}{I_*}\right)^m$$

$$\times\left[\alpha - \frac{6\pi bd_0\kappa\gamma\nu^2}{RI}\frac{1}{d_0^2}C^2\left(\frac{\Gamma_1}{\Gamma_2}\right)\left(\frac{I}{I_*}\right)^{2m}\right],$$

or

$$Q = A(\alpha g^m - B g^{3m-1}), \qquad (9)$$

where

$$A \equiv 2\gamma bR\frac{\nu}{d_0}C\left(\frac{\Gamma_1}{\Gamma_2}\right); \quad g \equiv \frac{I}{I_*}; \quad I_* \equiv \frac{3\pi b\kappa\gamma^2}{d_0^2};$$

$$B \equiv \frac{6\pi b\kappa\gamma\nu^2}{RI_*d_0}C^2\left(\frac{\Gamma_1}{\Gamma_2}\right). \qquad (10)$$

Examine (9) for the extremum:

$$\frac{dQ}{dg} = A\alpha m g^{m-1}\left(1 - \frac{B(3m-1)}{\alpha m}g^{2m-1}\right).$$

Taking this expression equal to zero, we find the extremal value of the dimensionless current intensity:

$$g_0 = \left[\frac{\alpha m}{B(3m-1)}\right]^{\frac{1}{2m-1}}. \qquad (11)$$

We find the second derivative

$$\frac{d^2Q}{dg^2} = A\alpha m(m-1)g^{m-2}$$

$$\times\left(1 - \frac{B(3m-1)(3m-2)}{\alpha m(m-1)}g^{2m-1}\right).$$

Substituting (11) here, we obtain

$$\frac{d^2Q}{dg^2} = -A\alpha m(2m-1)g^{m-2}.$$

As $0.5 < m \le 1$, then $d^2Q/dg < 0$, and function (9), i.e., the flow rate, has its maximum given by expression (11) with

$$Q_{max} = \frac{\alpha A(2m-1)}{3m-1}\left[\frac{\alpha m}{B(3m-1)}\right]^{\frac{m}{2m-1}}. \qquad (12)$$

We present the numerical calculation of Q_{max}, assuming $\alpha = \arctan\frac{\delta}{2d_1} = \arctan\frac{5.6}{2\cdot 1.5} \cong 1.21$ rad, $b = 10 \times 10^{-3}$ m; $R = 3.18 \times 10^{-3}$ m; $\kappa = 10^{-8}$ m^2/V s; $d = 10^{-3}$ m; $\nu = 22 \times 10^{-6}$ m^2/s; $\gamma = 0.9 \times 10^3$ kg/m^3; $A = C(\Gamma_1/\Gamma_2) \times 1.26 \times 10^{-3}$ kg/s; $I_* \cong 0.4 \times 10^{-9}$ A; $B = C(\Gamma_1/\Gamma_2) \times 1.7 \times 10^{-1}$; $m \cong 0.7 \in (0.5; 1.0)$.

We obtain

$$Q_{max}^{\text{flow rate}} = C^{-0.75} \times 2.86 \times 10^{-3} \text{ (kg/s)}.$$

In the experiments $\upsilon \sim 1$ cm/s $= 10^{-2}$ m/s; $S \sim 1$ cm$^2 = 10^{-4}$ m^2 and $Q_{max}^{\exp} \sim \gamma\upsilon S \sim 10^{-3}$ kg/s), i.e. according to the order of magnitude, empirical proportionality factor ~ 1 is also the necessary and true indication of the theoretical conception justifiability.

From (9), it follows that, if the current intensity reaches the critical value

$$g_{cr} = \left(\frac{\alpha}{B}\right)^{\frac{1}{2m-1}}, \qquad (13)$$

the pump operation stops.

Substituting numerical data into (13), we find $g_{cr} \sim 5/C^{2.5}$; i.e., the critical currents are of the same order as I, which we call "reduced."

The connection between them is defined by the formula

$$g_{cr} = g_0\left(\frac{3m-1}{m}\right)^{\frac{1}{2m-1}}, \tag{14}$$

which gives a ~3-fold value of g_0 at $m \sim 0.7$.

It should be noted that formulas (9)–(14) have a power nature with a variable exponent changing in narrow limits (0.5–1.0) and, together with the single empirical proportionality factor, make them suitable and adaptable for the purposes of the calculation.

Thus, it is shown that the instability of the liquid jet directed from the central electrode (blade) and the eddy formation in the three-electrode system can be partially suppressed using the additional electrode placed behind the IES or by reducing the gap between the lateral electrodes, thus decreasing their defocusing effect on the central flow jet, resulting in the growth of the dielectric liquid pumping through rate. It is found experimentally and confirmed theoretically the presence of the pumping rate maximum depending on the current intensity (voltage) in the EHD pump. Calculating formulas to determine the liquid flow rate through the EHD pump and its optimal regimes are obtained on the basis of a simple physical model of the EHD flow. The theoretical results are in good agreement with the experimental ones.

REFERENCES

1. Stishkov, Yu.K. and Ostapenko, A.A., Electrohydrodynamic Flows in Liquid Dielectrics, Leningrad, 1989, 174 p.
2. Bologa, M.K. and Kozhevnikov, I.V., Effect of the Insulating Coating on Processes of Charge Exchange Between Electrode and Liquid, Elektron. Obrab. Mater., 2006, no. 1, pp. 32–36 [Engl. Transl.].
3. Landau, L.D. and Lifshits, E.M. Hydrodynamics, Moscow: Nauka, 1988.
4. Kaptsov, N.A., Electric Phenomena in Gases and Vacuum, Moscow: Gostekhizdat, 1950, p. 836.
5. Bologa, M.K., Grosu, F.P and Kozhykhari, I.A., Elecroconvection and Heat Transfer, Kishinev: Shtiintsa, 1977, p. 320.
6. Ostroumov, G.A., Interaction of Electric and Hydrodynamic Fields, Moscow: Nauka, 1979, 320 p.

ELECTRICAL PROCESSES
IN ENGINEERING AND CHEMISTRY

Axisymmetric Nonlinear Oscillations of a Space-Charged Dielectric-Fluid Jet

A. I. Grigor'ev, N. V. Voronina, and S. O. Shiryaeva

Demidov Yaroslavl State University, ul. Sovetskaya 14, Yaroslavl, 150000 Russia

Received March 16, 2007

Abstract—The solution for nonlinear axisymmetric oscillations of a space-charged dielectric-fluid jet is found. The nonlinear corrections for the space-charged dielectric-fluid jet differ only slightly from those for the conducting fluids.

INTRODUCTION

As early as in the mid-eighteenth century, it was found that the charged surface of a fluid throws out jets disintegrating into individual drops [1]. In the subsequent years, this phenomenon was studied both experimentally [2] and theoretically [3–6] and taken as a basis for numerous applications [5–6]. The investigations of the last decades made it possible to single out about ten different modes of electrical spraying of fluids [7–9]. The observed variety of modes is associated both with the implementation of a very wide set of initial and boundary conditions in real experiments [5–8] and with the variation of physical and chemical properties of fluids [8, 10], as well as with the possibility of the initiation of multiple combinations of nonaxisymmetric oscillation modes [6, 10–12].

The investigation of oscillations and stability with respect to the disintegration into individual drops of space-charged dielectric-fluid jets is of interest in connection with multiple applications caused by the production of streams of mono- and polydisperse charged drops of fluids with various physical and chemical properties [5, 6, 13]. In a number of technical applications, it is necessary to obtain streams of charged drops of just dielectric fluids [5, 8, 13–15]. That is why the understanding of the features of the initiation of oscillations and the division of dielectric fluids into drops is of importance. Therefore, the theoretical analysis of nonlinear oscillations of space-charged jets of dielectric fluids is very actual.

The purpose of this work is to find the analytical asymptotic solution of the problem of nonlinear axisymmetric oscillations of a jet of space-charged dielectric fluid with zero conductivity in the second order of smallness in the initial-deformation amplitude and to compare it with the previously solved problem [10–12] on nonlinear axisymmetric oscillations of surface-charged jets of perfectly conducting fluid. All this is done on the basis of the multiscale method previously

used for calculating nonlinear oscillations of an uncharged jet [16].

1. PROBLEM FORMULATION

Let there be an infinite cylindrical jet of radius R of a perfect incompressible dielectric fluid with the mass density ρ, permittivity ε_d, surface-tension coefficient γ, uniformly charged with the volume density μ, and moving along the symmetry axis with a constant velocity $\vec{U}_0$. We carry out the entire subsequent analysis within the framework of the "frozen-in-charge" model in the inertial reference frame. The origin of the cylindrical coordinate system is (r, φ, z), which moves together with the jet with a velocity $\vec{U}_0$ along the unperturbed-jet symmetry z axis: $\vec{U}_0 \parallel \vec{n}_x$. In the chosen reference frame, the flow-velocity field $\vec{U}(r, t)$ in the fluid jet is completely determined by the possible capillary oscillations of its surface. When made dimensionless by dividing by the jet radius R, the surface-tension coefficient γ, and the fluid density ρ, the amplitude value of the velocity field is the same order of smallness as the oscillation amplitude, which is small in comparison with the jet radius.

We investigate the regularity of the implementation of nonlinear jet oscillations assuming that the equation of its free surface disturbed by the capillary wave motion can be written in the form

$$r(\varphi, z, t) = R + \xi(\varphi, z, t); \quad |\xi| \ll R,$$

where $\xi(\varphi, z, t)$ is the surface-jet deformation caused by its oscillations.

The mathematical formulation of the problem under discussion within the framework of the potential-flow model consists of the equations of hydrodynamics and,

assuming that the fluid-flow velocity is much less than relativistic, the equations of electrostatics:

$$\Delta\Psi = 0;$$

$$\Delta\Phi_{ex} = 0;$$

$$\Delta\Phi_{in} = -4\pi\frac{\mu}{\varepsilon_d}.$$

It also involves the boundedness conditions:

$$r \longrightarrow 0: |\vec{U}| < \infty, \quad |\nabla\Phi_{in}| < \infty;$$

$$r \longrightarrow \infty: |\Delta\Phi_{ex}| \longrightarrow 0;$$

the hydrodynamic boundary conditions on a free jet surface $r = R + \xi$; the kinematic condition

$$-\frac{\partial\xi}{\partial t} + (\nabla\Psi)\nabla[r - (R + \xi(\varphi, z, t))] = 0$$

the dynamic condition

$$-P(\vec{r}, t) + P_0 + P_\gamma - P_q = 0;$$

and the boundary conditions for the electric field:

$$r = R + \xi: \Phi_{in} = \Phi_{ex}, \quad \varepsilon_d\frac{\partial\Phi_{in}}{\partial n} = \frac{\partial\Phi_{ex}}{\partial n}.$$

In the written mathematical formulation of the problem, $P(\vec{r}, t) = -\rho\left[\frac{\partial\Psi}{\partial t} + \frac{1}{2}(\nabla\Psi)^2\right]$ is the hydrodynamic pressure related to the potential fluid flow; $P_q(\vec{r}, t)$ is the electric-field pressure on the jet surface; $P_\gamma(\vec{r}, t) \equiv \gamma(\nabla \cdot \vec{n})$ is the surface-tension pressure; P_0 is the constant environmental pressure; $\Psi(\vec{r}, t)$ is the velocity-field potential; $\Phi(\vec{r}, t)$ is the electrostatic potential; the subscripts "ex" and "in" characterize the electric field outside and inside the jet, respectively; and $\vec{n}$ is the normal to the disturbed free surface of the jet.

It is necessary to supplement the problem by the condition of conservation of the jet-portion volume, the length of which is equal to the wavelength λ:

$$\int_V r\,dr\,d\varphi\,dt = \pi R^2\lambda; \quad V = \begin{cases} 0 \leq r \leq R + \xi(\varphi, z, t) \\ 0 \leq \varphi \leq 2\pi \\ z_0 \leq z \leq z_0 + \lambda. \end{cases}$$

For closing the problem, it is necessary to also set the initial conditions, the first of which defines the initial deformation of the jet free surface:

$$r(\varphi, z, 0) = R + a[\zeta^{(+)}(0)\exp(im\varphi)$$

$$+ \zeta^{(-)}(0)\exp(im\varphi)]\exp(ikz) + O(\varepsilon^2).$$

From now on, we write no terms that are complex conjugated to the written ones, and a is the wave amplitude. The second initial condition, as is accepted in the problems on nonlinear waves [10, 16], is chosen at the final stage in order that the obtained solution have the least cumbersome form.

We carry out the further analysis in the dimensionless variables in which we chose the jet radius R, the surface-tension coefficient γ, and the fluid density ρ as fundamental units retaining their former designations for all these values.

2. SOLUTION METHOD

We search for the solution of the formulated problem within the framework of the asymptotic approach as an expansion in terms of the small parameter $\varepsilon \equiv (a/R)$ on the basis of the multiscale method [10, 16] accurate to the second order of smallness inclusively.

We represent the desired functions $\xi(\varphi, z, t)$, $\Psi(\vec{r})$, $\Phi_{in}(\vec{r}, t)$, and $\Phi_{ex}(\vec{r}, t)$ in the form of the asymptotic expansion in terms of ε assuming that the time evolution of the desired functions is determined by two time scales: the basic $T_0 = t$ and the slow $T_1 = \varepsilon t$:

$$\xi(\varphi, z, t) = \varepsilon\xi^{(1)}(\varphi, z, T_0, T_1)$$

$$+ \varepsilon^2\xi^{(2)}(\varphi, z, T_0) + O(\varepsilon^3),$$

$$\Psi(\vec{r}, t) = \varepsilon\Psi^{(1)}(r, \varphi, z, T_0, T_1)$$

$$+ \varepsilon^2\Psi^{(2)}(r, \varphi, z, T_0) + O(\varepsilon^3),$$

$$\Phi_{in}(\vec{r}, t) = \Phi_{in}^{(0)}(r) + \varepsilon\Phi_{in}^{(1)}(r, \varphi, z, T_0, T_1)$$

$$+ \varepsilon^2\Phi_{in}^{(2)}(r, \varphi, z, T_0) + O(\varepsilon^3),$$

$$\Phi_{ex}(\vec{r}, t) = \Phi_{ex}^{(0)}(r) + \varepsilon\Phi_{ex}^{(1)}(r, \varphi, z, T_0, T_1)$$

$$+ \varepsilon^2\Phi_{ex}^{(2)}(r, \varphi, z, T_0) + O(\varepsilon^3).$$

Assuming that the waves on the jet surface propagate in the positive direction of the OZ axis, we can describe the shape of the jet free surface at an arbitrary moment of time as

$$r(\varphi, z, t) = 1 + \varepsilon[\zeta^{(+)}(T_1)\exp(im\varphi)$$

$$+ \zeta^{(-)}(T_1)\exp(-im\varphi)]\exp(i\vartheta) + O(\varepsilon^2);$$

$\vartheta \equiv kz - \omega T_0$, where $\omega \equiv \omega_m(k)$ is the frequency of the wave with the wave number k and the azimuth number m, and $\zeta^{(\pm)}(T_1)$ are still unknown complex functions dependent on the slow time $T_1 \equiv \varepsilon t$.

3. FINAL EXPRESSIONS

Not stopping with the mathematical procedure of the search for the solution (described in detail in [10,

16]) because of its awkwardness, we directly write the solution of the problem.

The shape of the jet free surface at an arbitrary moment of time can be described by the relationship

$$r(z, t) = 1 + \varepsilon \cos(kz - \omega t)$$
$$+ 0.5\varepsilon^2 \{-0.5 + a\cos[2(kz - \omega t)]\},$$

and the expressions for the hydrodynamic and electric potentials inside and outside the jet have the following form:

$$\Psi(\vec{r}, t) = \varepsilon \frac{\omega I_0(kr)}{kI_0'(k)} \sin(kz - \omega t)$$
$$+ 0.5\varepsilon^2 b I_0(2kr) \sin[2(kz - \omega t)];$$

$$\Phi_{in}(\vec{r}, t) = -\frac{\pi\mu r^2}{\varepsilon_d} + \varepsilon \frac{2\pi\mu}{\varepsilon_d} g_{in} \frac{I_0(kr)}{I_0(k)} \cos(kz - \omega t)$$
$$+ 0.5\varepsilon^2 c I_0(2kr) \cos[2(kz - \omega t)];$$

$$\Phi_{ex}(\vec{r}, t) = -\frac{\pi\mu}{\varepsilon_d} - 2\pi\mu \ln r + \varepsilon 2\pi\mu g_{ex} \frac{K_0(kr)}{K_0(k)}$$
$$\times \cos(kz - \omega t) + 0.5\varepsilon^2 \{2\pi\mu[-1 + g_{in}G_0(k)/\varepsilon_d$$
$$- g_{ex}H_0(k) + (1 + L)\ln r]$$
$$+ dK_0(2kr)\cos[2(kz - \omega t)]\};$$

where

$$a \equiv P/Q; \quad Q = -\varepsilon_d f_0(2k)[4\omega^2(k) - \omega^2(2k)];$$

$$P = -(Y_1 G_0(2k) + 2\omega X)\varepsilon_d f_0(2k)$$
$$+ WG_0(2k)\{2\varepsilon_d(L + H_0(2k))$$
$$+ 0.5(\varepsilon_d^2 - 1)G_0(2k)H_0(2k) + 2k^2(g_{in} - g_{ex})(2\varepsilon_d$$
$$+ (\varepsilon_d - 1)H_0(2k)) - g_{in}G_0(k)[\varepsilon_d + 1$$
$$+ (\varepsilon_d - 1)G_0(2k)]H_0(2k) + g_{ex}H_0(k)[3\varepsilon_d - 1$$
$$+ \varepsilon_d(\varepsilon_d - 1)G_0(2k)]H_0(2k)\};$$

$$b = \frac{2\omega a - X}{2kI_0'(2k)},$$

$$c = \frac{2\pi\mu}{\varepsilon_d I_0(2k)f_0(2k)}\{[2\varepsilon_d + (\varepsilon_d - 1)H_0(2k)]a$$
$$- \varepsilon_d L - 2\varepsilon_d k^2(g_{in} - g_{ex}) - H_0(2k)M\},$$

$$d = \frac{2\pi\mu}{K_0(2k)f_0(2k)}\{[2 + (\varepsilon_d - 1)G_0(2k)]a$$
$$- L - 2k^2(g_{in} - g_{ex}) - G_0(2k)M\},$$

$$X = \omega(k)[2k^2 - G_0(k)]/G_0(k),$$

$$Y_1 = 1 + 0.5k^2 + \omega^2(k)[k^2 - 3G_0^2(k)]/2G_0^2(k)$$
$$+ W(2g_{in}G_0(k) - 1)/\varepsilon_d - \frac{\varepsilon_d - 1}{2\varepsilon_d}W[3 + k^2$$
$$- 4g_{ex}(k^2 - H_0(k)) + g_{ex}^2 H_0^2(k) - \varepsilon_d k^2(g_{ex} - 1)^2],$$

$$Y_2 = 1 - 0.5k^2 + \omega^2(k)[k^2 - G_0^2(k)]/2G_0^2(k)$$
$$+ W(2g_{in}G_0(k) - 1)/\varepsilon_d - \frac{\varepsilon_d - 1}{2\varepsilon_d}W[3 - k^2$$
$$+ 4g_{ex}H_0(k) + g_{ex}^2 H_0^2(k) + \varepsilon_d k^2(g_{ex} - 1)^2],$$

$$L \equiv 1 - g_{in}G_0(k) + g_{ex}H_0(k),$$

$$M \equiv 0.5(\varepsilon_d + 1) - g_{in}G_0(k) + \varepsilon_d g_{ex}H_0(k),$$

$$G_0(x) \equiv xI_0'(x)/I_0(x); \quad H_0(x) \equiv xK_0'(x)/K_0(x),$$

$I_0(x)$ and $K_0(x)$ are the modified Bessel functions of the zero order of the first and second kind, and the prime designates the derivative of the Bessel function with respect to the argument. The dispersion equation relating the oscillation frequency $\omega_m(k)$ with the wave number k obtained in the solution of the problem of the first order of smallness has the form

$$\omega_0^2(k) = \frac{G_0(k)}{\varepsilon_d f_0(k)}\{(k^2 - 1)\varepsilon_d f_0(k) + W[\varepsilon_d(4$$
$$+ (\varepsilon_d - 3)G_0(k)) + (3\varepsilon_d - 1 + (\varepsilon_d - 1)^2 G_0(k))H_0(k)]\};$$

$$f_0(x) \equiv \varepsilon_d G_0(x) - H_0(x); \quad W = \pi\mu^2.$$

4. DISCUSSION OF THE RESULTS

In the figure, we show the dependence of the quantity $\alpha \equiv a^d/a^c$ on the parameter W (representing the ratio between the pressure of the self-charge electric field on the jet surface and the surface-tension pressure) [10]. From the figure, it can be seen that the dependence of the coefficient a on the parameter W somewhat differs from that for a perfectly conducting fluid. It is interesting to also note that the difference between the magnitudes of the coefficients of the nonlinear corrections for the dielectric and perfectly conducting fluids increases with decreasing the permittivity of the fluid.

From the expression for the coefficients a, b, c, and d, it is easy to note that the position of the internal nonlinear resonances (in the neighborhood of which the nonlinear energy transfer takes place between the modes dependent on the condition of vanishing of the denominators a, b, c, and d for a dielectric fluid) formally is the same as for the perfectly conducting fluid:

$$4\omega_m^2(k) = \omega_{2m}^2(2k).$$

However, it is necessary to take into account that the dispersion equations from which the dependences

α

1.08

1.02

0.2   0.6   1.0

W
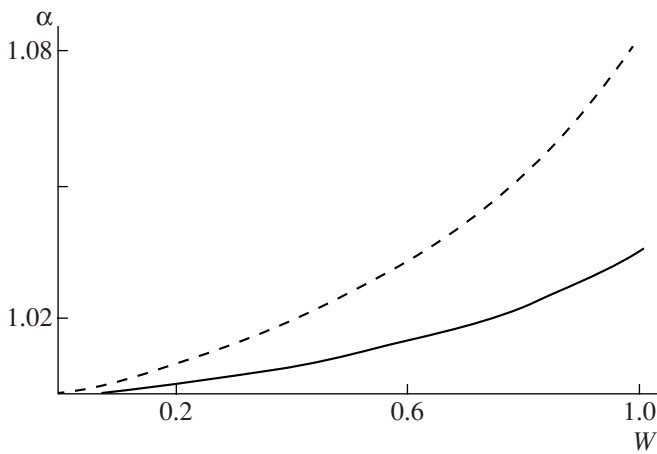
The dependence of the value $\alpha \equiv a^d/a^c$ on the parameter W (the ratio between the coefficient a^d of the nonlinear correction in the expression for the shape of the dielectric-fluid jet and the corresponding coefficient a^c of the nonlinear correction of the expression for the shape of the conducting-fluid jet). The prime designates the data for $\varepsilon_d = 30$, and the solid line, for $\varepsilon_d = 80$.

$\omega_m^2(k)$ and $\omega_{2m}^2(2k)$ are calculated differ for the dielectric and perfectly conducting fluids under consideration, and the resonant wavelengths for these two fluids can noticeably differ for the low permittivity ε_d.

CONCLUSIONS

In the second order of smallness with respect to the initial-deformation amplitude, the analytical asymptotic solution of the problem on the calculation of nonlinear axisymmetric oscillations is found for the uniformly space-charged jet of a perfect incompressible fluid. The analysis of the obtained results showed that the nonlinear corrections for the jet of dielectric fluid insignificantly differ from those for the jet of a perfectly conducting fluid (by no more than 10%) in comparison with the nonlinearly axisymmetrically oscillating charged jet of a perfectly conducting fluid with identical electric charges per jet-length unit.

ACKNOWLEDGMENTS

REFERENCES

1. Baily, A.G., Electrostatic Spraying of Fluids, *Phys. Bull.*, 1984, vol. 35, no. 4, pp. 146–148.

2. Savart, F., Memare sur la contitution veines liquides lancus par des orifices circulaires en mince paroi, *Annal. chimic.*, 1833, Ser. 2, vol. 53, no. 3, pp. 337–386.

3. Rayleigh, Lord, On the Capillary Phenomena of Jets, *Proc. Roy. Soc.* (London), 1879, vol. 29, no. 196, pp. 71–97.

4. Rayleigh, J., *Teoriya zvuka* (Theory of Sound), vol. 2, Moscow, 1955.

5. Entov, V.M. and Yarin, A.L., *Dinamika svobodnykh strui i plenok vyazkikh i reologicheski slozhnykh zhidkostei* (Dynamics of Free Jets and Films of Viscous and Rheologically Complex Fluids) Available from VINITI, Resume of science and engineering, Ser. Mechanics of fluid and gas, 1984, vol. 17, pp. 112–197.

6. Grigor'ev, A.I., Shiryaeva, S.O., Voronina, N.V., and Egorova, E.V., About Oscillations and Spontaneous Disintegration of Charged Fluid Jets, *Electron. Obrab. Mater.*, 2006, no. 6, pp. 23–34.

7. Cloupeau, M. and Prunet, Foch B., Electrostatic Spraying of Fluids: Main Functioning Modes, *J. Electrostatics*, 1990, vol. 25, pp. 165–184.

8. Shiryaeva, S.O., Grigor'ev, A.I., and Svyatchenko, A.A., Classification of Operation Modes of Electrohydrodynamic Sources of Liquid-Drop Beams (Survey), *Preprint of IMRAN*, no. 25, Yaroslavl, 1993.

9. Shiryaeva, S.O. and Grigor'ev, A.I., The Semifenomenological Classification of the Modes of Electrostatic Dispersion of Fluids, *J. Electrostatics*, 1995, vol. 34, pp. 51–59.

10. Belonozhko, D.F., Shiryaeva, S.O., and Grigor'ev, A.I., *Nelineinye volny na zaryazhennoi poverkhnosti zhidkosti* (Nonlinear Waves on Charged Fluid Surface), Yaroslavl: Izd. YarGu, 2006.

11. Shiryaeva, S.O., Grigor'ev, A.I., Levchuk T.V., and Rybakova, M.V., About Spontaneous Disintegration of Charged Jets of Viscous Conducting Fluid, *Electron. Obrab. Mater.*, 2003, no. 1, pp. 38–143.

12. Grigor'ev, A.I., Shiryaeva S.O., and Egorova, E.V., About Certain Features of Nonlinear Resonant Interaction of Charged-Jet Modes, *Electron. Obrab. Mater.*, 2005, no. 1, pp. 42–50.

13. Ametistov, E.V., Blazhenkov, V.V., Gorodov, A.K., et al., *Monodispergirovanie veshchestva: printsipy i primenenie* (Monodispersion of Substance: Principles and Application), Grigor'ev, V.A., Ed., Moscow, 1991.

14. Ginevskii, A. F., *Osobennosti kapilyarnogo raspada strui zaryazhennykh dielektrikov* (Features of Capillary Disintegration of Jets of Charged Dielectrics), *Issled. Protsessov i Sistem Monodisp. Rasp. Zhidk., Sbor. Nauchn. Trudov MEI*, no. 119, Moscow, 1986.

15. Ginevskii, A. F., *Osobennosti kapilyarnogo raspada strui vyazkikh zaryazhennykh dielektricheskikh zhidkostei* (Features of Capillary Disintegration of Jets of Charged Dielectric Fluids), *Phiziko-Tekhn. Prob. Monodisp. Sistem., Sbor. Nauchn. Trudov MEI*, no. 185. Moscow, 1988, pp. 54–58.

l6. Nayfeh, F.H., Nonlinear Stability of a Liquid Jet, *Phys. Fluids*, 1970, no. 4, pp. 841–847.

ELECTRICAL PROCESSES
IN ENGINEERING AND CHEMISTRY

Thin Films of Titanium and Tin Oxides and Semiconductor Structures on Their Basis Obtained by Pyrolytic Pulverization: Preparation, Characterization, and Corrosion Properties

O. L. Bersirova[b], L. I. Bruk[c], A. I. Dikusar[a], M. I. Karaman[c], S. P. Sidel'nikova[a], A. V. Simashkevich[a], D. A. Sherban[a], and Yu. S. Yapontseva[b]

[a] *Institute of Applied Physics, Academy of Sciences of Moldova, ul. Akademiei 5, Chisinau, MD-2028 Moldova*
[b] *Vernadskii Institute of General and Inorganic Chemistry, National Academy of Sciences of Ukraine, pr. Akademika Palladina 32/34, Kiev-142, 03680 Ukraine*
[c] *Moldova State University, ul. Mateevicha 60, Chisinau, MD-2012 Moldova*

Received August 2, 2007

Abstract—Peculiarities of obtaining of tin oxide and titanium oxide layers and semiconductor structures on their basis are described. The X-ray diffraction data show that the SnO_2 and TiO_2 layers possess the tetragonal crystal structure (anatase modification for TiO_2). The results of analysis of the elemental composition and impedance investigations of the fabricated structures in model chloride–sulfate solutions demonstrate that the oxide/SiO_2/Si structures are obtained if Si substrates are used. In the case of InP substrates, the oxide layer at the interface is not detected and the corresponding structure is oxide/InP. The results of investigations of corrosion show that a substantial shift of the corrosion potential to the anode region is observed in the case of deposition of SnO_2 and TiO_2 oxide layers on Si and InP crystals and fabrication of corresponding semiconductor structures. This demonstrates the possibility of the use of these materials in photoelectrochemical applications.

DOI: 10.3103/S1068375507060075

INTRODUCTION

It is known that, on the base of transparent conducting metal oxides (TCO) such as SnO_2, In_2O_3, TiO_2, and ITO, semiconductor–insulator–semiconductor (SIS) structures are formed, which are used for conversion of solar energy into electric energy [1–5]. In such structures, silicon and semiconductor III–V compounds, for example, indium phosphide, are mainly used as materials absorbing solar radiation. The TCO layers are the components of not only of photovoltaic but also of photoelectrochemical cells [6, 7], where they play the protective role against corrosion of the matrix semiconductor material. Wide-gap oxide layers, in addition to the immediate anticorrosion function, also promote the extension of the spectral characteristics of the photosensitivity due to a decrease in the surface recombination in the narrow-gap absorbing material. In addition, the SnO_2 and TiO_2 layers can be successfully used in Si-based and InP-based solar cells as an antireflection coating due to their transparency in the visible spectral range and appropriate values of the refraction indices ($n = 2.0$ and $n = 1.72–2.60$, respectively), which increases the efficiency of transformation of solar energy into electric energy.

Properties of semiconductor films and structures are largely determined by the technology of their preparation. However, there are few works in the available literature where the properties of these materials, specifically photocorrosion properties, are described depending on the conditions of their obtaining. In this work, we describe the technology of obtaining the SnO_2-based and TiO_2-based layers and heterostructures as well as investigation of their structural, optical, and photocorrosion properties. The used method of pyrolytic pulverization for obtaining the layers and structures is rather simple and economical, does not require complex equipment, and can be used for obtaining efficient photovoltaic converters.

EXPERIMENTAL

The TiO_2 and SiO_2 films were formed during deposition of $TiCl_4$ solutions in ethyl acetate, ethanol, or $SnCl_4$ in ethanol on the substrates heated to 450°C. The substrates were quartz, sapphire, as well as Si and InP. Depending on the concentration of the used solutions and sprayed volumes, their nature, and the substrate, the films were of various thicknesses (from 50 to 400 nm).

To obtain SnO_2, we used a 0.5 M $SnCl_4$ solution in ethanol. In certain cases, for doping of the film by antimony, a 0.1 M $SbCl_3$ solution in ethanol was used. To prepare the solution with a dopant, up to 2 ml of the 0.1 M $SbCl_3$ solution was added to 11 ml of the 0.5 M $SnCl_4$ solution. To obtain the TiO_2 layers, we used solu-

tions prepared by mixing of a 1 M $TiCl_4$ solution and the solvent in the following ratios: 1 : 1, 1 : 2, and 1 : 3.

During pulverization in air and subsequent pyrolysis, a series of reactions proceeds. These reactions, which are associated with hydrolysis, evaporation, and oxidation, in the general form, can be presented as follows:

$$TiCl_4 + O_2 = TiO_2 + 2Cl_2,$$

$$SnCl_4 + O_2 = SnO_2 + 2Cl_2, \qquad (1)$$

$$4SbCl_3 + 3O_2 = 2Sb_2O_3 + 6Cl_2.$$
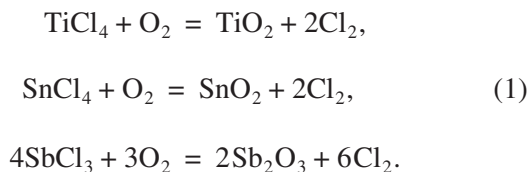
To obtain the films, equipment preliminary described in [15] was used.

The structure was analyzed by X-ray diffraction with the use of a Brucker linear diffractometer (CuK_α radiation, Ni filter, θ–2θ scanning).

In this work, we used the following methods of analysis of the composition and morphology of the obtained films:

(i) scanning electron microscopy (SEM) with the use of a TESCAN VEGA scanning electron microscope;

(ii) a system for investigation of the chemical composition (INGA Energy EDX) for determination of the elemental composition. A special feature of the method used in this investigation consisted of performing the analysis over a region with a diameter of several micrometers to a depth of up to 2 μm. The analysis was carried out at three points of each sample, after which the average value was calculated. The interval values given below correspond to standard deviations from the average value.

The transmission and reflection spectra of the SnO_2 and TiO_2 layers obtained on various substrates (glass, quartz, sapphire) were measured using a Specord spectrophotometer in the wavelength range of 0.2–1.5 μm.

The photocorrosion of the obtained layers and narrow-gap semiconductors on which they were deposited (Si, InP) was investigated by two methods, namely, electrochemical impedance spectroscopy and voltammetry using an AUTOLAB (GPSTAT 20+FRA) system with GPES 4.9 and FRA 4.9 software. The current–voltage measurements were carried out both in the dark and in the light. In the first case, the electrochemical cell was coated with a material not transmitting the light, and, in the second case, the measurements were carried out under illumination by an incandescence lamp with a power of 60 W, which was arranged at a distance of approximately 30 cm from the measuring cell. The corrosion behavior of all the samples was investigated in a neutral (pH = 6.0 ± 0.1) medium. As a model solution, we selected a solution of a mixture of sulfates and chlorides (7 g/l Na_2SO_4 + 7 g/l NaCl). The measurements were carried out at a temperature of 24 ±

1°C in the cell with a saturated silver–silver chloride electrode and an auxiliary electrode in the form of a platinum grid. All the values of the potentials are given relative to the saturated silver–silver chloride electrode.

The spectra of the electrochemical impedance were recorded after holding the sample in the corrosion solution for 15 min to establish the steady-state potential. The voltage was supplied sinusoidally with an amplitude of 5 mV. The spectra are obtained in a frequency range of 50 kHz–1 MHz. The parameters of the corrosion process and corresponding equivalent circuits were determined based on the analysis of these spectra.

The current–voltage measurements consisted of obtaining the anode and cathode polarization curves for a rate with specifying a potential of 1 mV/s. The polarization curves were corrected by the magnitude of the ohmic voltage drop IR. Based on the obtained curves, the corrosion characteristics were calculated.

RESULTS AND DISCUSSION

Chemical Composition of the Films and Heterostructures Obtained on Various Substrates and Peculiarities of the Interrelation of the Measured Chemical Composition and Film Thickness

The chemical composition of the films during their deposition on transparent materials (glass, sapphire) and heterostructures obtained on their deposition on Si and InP, as was already noted above, was carried out using a variant of EDX analysis in which the surface layer with a thickness of 2–3 μm was studied. It is evident that, with the presence of heterostructures and adsorbed layers on the surface, an unambiguous interpretation of the obtained data is not always possible. To do this, we need both different variants of the EDX analysis, e.g., the analysis of the surface and transverse cleavages, and additional methods, e.g., the analysis of the layer thicknesses, which allow one to more exactly interpret the obtained results. Such additional methods were an optical method of determination of the layer thickness and the X-ray diffraction method.

Figure 1 shows the surface morphology, EDX spectrum, and chemical composition of the SnO_2 film obtained on sapphire in a variant of deposition with the antimony dopant.

It is evident that, in this case, the obtained composition, making allowance for the measurement accuracy, corresponds to the SnO_2 film on Al_2O_3. In contrast with this, the composition of the film obtained on silicon, also in the variant of deposition with the antimony dopant, does not correspond to stoichiometric SnO_2. A substantial excess of oxygen is observed (Fig. 2). A similar pattern is observed for obtaining the TiO_2 films on silicon (Fig. 3). In the last case, the average results over the sample surface are presented along with the standard deviations.
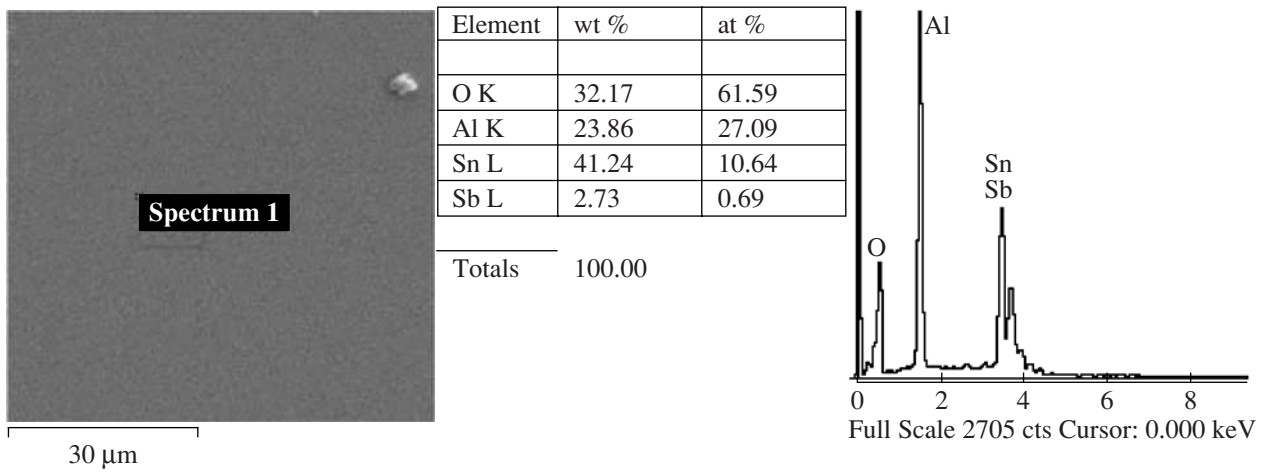
Element	wt %	at %
O K	32.17	61.59
Al K	23.86	27.09
Sn L	41.24	10.64
Sb L	2.73	0.69
Totals	100.00	

Full Scale 2705 cts Cursor: 0.000 keV

Fig. 1. Surface morphology, EDX spectrum, and chemical composition of the antimony-doped tin oxide film deposited on sapphire.
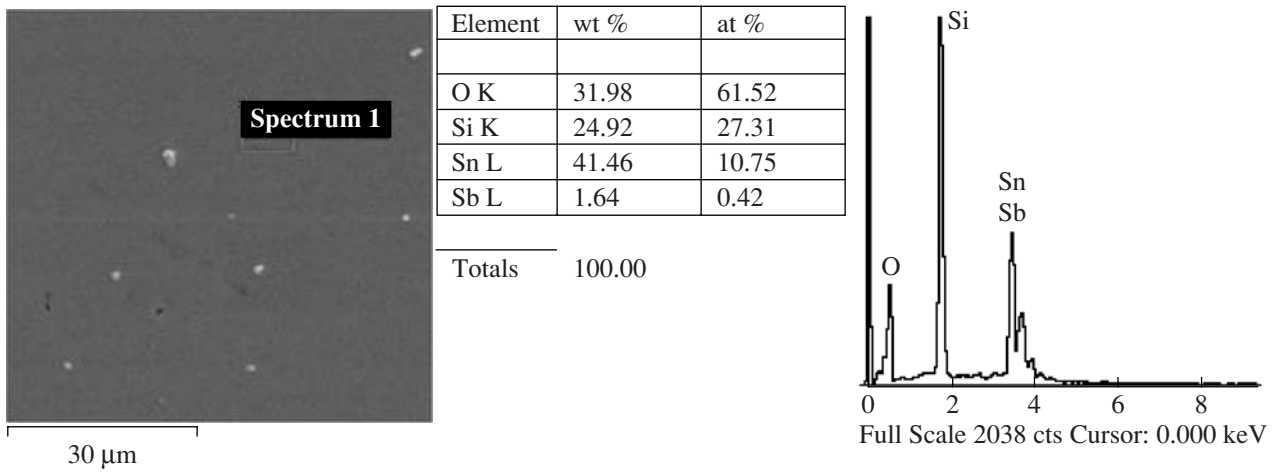
Element	wt %	at %
O K	31.98	61.52
Si K	24.92	27.31
Sn L	41.46	10.75
Sb L	1.64	0.42
Totals	100.00	

Full Scale 2038 cts Cursor: 0.000 keV

Fig. 2. Surface morphology, EDX spectrum, and chemical composition of the antimony-doped tin oxide film deposited on silicon.

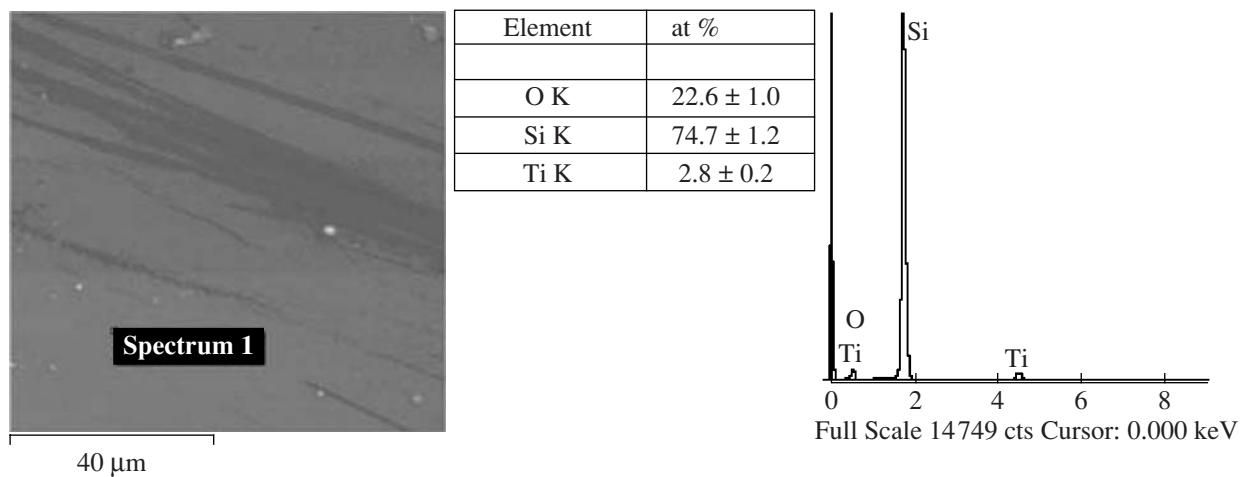| Element	at %
O K	22.6 ± 1.0
Si K	74.7 ± 1.2
Ti K	2.8 ± 0.2

Full Scale 14 749 cts Cursor: 0.000 keV

Fig. 3. Surface morphology, EDX spectrum, and chemical composition of the titanium oxide film deposited on silicon.
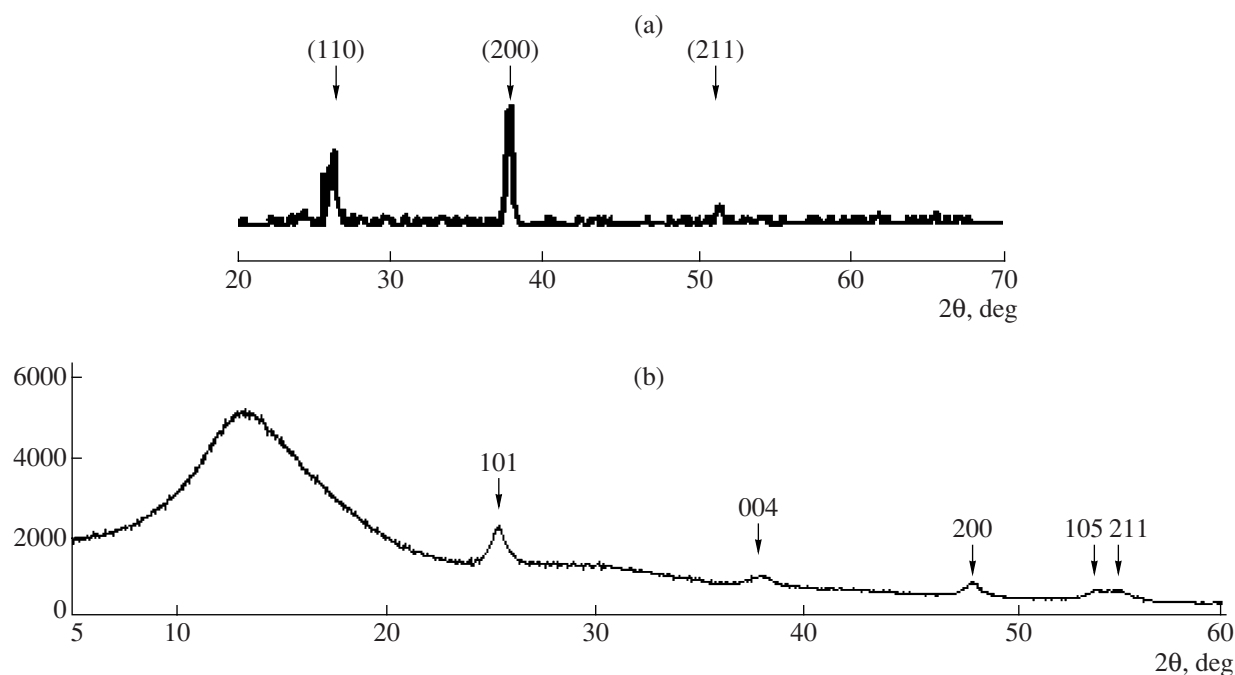
Fig. 4. X-ray diffraction spectra of the films of (a) tin oxide and (b) titanium oxide obtained by pyrolytic pulverization.
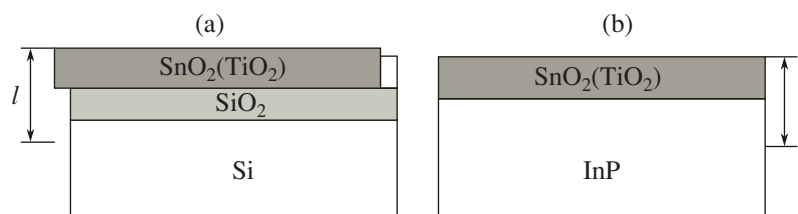

Fig. 5. Schematic image of the oxide–semiconductor structures obtained by pyrolytic pulverization. *l* is the thickness of the layer in which the EDX analysis is performed.

To study the structure, the films of tin and titanium oxides were removed from the surfaces of the substrates and analyzed using X-ray phase analysis, whose results are presented in Fig. 4 and Table 1.

The X-ray diffraction patterns of the surface indicate that the films obtained by pyrolytic pulverization are SnO_2 and TiO_2 oxides and possess the tetragonal crystal structure. The TiO_2 film corresponds to the anatase modification. As for the presence of excess oxygen, it can be associated with the fact that, for deposition on Si, a more complex structure is observed (Fig. 5a), in which the intermediate phase of silicon oxide is observed for deposition of both TiO_2 and SnO_2.

With the proviso of the correctness of the assumptions made, it seems to be evident that the obtained TiO_2 layer is substantially (by a factor of several times) thinner than the tin oxide layer, which can be judged by the difference in the concentrations (in atomic percent) obtained using this method (compare the data of Figs. 2 and 3).

This can be confirmed by the results of optical measurements given below and the data of the EDX analysis for the films containing the antimony dopant (Fig. 2) and without it (Table 2). According to the results of the

Table 1. X-ray diffraction parameters of titanium oxide films

Peak no.	Miller index, *hkl*	Interplanar spacing, Å
1	101	3.507
2	004	2.371
3	200	1.891
4	105	1.699
5	211	1.667

Element	wt %	at %
O K	0.20	0.89
P K	22.33	51.07
Ti K	0.28	0.42
In L	77.19	47.63
Totals	100.00	

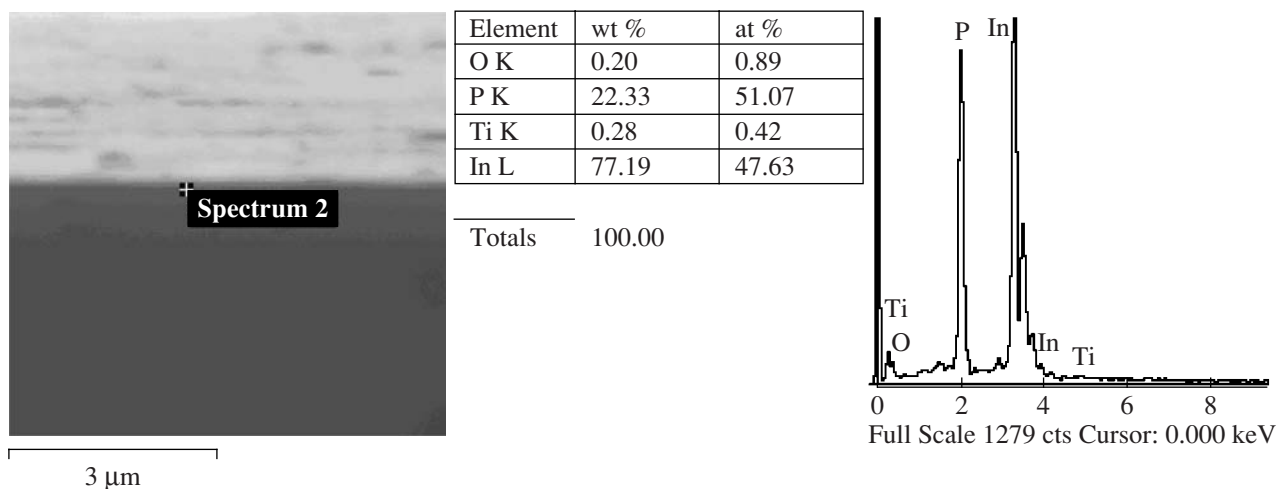Full Scale 1279 cts Cursor: 0.000 keV

Fig. 6. Microphotograph of the transverse cut, EDX spectrum, and chemical composition of the titanium oxide film deposited on indium phosphide.

optical measurements (the calculation methods will be presented in the following section), the thickness of the SnO_2 films without the antimony additive is 330 nm, and, with the additive, it is 200 nm for the deposition of these films on glass. Exactly the same ratio of the tin concentrations determined by the EDX method takes place for the deposition of the SnO_2 film on silicon (1.64) without antimony and with antimony during the pyrolysis (Fig. 2, Table 2). Under the assumptions made, the thickness of the titanium oxide film with the anatase structure deposited on Si is about 50 nm (see Figs. 2, 4).

The possibility of formation of an intermediate layer of silicon oxide for deposition of the films of titanium oxide on silicon by other methods at the same temperatures that were used in this study was shown more than once. The efficiency of the use of such a structure in photovoltaic systems was also pointed out [8].

In contrast with the deposition on silicon, the intermediate layer does not manifest itself during preparation of TiO_2 films on InP. The results of the elemental analysis of the diagonal cut indicate this fact. The observed stoichiometric ratio between titanium and oxygen equals approximately two (Fig. 6).

Simultaneously, the obtained results can indicate that the film of titanium oxide on InP is even thinner than on silicon because of the lower Ti content (compare the data of Figs. 3 and 6).

Taking into account the qualitative similarity of the processes of formation of the SnO_2 and TiO_2 films, we can suppose that a similar pattern will be also observed for the formation of the SnO_2 films on InP; i.e., the scheme of the forming heterojunction will correspond to that presented in Fig. 5b with the only difference being that the obtained films should be thicker. However, the results of the measurements of the composi-

tion of the surface layer after deposition of SnO_2 on InP presented in Fig. 7 contradict the statement on the absence of the intermediate oxide layer, i.e., correspondence to Fig. 5b, since, as follows from the results presented in Fig. 7, excess oxygen is present in this case.

It is evident from the comparison of the data presented in Fig. 7 and Table 2 that, for deposition on InP, the layer of tin oxide is somewhat thinner than for deposition of this oxide on Si but substantially thicker than the titanium oxide layer deposited on InP. As for the presence of excess oxygen and the possibility of formation of the heterostructure with tin oxide and the intermediate oxide layer on InP, which is not observed in the case of deposition of titanium oxide on InP, this question should be answered based on additional investigations.

Optical Properties of Films and Heterojunctions

Transmission spectra were investigated for the obtained SnO_2 and TiO_2 layers. Figure 8 presents such spectra for the SnO_2 layers deposited on glass substrates. The transparency of the undoped layers in this wavelength region reaches 85%, and, for the antimony-doped layers, it falls to 53%. The observed interference

Table 2. Chemical composition of the undoped SnO_2 film deposited on silicon

Element	wt %	at %
O	32.11	71.22
Si	8.80	11.12
Sn	59.09	17.66

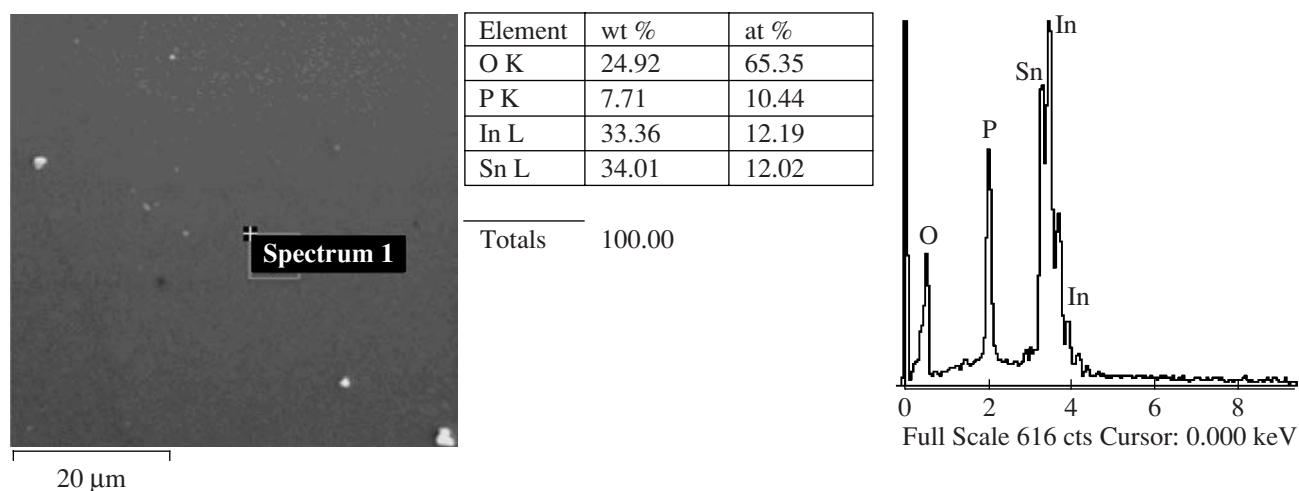| Element	wt %	at %
O K	24.92	65.35
P K	7.71	10.44
In L	33.36	12.19
Sn L	34.01	12.02
Totals	100.00	

Full Scale 616 cts Cursor: 0.000 keV

20 μm

Fig. 7. Surface morphology, EDX spectrum, and chemical composition of the titanium oxide film deposited on indium phosphide.
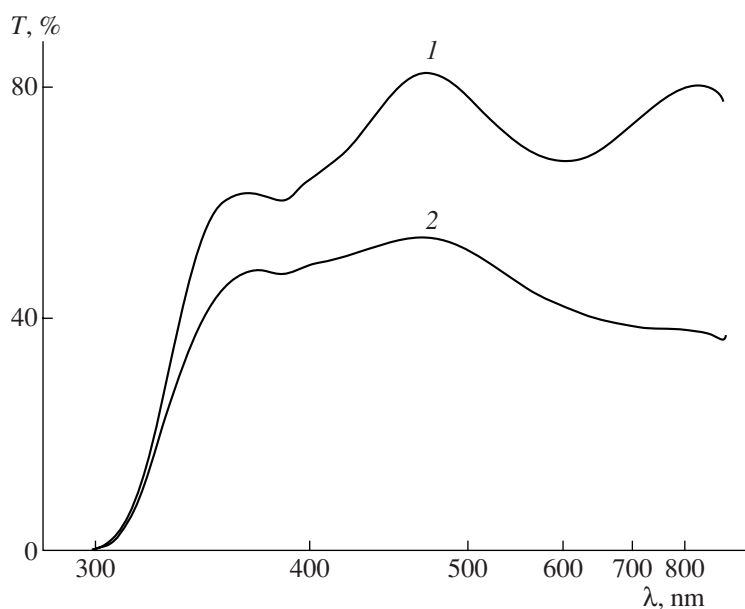

Fig. 8. Transmission spectra of (*1*) the undoped and (*2*) Sb-doped SnO_2 film.

pattern allows one to estimate the thickness *D* of the SnO_2 films using the known relation [9]

$$D = \lambda_1\lambda_2/(\lambda_1 - \lambda_2)2n, \qquad (2)$$

where λ_1 and λ_2 are the wavelengths of the nearest peaks or valleys and *n* is the refraction index for SnO_2 equal to 2 at a wavelength of 550 nm [10]. The thus obtained thicknesses of the SnO_2 layers are 330 nm for the undoped film and 200 for the doped film.

The corresponding spectra of the films deposited on quartz and sapphire substrates differ by the smoother transparency decay in the region of short wavelengths.

The edge of the transmission band at 4.96 eV is independent of the substrate nature in this case. These results allowed us to more exactly determine the band gap of SnO_2 equal to 4.7 eV.

In the case of TiO_2 films deposited on glass and silicon, the spectral distribution of the transmittances and reflectances is presented in Fig. 9. One can see that these films are transparent in the wavelength range of 500–2500 nm. The maximum value of the reflectance equal to 35% is observed at $\lambda = 425$ nm. As the wavelength increases, the reflectance monotonically decreases to 10%.
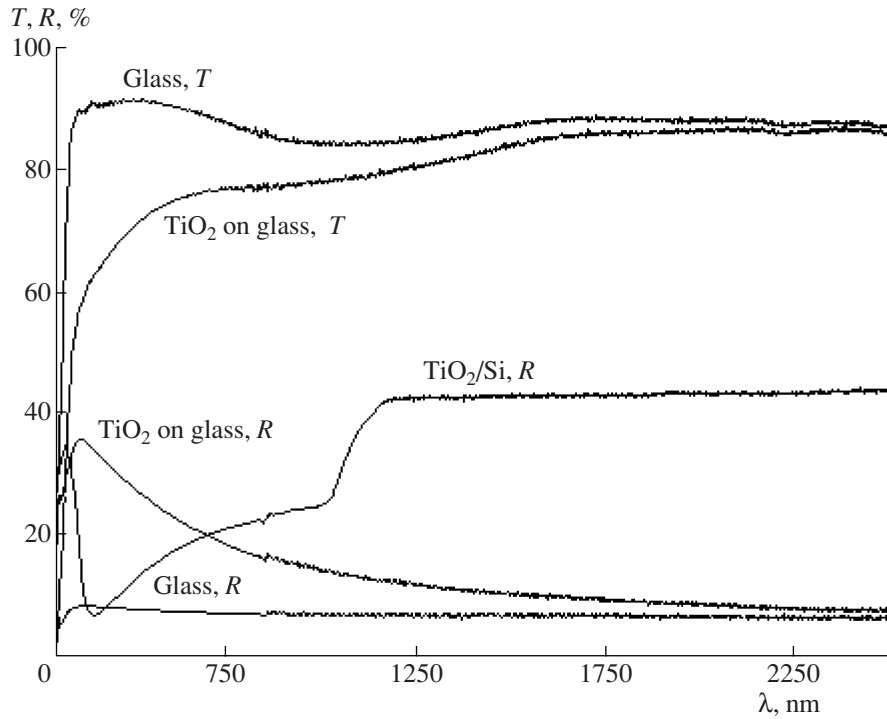
Fig. 9. Spectral distribution of the transmittances T and reflectances R of the titanium oxide films on glass and silicon.
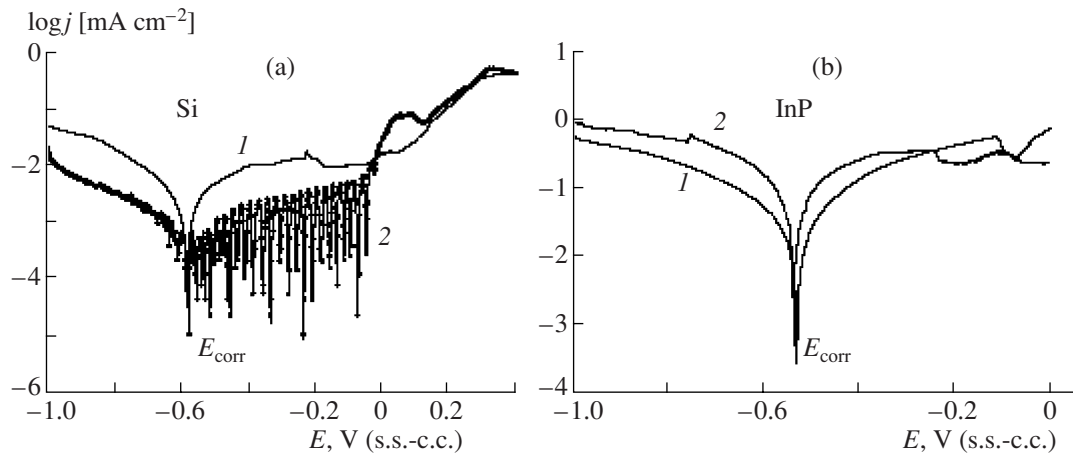

Fig. 10. Corrosion diagrams of (a) silicon ($n_0 = 5 \times 10^{15}$ cm^{-3}) and (b) indium phosphide ($n_0 = 10^{18}$ cm^{-3}) in the chloride–sulfate corrosion solution (*1*) in the dark and (*2*) in the light.

Corrosion Characteristics

Corrosion tests carried out by the above-described procedures allowed us to judge the efficiency of the obtained heterojunctions from the viewpoint of photo-corrosion and photodegradation. Figure 10 shows the voltammetric corrosion diagrams of the narrow-gap semiconductors used as the substrates, and Table 3

gives the characteristics of the corrosion process for the used corrosion medium calculated based on these diagrams.

Table 3 also shows the values of the resistance to the charge transfer obtained based on impedance measurements, which can be considered as a characteristic of the corrosion process for these systems. It is evident

Table 3. Characteristics of the corrosion process in a neutral medium (pH = 6.0) of semiconductor materials and oxide–semiconductor heterojunctions

Material	Voltampermetry					
	E_{corr}, V		j_{corr}, A/cm^2		Resistance to charge transfer, kΩ	
	Dark	Light	Dark	Light	Dark	Light
Si	−0.58	−0.58	2.8×10^{-6}	2.8×10^{-7}	30	164
InP	−0.52	−0.51	3.4×10^{-5}	2.1×10^{-5}	14	7.6
SnO$_2$/Si	−0.35	−0.43	1.4×10^{-6}	3.1×10^{-7}	260	423
TiO$_2$/Si	−0.16	−0.03	4.5×10^{-7}	1.6×10^{-6}	300	45
SnO$_2$/Si	−0.01	−0.02	2.6×10^{-6}	1.7×10^{-5}	74	41

that silicon is much more resistant to photodegradation (photoelectrochemical corrosion) than InP, while their corrosion potentials are close to each other (Fig. 10, Table 3).

The used semiconductor materials had various carrier concentrations (n_0). For example, for Si, it was equal to 5×10^{15} cm^{-3}, and, for InP, 10^{16} and 10^{18} cm^{-3}. In the experiments with high-resistivity samples, oscillations were observed, specifically, those of the anode current in the light (Fig. 10), which can be attributed precisely to a low carrier concentration. It is evident that their periodic generation and recombination are caused by phenomena of passivation and repassivation of the surface under the effect of the light in the anode region of the potentials. At a high carrier concentration (see Fig. 10b), this phenomenon is not observed. It

should be noted that the oscillations observed in corrosion experiments with Si in the light are not specific for silicon only. They were also observed in other systems, for example, for InP, if the carrier concentration was sufficiently low.

Deposition of oxides with obtaining the heterojunctions leads to a considerable shift of the corrosion potential into the anode region (Fig. 11, Table 3).

To the largest extent, this is characteristic of the films of titanium oxide on silicon and tin oxide on indium phosphide. The densities of the corrosion currents have the same order of magnitude in this case. The shift of the corrosion potentials into the anode region makes these materials very promising not only from the viewpoint of corrosion but also for electrochemical applications, specifically as photoanodes for photo-electro-chemical obtaining of hydrogen.

The results of the impedance measurements, which were performed only in the light, qualitatively agree with the results of the voltammetric tests, with the data of the chemical analysis, and with the structure of the heterojunctions.

Figures 12–14 show the impedance spectra both for pure materials and for heterojunctions, as well as the corresponding equivalent circuits.

The obtained equivalent circuits demonstrate the formation of various heterojunctions. Specifically, simple systems such as silicon/electrolyte and indium phosphide/electrolyte can be described by a simplest circuit with a single interface (semiconductor–electrolyte since only one semicircle is observed in the complex plane (Fig. 12). Unlike for InP-based heterojunctions, two semicircles are observed, which corresponds to the equivalent circuit with two barriers (two interfaces, Fig. 13). It seems likely that the assumption made above by the results of chemical analysis with
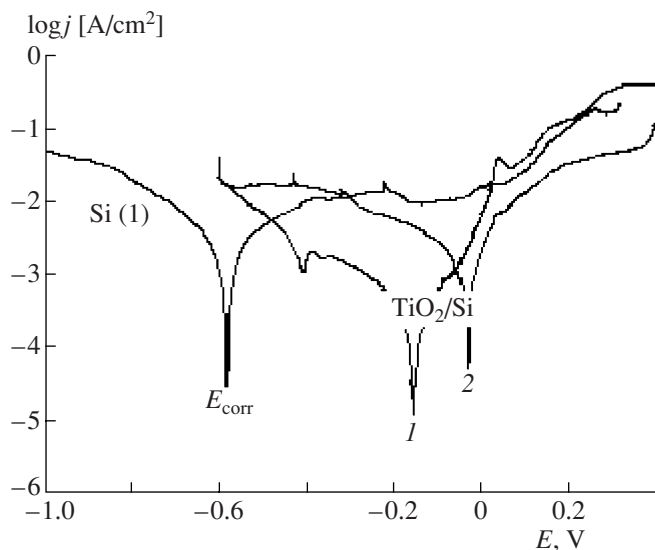
Fig. 11. Corrosion diagrams of silicon and the structure of titanium oxide–silicon (*1*) in the dark and (*2*) in the light.
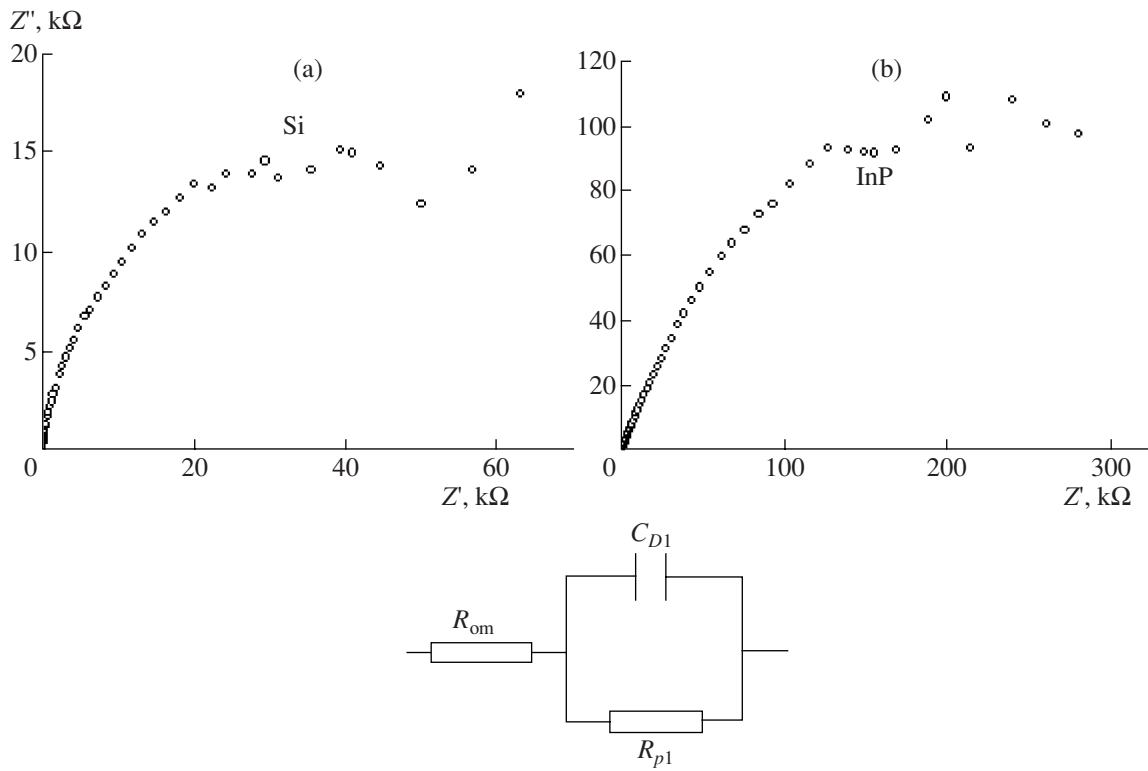
Fig. 12. Impedance spectra of (a) silicon ($n_0 = 5 \times 10^{15}$ cm^{-3}) and (b) indium phosphide ($n_0 = 10^{18}$ cm^{-3}) and the corresponding equivalent circuit obtained in the chloride–sulfate corrosion solution.
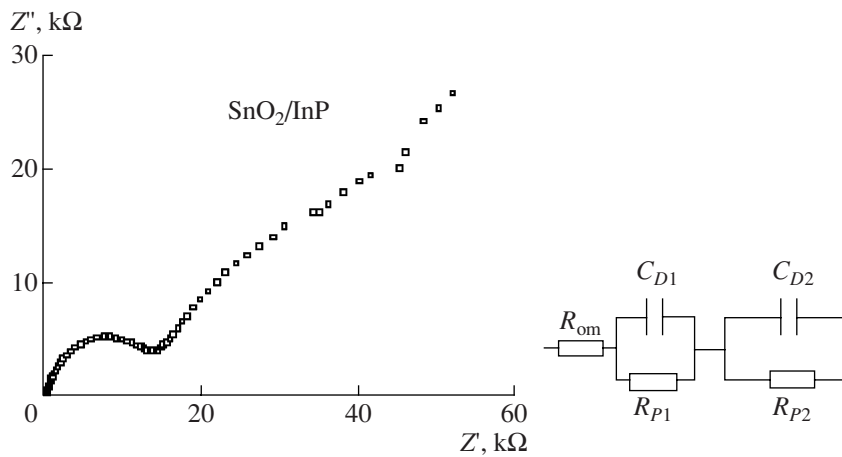
Fig. 13. Impedance spectrum of the SnO$_2$/InP structure (carrier concentration in InP $n_0 = 5 \times 10^{16}$ cm^{-3}) and the corresponding equivalent circuit.

respect to a relatively simple heterojunction, which is not complicated by the intermediate oxide layer for the systems oxide/InP (see Fig. 5b), is righteous.

For the system SnO$_2$/silicon, a considerably more complex pattern is observed (Fig. 14). The equivalent circuit involves several junctions and inductance, which corresponds to a more complex heterostructure and the data of the chemical analysis indicating the presence of the silicon oxide layer under the tin oxide layer (see Fig. 5a).
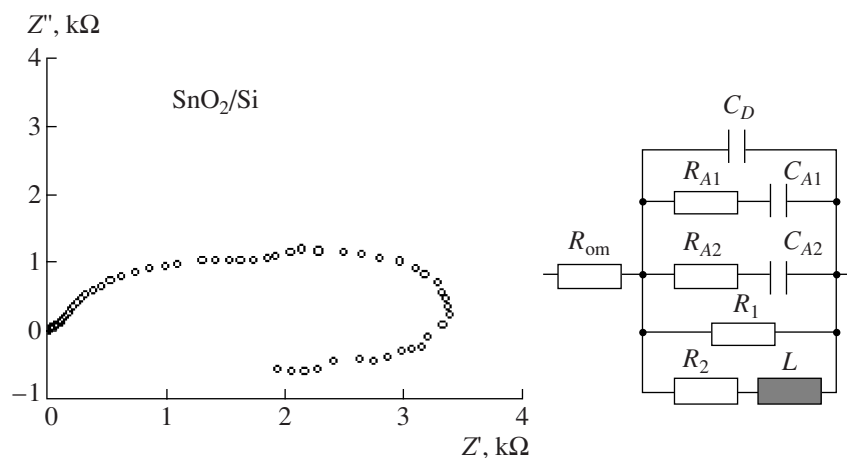
Fig. 14. Impedance spectrum of the SnO$_2$/Si structure (carrier concentration in Si $n_0 = 5 \times 10^{15}$ cm^{-3}) in the chloride–sulfate corrosion solution and the corresponding equivalent circuit.

CONCLUSIONS

Peculiarities of obtaining the films of tin and titanium oxides, as well as semiconductor structures on their basis, by the method of pyrolytic pulverization are described. The x-ray diffraction data showed that crystalline tetragonal structures are formed in this case (anatase modification for TiO$_2$). The results of the elemental analysis and impedance investigations of the obtained semiconductor structures in a model chloride–sulfate solution showed that, in the case of oxidation on silicon, the structure oxide/SiO$_2$/Si is formed and, in the case of deposition on InP, the structure oxide/InP is formed. The results of the corrosion investigations showed that, during the deposition of the above-mentioned oxides on the Si and InP crystals and obtaining the corresponding semiconductor heterostructures, a substantial shift of the corrosion potential into the anode region is observed, which makes them promising materials for photovoltaic applications.

REFERENCES

1. Adeeb, N., Kretsu, I., Sherban, D., Sushkevich, V., and Simashkevich, A., Spray Deposited ITO–CdTe Solar Cells, *Sol. Energy Mater.*, 1987, vol. 15, no. 1, pp. 9–19.
2. Vasu, V., Subrahmanyam, A., Kumar, J., and Pamasamy, P., Spray-Pyrolytic-Grown ITO/InP Junctions: Effects of Tin Doping, *Semicond. Sci. Technol.*, 1993, vol. 8, pp. 437–440.
3. Do Quoc Hung, Bobeico, E., Gorceac, L, Sherban, D., and Simashkevich, A., Solar Cells Based on SIS structures, *Proc. 3rd Int. Workshop on Material Science, Part I*, Hanoi, 1999, pp. 56–59.
4. Gagara, L., Gorcheac, L., Radu, C., Sherban, D., and Simashkevich, A., Photovoltaic Converters of Solar Energy on the Base of SIS Structures, *Proc. Int. Conf. "Euro-Sun 96"*, Munchen, 1996, vol. 2, pp. 665–669.
5. Simashkevich, A., Sherban, D., Bruk, L., Bobeico, E., Coval, A., Fedorov, V., and Usatyi Iu, Spray Deposited ITO–*n*-Si Solar Cells with Enlarged Area, *Proc. 20th European PV Solar Energy Conf.*, Barcelona, 2005, pp. 980–982.
6. Grätzel, M., Photoelectrochemical Cells, *Nature*, 2001, vol. 414, pp. 338–344.
7. Badawy, W.A., Improved *n*-Si/oxide Junctions for Environmentally Safe Solar Energy Conversion, *Sol. Energy Mater. Sol. Cells*, 2002, vol. 71, pp. 281–294.
8. Green, M.A., *Silicon Solar Cells: Advanced Principles and Practice*, Sydney: Bridge Printery, 1995.
9. Moss, T., Barrel, G., and Ellis, B., *Semiconductor Optoelectronics*, New York, Halsted Press, 1973.
10. Voronkova, E.M., Grechushnikov, B.N., Distler, G.I., and Petrov, I.P., *Opticheskie materialy dlya infrakrasnoi tekhniki* (Optical Materials for Infrared Technique), Moscow: Nauka, 1965.

ELECTRICAL PROCESSES
IN ENGINEERING AND CHEMISTRY

Electric-Discharge Cleaning of Surfaces of Manufacturing Equipment from Foreign Nonmetallic Deposits

T. D. Denisyuk, A. R. Rizun, and Yu. V. Golen'

Institute of Pulse Processes and Technologies, National Academy of Sciences of Ukraine,
pr. Oktyabr'skii 43a, Nikolaev, 54018 Ukraine

Received March 29, 2007

Abstract—Processing characteristics of the electric-discharge cleaning of surfaces of manufacturing equipment from foreign nonmetallic deposits of different durability are researched. To expand the capabilities of the cleaning of manufacturing equipment, a complex cleaning method is proposed.

The cleaning of working surfaces of manufacturing equipment and power plant units and components from all kinds of contaminations, residua of lacquer coatings, glue compounds, preservative oils, and other foreign deposits is often a big problem. One can solve it by electric-discharge treatment of these surfaces. The electric-discharge cleaning technique differs favorably from other known ones in the relatively simple controllability of the process, the capability of easy proportioning of energy, and its high cost efficiency. The technique is nonpolluting and provides a high quality of the cleaning of inner spaces and outer surfaces having a very irregular shape.

The objective of this work is to determine the process-dependent parameters of the electric-discharge cleaning of equipment from contaminations with different strengths.

The amount of breakdown strength of nonmetallic coatings depends on the value of the pressure pulse, the geometry, and the coating strength. In this case, the energy should not exceed the critical energy ($\sigma_{comp.s}$) of the surface failure of the cleaned equipment.

The required value of the energy can be determined by the following expression [1]:

$$\sigma_{comp.s} \leq E \geq \sigma_{comp} V, \qquad (1)$$

where $\sigma_{comp.s}$ is the ultimate compression strength of the work surface, MPa; σ_{comp} is the ultimate compression strength of the nonmetallic materials, MPa; and V is the amount of breakdown strength toward the nonmetallic surfaces of one discharge, m^3.

The value of the specific energy E of a discharge channel of length l, which is introduced in the time τ, is determined from the discharge parameters by the following relationship [2]:

$$E = \frac{R_0^4 \pi \rho_0 l}{2(\gamma - 1)\pi^2 LC(r + l)}, \qquad (2)$$

where R_0 is the discharge channel radius equal to 0.001 m; ρ_0 is the density of an undisturbed discharge medium (water), kg/m^3; γ is the effective adiabatic index equal to 1.26; L is the discharge circuit inductance, μH; C is the discharge circuit capacitance, μF; l is the discharge channel length, m; and r is the radius of the effective action of a compression wave, m.

Thus, expression (1) can be written in the following form:

$$\frac{R_0^4 \pi \rho_0 l}{2(\gamma - 1)\pi^2 LC(r + l)} = \sigma_{comp} V. \qquad (3)$$

Relationship (3) obtained relates the discharge circuit parameter to the characteristics of the nonmetallic deposits and the amount of their breakdown. Figure 1 shows the amount of breakdowns (performance rate) as a function of the discharge energy at an impulse frequency of 2 Hz.

Using expression (3), through the electric discharge parameters, one can make an evaluative calculation of the process-dependent parameters: the amount of breakdown by one discharge and the performance rate of the electric-discharge equipment at the preset discharge frequency. One can also determine the area of the cleaned surface as a function of the deposit thickness.

Data obtained for the energy that is necessary for the breakdown of the nonmetallic deposits are compared with the accepted values of the energies for the breakdown of the material of the cleaned surfaces. We experimentally determined the dependence (Fig. 2) of the accepted values of the electric-discharge cleaning energies on the wall thickness of equipment work surfaces produced from steel, cast iron, and aluminum alloys [3].

If the energy for the breakdown of the nonmetallic deposits exceeds the accepted values of the energy for the treatment of the equipment surfaces, one should use
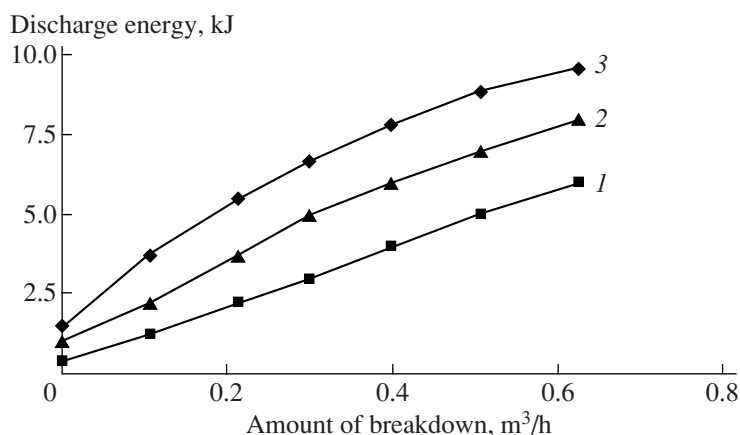
Discharge energy, kJ

Fig. 1. Amount of breakdown of nonmetallic coatings with different strength characteristics versus the discharge energy: (*1*) 5, (*2*) 10, and (*3*) 20 MPa.

a lesser discharge energy. For breakdown of strong deposits, the missing energy is compensated for by their softening by means of the combination of electro-hydro-impulsive cleaning with application of active discharge mediums.

The discharge medium was a solution of surface-active substances. Application of these substances is due to the absorption properties at interfaces and their capability of reducing surface tension. This process is based on the dispersive power of surface-active substances [4].

Under mechanical loading at the surface of a solid (in the present case, it is the surface of strong deposits), microcracks are formed which are a basic cause of the strength reduction. Under the influence of outer deforming forces, microcracks can be developed very easier under adsorption of various substances from the medium in which the dispersion process takes place (breakdown).

The active discharge medium is an adipic acid solution (the chemical formula is $(CH_2)_4 (COOH)_2$). It is easily water soluble and nontoxic.

Findings are directed to the development of new more-effective electro-hydro-impulsive technologies for cleaning equipment from foreign coatings and contaminations.

Application of the electric-hydraulic cleaning technology will allow one to solve the problem of the breakdown and removal of foreign deposits during repair works and cleaning of tight-area breakable thin-walled surfaces and to greatly improve the hygiene and sanitary conditions of work and ecology.

Discharge energy, kJ
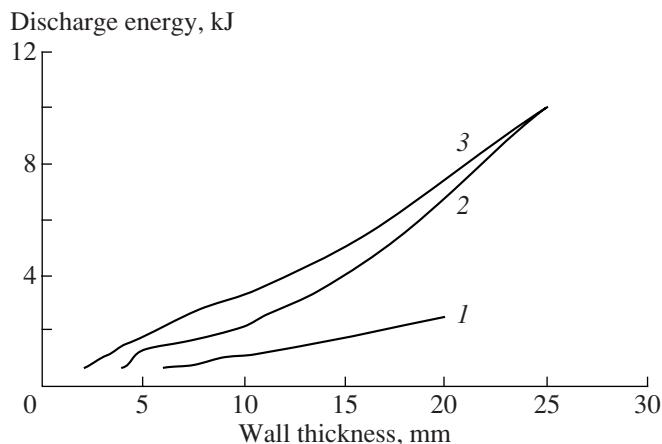
Fig. 2. Accepted values of the discharge energy versus the part's wall thickness: (*1*) for AL 6; (*2*) for SCh 28-48; and (*3*) for St 45.

REFERENCES

1. Denisyuk, T.D. et al., Ukraine Patent 20898, *Byull. Izobret.*, 2007, no. 2.

2. Rizun, A.P., Ivanov, V.V., and Rybka, O.M., *Metodika rascheta gidrodinamicheskikh i elektricheskikh kharakteristik kanala razryada elektrogidravlicheskikh ustanovok* (Design Procedure of Hydrodynamic and Electrical Characteristics of a Discharge Channel of Electrohydraulic Plants), Kiev: Proektno-konstruktorskoe Byuro Elektrogidravliki AN UkSSR, 1982.

3. Denisyuk, T.D. and Rizun, A.P., Electric-Discharge Cleaning of Precision Casting, *Elektron. Obrab. Mater.*, 2005, no. 3, p. 83.

4. Rizun, A.P., Golen', Yu.V., and Denisyuk, T.D., Ways of Increasing the Efficiency of Electric-Discharge Cleaning of Precision Castings, *Liteinoe Proizvod.*, 2006, no. 6, p. 21.

ELECTRICAL PROCESSES
IN ENGINEERING AND CHEMISTRY

Effect of the Discharge-Gap Distance on the Formation of Hydrogen Peroxide in a Plasma–Solution System with Atmospheric-Pressure Glow Discharge

L. A. Kuz'micheva, Yu. V. Titova, and A. I. Maksimov

Institute of Chemistry of Nonaqueous Solutions, Russian Academy of Sciences,
ul. Akademicheskaya 1, Ivanovo, 153045 Russia

Received April 26, 2007

Abstract—The accumulation of hydrogen peroxide in an inert electrolyte solution (Na_2SO_4) under the action of an atmospheric-pressure glow discharge was studied. The amounts of OH radicals and hydrogen peroxide transferred from the solution to gas phase were estimated. The H_2O_2 yield was shown to decrease with increasing the interelectrode distance due to the growth of hydrogen-peroxide transfer to the gas phase under the action of the ion bombardment of the solution surface.
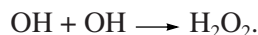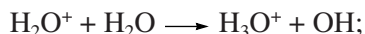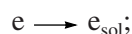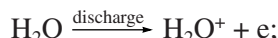
INTRODUCTION

Electric discharges affecting water solutions of electrolytes make it possible to implement many technological processes such as the sterilization of solutions, materials, and items for medical purposes [1]; water purification from organic contaminants [2]; and modification of polymeric surfaces [3].

In this paper, we consider an atmospheric-pressure glow discharge (APGD) with an electrolyte cathode. The schematic representation of the discharge is shown in Fig. 1.

When the glow discharge burns at atmospheric pressure with the electrolyte cathode, the ion bombardment of the thin surface solution layer directly contacting with the plasma area (the cathode spot) takes place. As a result of such activation, the primary active particles—H, e, and OH [4]—are formed in the cathode area:

$$H_2O \xrightarrow{\text{discharge}} OH + H;$$

$$H_2O \xrightarrow{\text{discharge}} H_2O^+ + e;$$

$$e \longrightarrow e_{sol};$$

$$H_2O^+ + H_2O \longrightarrow H_3O^+ + OH;$$

$$OH + OH \longrightarrow H_2O_2.$$
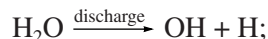
The dimerization of hydroxyl radicals leads to the generation of H_2O_2. The same ion bombardment induces the transfer of solution components from the cathode-spot area to the gas phase—an analog of cathode sputtering of metals. A characteristic of the solution–component transfer is the transfer coefficient—the number of water molecules that are knocked out by an

ion hitting the solution surface. It is shown in [5] that a dissolved substance is transferred to the gas phase according to its mole fraction in the solution. In this case, there are data indicating the fact that the anode–solution distance affects the efficiency of the chemical activation of the solution, which can be related to variation in the hydrogen-peroxide yield [2].

The purpose of this work is to investigate the effect of the interelectrode distance on the accumulation of hydrogen peroxide and the transfer of solution components to the plasma area.

Fig. 1. Principal schematic representation of the atmospheric-pressure glow discharge with an electrolyte electrode: (*1*) anode, (*2*) cathode, (*3*) plasma area, and (*4*) electrolyte solution.

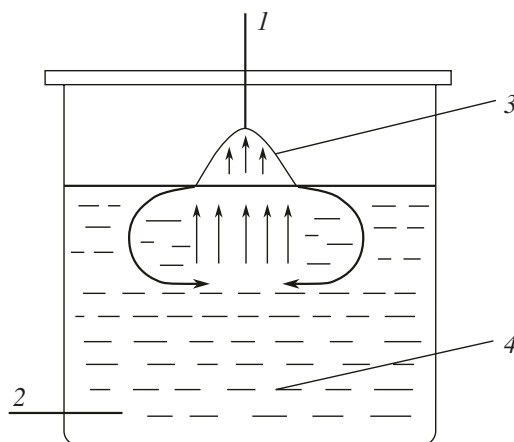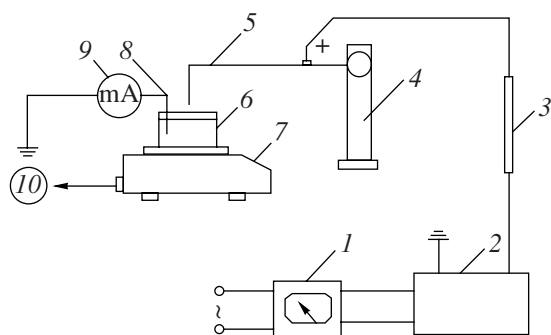**Fig. 2.** Schematic representation of the experimental installation for studying the effect of the interelectrode distance on the transfer coefficient of solution components to the gas phase: (*1*) autotransformer; (*2*) power supply; (*3*) ballast resistor; (*4*) support with the fine adjustment screw; (*5*) anode; (*6*) glass cell with electrolyte solution; (*7*) electronic balance; (*8*) cathode; (*9*) micrometer; and (*10*) computer.
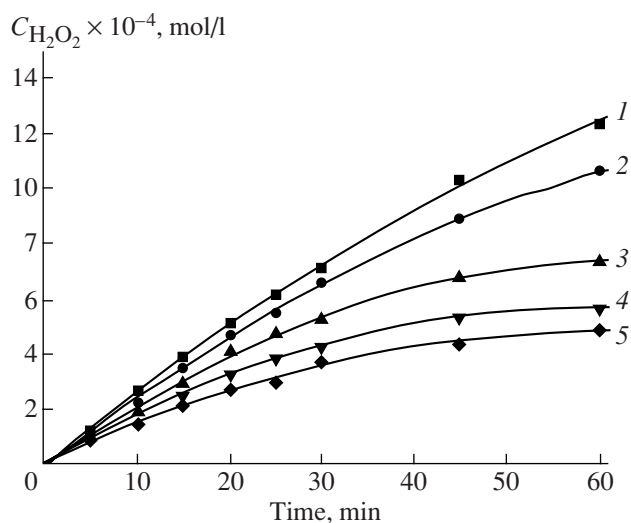

Fig. 3. Effect of the interelectrode distance on the kinetics of hydrogen-peroxide accumulation under the action of the atmospheric-pressure glow discharge. The interelectrode distance, mm: (*1*) 0.5; (*2*) 1; (*3*) 2; (*4*) 3; and (*5*) 4. Experimental conditions: 0.01M Na_2SO_4, the current is 20 mA, and the solution volume is 400 ml.

EXPERIMENTAL

The H_2O_2 concentration was determined by the method of iodometric titration with ammonium molybdate as a selective catalytic agent of the reaction of hydrogen peroxide with iodide ion [6]. As a working solution, we used 0.01M Na_2SO_4. The discharge current was equal to 10 and 20 mA, and the volume of the treated solution was 50, 250, and 400 ml. The treatment time amounted to 60 min. During the plasma treatment, the solution was not forcedly stirred. The anode–solu-

tion distance was 0.5–4 mm. We used the weight method for investigating the mass transfer of solution components from the liquid to gas phase under the action of the ion bombardment. The schematic representation of the installation is shown in Fig. 2.

The transfer coefficient was determined as the ratio between the measured stream of solution components to the gas phase and the stream of ions incident on the solution surface.

RESULTS AND DISCUSSION

The investigations show that the anode–solution distance affects the H_2O_2-accumulation kinetics. An example of the kinetic dependence of the accumulation of hydrogen peroxide on the interelectrode distance for a treated-solution volume of 400 ml is shown in Fig. 3. Similar dependences were obtained for solution volumes of 250 and 50 ml and discharge currents of 10 and 20 mA.

According to the results of the experiments, the initial hydrogen peroxide yield decreases with increasing the interelectrode distance. The initial H_2O_2 yield amounts to 1.8 mol/F for the interelectrode distance equal to 0.5 mm and to 1.0 mol/F for 4 mm with the solution volume of 400 ml and the current of 20 mA. For all the interelectrode distances, we calculated the initial H_2O_2-generation rates (Fig. 4). Similar data were obtained for the treated-solution volumes of 250 and 50 ml and the discharge currents of 10 and 20 mA.

Figure 3 shows that the H_2O_2 yield decreases with increasing the interelectrode distance. In [2], it is shown for the APGD in the flow-through system that the cathode-spot area and the hydrogen-peroxide yield increase with the anode–solution distance. In our case (the stationary system without forced stirring), we see the cause of the decrease in the hydrogen-peroxide yield with the growth of the anode–solution distance in increasing the H_2O_2 transfer to the gas phase under the action of the ion bombardment, which confirms our calculations presented below.

The transfer coefficients for the solution components to the plasma area were obtained by the weight method (a current of 10 mA and a solution volume of 50 ml), and these data are shown in Fig. 5. We propose the kinetic model of the redox processes proceeding in the solution under the APGD action [7], where OH and H_2O_2 are the basic oxidizing agents. The calculations were carried out under the following experimental conditions: the working solution volume of the inert electrolyte is 50 ml, and the discharge current is 10 mA. Because an inert electrolyte is used in this case, the OH and H_2O_2 balances can be presented in the following form. The hydroxyl-radical balance includes the OH formation in the cathode-spot area under the action of the ion bombardment, the OH expenses during the dimerization with the H_2O_2 formation and recombina-
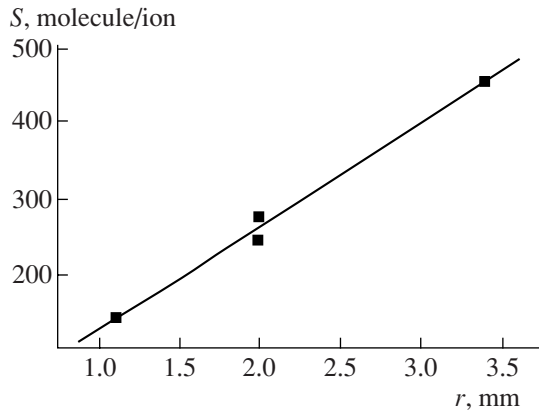
Fig. 4. Effect of the interelectrode distance r on the hydrogen-peroxide accumulation rate R_0 for 0.01M Na_2SO_4 (400 ml, 20 mA).
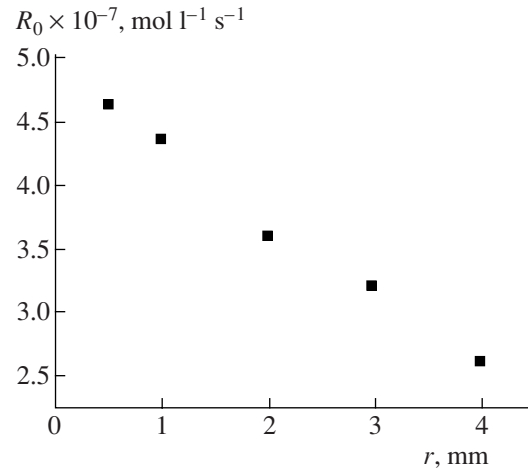

Fig. 5. Dependence of the transfer coefficient S of the solution components on the discharge-gap length r (0.01M Na_2SO_4, 50 ml, 10 mA).

tion with atomic hydrogen, and also the OH transfer to the gas phase under the action of the APGD:

$$\frac{Sn}{N_aV} = k_1[OH^\cdot]^2 + k_2[OH^\cdot][H^\cdot] + \frac{Ss}{N_{H_2O}VN_a}[OH^\cdot],$$

where S is the ion stream from the plasma amounting to 6.25×10^{16} ion/c for the current of 10 mA; s is the transfer coefficient of the solution components, which varies for water molecules from 100 to 500 molecules/ion depending on the interelectrode distance; N_{H_2O} is the concentration of water molecules in the solution equal to 55.5 mol/l; V is the cathode-area volume, 3×10^{-10} l; N_A is the Avogadro number, 6.02×10^{23} molecule/mol; k_1 is the interaction-rate constant for the OH radicals, 8×10^9 l mol^{-1} s^{-1} [4]; k_2 is the rate constant for the recombination of OH radicals with atomic hydrogen, 2.2×10^{10} l mol^{-1} s^{-1} [4]; and the concentrations (in mol/s) of the corresponding particles are indicated in square brackets.

The hydrogen-peroxide balance includes its formation in the reaction of OH-radical dimerization and also the transfer to the gas phase under the action of the ion

bombardment and the accumulation of H_2O_2 in the solution calculated from the experimental data:

$$k_1[OH^\cdot]^2V = \frac{Ss}{N_{H_2O}N_a}[H_2O_2] + \frac{R_0}{C_\infty}[H_2O_2],$$

where R_0 is the initial H_2O_2-generation rate obtained from the experimental data (1.24×10^{-7} mol/s) and C_∞ is the limiting concentration of H_2O_2 equal to 1.1×10^{-2} mol/l.

On the basis of the presented balances, we calculated the OH-radicals and hydrogen-peroxide fractions transported from the solution to the gas phase under the action of the ion bombardment for the transfer coefficients equal to 100 and 500 molecule/ion corresponding to the minimal and maximal interelectrode distances. The results of the calculations are listed in the table.

The calculations carried out under such conditions show that the hydrogen-peroxide fraction transported to the gas phase under the action of the ion bombardment considerably exceeds the similar value for the OH radicals. Thus, the transport of solution components to the gas phase under the action of the ion bombardment affects the physical properties of the gas-discharge system, and this fact should be taken into account in the analysis of arbitrary chemical reactions initiated by an atmospheric-pressure glow discharge with an electrolyte electrode.

Amount of OH radicals and hydrogen peroxide transported under the action of the ion bombardment to the gas phase

Transfer coefficient s, molecule/ion	Fraction of OH radicals transported to the gas phase, %	Fraction of H_2O_2 transported to the gas phase, %
100 (r min)	7.55×10^{-3}	0.75
500 (r max)	3.78×10^{-2}	3.6

REFERENCES

1. Stroikova, I.K. and Maksimov, A.I., Decontamination of Solutions by Glow and Diaphragm Discharges at Atmospheric Pressure, *Electron. Obrab. Mater.*, 2002, no. 6, pp. 43–49.

2. Ivannikov, A.A., Lelevkin, V.M., Tokarev, A.V., and Yudanov, V.A., Effect of the Atmospheric-Pressure Glow Discharge on Water, *Khim. Vys. Energ.*, 2003, vol. 37, no. 2, p. 148.

3. Titov, V.A., Shikova, T.G., Maksimov, A.I., and Titov, Yu.V., Modification of Polymers in Plasma–Solution System, *Electron. Obrab. Mater.*, 2004, no. 3, pp. 22–28.

4. Pikaev, A.K., Kabakchi, S.A., and Makarov, I.E., *Vysokotemperaturnyi radioliz vody i vodnykh rastvorov* (High-Temperature Radiolysis of Water and Aqueous Solutions), Moscow: *Energoatomizdat*, 1988.

5. Kutepov, A.M., Zakharov, A.G, and Maksimov, A.I., *Vakuumno-plazmennoe i plazmenno-rastvornoe modifitsirovanie polimernykh materialov* (Vacuum-Plasma and Plasma–Solution Modification of Polymeric Materials), Moscow, 2004.

6. Skoog, D. and West, D., *Fundamentals of Analytical Chemistry*, New York, Holt, Rinehart, and Winston, 1976. Translated under the title *Osnovy analiticheskoi khimii*, vol. 1, Moscow: Mir, 1979.

7. Kuz'micheva, L.A., Maksimov, A.I., and Titov, Yu.V., Kinetic Model of Oxidizing Reactions Initiated in Solutions of Electrolytes by Glow Discharge, *Gorenie i Plasmokhim.*, 2005, vol. 3, no. 4, p. 247.

ELECTRICAL PROCESSES
IN ENGINEERING AND CHEMISTRY

Influence of the Preliminary Radiation-Oxidation Treatment of Zirconium on the Radiation-Heterogeneous Processes in the Zr + H$_2$O System

A. A. Garibov, A. G. Aliyev, N. N. Gadzhieva, T. N. Agaev, and G. Z. Velibekova

Institute of Radiation Research, Academy of Sciences of Azerbaijan,
F. Agaeva 9, Baku, AZ-1143 Republic of Azerbaijan

Received May 10, 2007

Abstract—The oxidation processes are studied of untreated and radiation-oxidation preliminary treated (in an H$_2$O$_2$ solution at room temperature) zirconium specimens in contact with water by reflection-absorption infrared spectroscopy. A comparison is performed of their kinetic characteristics. Passivation of the metal surface is revealed as evidence of the surface oxide layer.

INTRODUCTION

Zirconium and its alloys are widely used as nuclear reactor materials. However, in spite of the large number of works on studying the corrosion of the above materials, a clear understanding of the zirconium corrosion mechanism has not yet been reached: not only under the conditions of reactor radiation but also in laboratory experiments. Generation and collection of new experimental data on zirconium material corrosion and searching for new methods of protection against it are important both for the development of the production of articles made of these materials and for optimizing their operation conditions. The surface coating of zirconium materials by a protective oxide layer is one of the ways to solve the above problems. It is possible to produce a passivating coating by preliminary radiation-oxidation treatment of Zr in a 30% hydrogen peroxide solution. Such preliminary radiation treatment is shown to influence the electrophysical properties of metal zirconium [1–6] as well.

The present work is a continuation of the previous investigations and is aimed at a comparative study of the kinetics of the radiation oxidation when in contact with room temperature water and the processes influencing metal zirconium both untreated and radiation-oxidation treated in H$_2$O$_2$ media. The surface Zr modifications caused by the radiation oxidation were controlled by reflectance-absorption infrared spectroscopy (RAIS): RAIS is already acknowledged as a sound technique for studying the oxide layer on the metal surface [7, 8].

EXPERIMENTAL

The experimental study was concerned with 20 × 10 × 5 mm metal zirconium plates subjected to grinding and polishing and having a slick polished surface with reflectance of $R = 0.70 \pm 0.05$ within the infrared (IR) range of 15 to 2.2 μm. The specimens were prepared with similar R values to perform parallel experiments on the radiation oxidation of the nontreated (initial) samples against the preliminary radiation-oxidation samples treated in the H$_2$O$_2$ media zirconium under contact with water at room temperature.

The radiation-oxidation treatment of the metal zirconium in the 30% H$_2$O$_2$ solution was performed according to the technique described in [5]. To decontaminate the samples from organic pollution and to dehydroxylate the nontreated and the treated specimens, the Zr surfaces were subjected to thermovacuum treatment at $T = 373$ K and $P = 10^{-5}$ Pa for 6 h. Bidistilled water was used as the adsorbate; the foreign gases were removed from the water by multiply freezing in a liquid nitrogen trap and subsequent degassing. The adsorption was performed by means of a volume-adsorption facility [7].

The specimens were irradiated by γ-quanta with a ^{60}Co isotopic source with the dose rate being $\dot{D} = 1.03$ Gy/s. The dosimetry was performed by the ferrosulphate technique, and the absorbed dose was calculated with account for the electron density of the system investigated and the dosimetric solution [9]. Here, the absorbed dose was equal to $D = 5$–420 kGy. The low thickness, d, of the oxide layers on the metal was estimated according to the relative reflectance obtained from the RAIS data [10], whereas the larger thickness was weighted [11].

The IR reflectance spectra received under incidence of the linearly polarized radiation at an angle of $\varphi = 10°$ were measured at room temperature using a Specord 75 JR (Carl Zeiss) spectrophotometer within the frequency
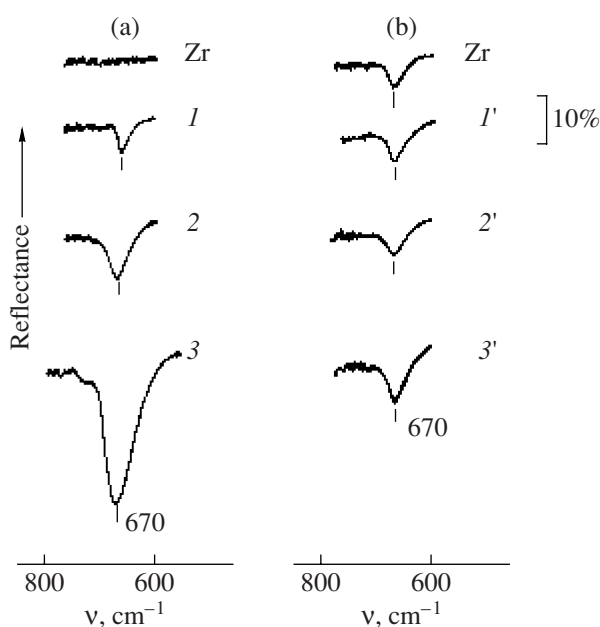
Fig. 1. Oscillation band of the valency oscillation Zr–O bond as a function of the duration, τ of the nontreated (a) and preliminary radiation-oxidation treated (b) zirconium with water under the Zr radiation oxidation ($T = 300$ K): $\tau = $ 3, 30, and 120 h for curves *1*, *1'*; *2*, *2'*; and *3*, *3'*, respectively; the dose rate is $\dot{D} = 1.03$ Gy/s.

range of 1000–500 cm^{-1} using a special reflectance device (Shimadzu, Japan) [12]. Here, we designed and used a specialized quartz cell with a CaF$_2$ window making it possible to trace the Zr surface changes at the contact with H$_2$O under the γ-radiation impact [13].

The optical densities of the Zr–O oxide layer valency oscillations band were determined from the expression

$$D = -\log(R/R_0),$$

where R and R_0 are the reflectance of the pure metal and of the metal with the oxide layer [8].

RESULTS AND DISCUSSION

Figure 1 shows the IR reflectance spectra of the zirconium specimens in the contact with H$_2$O: nontreated (curves *1–3*) and preliminarily radiation-oxidation treated in the H$_2$O$_2$ media (curves *1'–3'*) at $T = 300$ K, $\dot{D} = 1.03$ Gy/s. Beginning from the particular absorbed dose of the γ-irradiation, $D = 10$ kGy, a thin oxide layers occurs on the Zr surface, thus causing a very weak and narrow Zr–O valency oscillation reflectance band with the maximum at $\nu = 670$ cm^{-1} (curve *1*) [10, 14]. With the absorbed dose D increased from 10 up to 420 kGy (or the contact duration τ increases from 3 up to 120 h), the above band intensity increases by an order of magnitude and its half-width ($\nu_{1/2}$) increases by 2.7 times (from 30 up to 80 cm^{-1}, curves *2–3*). The fuzzy maximum of the Zr–O oscillation band is typical for the polycrystalline structures and indicates the nonuniformity of the relatively thick ($d = 0.35$ μm) oxide layer. The observed increase of the $\nu_{1/2}$ value by 2.7 times for the Zr–O oscillation band in the oxide layer under the radiation oxidation of the nontreated Zr specimens is probably connected with the metal structure nonuniformities produced by the γ-irradiation [15].
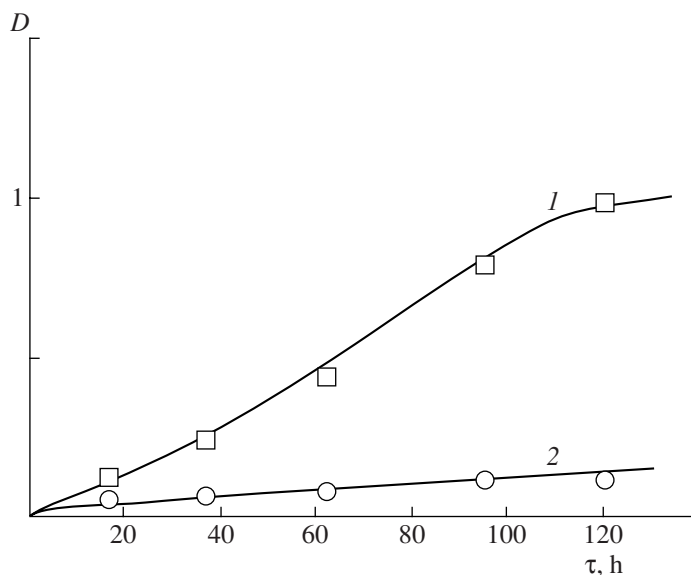

Fig. 2. Optical density of the absorption oscillation band of the Zn–O oxide layer as a function of the duration of the nontreated (*1*) and preliminary radiation-oxidation treated (*2*) zirconium with water under its radiation oxidation ($T = 300$ K); $\dot{D} = 1.03$ Gy/s.

The IR reflectance spectrum of the preliminary treated zirconium (the radiation-oxidation treatment in the H_2O_2 media) shows the presence of a thin (12 nm) oxide layer (Fig. 1b). After the contact of Zr with water, under the γ-irradiation, no marked variation takes place within the range of the absorbed dose of $D = 5$–420 kGy (Figs. 1'–3'). Then, the Zr–O valency oscillation band intensity and half-width vary insignificantly ($\nu_{1/2}$ ~30–40 cm^{-1}), which is probably connected with the formation of the passivating protective oxide layer on the specimen surface after its preliminary radiation-oxidation treatment in the H_2O_2 media.

To reveal the regularities of the radiation oxidation of the zirconium surface in the Zr–H_2O system at room temperature, the kinetic curves are investigated of nontreated and treated Zr specimens, that is, the optical density variation of the Zr–O valency oscillation band with the maximum at $\nu = 670$ cm^{-1} as a function of the duration of the contact with the water, τ, under the γ-irradiation (Figure 2). The comparison of the kinetic dependencies shows that the mechanisms of the radiation oxidation of Zr differ depending on its surface state.

For the radiation treated Zr specimens, the oxidation kinetics are governed by a near-parabolic low (curve 2): the kinetic diffusion takes place of neutral particles through the passivating oxide layer. The protective oxide layer makes it very difficult for both the oxygen atom to embed into the volume and the new metal atom to emerge to the surface; thus, the oxide–metal boundary is totally shielded and the oxide layer depth varies only slightly (from 12 to 25 nm). For the nontreated Zr specimens, the oxidation kinetics are governed by a more complicated law (curve 1). Here, the intercrystalline gas corrosion (H^+, OH^-) is probably connected with the microstructure nonuniformities caused by the γ-irradiation.

CONCLUSION

A possibility is shown to use the RAIS technique to study the radiation oxidation of metal zirconium in contact with water within a wide range of the absorbed dose values, $D = 5$–420 kGy. The process is investigated of radiation oxidizing of untreated and preliminary radiation-oxidation treated (in an H_2O_2 media) zirconium specimens in contact with water at room temperature, and their kinetic regularities are compared. From the kinetics of the radiation oxidation of the preliminary treated Zr specimens, passivation is revealed of the metal surface, thus providing evidence of the presence of a surface protective oxide layer.

REFERENCES

1. Waterside Corrosion of Zirconium Alloys in Nuclear Power Plants, *IAEA-TECDOC*, IAEA: Vienna, 1998, pp. 13–17.

2. Konobeevskii, S.T., *Deistvie oblucheniya na materialy. Vvedenie v radiatsionnoe materialovedenie (*Radiation Impact on Materials. Introduction into Radiation Material Science), Moscow: Atomizdat, 1967, pp. 39–47.

3. Azhazha, V.M., V'yugov, P.N., Petel'guzov, I.A., Butenko, I.N., and V'yugov, N.P., Study of the Corrosion Resistance of Band Specimens of a Zr|Nb Calcium-thermal Alloy with Oxygen Content up to 0.1% (in Mass), *Trudi XVII mezhdunarodnoii konferentsii po fizike radiatsionnykh yavlenii i radiatsionnomu materialovedeniyu* (Proc. XVII Int. Conf. Phys. Radiation Phenomena and Radiation Material Science), Alushta, Krimea (Ukraine), Sept. 4–9, 2006, pp. 135–136.

4. Petel'guzov, I.A., Ischenko, N.I., Slabonitskaya, E.A., and Mukhin, M.V., Influence of Long-Continued High-Temperature Oxidation in the Water Vapor on the Structure and Mechanical Properties of the Zr|Nb Combustion Element Tubes. *Trudi XVII mezhdunarodnoii konferentsii po fizike radiatsionnykh yavlenii I radiatsionnomu materialovedeniyu* (Proc. XVII Int. Conf. Phys. Radiation Phenomena and Radiation Material Science), Alushta, Krimea (Ukraine), Sept. 4–9, 2006, pp. 127–128.

5. Garibov, A.A., Aliyev, A.G., Agaev, T.N., and Velibekova, G.Z., Influence of Preliminary Radiation-Oxidizing Treatment on the Corrosion Resistance of Zirconium in Conditions of Ionizing Radiation, *Eurasia Nuclear Bull.,* Turkey, 2004, no. 3, pp. 45–51.

6. Garibov, A.A., Aliyev, A.G., and Agaev, T.N., Influence of Preliminary Radiation-Oxidizing Treatment of Zirconium on Its Radiation-Catalytic Activity in the Water Radiolysis Processes, *Azerbaijanskii khimicheskii zhurnal* (Azerbaijan Chem. J.), 2005, no. 4, pp. 178–181.

7. Gadzhieva, N.N., Oxidation and H_2 Accumulation in the Aluminum-Water System under Radiation-Thermal Impact, *Zhurnal prikladnoii spektroskopii* (J. Appl. Spectroscopy), 2005, vol. 72, no. 4, pp. 440–445.

8. Hollins, P. and Princhard, I., *Vibration Spectroscopy of Absorbates*, Ed. Willis, R.F., Berlin–Heidelberg–New-York: Springer-Verlag, 1980, pp. 89–96.

9. Pikaev, A.K., *Dozimetriya v radiatsionnoi khimii* (Dosimetry in Radiation Chemistry), Moscow: Nauka, 1975.

10. Vasil'ev, A.F., Gushanskaya, N.Yu., Zhizhin, G.N., et al., *Optika i spektroskopiya* (Optics and Spectroscopy), 1990, vol. 69, no. 3, p. 612.

11. Garibov, A.A., Gadzhieva, N.N., Velibekova, G.Z., et al., *Khimiya vysokikh energii* (High Energy Chemistry), 1992, vol. 26, pp. 235–238.

12. Gadzhieva, N.N., *Proc. 2nd Int. Conf. On Technical and Physical Problems in Power Engineering (TPE-2004),* Tabriz, Iran, Sept. 6–8, 2004, pp. 502–504.

13. Gadzhieva, N.N., Rimikhanova, A.N., and Garibov, A.A., *Zhurnal fizicheskoi khimii* (J. Physical Chemistry), 2007, no. 5, pp. 1–4.

14. Vibrational Spectroscopy. Modern Trends (Eds. Barnes, A.J. Orville-Thomas, W. J.) Elsevier, Amsterdam, 1977.

15. Platonov, P.A., Tursunov, I.E., and Levit, V.I., *Voprosy atomnoi nauki i tekhniki. Ser. Fizika radiatsionnykh povrezhdenii i radiatsionnoe materialovedenie* (Problems of Nuclear Science and Technology. Ser. Physics of Radiation Damages and Radiation Material Science), 1987, issue 2 (40), pp. 65–76.

ELECTRICAL PROCESSES
IN ENGINEERING AND CHEMISTRY

The Treatment Influence on the Electric Strength and Conductivity of Fibroin

R. S. Ismaiilova and S. G. Alieva

Institute of Radiation Problems, National Academy of Sciences of Azerbaijan,
F. Agaeva 9, Baku, AZ-1143 Republic of Azerbaijan

Received May 14, 2007

Abstract—The influence of thermal treatment and liquid nitrogen treatment of cocoons on the electric properties of natural silk fibroin has been studied. It is found that, at the cocoon treatment by liquid nitrogen, the ratio of the amorphous and crystalline parts of the fibroin is preserved and the concentration of submicrocracks in them changes to a lesser extent than at treatment by heated air and a UHF field. The increase of the degree of crystallinity in the polymers leads to a certain increase of their breakdown voltage.

INTRODUCTION

Wide application of natural silk in various branches of industry is caused by its high strength, hygroscopicity, elasticity, and isolating properties. Natural silk considerably exceeds artificial fibers in strength, radiation resistance, electric field resistance, mechanical loading, and temperature. This allows its successful use in aviation, space systems engineering, and surgery; due to its low dielectric permeability and low dielectric losses, it is applied in UHF engineering [1].

The basic parameters determining the electrophysical properties of polymer dielectrics, including natural silk, are the electric strength E_{str} and the electric conductivity ρ [2]. These parameters are closely related to the structure and composition of the polymer, and they change with variation of the temperature and the supply voltage frequency [3].

Studying the structural influence on E_{str} of polymer dielectrics is important for obtaining of new modified isolation materials with specified properties. It is known that E_{str} is determined by defects in the amorphous and crystalline parts of the polymer. If the polymer contains large supermolecular formations, e.g., spherulites, then, with an increase of the spherulite dimension R, the values of E_{str} decrease; when $R \cong h$, (h is the film thickness) the electric strength takes a constant value. The growth of the E_{str} values may be due to a crystallinity increase and to the processes of internal stress relaxation.

EXPERIMENTAL

The present work describes the results of investigation of the electric strength of silk fibroin obtained from cocoons treated by various methods: by liquid nitrogen (immersion into liquid nitrogen for 2 min), by heated air (treatment at 358 K for 60–90 min), and by a UHF field (915 MHz, up to 6 min).

For determination of the electric strength, the samples were prepared in the form of plane capacitors with a diameter of 13 mm and a thickness of 0.5–1.5 mm. Fine powder of natural silk fibroin obtained by virtue of a ball grinder was dried to constant weight. Then, it was pressed under similar conditions (960 MPa, 10 min) and in vacuum (0.13 Pa). The tablet thickness was measured by virtue of the installation IZV-21.

Before the samples were tested for the breakdown voltage, they were kept for 24 h at a temperature of 293 ± 2 K and a relative humidity of $65 \pm 2\%$. The tests were carried out with application of cylindrical brass electrodes (the diameter of the upper and the lower electrodes was 4 mm and 8 mm, respectively). The breakdown was realized by a gradual voltage increase on the installation (AIM-80).

Studying the strength properties of fibroin [1, 4] has shown that, depending on the method of the initial treatment of the cocoons, various defects (microcracks and submicrocracks) are formed in the fibroin; their quantity depends on the type and parameters of the initial treatment.

The electric properties of polymers are characterized by their electric conductivity (or by their specific bulk and surface resistance) and electric strength. For real polymers applied as dielectrics, the electric conductivity depends on their composition, molecular structure, and supermolecular structure [5, 6]. However, it should be noted that, for the majority of polymer dielectrics, the mechanism of ionic electric conductivity is of fundamental importance.

RESULTS AND DISCUSSION

According to the experimental data, the dependence of the logarithm of the specific bulk resistance ρ on $1/T$ was determined at identical conditions for the fibroin obtained from cocoons treated by different methods; the result is graphically shown in Fig. 1.

One can see from Fig. 1 that ρ for the fibroin obtained from the cocoons treated by liquid nitrogen is less than that for the fibroin prepared from the cocoons treated by heated air and a UHF field. This is due to the fact that, at the initial treatment of the cocoons by heated air and the UHF field, the rate of the amorphous parts decreases and the number of submicrocracks in the fibroin increases. As a result of the growth of the submicrocracks, an increase of the traps for ions causes a decrease of the mobility of the latter. Thus, the electric conductivity of the fibroin treated by heated air and the UHF field decreases. Moreover, at the cocoon treatment by the UHF field, the conductivity is the lowest. According to [1], on the curve of the temperature dependence of the silk fibroin specific resistance, it is possible to appreciate three temperature ranges: I—corresponding to the glassy state, II—the transitional one, and III—the high-elastic state. This is in good agreement with the results of thermomechanical investigations [7]. The bulk specific resistance ρ was calculated by the formula [2]

$$\rho = \pi \frac{D_0^2 R}{4h},$$

where R is the measured resistance of the sample, $D_0 = (d_1 + d_2)/2$ (d_1 is the measuring electrode diameter equal to 10 mm, d_2 is the bore diameter of the guard electrode equal to 14 mm), and h is the sample thickness equal to 0.5 mm.

Due to wide application of polymer isolation in engineering for reliable operation of products, the isolation must be characterized by sufficient electric strength (the value being numerically equal to the homogeneous field intensity whereby the dielectric breakdown takes place). An increased intensity results in breakdown of the dielectric; that is, destruction of its structure occurs. The process of dielectric breakdown in its development passes through the stage of electric strength loss and destruction [8].

The electric breakdown resulting from the processes of "electric aging" of the dielectric is due to changing of its chemical composition and structure under the action of electric discharges in the surroundings or the external electric field. The electric aging processes, though proceeding at relatively lower rates, may be realized at voltages considerably less than the breakdown one [9].

Figure 2 shows the dependences of the electric field breakdown intensity on the sample thickness, which was determined by us as the electric conductivity for
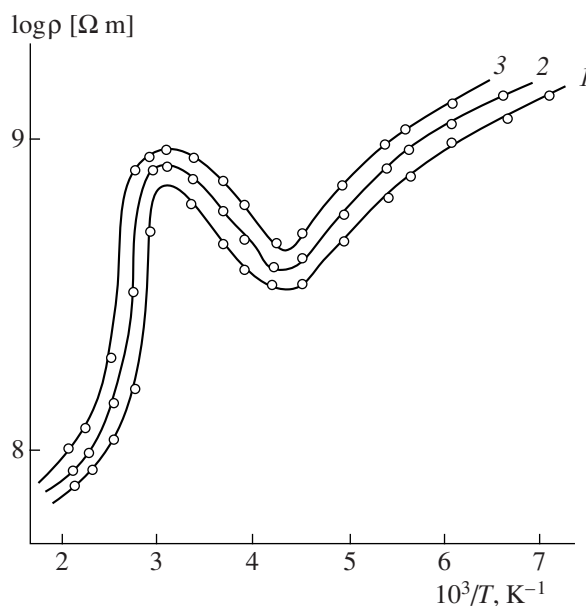
Fig. 1. Temperature dependence of the specific resistance of fibroin at alternating current. Treatment by (*1*) liquid nitrogen; (*2*) heated air; (*3*) a UHF field.
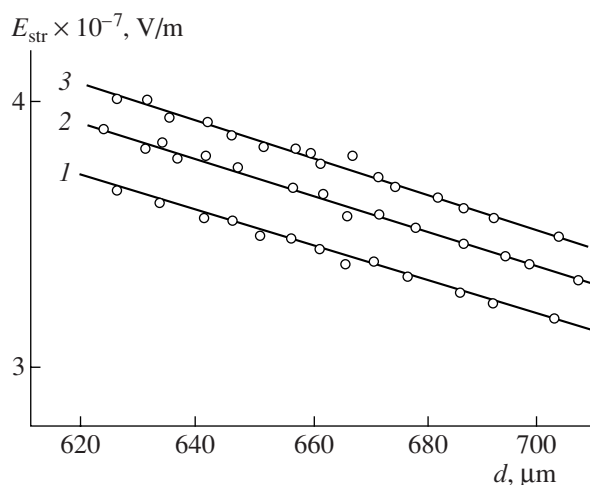
Fig. 2. Dependence of the breakdown intensity of the electric field (50 Hz) on the sample thickness. Treatment by (*1*) liquid nitrogen; (*2*) heated air; (*3*) a UHF field.

the fibroin obtained from cocoons treated by liquid nitrogen, heated air, and a UHF field.

One can see from the figure that the breakdown intensity value for the fibroin is 10^7 V/m and it decreases as the sample thickness increases. This dependence shows that heat breakdown takes place in the fibroin. As is known, in the initial stage of the field application, due to poor heat conductivity of fibroin and dielectric losses, there occurs heating; that is, the quantity of heat appearing inside the sample becomes higher

than the abstracted heat; as a result, the temperature increases. Therefore, heat breakdown and fibroin charring take place. As the sample thickness increases, the condition of the heat abstracting from internal zones into the surroundings is impeded and heat accumulation in the bulk becomes easier; thus, the condition of heat breakdown appearance is lightened. Besides, at the fibroin breakdown, there occurs charring; the breakdown channel can be found with the naked eye and by the characteristic smell of the heat breakdown. On the other hand, the electric strength decrease with the applied electric field frequency increasing also confirms the heat nature of the breakdown in the fibroin.

CONCLUSIONS

It is shown that, in the fibroin obtained from the cocoons treated by liquid nitrogen, the bulk specific resistance and electric conductivity are lower than those of the fibroin obtained from the cocoons treated by heated air and a UHF field. The decrease of the electric conductivity of the fibroin treated by liquid nitrogen is due to the concentration of traps for ions in submicrocracks and their mobility.

At the cocoon treatment by liquid nitrogen, the ratio of the amorphous and crystalline parts of the fibroin is preserved; the concentration of submicrocracks in them changes to a lesser extent than at treatment by heated air and a UHF field. The increase of the degree of crystallinity of polymers leads to a certain increase of their breakdown voltage.

REFERENCES

1. Ismayilova, R.S., The influence of Cocoon Filament on the Electric Properties of the Natural Silk, *J. Fizika*, 2001, no. 4, pp. 22–23.

2. *Elektricheskie svoistva polimerov* (Electric Properties of Polymers), Sazhin, B., Ed, Leningrad, 1986.

3. Lushcheikin, G.A., *Metody issledovaniya elektricheskikh svoistv polimerov* (Methods of Study of Electric Properties of Polymers), Moscow, 1988.

4. Ismaiilova, R.S., Influence of Gamma Irradiation on Deformation–Strength Properties of Silk Fiber, *III Vsesoyuznaya karginskaya konferentsiya "Polimery-2004"* (III All-Union Kargin Conference "Polymers-2004"), Moscow, 2004, p. 312.

5. Ul'yanova, T.M., Titov, D.V., Krutko, M.P., and Zub, E.M., Investigation of Structure and Electrophysical Properties of Film Composites with Fiber Reinforcement, *Ross. Akad. Nauk*, 200, vol. 64, no. 6, pp. 1207–1210.

6. Vannikov, A.V., Matveev, V.K., Sichkar', V.P., and Tyutnev, A.P., *Radiatsionnye effekty v polimerakh. Elektricheskie svoistva* (Radiation Effects in Polymers. Electric Properties), Moscow, 1982.

7. Ismaiilova, R.S., Influence of Gamma Irradiation on Deformation of Silk Fiber after Preliminary Treatment by Various Methods, *Elektron. Obrab. Mater.*, 2006, no. 2, pp. 44–46.

8. Magerramov, A.M., *Strukturnoe i radiatsionnoe modifitsirovanie elektretnykh, p'ezoelektricheskikh svoistv polimernykh kompozitov* (Structural and Radiation Modification of Electret, Piezoelectric Properties of Polymer Composites), Baku, 2001.

9. Bartenev, G.M. and Zelenev Yu.V., *Fizika i mekhanika polimerov. Uchebnoe posobie dlya vuzov* (Physics and Mechanics of Polymers. Handbook for Higher Institutions), Moscow, 1983.

ELECTRICAL PROCESSES
IN ENGINEERING AND CHEMISTRY

The Discharge Mode Influence on the Hydrodynamic Processes of Underwater Electric Explosions

G. A. Barbashova and V. V. Shomko

Institute of Pulse Processes and Technologies, National Academy of Sciences of Ukraine,
pr. Oktyabr'skii 43a, Nikolaev, 54018 Ukraine

Received May 17, 2007

Abstract—The results of numerical experiments pertaining to the influence of high-voltage discharges in liquid on the discharge hydrodynamics are presented. It is shown that, with a fixed power source, parameters of the oscillating discharge modes have to be used to obtain higher values of the discharge channel broadening velocity, pressure, and specific momentum; critical modes must be chosen for prolonged intervals of increased pressure influence and higher values of the specific pulse pressure in the liquid.

INTRODUCTION

Depending on the mode of the energy injection (discharge mode) into the plasma channel of an underwater electric explosion (UEE), the latter may be "fast," manifesting its shattering action, or "slow." In the first case, the electric energy of an external source (most often it is a capacitance energy accumulator) is evolved in the discharge channel in the form of single pulses for a short time [1]; in the second case, it is evolved in the form of a sequential cycle of pulses for longer times [2]. A part of the injected energy is used for formation of a primary compression wave (it may also be a shock wave) in the liquid surrounding the discharge channel; the remaining energy is used for increasing the channel internal energy and the kinetic energy of the spreading liquid flow. As experience shows (see, e.g., [3, 4]), the explosive wave front breaks away from the channel boundary at the moment of the energy injection beginning, except for, apparently, a short initial time interval when the contours of the channel boundaries and the wave front cannot be well seen due to the very bright glow of the discharge plasma. There appears the problem of the contribution of subsequent cycles of energy injection to the process of the primary compression wave formation at oscillatory discharge modes. It is assumed [3, 5] that the impressed energy increases the internal energy of the discharge channel, favoring generation of additional perturbations in the liquid, which spreading with a high velocity over the already compressed medium may catch up to the main front of the wave and change its parameters (form, amplitude P_m, or duration of positive pressure phase τ_+). Special physical experiments [5, 6] have registered the influence on P_m and τ_+ exerted only by energy parameters of the first pulse of electric power, i.e., the injected energy value W_1 and time of its injection τ_1. The discharge mode (and, accordingly, the degree of its oscillation) influences the compression wave parameters differently, depending on the way of its obtaining—by changing the parameters of the active or reactive element of the discharge circuit [5, 7]. Results of the numerical experiment on studying the shock wave formation at UEE [8] have shown that influence on P_m, at least of the second power pulsation, is possible for nonstabilized (self-breakdown) discharge modes in strongly conducting liquids when the compression wave is formed for times exceeding the first power pulsation duration.

Therefore, such aspects of the UEE dynamics as the formation and development in space and time of the generated compression waves, as well as the discharge mode influence on this process, have been studied insufficiently. The aim of the present work is to fill this gap a measure.

PROBLEM STATEMENT AND NUMERICAL EXPERIMENT RESULTS

In the numerical experiment, we assume that a plasma discharge channel has the form of a straight circular cylinder of a finite length; in the broadening process, the electric power $N(t)$ is injected into it for the time τ. The liquid flow in the region is restricted by a contact plasma–water break and by a wave that has gone away from the channel (we suppose that this is a shock wave) described by a system of two-dimensional nonlinear equations of gas dynamics. On the internal boundary of the calculated region (contact break), there is specified a condition connecting the discharge channel hydrodynamic characteristics with the electric power (energy balance equation [4]); on the external boundary (shock wave), conditions of dynamic compatibility are set. For obtaining the power time dependence, a physical experiment was carried out. The initial values of the hydrodynamic parameters of the liq-
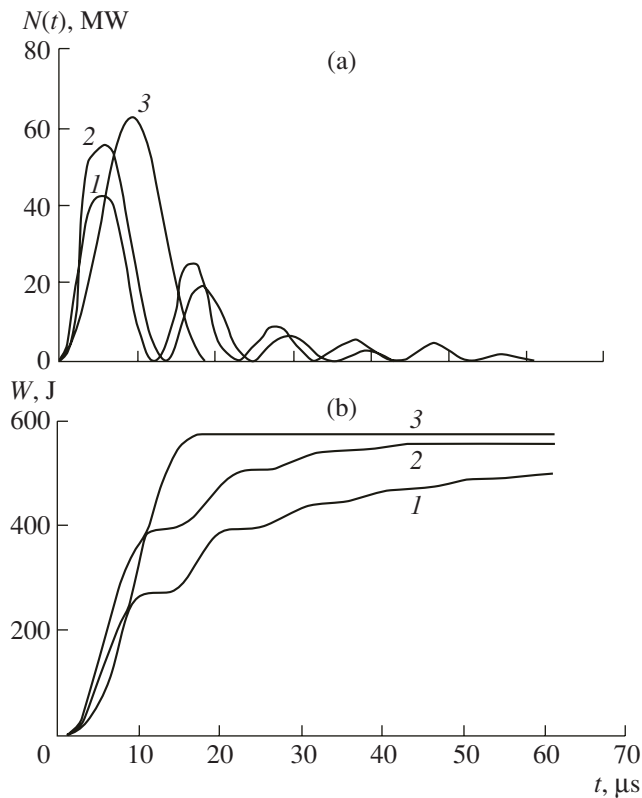
Fig. 1. Time functions of the electric power (a) and energy evolved in the discharge channel (b) versus the discharge mode η: 0.4 (*1*), 0.7 (*2*), 0.96 (*3*).

uid surrounding the channel are assumed to be equal to the values in an unperturbed medium, and the initial values of the radius of the discharge channel and pres-

Characteristic energy, hydrodynamic, and time parameters

l, m	0.040	0.055	0.100
η	0.40	0.70	0.96
W_1, J	271	396	576
W_τ, J	498	555	576
τ_1, μs	12	14	19
τ, μs	64	44	19
τ_N, μs	5.5	6.0	9.2
$\langle N'_+ \rangle$, 10^{12} W/s	15.4	18.5	9.7
$\langle N'_+ /l \rangle$, 10^{14} W/(s m)	3.8	3.4	0.97
$\dot{a}_m$, m/s	246	245	171
$t_{\dot{a}}$, μs	4.32	3.91	8.33
P_{am}, MPA	178	176	106
t_{P_a}, μs	3.62	3.52	7.42
P_m, MPa	12.8	16.0	14.3

sure in it are calculated by technique [9]. The problem is solved by Godunov's finite difference method by the algorithm developed earlier [2].

The hydrodynamic characteristics of the discharge channel (the radius $a(t)$, the broadening velocity $\dot{a}(t)$ of the mid section, the pressure $P_a(t)$, and the specific momentum of the pressure $I_a(t) = \int_0^t P_a(\tau)d\tau$ and those of the liquid (the pressure $P(r_1, t)$ and the specific momentum of the pressure $I(t) = \int_0^t P(r_1, \tau)d\tau$ at the point where the equatorial plane of the discharge channel is at the distance $r = 0.08$ m from the channel symmetry axis were subject to numerical analysis.

The selection of modes of the energy injection into the UEE plasma channel was realized so that the influence on the discharge mode characteristics under study could be analyzed. The discharge mode was characterized by value of the UEE energy similarity criterion η [5] determining the part of the energy evolved in the first half-period of the discharge current. In the physical experiment (its technique is described in detail in work [10]), there was applied a capacitance energy source with a stored energy of 600 J charged to a voltage of 20 kV. The inductance and capacity of the discharge circuit were 3.4 μH and 3 μF, respectively. The discharge was realized in a reservoir filled with distilled water with the overall dimensions $0.5 \times 0.5 \times 0.5$ m^3. For suppression of energy losses at the stage of formation of the plasma discharge channel and for giving it the cylindrical form, the discharge was initiated by an aluminum conductor with a diameter of 11 μm. The electric power $N(t)$ evolved in the channel and the energy $W(t)$ were determined by the discharge current and voltage registered by the oscillography method. The discharge mode was changed due to variation of the conductor length l (see the table) at a fixed energy source.

The energy characteristics corresponding to two oscillatory modes of UEE ($\eta = 0.4, 0.7$) and to one critical mode ($\eta = 0.96$) are shown in Fig. 1; their most characteristic values are given in the table, where W_τ is the value of the energy injected into the discharge channel for the time τ; $\langle N'_+ \rangle$ and $\langle N'_+ /l \rangle$ are the mean values the power rate and specific (per the microconductor unit length) power rate, respectively; and t_N is the time of maximum achievement by the first power pulse. The numbering of the modes in all the figures is done in increasing order of the parameter η: $\eta = 0.4$ for mode 1; $\eta = 0.7$ for mode 2; $\eta = 0.96$ for mode 3. The given modes are most distinguishable by the value of the energy injected in the first pulse and by the total time of the energy injection. The values of the total energy for all the modes are very close to each other, as well as the values of the average and specific rates of the power rise of the first pulse of the oscillatory modes, being signif-

icantly different from the corresponding values of these characteristics for the critical discharge mode.

It follows from the analysis of the channel radius time dependences (Fig. 2a) that they are very sensitive to the discharge mode change. In oscillatory modes 1 and 2, an appreciable respond of the radius to the mode change is shown closer to the end of the energy evolution, whereas, in the critical mode, it appears practically from the beginning of the discharge, this being due to the slower impression of energy in the initial period of these modes (Fig. 1b). In contrast to the energy dependences, the time functions of the radii are more monotonous; therefore, no appreciable correlation between them and the injected energy $W(t)$ is observed. Most probably, this correlation is possible between the radius and more monotonous integral function of energy $f_W(t) = \int_0^t W(t)dt$. Being plotted according to the data of Figs. 1b and 2a, the normalized logarithmic dependences of the radii $\bar{a}(\bar{t}) = a(t/\tau)/a(\tau)$ on $\int_0^{\bar{t}} \bar{W}(\bar{t})d\bar{t}$ (Fig. 3) show at $\ln\bar{a} \geq -3$ availability of correlations of the type $a(\bar{t}) = k_a a(\tau)[\int_0^{\bar{t}} \bar{W}(\bar{t})d\bar{t}]^{1/3}$ with $k_a \approx 1.14$ for the oscillatory modes and $k_a \approx 1.3$ for the critical ones ($\bar{W}(\bar{t}) = W(t/\tau)/W(\tau)$). Analytical dependences of the kind $a(\bar{t})$ have been obtained earlier [11] while solving the problem in a quasi-auto-model approximation.

The time dependences of the broadening velocity of the channel (Fig. 2b) and the pressure in it (Fig. 4a) are qualitatively similar. Their amplitude values are minimal for the critical discharge, and they increase as the discharge oscillation degree grows. In the initial stage of the discharge (approximately up to the time of the maximum achievement by the critical discharge power), the level of the velocities and pressures of the more oscillatory discharge modes is higher than those of the critical mode: in some moments the exceeding is 1.5–2 times. The maximal values of the broadening velocity $\dot{a}_m$ and pressure in the channel P_{am} in oscillatory modes 1 and 2 are very close to each other (see the table). This means that the difference between the energy parameters of these modes determining $\dot{a}_m$ and P_{am} must also be small. According to the data given in the table, such a parameter, most probably, is the specific (per initial unit length of the discharge channel) rate of the first power pulse rise, being equal to 3.8×10^{14} W/(m s) for the first mode and to 3.4×10^{14} W/(m s) for the second one. The values of the velocity amplitude and pressure are significantly less in the third mode, for which the specific rate of the power is less by more than a factor of three. The most oscillatory discharge mode is also characterized by higher values of velocities and pressures in the whole observed time interval, which exceeds the energy evolution time of mode 1 by more
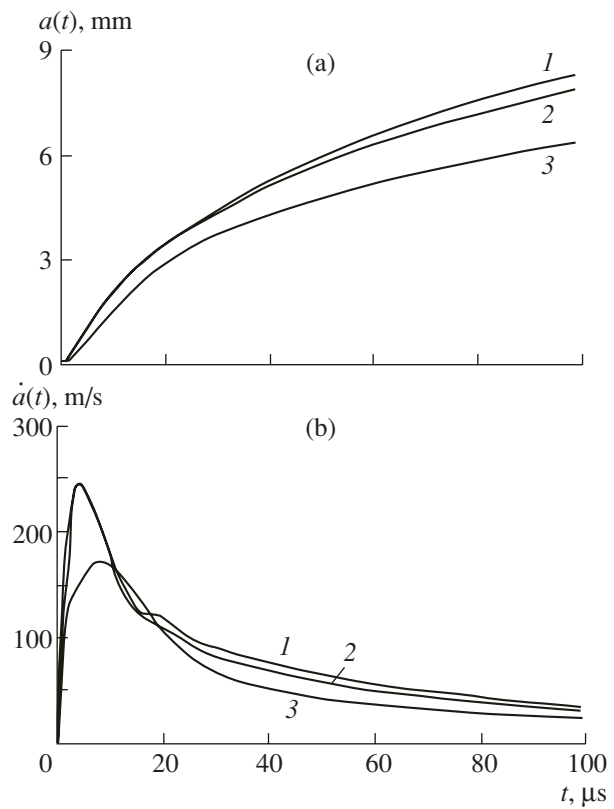

Fig. 2. Time functions of radii (a) and spread velocities (b) of the mid section of the discharge channel versus the discharge channel.
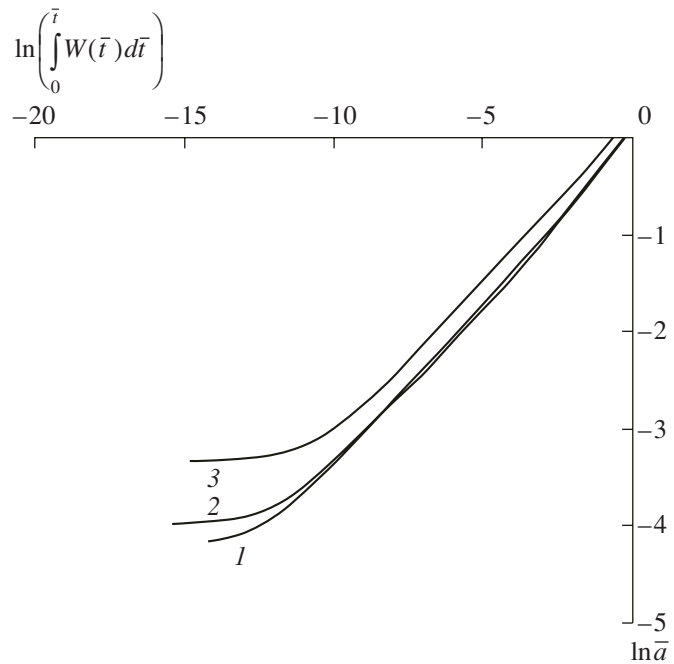

Fig. 3. Normalized logarithmic dependences of the discharge channel radii on the energy integral.
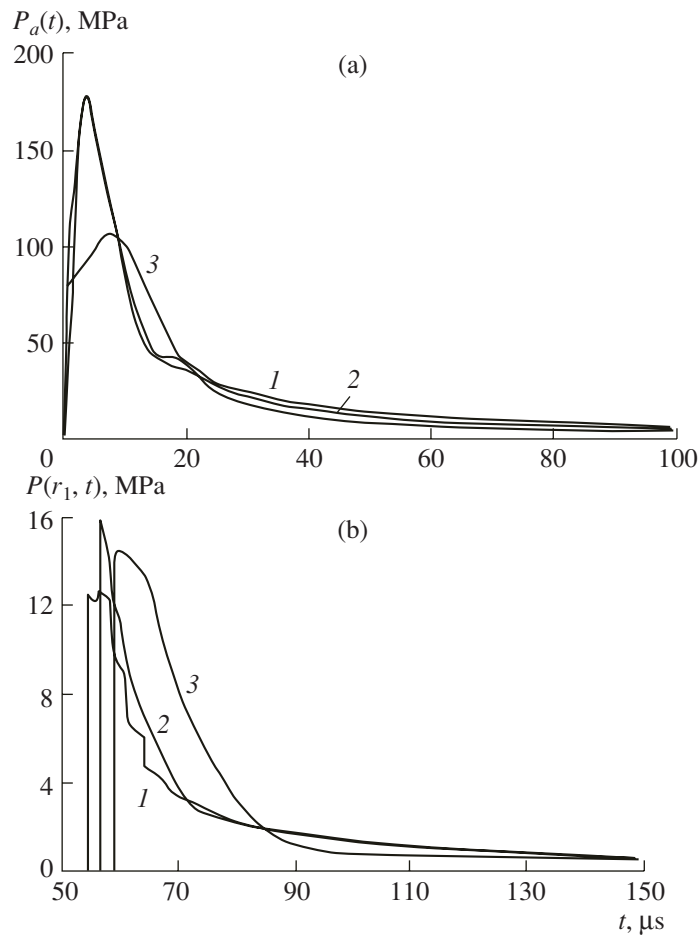
Fig. 4. Pressure profiles in the discharge channel (a) and in the liquid (b) versus the discharge mode.

than a factor of 1.5. The level of the velocity and pressure in the critical discharge channel only at the stage of its electric power decrease (at $11 \leq t \leq 18$ μs for velocity and $8.5 \leq t \leq 22$ μs for pressure) exceeds the corresponding level of the oscillatory discharge modes up to 10% in velocity and up to 60% in pressure.

The times of the maximum achievement of the pressure in the channel t_{P_a} are somewhat less than the times of the maximum achievement of the channel broadening velocity $t_{\dot{a}}$. No appreciable correlation is observed between these times and the characteristic times of the energy evolution (for example, the time of the first maximum achievement by the power t_N and the duration of the first power pulsation τ_1) (see the table). As was mentioned earlier [1], this may be due to the fact that the parameters determining the times $t_{\dot{a}}$ and t_{P_a} may be, in parallel with the time t_N, energy parameters, e.g., the specific rate of the power rise: as it increases, the times $t_{\dot{a}}$ and t_{P_a} decrease. For the considered modes $t_{\dot{a}} = (0.65–0.91)t_N$ and $t_{P_a} = (0.60–0.80)t_N$, the

highest coefficient value is observed in the critical discharge mode.

The pressure–time profiles in the liquid $P(r_1, t)$ (Fig. 4b) calculated for the near discharge zone ($r_1 \leq 2l$), depending on the discharge mode, have more significant differences than the pressure profiles in the channel $P_a(t)$. At a spread of the pressure amplitudes less than in $P_a(t)$ in the dependences $P(r_1, t)$, a more considerable divergence of their descending branches is observed, where, in an appreciable time interval ($t = 56.4–84$ μs), the pressure values in the critical discharge mode are several times higher than in oscillatory modes 1 and 2. As a result, the time functions of the specific pressure moments in the liquid $I(r_1, t)$ (Fig. 5) respond to the discharge mode change otherwise than in the discharge channel $I_a(t)$. Thus, the graphs of $I_a(t)$ of more oscillatory discharge modes lie above the critical one (Fig. 5a), whereas the situation with the location of the $I(r_1, t)$ curves is exactly opposite: the values of $I(r_1, t)$ of the critical mode exceed the corresponding values of specific moments of the oscillatory discharge modes by a factor of 1.2–1.6.
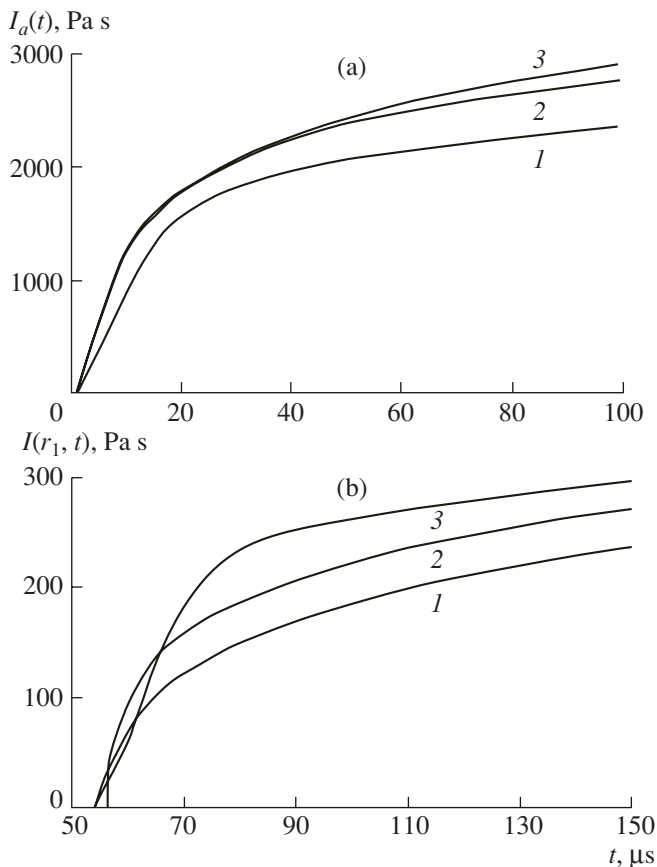
$I_a(t)$, Pa s

$I(r_1, t)$, Pa s

Fig. 5. Specific pulses of pressure force of the discharge channel (a) and at the liquid point (b) versus the discharge channel.

CONCLUSIONS

The numerical experiment results have shown that, at a fixed energy source, the following are true:

—The oscillatory discharge modes are characterized by higher velocities of the discharge channel broadening and pressures in the channel. The times of the maximum achievement by the velocity and pressure in the channel are determined mainly by the specific rate of the power rise, decreasing as it increases.

—The pressure amplitudes in the liquid weakly depend on the discharge mode. At the same time, on the descending branch, the critical mode pressure exceeds the pressure level of the oscillatory modes by several times. In the latter, the pressure relaxes more intensively.

—The specific moments of the pressure in the discharge channels of the more oscillatory discharge modes are higher than in the critical mode, and, in the liquid, they are lower by a factor of 1.2–1.6.

REFERENCES

1. Shamko, V.V., Vovchenko, A.I., Kamenskaya, L.A. and Barbashova, G.A., Control of Hydrodynamic Processes at Single–Pulse Electric Explosion Transformation of Energy, *Elektron. Obrab. Mater.*, 2005, no. 1, pp. 61–67.

2. Barbashova, G.A., Vovchenko, A.I., Kamenskaya L.A., and Shamko, V.V., Control of Hydrodynamic Processes at Electric Explosion Programmed Multipulse Injection of Energy, *Akustichnii Visnik*, 2004, vol. 7, no. 4, pp. 3–9.

3. Komel'kov, V.S. and Skvortsov, Yu.V., Broadening of Power Spark Discharge Channel in Liquid, *DAN SSSR*, 1959, vol. 129, no. 6, pp. 1273–1276.

4. Naugol'nykh, K.A. and Roi, N.A., *Elektricheskie razryady v vode* (Electric Discharges in Water), Moscow: Nauka, 1971.

5. Krivitskii, E.V. and Shamko, V.V., *Perekhodnye protsessy pri vysokovol'tnom razryade v vode* (Transition processes at High–Voltage Discharge in Water), Kiev: Naukova Dumka, 1979.

6. Okun', I.Z., Application of Dimensional and Similarity Methods in Investigation of Pulse Discharge in Water, *Zh. Teor. Fiz.*, 1967, vol. 37, no. 9, pp. 1729–1738.

7. Vovchenko, A.I., Shamko, V.V., and Shishov, A.M., Peculiarities of Wave Train Emitted at High–Voltage Electric Discharge in Water, *Akustichnii Visnik*, 2003, vol. 6, no. 6, pp. 26–28.

8. Ivanov, V.V., Gulyi, G.A., Shvets, I.S., and Ivanov, A.V., On Some Peculiarities of Development of Underwater Spark Discharges, in *Novoe v razryadnoimpul'snoi tekhnologii* (News in Discharge–Pulse Technology), Kiev: Naukova Dumka, 1979, pp. 82–93.

9. Vovchenko, A.I., Initial Conditions for Problem of Numerical Study of Underwater Spark Discharge Dynamics, in *Pratsi IED NANU, Elektrodinamika: Zb. Nauk Pr.: K: IED NAN Ukraini*, 2001, pp. 117–120.

10. Shamko, V.V. and Kucherenko, V.V., Theoretical Bases of Engineering Analysis of Energy and Hydrodynamic Parameters of Underwater Spark Discharge, *Preprint of Inst. of Pulse Processes and Technologies, National Acad. Sci. of Ukraine*, Nikolaev, 1991, no. 20.

11. Shamko, V.V., Hydrodynamic Description of Underwater Electric Explosion in Quasi–Automodel Approximation, in *Fizikomekhanicheskie protsessy pri vysokovol'tnom razryade v zhidkosti* (Physicomechanical Processes at High–Voltage Discharge in Liquid), Kiev: Naukova Dumka, 1980 pp. 101–112.

ELECTRICAL PROCESSES
IN ENGINEERING AND CHEMISTRY

Peculiarities of Electric Conductivity Changes of Solutions of Acids and Alkalis under the Effect of a Glow Discharge

A. V. Khlyustova[a], T. V. Zamaeva[b], and A. I. Maksimov[a]

[a] Institute of Solution Chemistry, Russian Academy of Sciences, ul. Akademicheskaya 1, Ivanovo, 153045 Russia
[b] Ivanovo State Chemicotechnological University, pr. F. Engel'sa 7, Ivanovo, 153000 Russia
Received May 18, 2007

Abstract—The influence of atmospheric pressure glow discharges on the electric conductivity of H_2SO_4, Na_2SO_4, and NaOH solutions as electrolyte cathodes has been investigated. The electric conductivity has been calculated taking into account changes in the solution pH. These values are compared with experimental ones. The qualitative differences of the experimental and calculated dependencies are explained by the modification of structural features of the solution under the action of the glow discharge.

DOI: 10.3103/S1068375507060130

INTRODUCTION

It is well known that the action of a glow discharge on electrolyte solutions used as cathodes causes a change in the acidity and electric conductivity of the solutions [1]. The effect observed at atmospheric pressure with a glow discharge burning in air is most commonly associated with the oxidation of nitrogen in a plasma zone over the solution and the following dissolving of the generated oxides [2], though there are some data on the process indicating other reasons for the pH variation [3]. The alterations of the pH and electric conductivity observed in the wide range of their values qualitatively agree with each other; that is, at a pH value ~7, there occurs the minimum of electric conductivity [4]. This confirms the rather evident assumption that the change of the electric conductivity is first and foremost caused by interrelated variations of the ion concentration of hydronium and hydroxyl. However, quantitative comparisons of the experimental changes of the solution electric conductivity with the expected ones under the condition of fulfillment of the mentioned mechanism are not yet known. Apparently, the agreement of the measured and calculated magnitudes is possible only in the case when the gas-discharge effect on the solution doesn't change the mobility of ions in the solution, which can be associated with its structure characteristics. To test this assumption is the aim of this work.

EXPERIMENTAL RESULTS AND DISCUSSION

Solutions of NaOH, H_2SO_4, and Na_2SO_4 with concentrations from 10^{-3} to 0.01 mol/l were treated by glow discharge in open type cells in which the electrolyte solution served as the cathode. The cell diagram is presented in Fig. 1. The cathode, which was submerged into the solution, and the anode, which was placed over

the solution, were made of graphite. The discharge current was 40 mA. The measurements of the solution acidity and the electric conductivity were taken at regular intervals with the help of an I-500 pH meter and an Ion Lab conductance meter directly in the cell after the solution temperature stabilization.

The solution electric conductivity was also calculated using the measured values of the acidity and the initial quantities of the salt concentration, which were assumed not to change during the gas-discharge treatment. The values of the ion electric conductivities and their dependence on the ion concentration are taken from [5]. In order to more correctly analyze the influence of the plasma treatment on the electric conductivity, the table values were corrected in such a way that
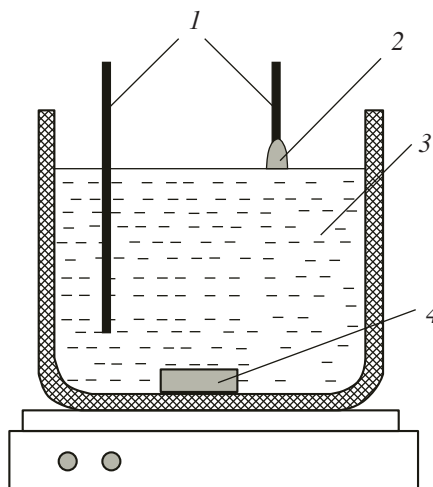

Fig. 1. Diagram of the experimental cell of the open type: *1*, electrodes; *2*, discharge zone; *3*, electrolyte solution; *4*, magnetic mixer.
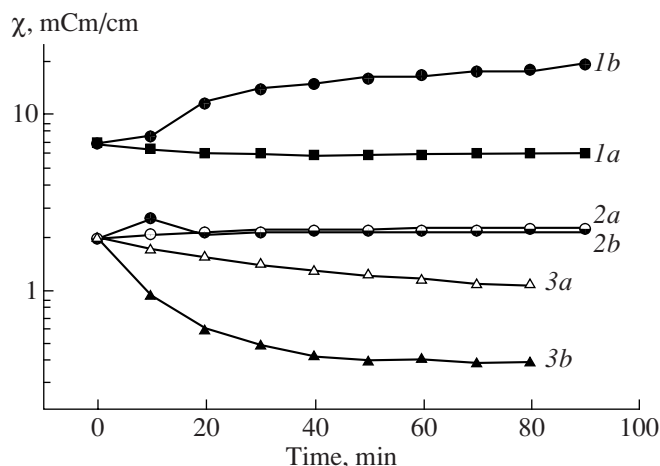
Fig. 2. Influence of the discharge effect time on the change of the electric conductivity of aqueous solutions: H_2SO_4 (*1*), Na_2SO_4 (*2*), NaOH (*3*): *a*, experimental data; *b*, calculated data.

Fig. 3. The NH_4Cl +HCl solution electric conductivity versus the characteristic discharge effect time: *1*, experiment; *2*, calculation.

the initial magnitudes of the electric conductivity (measured in the starting solution and not processed by the discharge) coincide with the calculated ones. The found measured and calculated values of the electric conductivity of the salt, acid, and alkali are presented in Fig. 2.

Obvious variations of the measured electric conductivity of the solution during the gas-discharge treatment were observed only for the alkali (reduction). At the same time, it should be taken into account that the acidification of the solution as a result of the plasma processing leads to some growth of the acid electrical conductivity and decrease of the alkali electrical conductivity. Correcting for the change of acidity causes a systematic discrepancy between the calculated and measured values of the electric conductivity of the solutions of both the acid (Fig. 2, curves *1a* and *1b*) and alkali (Fig. 2, curves *3a* and *3b*). Alongside this, there is no such discrepancy for the salt solutions. These data can be considered as the reduction of mobility of hydronium ions and decrease of mobility of hydroxyl ions as a result of the gas-discharge effect on the solution. At the same time, the mobility of the salt cation and anion didn't change. The cause of this difference could consist of the different mechanism of transport of the mentioned ions. The displacement of the hydronium and hydroxyl ions is of relay-race nature [6]. Consequently, their mobility can be more sensitive to the variation of the solution structure characteristics.

In the case of the acidified salt NH_4Cl + HCl, the behavior of the electric conductivity is presented in Fig. 3. The shape of the calculated electric conductivity curve reminds one of the shape of the electric conductivity curve for the case of the acid (Fig. 2, curve *1a*), but, at the same time, the direct measurement gives a sharp drop of the electric conductivity, even more sharp than for the alkali (Fig. 2, curve *3b*). It is suggested that,
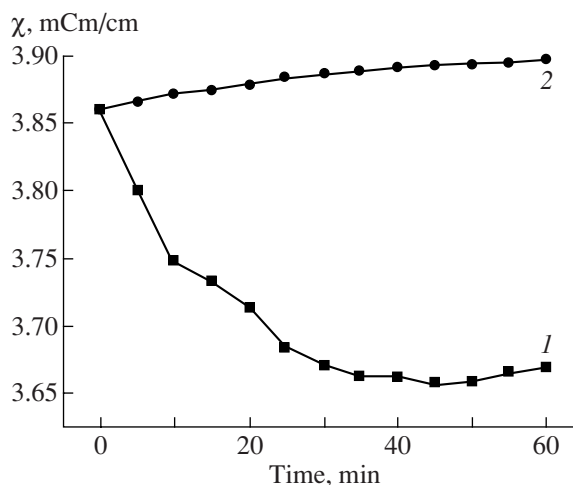
at the calculation of the electric conductivity values for the case of NH_4Cl + HCl, they haven't taken into account the influence of the ion NH_4^+, whose concentration changes during the process of the discharge action.

REFERENCES

1. Kutepov, A.M., Zakharov, A.G., and Maksimov, A.I., Problems and Prospects of Research of Technological Processes Activated by Plasma (Problemy i perspektivy issledovanii aktiviruemykh plazmoi tekhnologicheskikh protsessov) *Doklady Akademii Nauk (DAN) (Reports of the Academy of Sciences) (DAN)*, 1997, vol. 357, no. 6, pp. 782–786.

2. Kuz'micheva, L.A., Titova, Yu.V., and Maksimov, A.I., Influence of Gasphase Processes, Initiated by Glow Discharge, on Electrolyte Solution Properties (Vliyanie gazofaznykh protsessov, initsiiruemykh tleyushchim razryadom, na svoistva rastvorov elektrolitov) *Surface Engineering and Applied Electrochemistry (Elektronnaya Obrabotka Materialov)*, 2006, no. 3, pp. 148–152.

3. Brisset, J.L., Lelive, J., Doubla, A., and Amouroux J., Interactions with Aqueous Solutions of the Air Corona Products. *Revue Phys. Appl.*, 1990, vol. 25, no. 6, pp. 535–543.

4. Troshenkova, S.V., Khlyustova, A.V., and Maksimov, A.I., Effect of Glow Discharge on Acidity of Electrolyte Solutions (Vliyanie tleyushchego razryada na kislotnost' rastvorov elektrolitov) *Surface Engineering and Applied Electrochemistry (Elektronnaya Obrabotka Materialov)*, 2004, no. 6, pp. 31–35.

5. Reference Book for a Chemist. V. 3. Chemical Kinetics. Properties of Solutions. *Electrode Processes (Spravochnik khimika. Khimicheskaya kinetika. Svoistva rastvorov. Elektrodnye protsessy)* Moscow, Leningrad: Khimiya, 1964.

6. Denaro, A.R. and Hough, K.O., *Electrochim. Acta.*, 1972, vol. 17, no. 3, pp. 549–559.

ELECTRICAL PROCESSES
IN ENGINEERING AND CHEMISTRY

Layer-by-layer Glass-Reinforced Plastic Formation with Application of Infrared Heating

T. A. Man'ko, I. M. Ermolaev, and N. I. Volkov

Dnepropetrovsk National University, per. Nauchnii 13, Dnepropetrovsk, 49050 Ukraine
Ukrainian Research Institute for Mechanical Engineering and Technology, 46 Kirova av., Dnepropetrovsk, 49054 Ukraine
Received May 18, 2007

Abstract—The interconnection is determined between the parameters of glass-reinforced plastics formation: the coiling velocity, the emitter voltage drop, and the distance from the rotated envelope surface for the fixed heating temperature.

Infrared (IR) heating is used at different stages of forming envelopes made of polymer composite materials coiling on NC machines in order to reduce the binding agent viscosity under the "wet" formation technique: for the prepreg softening, binding agent hardening, stimulation of chemical reactions. Use of the IR heating for the glass-reinforced plastic hardening is realized via the layer-by-layer envelope formation in the field of IR emitters [1].

The technique consists of combining the processes of coiling and local IR heating of the formation zone. The IR emitters generate large specific power under high efficiency; then, the external location of the heaters facilitates the efficient use of the heating, because the internal layer hardening comes from the side of the heated metal holder.

Experimental study [2] makes it possible to select the parameters of the technological modes of forming glass-reinforced plastic envelopes on the basis of phenol-formaldehyde binding agents with application of IR heating; the linear coiling velocity defined by the envelope diameter and rotational speed is the governing one.

Different variations are possible of the forming parameters. Yet, a combination should exist of optimal (near-optimal) parameters providing the necessary quality of the glass-reinforced plastics; hence, a definite interconnection should exist between the parameters making it possible to find, under the compelled variation of one or several parameters, the respective values of another ones in such a way that their combination should be near-optimal.

To find the particular dependencies between all the forming parameters is difficult; yet, the connections between the particular values can be determined from the experimental data with use of the known physical regularities. Here, the coiling velocity, the distance from the emitter, and the emitter power specify the dependent parameter—the formed surface temperature.

Let the variations be tolerated of the coiling velocity, the distance from the irradiated surface, and the voltage drop on the emitter; yet, the formation temperature should remain constant. The temperature on the surface of the glass-reinforced plastic envelope depends on the emitter parameters, the heated material's physical properties, the envelope thickness, the heat sink conditions, and other factors. Under the constancy of all the main parameters, the energy application variation causes a respective change in the envelope surface temperature. The temperature increment, ΔT, can be assumed to be proportional to the IR emission flux density, E. Then, for the time interval t,

$$k\Delta T = E\Delta t, \tag{1}$$

where k is the proportionality coefficient.

The total differential of the temperature is

$$dT = tdE + Edt. \tag{2}$$

In the photometry terms, the surface irradiance is

$$E = \frac{I\cos\alpha}{r^2}, \tag{3}$$

where I is the radiant intensity, α is the radiant flux incident angle, and r is the distance from the heater to the envelope surface.

The heating layout can be arrange so as that $\alpha = 0°$. With account for the taken assumption,

$$dE = \frac{dI}{r^2} - 2\frac{Idr}{r^3}. \tag{4}$$

The duration of the rotating envelope surface area being within the irradiation zone is

$$t = \frac{L}{V_e}, \tag{5}$$

where L is the length of the envelope surface arc covered by the emitter irradiation zone, and V_e is the linear coiling velocity.

With account for the initial condition of the formation temperature constancy, it can be taken that $dT = 0$. Then,

$$dE = -\frac{E}{t}dt \qquad (6)$$

or

$$dI - \frac{2Idr}{r} - \frac{IdV_e}{V_e} = 0. \qquad (7)$$

For the particular irradiation pattern I, the radiant intensity variations can be considered proportional to the emitter voltage drop, U, variations:

$$dI = AdU,$$

where A is the proportionality coefficient.

Expression (7) can be rewritten in the form

$$dU - \frac{2U}{r}dr - \frac{U}{V_e}dV_e = 0. \qquad (8)$$

The above expression (8) defines the connection between the coiling velocity, the emitter voltage drop, and the distance from the envelope surface for the fixed heating temperature.

REFERENCES

1. Man'ko, T.A., Ermolaev, I.M., Volkov, N.I., Shcheneva, V.B., Solov'ev, A.V., and Ryabovol, A.A., *Elektron. Obrab. Mater.*, 1994, no. 1, pp. 74-75.
2. Man'ko, T.A., Shcheneva, V.B., Ermolaev, I.M., Volkov, N.I., and Ryabovol, A.A., *Tekhn. Mekh.*, 1997, issue 7, pp. 142–145.

Modeling of Kinetic Characteristics of Substances with a Complex Energy Spectrum

N. I. Botoshan

Institute of Applied Physics of the Academy of Sciences of Moldova,
ul. Academiei 5, Chisinau, MD-2028 Republic of Moldova

Received June 8, 2006

Abstract—The coefficient of electric conductivity of some substances is studied; peculiarities of the general character are outlined in the process of the description. For generalization of the kinetic characteristics in solids, the factors of reciprocity determining the level of interband exchange and allowing presentation of the kinetic characteristics of metals, semimetals, and semiconductors from one point of view are introduced. The technique of the description taking into account the interband exchange and the presence of common electrons in the long-range order of their interaction is developed. In particular, there are obtained analytical expressions for generalized electric conductivity coefficients, the Hall coefficient, and the thermopower, which permit description of these characteristics in metals, semimetals, and semiconductors using unique formulae. The peculiarities in the description of the electric conductivity coefficient for unordered structures and conductors of nonelectron type are found. There are presented common approaches in the description of various liquids by means of defining of the effective charge characteristic by analogy with the description of free quasiparticles in solids by the effective mass method. The effective charge of an arbitrary current carrier in liquids is determined by means of a transference number expressed through the ion radii and masses of the charge carriers, and it can be overdetermined up to the change of the charge sign.

INTRODUCTION

In isotropic materials, the electric conductivity coefficient σ determines the analytical correlation between the current density $\vec{j}$ and the electric field $\vec{E}$ in a substance by Ohm's law $\vec{j} = \sigma\vec{E}$. In general, the electric field density is a product of the charge density by the mean velocity of the carrier motion in the electric field $\vec{j} = \rho\vec{v}$. Determination of the mean velocity of homotypic charge carriers, e.g., electrons, in a field intensity of 1 V/cm by the kinetic characteristic termed mobility $u(\vec{v} = u\vec{E})$ allows us to present the electric conductivity coefficient by the formula $\sigma = enu$, where n is the concentration of homotypic charge carriers (electrons). Ohm's law is true till the concentration and mobility of the charge carriers do not depend on the external electric field. In particular, this condition is realized at moderate fields only.

The classical theory of electric conductivity of solids was developed by Drude [1]. Afterwards, the theory was enlarged on account of the distribution of electron velocities by means of the Boltzmann statistics (by Lorentz) and the Fermi–Dirac quantum statistics (by Sommerfeld). Despite the obvious success of the theory with respect to the specification of the ratio between the coefficients of the electric conductivity and heat conductivity confirmed by the Wiedemann–Franz law

$\dfrac{\chi}{\sigma T}$ = const, where χ is the heat conductivity coefficient and T is the absolute temperature, the Drude–Lorenz–Sommerfeld theory has not significantly improved the explanation of the temperature dependence of σ for various solids. For example, the temperature dependence of the electric conductivity in metals and semiconductors is absolutely different. Besides, in metals, in a wide temperature range, σ is proportional to T^{-1}, and, at low temperatures, it is proportional to T^{-5}. The concentration of electrons in metals practically does not depend on the temperature, whereas, in semiconductors, it strongly changes with the temperature. It is proved that, in semiconductors, new quasiparticles termed "holes" take part in conductivity origination and the number of electron–hole pairs is proportional to $\exp\left(-\dfrac{E_G}{2kT}\right)$, where k is the Boltzmann constant, and E_G is the semiconductor gap energy [2].

A successful explanation of the temperature dependence of the electric conductivity in solids is the quantum conception of the charge carrier scattering for the calculation of the mobility. The modern theory of the electric conductivity of metals was founded in the beginning of the thirties, mainly in works of Bloch and Peierls [3]. The electric conductivity calculations made in that period were based on very rough ideas on both the spectra of electrons and phonons and their interac-

tion. However, the qualitative considerations of Peierls, being characterized by special clarity and comprehension, appeared to be very fruitful for further development of the theory. On the basis of the kinetic equation analysis, Bloch has shown that the electric resistance of a metal due to the electron–phonon interaction is proportional to the fifth power of the temperature. He proceeded from a simplest model of free electrons interacting with longitudinal phonons, their dispersion law being linear and isotropic; he also assumed that the phonons are described by the Bose distribution function.

It is quite difficult to prove the difference between the electron and ionic electric conductivities as well as the determination of ratio of these two types of electric conductivity at their simultaneous existence. The difficulties are especially great at high temperatures and low currents. It is important that some characteristics as such are not decisive; only consideration of the problem from an integrated viewpoint can favor resolving the differences.

The feasibility of the Faraday law may be considered proof of the existence of pure ionic electric conductivity. Deviations from the Faraday law allow determination of the rate of the electron participation in the total electric conductivity of the substance. Insignificant physical changes on electrodes are less demonstrative even when they are observed only at the current passing; the same is true of insignificant deviations from Ohm's law at low voltages due to the presence of decomposition potentials and polarization. Signs of the electric conductivity, first of all, are the following: an absolutely linear current dependence on the voltage surviving up to the lowest voltage values and, especially, the Hall effect presence.

A correlation between the ionic conductivity and the chemical structure exists in fact; however, it is not unambiguous enough for prediction of the conductivity nature in each separate case.

Gudden and Pohl, and Pohl and Hilsch have pointed to the fact that, in pure ionic conductors, additional electron currents may pass [4]. Tubandt and colleagues have found several cases of composite electric conductivity, where both parts have approximately equal value. Correlation between the ionic and electron parts of conductivity could hardly be considered a characteristic of a substance, since it depends not only on the temperature but also on other factors determining the electric conductivity.

The given representation is based on a certain group of closely related problems on the nature of the influence of the interband exchange processes and temperature on the kinetic characteristics of a number of substances having different structures of energy bands. Our primary purpose is to achieve a fundamental clarity in problems of determination of the Fermi level energy and classification of the majority charge carriers taking part in the interband exchange and electric current.

Simple models allowing analytical study of the qualitative aspect of the problem and quantitative numerical calculations based on concrete data will be favored. We do not state the problem of the experimental situation representation; we just take experimental data to illustrate basic conclusions of the developed technique. The representation is based on the method developed by the author for taking into account the interband exchange reciprocity factor and on deduction of charge transference numbers in description of the electric conductivity coefficient of unordered structures and liquids, as well as on equations allowing us to elucidate kinetics of electronic conductors from an integrated point of view.

ELECTRONS AND TYPES OF STRUCTURE BONDS

The space distribution of electrons, being the most mobile particles of the atomic structure of a substance, determines the type of feasible bond at formation of the substance structure. Metallic, covalent, ionic, and molecular types of bond are recognized in solids. Formation of a certain type of bond is completely due to the electric properties of the constituents and to the condition of their meeting or approaching for its realization. For example, for ionic and molecular bonds, a crucially important characteristic is the electronegativity of the atoms constituting the given structure [5]. For crystals with covalent bonds, approaching of the constituents at distances of space overlapping of their electron density clouds is of fundamental importance. For metals, in addition to the condition of the electron shell overlapping, realization of the long-range order in the arrangement of the structure constituents is essential.

In metals, electrons of all the atoms of a crystal take part in a collective bond analogous to a covalent one. In other words, in metals, the whole sample is bound by common collectivized electrons by a comprehensive covalent bond. The motion of electrons in crystals is described by the spectrum of alternating bands of allowed and forbidden energies. As a matter of fact, the origin of the band structure of the electron energy spectrum in the crystal is due to formation of the crystal itself out of N atoms, each of them in the free state being characterized by a discrete electron energy spectrum. As a result of interaction of the crystal atoms, N-fold degenerate atomic levels broaden and form the crystal band structure.

Let us note that the structure constituents may be both single atoms and structure formations possessing a well-defined internal symmetry. For example, atoms of the unit cell of covalent crystals (semiconductors) are characterized by a more rigid bond between the cell constituents than the long-range order bonds with constituents of other cells. The collectivized part of the electrons from the metallic bond is usually more rigid in comparison with the covalent one. In covalent crystals, it is less rigid due to participation in it of a small part of all the electrons of the structure bond. However,

their key role for the kinetic characteristics of the medium does not allow us to neglect them even in the case of their low concentration.

It should be noted that, between covalent, molecular, and ionic crystals, there exists a smooth transition realized either by close approaching of the constituents of the latter or by weakening of the intercell bond of the former. If we continue this ideology for noncrystalline structures or unordered crystals, we can observe that the latter are a continuation of the weakening of structure bonds between the constituents in the long-range order, i.e., a suppression of the long-range order in the structure ordering.

In this paper, for determination of the kinetic characteristics of substances, the influence of elements of the long-range order bonds is taken into account, allowing description of condensed media of various bond structures from an integrated point of view. For unordered structures, there are deduced important characteristics of the process of transfer of opposite charges—charge transference numbers.

TWO-BAND MODEL OF SEMICONDUCTORS AND SEMIMETALS

The band conception of the electron energy spectrum in crystals allows explanation of a number of properties due to which solid crystal structures are divided into dielectrics, metals, semimetals, and semiconductors. An important distinctive characteristic of them is the electric conductivity coefficient being determined by the kinematics of the majority charge carriers taking part in the electric current. The energy structure of bands is described by the band function of the charge carrier energy $\varepsilon_i(\vec{p})$ and by the dispersion law, where i is the band number index. Electron occupation of the energy states occurs according to the Fermi–Dirac distribution and depends on the function of the density of states $g(\varepsilon) = \dfrac{dn}{d\varepsilon}$ being determined by the band dispersion law. In the simplest isotropic case, when $\varepsilon(\vec{p}) = \dfrac{p^2}{2m^*}$, the function of the density of states takes the root form $g(\varepsilon) = A\varepsilon^{\frac{1}{2}}$ where $A = \dfrac{1}{4\pi^2}\left(\dfrac{2m^*}{\hbar^2}\right)^{\frac{3}{2}}$ and m^* is the effective mass of charge carriers in the band.

The multiband consideration of the substance's kinetic characteristics is reduced to an overdetermination of the reciprocity factor on the basis of the multiband pattern of the spectrum of the electron energy states. The system of charges, potential current carriers, is subdivided into three main components: n_s being the total concentration of collectivized metal electrons of all the bands (electrons movable across the whole sample volume), n being the total concentration of electrons

of all the substance conduction bands taking part in the current formation, and n_p being the total concentration of holes in all the valence bands taking part in the current formation.

Let us note that electrons and holes movable only within a unit cell or cluster formations do not directly participate in the charge transfer processes. Their participation in current formation requires a special consideration on the basis of Mott's theory of hopping conduction, taking into account localized states of electrons and holes in the Anderson model [6]. The substances possessing a hopping charge transfer constitute a separate class of condensed media with unordered atomic structure. Their most important representatives are liquids and amorphous solids; the most widespread ones are solutions of electrolytes and biologic media.

The isoenergetic surface of the last energy level occupied by electrons $\varepsilon(\vec{p}) = \varepsilon_F$ is termed the Fermi surface, and the energy corresponding to it is termed the Fermi energy. For metals, occupation of a single band is essential, when electrons occupy all the states calculated from the band bottom energy to the Fermi energy ε_F that depends on the carrier concentration n_c.

In the case of semiconductors and dielectrics, all available bands at the temperature $T = 0$ are completely occupied by electrons. Therefore, dielectrics and semiconductors at the temperature $T = 0$ do not conduct current. However, at the temperature $T \neq 0$, electrons can cover the forbidden energy space of width ε_G, being sufficiently narrow in semiconductors, by quantum transitions into the nearest empty band. Hence, having covered the energy ε_G, being termed the gap for a semiconductor, electrons occupy the open band, wherein they are available for participation in current. Let us note that holes take part in formation of the conduction current equally with electrons, though their dispersion law calculated from the band top is determined by the negative effective mass $-m_P^*$. For simplification of calculations by the band pattern, let us introduce the negative calculation of hole energy. In this aspect, the bands of metallic and hole conductivity will be separated by the presence of a common zero level of the energy calculation.

Let us consider the technique for determination of the Fermi energy and the carrier concentrations in the proposed two-band pattern of a semiconductor (Fig. 1).

Calculation of the density of states in bands for the parabolic dispersion law and calculation of concentrations of the carriers with the Fermi–Dirac distribution function leads to the following results:

$$n_s = N_C \exp\frac{\varepsilon_S - \varepsilon_C}{kT},$$

$$n = N_C \exp\frac{\varepsilon_F - \varepsilon_C}{kT},$$

$$n_P = N_P \exp\frac{\varepsilon_V - \varepsilon_F}{kT},$$

where $N_C = 2\left(\frac{2\pi m_n kT}{h^2}\right)^{\frac{3}{2}}$ and $N_P = 2\left(\frac{2\pi m_p kT}{h^2}\right)^{\frac{3}{2}}$ are

the effective densities of states in the conduction band and the valence band, respectively, and m_n and m_p are the effectives masses of the electrons and holes.

The Fermi energy determined by the edge level of occupation of the states is equal for all the bands. Therefore, the bands are employed in the transfer phenomena according to the ratio between the Fermi energy and the energy distance from the beginning of the energy calculation and bottom or top of the respective bands of electrons and holes. That is why, in the conduction band, the presence of the concentration n_s of metal electrons is assumed.

Let us introduce the parameter of interband reciprocity of electron exchange, which determines the semiconductor intrinsic conductivity due to the tunnel transition n_P of electrons in the conduction band from the valence band

$$\alpha = n n_P = N_C N_P \exp\frac{\varepsilon_V - \varepsilon_C}{kT}.$$

Electrons of the intrinsic conductivity of the semiconductor description give the difference between the complete occupation and the number of collectivized metal electrons: $n_P = n - n_s$.

The Fermi energy is determined by the relative occupation of the bands by charge carriers—electrons and holes:

$$\varepsilon_F = \frac{\varepsilon_C + \varepsilon_V}{2} + \frac{kT}{2}\ln\frac{N_P}{N_C} + \frac{kT}{2}\ln\frac{n}{n_P}.$$

The ratio for the Fermi energy of the semiconductor is determined by the condition of absence of collectivized metal electrons $n_s = 0$,

$$\varepsilon_P = \frac{\varepsilon_C + \varepsilon_V}{2} + \frac{3}{4}kT\ln\frac{m_p}{m_n}$$

In general, the Fermi level energy depends on ratio of the total concentrations of opposite charge carriers—electrons and holes $\left(\varepsilon_F = \varepsilon_P + \frac{kT}{2}\ln\frac{n}{n_P}\right)$—and may shift with respect to the value of ε_P to different sides, thus increasing or decreasing in dependence on the ratio of the concentrations of opposite charge carriers n/n_P. For example, the Fermi level of the zero energy may be in accord with the ratio between the concentrations of opposite charge carriers of the form $n_0 = n_P\exp\left(-\frac{2\varepsilon_P}{kT}\right)$. This equation implies the possibility of
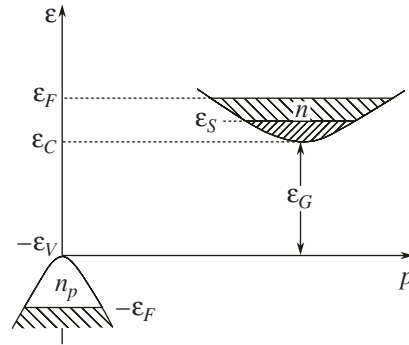
Fig. 1. Energy pattern of a two-band semiconductor.

existence of collectivized holes and localized electrons, since the condition $n_0 < n_p$ at the semiconductor Fermi energy $\varepsilon_p > 0$ corresponds to a supposition about the hole conductivity. The analysis of this possibility of the description is analogous to that for collectivized electrons.

The conductor Fermi energy is determined by the relative characteristic of the occupations, i.e., by the chemical potential calculated from the level ε_p : $\varepsilon_F = \frac{kT}{2}\ln\frac{n}{n_0}$.

THREE-BAND DESCRIPTION OF SEMICONDUCTORS AND SEMIMETALS

The description of the kinetic processes in the semimetal model assumes representation of the kinetic coefficients of the transfer phenomena through the characteristics of the subsystems of electrons and holes determined by the mobilities and concentrations of the charge carriers in various energy bands [7]. In this aspect, formulae for the kinetic coefficients have an integrated form, including characteristics of the subsystems in the form of sums of the bands. For example, the electric conductivity coefficient is expressed by a standard formula of the form $\sigma = q\sum_{i=1}^{k} n_i u_i$, where q is the particle elementary charge, and u_i and n_i are the mobility and concentration of particles in the ith band. The proposed three-band model of the description of the charge carrier kinetics contains division of the conduction electrons into subsystems of collectivized metallic and intrinsic conductivities induced by excitation of transitions from the valence bands into the conduction bands. The basic difference in the description of a semiconductor and a semimetal is the sign of the parameter of the energy gap ε_G: it is negative for a semimetal.

The three-band description allows us to distinguish two parameters of the semimetal band structure: the tra-

Fig. 2. Three-band presentation of the semimetal energy spectrum.

ditional semiconductor energy gap ε_G and the energy parameter of overlapping Δ.
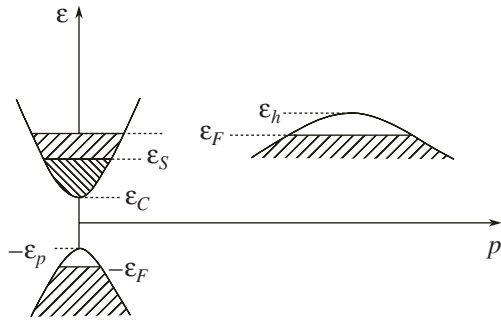
Let us consider the calculation of the concentrations of opposite charge carriers with a standard form of description of the kinetic characteristics taking into account two valence bands of a semiconductor or a semimetal (Fig. 2).

The presentation of the concentrations in the bands according to the given band pattern has the form

$$n_s = N_C \exp\frac{\varepsilon_S - \varepsilon_C}{kT}, \quad n = N_C \exp\frac{\varepsilon_F - \varepsilon_C}{kT},$$

$$n_P = N_P \exp\frac{\varepsilon_P - \varepsilon_F}{kT}, \quad n_h = N_h \exp\frac{\varepsilon_h - \varepsilon_F}{kT},$$

where n_s is the concentration of collectivized metal electrons of the conduction band, n is the total concentration of electrons of the conduction band, and n_P and n_h are the concentrations of holes in two valence bands.

Let us determine the characteristics of the exchange reciprocity between the conduction band and the valence bands by the factors α_h and α_p:

$$nn_h = N_C N_h \exp\frac{\varepsilon_h - \varepsilon_C}{kT} = \alpha_h,$$

$$nn_p = N_C N_p \exp\frac{\varepsilon_p - \varepsilon_C}{kT} = \alpha_p.$$

Taking into account the ratio between the concentrations of intrinsic conduction electrons and the total contribution of the two valence bands $n - n_C = n_h + n_p$ for determination of the charge carrier concentration in the conduction band, we obtain the equation $n^2 - nn_C = \alpha_h + \alpha_p$; its solution has the form

$$n = \frac{1}{2}\{\sqrt{n_s^2 + 4(\alpha_h + \alpha_p)} + n_s\}.$$

The hole concentrations in the bands are expressed through the value $n_p = \frac{1}{2}\{\sqrt{n_s^2 + 4(\alpha_h + \alpha_p)} - n_s\}$ as follows: $n_h = \dfrac{\alpha_h n_p}{\alpha_h + \alpha_p}$, $n_p = \dfrac{\alpha_p n_p}{\alpha_h + \alpha_p}$.

One can see that the multiband description by introduction of parameters of the exchange reciprocity between the conduction band and the valence bands in the general case of many overlapping bands is determined by functions of the concentrations of electrons and holes of the form

$$n = \frac{1}{2}\left\{\sqrt{n_s^2 + 4\sum_{i=1}^{k}\alpha_i} + n_s\right\}, \quad n_i = \frac{\alpha_i n_p}{\sum\limits_{i=1}^{k}\alpha_i},$$

$$n_p = \frac{1}{2}\left\{\sqrt{n_s + 4\sum_{i=1}^{k}\alpha_i} - n_s\right\}.$$

In this aspect, the electric conductivity coefficient is simply presented in the form

$$\sigma = q\left(nu_n + \sum_{i=1}^{k}n_i u_i\right) = \frac{q}{2}\left\{\sqrt{n_s^2 + 4\sum_{i=1}^{k}\alpha_i}\right.$$

$$\times \left(u_i + \frac{\sum\limits_{i=1}^{k}\alpha_i u_i}{\sum\limits_{i=1}^{k}\alpha_i}\right) + n_s\left(u_n - \frac{\sum\limits_{i=1}^{k}\alpha_i u_i}{\sum\limits_{i=1}^{k}\alpha_i}\right)\right\}.$$

Here, the role of partial factors of the interband exchange reciprocity for the electric conductivity coefficient is identified taking into account the participation in the conductivity of the hole carries of various valence bands.

Let us note that the results of the Fermi energy calculation in the two-band model are completely adequate for description in the three-band model, though with an overdetermined total concentration of electrons in the conduction band.

KINETIC CHARACTERISTICS OF SEMICONDUCTORS AND SEMIMETALS

Electric conductivity is a basic kinetic characteristic of condensed media, especially of solids: $\sigma = q(nu_n + n_p u_p)$. The charge carrier mobilities significantly depend on the temperature.

Let us consider the technique of calculation of the kinetic characteristics of a semiconductor or a semimetal with one valence band. The reciprocity factor in this case has the form

$$\alpha = n n_p = N_c N_p \exp \frac{\varepsilon_p - \varepsilon_c}{kT}.$$

The concentration of collectivized metal electrons is determined by the Maxwell distribution in the conduction band:

$$n_s = N_c \exp \frac{\varepsilon_s - \varepsilon_c}{kT}.$$

For semiconductors, the gap has a positive value $\varepsilon_G = \varepsilon_c - \varepsilon_p > 0$, and for semimetals—vice versa ($\varepsilon_p - \varepsilon_c > 0$).

The concentrations of electrons in the conduction band n and of holes in the valence band n_p for a composite system of the charge carriers are determined by the ratios

$$n = \frac{1}{2}(\sqrt{n_s^2 + 4\alpha} + n_s),$$

$$n_p = \frac{1}{2}(\sqrt{n_s^2 + 4\alpha} - n_s).$$

The electric conductivity is determined by the equation

$$\sigma = \frac{q}{2}\{\sqrt{n_c^2 + 4\alpha}(u_n + u_p) + n_c(u_n - u_p)\}.$$

Let us consider the case when the drift velocities of the carriers differ only by the degree of their motion inertia, i.e., by the effective masses. In order to find the peculiarities of the inertia characteristics of the carriers, let us introduce the parameter of the ratio of the hole effective masses to the electron ones $\gamma = \dfrac{m_p}{m_n}$ and the reduced mass of the charge carriers $\bar{m} = \dfrac{m_n m_p}{m_n + m_p}$. In these notations for the mobilities u_n and u_p, we obtain the ratios

$$u_n + u_p = \frac{q\langle \tau \rangle}{\bar{m}} \quad \text{and} \quad u_n - u_p = \frac{q\langle \tau \rangle(1 - \gamma)}{\bar{m}(1 + \gamma)},$$

where $\langle \tau \rangle$ is the carrier relaxation time.

As a result of the transformations, the electric conductivity coefficient takes the form where the dependence on the parameter γ is shown:

$$\sigma = \frac{q^2 \langle \tau \rangle}{2\bar{m}}\left(\sqrt{n_s^2 + 4\alpha} - n_s \frac{1 - \gamma}{1 + \gamma}\right).$$

In the case of the metallic conductivity $\alpha \longrightarrow 0$; therefore, $\sigma_m = \dfrac{q^2 n_c \langle \tau \rangle}{m_n}$.

In the case of the intrinsic conductivity, when $n_s \longrightarrow 0$, we have $\sigma_p = \dfrac{q^2 \langle \tau \rangle}{\bar{m}}\sqrt{\alpha}$.

Therefore,

$$\sigma_m = \frac{q^2 N_c \langle \tau \rangle}{m_n} \exp \frac{\varepsilon_s - \varepsilon_c}{kT},$$

$$\sigma_p = \frac{q^2 N_c \langle \tau \rangle}{\bar{m}} \gamma^{\frac{3}{4}} \exp\left(-\frac{\varepsilon_G}{2kT}\right).$$

The Hall coefficient transformations result in the following:

$$R = \frac{n_p u_p^2 - n u_u^2}{q(n u_n + n_p u_p)^2}, \quad \text{or}$$

$$R = \frac{q}{2\sigma^2}\{\sqrt{n_s^2 + 4\alpha}(u_p^2 - u_n^2) - n_s(u_p^2 + u_n^2)\}.$$

In the earlier adopted notations, the Hall coefficient takes the form

$$R = \frac{2[\sqrt{n_s^2 + 4\alpha}(1 - \gamma^2) - n_s(1 + \gamma^2)]}{q[\sqrt{n_s^2 + 4\alpha}(1 + \gamma) - n_s(1 - \gamma)]^2}.$$

In the limiting case of a pure metal, $\alpha \longrightarrow 0$; therefore, $R_m = -\dfrac{1}{q n_c}$. In the case of the intrinsic semiconductor, $n_s \longrightarrow 0$; therefore, $R_p = \dfrac{1 - \gamma}{q\sqrt{\alpha}(1 + \gamma)}$.

Thus, the Hall coefficient sign depends on the difference $1 - \gamma$, which is determined by the structure of the conduction and valence bands in the Brillouin zone

$$R_m = -\frac{\exp\left(-\dfrac{\varepsilon_s - \varepsilon_c}{kT}\right)}{q N_c}, \quad R_p = \frac{(1 - \gamma)\exp\dfrac{\varepsilon_G}{kT}}{q N_c \gamma^{\frac{3}{4}}(1 + \gamma)}.$$

THE THERMOPOWER α_T

If along a conductor a temperature gradient exists, then, on a hot face end, electrons take higher energy and velocity; as a result, a current of electrons appears forming a potential difference on the sample edges. The charge accumulation proceeds until the appearing thermopower induces a compensatory countercurrent of electrons.

Thermopower is one of the basic electric effects in solids. The thermopower coefficient [8], which deter-

mines the correlation of the thermopower and the temperature gradient observed on face ends of the crystal being at the temperature difference ΔT, is equal to

$$\alpha_T = \frac{k}{q}\frac{\left[A(nu_n - n_p u_p) + nu_n \ln\left(\frac{N_c}{n}\right) - n_p u_p \ln\left(\frac{N_p}{n_p}\right)\right]}{nu_n + n_p u_p},$$

where A is the constant depending on the crystal lattice type and on the charge carrier scattering type. As a

result of these transformations, the thermopower coefficient takes the form

$$\alpha_T = \frac{k}{q}\frac{\left[A(n\gamma - n_p) + n\gamma \ln\frac{N_c}{n} - n_p \ln\frac{N_p}{n_p}\right]}{n\gamma + n_p}.$$

Taking into account the ratios of the reciprocity in the expressions for concentrations of opposite charge carriers, one can find in the formula α_T an obvious dependence on the parameters γ and α:

$$\alpha_T(n_s, \alpha) = \frac{k}{q}\frac{\left\{n_s\left[A(1+\gamma) + (1-\gamma)\ln\frac{n}{N_c} + \frac{\varepsilon_G}{kT}\right] - \sqrt{n_s^2 + 4\alpha}\left[A(1-\gamma) + (1+\gamma)\ln\frac{n}{N_c} + \frac{\varepsilon_G}{kT}\right]\right\}}{(1+\gamma)\sqrt{n_s^2 + 4\alpha} - (1-\gamma)n_s},$$

where the concentration of conduction electrons is determined by the standard ratio $n = \frac{1}{2}(\sqrt{n_s^2 + 4\alpha} + n_s)$.

Considering the limiting case of preservation of metal conduction electrons only $\alpha \longrightarrow 0$ (metal case), for the thermopower coefficient we obtain the expression

$$\alpha_T(n_s, 0) = \frac{k}{q}\left(A - \frac{\varepsilon_s - \varepsilon_c}{kT}\right).$$

In the opposite limit of an intrinsic semiconductor or a semimetal, when $n_s \longrightarrow 0$, the thermopower coefficient takes the form

$$\alpha_T(0, \alpha) = -\frac{k}{q}\left[\frac{3}{4}\ln\gamma + \frac{1-\gamma}{1+\gamma}\left(A + \frac{\varepsilon_G}{2kT}\right)\right],$$

where it should be taken into account that ε_G in the semimetal case is a negative value.

MULTIBAND CONSIDERATION OF THE SUBSTANCE KINETIC CHARACTERISTICS

Let us assume that a crystalline substance possesses a multiband structure of energy states of the charge carries—electrons and holes—constituted by the conduction bands k and by the valence bands l. We will appreciate electrons of the collectivized metallic states in each separate conduction band, their total concentration being determined by the sum of their individual concentrations in the bands: $n_S = \sum_{i=1}^{k}\lambda_i N_{ci}\exp\frac{\varepsilon_S - \varepsilon_{ci}}{kT}$,

where ε_{ci} is the energy of the ith conduction band, N_{ci} is the density of states in the ith band, λ_i is the multiplicity of equivalent energy minima inside the Brillouin zone,

and ε_S is the energy of the state occupation by collectivized metal electrons.

The total concentration of charge carriers in the conduction band is determined by an analogous ratio of the form $n = \sum_{i=1}^{k}\lambda_i N_{ci}\exp\frac{\varepsilon_F - \varepsilon_{ci}}{kT}$, where ε_F is the energy of the level of complete extreme occupation of states termed the Fermi energy.

The occupation of states of the valence band is determined by an analogous ratio of the form $n_p = \sum_{j=1}^{l}\kappa_j N_{Vj}\exp\frac{\varepsilon_{Vj} - \varepsilon_F}{kT}$, where ε_{Vj} is the energy of the jth valence band top level, N_{Vj} is the number of density of energy states in the jth band, and κ_j is the multiplicity of equivalent energy maxima inside the Brillouin zone.

For the total number of electrons n and the total number of holes n_p, there is a ratio of reciprocity of exchange by opposite charge carriers between the conduction and valence bands

$$\alpha(T) = nn_p = \sum_{i=1}^{k}\lambda_i N_{ci}\exp\left(-\frac{\varepsilon_{ci}}{kT}\right)$$
$$\times \sum_{j=1}^{l}\kappa_j N_{Vj}\exp\left(\frac{\varepsilon_{Vj}}{kT}\right).$$

The reciprocity factor $\alpha(T)$, depending exclusively on the structure of the substance bands and temperature, determines the exchange between all the substance bands. Concentrations of carriers, electrons in

the conduction bands n, and holes in the valence bands n_p satisfy the system of algebraic equations of the form

$$\begin{cases} nn_p = \alpha, \\ n - n_S = n_p. \end{cases}$$

Therefore, the total concentrations of charge carriers, electrons n, and holes n_p are determined by the concentration of collectivized metal electrons n_S and by the factor of multiband reciprocity α by already known ratios for the n and n_p concentrations.

The value of the Fermi level energy is determined by one of two ratios of the form

$$\varepsilon_F(T) = kT\ln\frac{n}{\zeta_c} = kT\ln\frac{\zeta_V}{n_p},$$ where the values ζ_c and ζ_V are determined by the formulae

$$\zeta_c(T) = \sum_{i=1}^{k} \lambda_i N_{ci}\exp\left(-\frac{\varepsilon_{ci}}{kT}\right),$$

$$\zeta_V(T) = \sum_{j=1}^{l} \kappa_j N_{Vj}\exp\left(\frac{\varepsilon_{Vj}}{kT}\right).$$

Preserving the perfect analogy with respect to the conception of the Fermi level of the intrinsic semiconductor, let us determine the Fermi energy by the expression $\varepsilon_F(T) = \dfrac{kT}{2}\ln\left(\dfrac{n\zeta_V}{n_p\zeta_c}\right)$, which, in the case of a substance with one valence band and one conduction band, turns into the known formula of the Fermi energy of a semiconductor [7].

Thus, determination of the concentrations of charge carriers n and n_p, as well as of the Fermi energy $\varepsilon_F(T)$, is reduced to calculation of the temperature functions $\alpha(T)$, $\zeta_c(T)$, and $\zeta_V(T)$, being easily calculated for a known structure of the substance bands.

The charge carrier concentrations in each separate conduction and valence band are determined by the Fermi energy by the formulae

$$n_i = \lambda_i N_{ci}\exp\frac{\varepsilon_F - \varepsilon_{ci}}{kT}, \quad n_{pj} = \kappa_j N_{Vj}\exp\frac{\varepsilon_{Vj} - \varepsilon_F}{kT}.$$

According to the Fermi energy determination, the expressions for the band concentrations may be presented through the total charge carrier concentrations by the formulae

$$n_i = \lambda_i N_{ci}\exp\left(-\frac{\varepsilon_{ci}}{kT}\right)\frac{n}{\zeta_c},$$

$$n_{pj} = \kappa_j N_{Vj}\exp\left(\frac{\varepsilon_{Vj}}{kT}\right)\frac{n_p}{\zeta_V}.$$

The concentration of collectivized electrons depends on the structure factor ζ_c and energy ε_S. The total charge carrier concentrations satisfy the equation $n - n_S = n_p$, allowing derivation of the following formula for calculation of the Fermi energy $\varepsilon_F(T) = \varepsilon_S + kT\ln\left[\left(1 + \sqrt{1 + 4\dfrac{\zeta_V}{\zeta_c}\exp\left(-\dfrac{2\varepsilon_S}{kT}\right)}\right)\middle/2\right]$. The intrinsic conductivity limit is in accord with $\varepsilon_S \longrightarrow -\infty$.

The kinetic characteristics of a substance characterized by electron–hole conductivity are determined by standard formulae of the general form. For example, the electric conductivity, Hall effect, and thermopower are determined by the known formulae [8].

SUBSTANCES WITH A COMPOSITE SYSTEM OF CHARGE CARRIERS

Substances being intermediate in the electric properties between metals and semiconductors are semimetals. A characteristic peculiarity of the structural description of the semimetal properties is weak overlapping of the valence and conduction bands. This circumstance leads to the fact that semimetals remain conductors up to the absolute zero of the temperature at a relatively low concentration of current carriers (10^{18}–10^{20} cm^{-3}). As the temperature grows, the number of current carriers and the electric conductivity increase; this is a characteristic peculiarity of semiconductors. Semiconductors differ from metals by the fact that their electric conductivity exponentially depends on the energy of the conductivity activation: ε_A – $\sigma = \sigma_0\exp\left(-\dfrac{\varepsilon_A}{kT}\right)$. This means that the value ε_A is the bond energy for charge carriers; having overcome it, they become free for participation in current. The best current carriers—metals—are characterized by high specific electric conductivity with a concentration of conduction electrons of about 10^{22}–10^{23} cm^{-3}. With respect to the analytical description of the electric properties, metals are a skeleton of positive ions immersed into a high-mobility electron gas. This gas of electrons hardens the skeleton lattice structure due to the high level of translational symmetry.

The different levels of the specific electric conductivity of metals, semimetals, and semiconductors don't appear to be the single key difference of these substances. Their fundamental difference is that, in semimetals and semiconductors, current carriers are, in addition to electrons, positive charges. They are not ions but vacancies of electrons in the valence band wherefrom the electrons have passed into the conduction bands. In other words, the electron density of the charge in the Brillouin zone possesses spatial regions of decreased density with respect to its mean value. This is experimentally confirmed by the Hall effect measurements, i.e., generation of the potential difference perpendicular to the current and magnetic field. In some metals, an insignificant Hall effect is observed, allow-

ing us to state that holes take part in the electric conductivity of metals too. In other words, the conductivity of substances of metals, semimetals, and semiconductors seems to be a composite of collectivized electrons, holes, and the electrons that have passed into the conduction bands from the valence ones. For metals, the intrinsic conductivity may be successfully neglected, whereas, for semiconductors, the metallic conductivity is usually ignored. It is natural that, in semimetals, the composite conductivity should be preserved. It turns out that, in the description of the kinetic phenomena, the metallic conductivity in semimetals is, nevertheless, neglected. As a result, for providing kinetics of the charge carriers in the ideology of the description of only the intrinsic conductivity, there appears the necessity of redistribution of the energy and pulse (inertia) to the current carriers—electrons and holes. A decrease of the hole number due to neglect of the metallic conductivity leads to an upward bias of the values of their effective masses, sometimes exceeding the effective masses of electrons by hundreds of times. Another peculiarity of the kinetic characteristics is their explicit dependence on the ratios of the effective masses of charge carriers. Since the Fermi level energy essentially depends on both the temperature and concentration of the state occupation by collectivized carriers, the level may shift towards the range of nonparabolicity of the dispersion law according to the real pattern of the substance bands. For account of the last peculiarities, the total pattern of the energy bands in the Brillouin zone is required.

In the present paper, the kinetic phenomena in semimetals are overdetermined on the basis of the composite conductivity taking into account subsystems of metal electrons. Basic modifications of the description are the redistribution of the Fermi level energy and revealing of the temperature dependence of the substance's kinetic characteristics.

According to the presented three-band pattern, let us consider the case of a semimetal in the presence of two valence bands analogous to bismuth bands [9]. The technique of calculation of the kinetic characteristics consists in selection of energy counting by the band pattern from the bottom of the main conduction band. The main band is in accordance with the minimal energy of the band bottom level among all the conduction bands. Semimetals are usually characterized by two key parameters: the gap $E_G = \varepsilon_c - \varepsilon_p$ and the overlapping energy $\Delta = \varepsilon_V - \varepsilon_c$. The level of the energy of the main conduction band bottom may be taken as a starting point for counting; therefore, the energies of the tops of the valence bands are on different sides with respect to the counting starting point $\varepsilon_V = \Delta$ and $\varepsilon_p = -E_G$. Thus, the formula for the calculation of the Fermi energy takes the form $\varepsilon_F(\bar{n}_s, T) = kT\ln\dfrac{\bar{n}}{\bar{\zeta}_c} = kT\ln\dfrac{\bar{\zeta}_V}{\bar{n}_p}$,

where we have introduced the relative concentrations of the form $\bar{n}_s = \dfrac{n_s}{N_{c0}}$, $\bar{n} = \dfrac{n}{N_{c0}}$, and $\bar{n}_p = \dfrac{n_p}{N_{V0}}$; and N_{c0} and N_{V0} are the densities of states in the main conduction and valence bands.

The relative values $\bar{\zeta}_c$ and $\bar{\zeta}_V$ are determined by the ratios

$$\bar{\zeta}_c = \frac{\zeta_c}{N_{c0}} = \sum_{i=1}^{k} \lambda_i (\gamma_{i0})^{\frac{3}{2}} \exp\left(-\frac{\varepsilon_{ci}}{kT}\right),$$

$$\bar{\zeta}_V = \frac{\zeta_V}{N_{V0}} = \sum_{j=1}^{l} \kappa_j (\gamma_{j0})^{\frac{3}{2}} \exp\left(\frac{\varepsilon_{Vi}}{kT}\right).$$

Here, the ratios of the effective masses of the electron conduction and valence bands to the corresponding effective masses of the main bands are introduced:

$\gamma_{i0} = \dfrac{m_{ci}}{m_{c0}}$ and $\gamma_{j0} = \dfrac{m_{Vj}}{m_{V0}}$. The energies ε_{ci} and ε_{Vj} are determined by the differences $\varepsilon_{ci} = \varepsilon_i - \varepsilon_c$ and $\varepsilon_{Vj} = \varepsilon_j - \varepsilon_V$.

The concentrations of opposite charge carriers are calculated by the formulae

$$\bar{n} = \frac{1}{2}\left[\sqrt{\bar{n}_s^2 + 4\gamma_{Vc}^{\frac{3}{2}}\bar{\alpha}} + n_s\right],$$

$$\bar{n}_p = \frac{1}{2\gamma_{Vc}^{\frac{3}{2}}}\left[\sqrt{\bar{n}_s^2 + 4\gamma_{Vc}^{\frac{3}{2}}\bar{\alpha}} - \bar{n}_s\right].$$

Here, the ratio of the effective masses of the main valence and conduction bands is $\gamma_{Vc} = \dfrac{m_V}{m_c}$, and the relative factor of reciprocity of the bands is determined by the ratio $\bar{\alpha} = \bar{\zeta}_c\bar{\zeta}_V$.

Calculation of the kinetic characteristics of the semimetal substance is made by the pattern of existence of two types of charge carriers—electrons and holes. The carrier mobilities are determined by the general form formulae $u_{n,p} = \dfrac{q}{m_{n,p}}\langle\tau\rangle$, where q is the absolute value of the carrier charge, and $m_{n,p}$ are the effective masses of the electrons and holes irrespective of the structure of the substance bands. The relaxation time τ is equal for both subsystems of the charge carriers irrespective of their belonging to the substance bands.

In the presented interpretation of the two-component system of charge carriers—electrons and holes—the times of their relaxation are equal in the sense that they present the time of stabilization of the equilibrium current mode in the medium. In this aspect, the analytical description of the substance's kinetic characteris-

Table 1. Identifier of curves by the parameter ε_s determining the energy level of the concentration of collectivized quasiparticles (electrons)

Curve number	1	2	3	4	5	6	7	8	9
ε_s, meV	−20	−15	−10	−5	0	5	10	15	20

Table 2. Identifier of curves by temperature

Curve number	1	2	3	4	5	6	7	8	9	10
T, K	30	45	60	75	90	105	120	135	150	165
Curve number	11	12	13	14	15	16	17	18	19	20
T, K	180	195	210	225	240	255	270	285	300	315

tics is simplified by introduction of the inertia ratio

$$\frac{u_n}{u_p} = \frac{m_p}{m_n} = \gamma_{pn}.$$

As a result of simple transformations, the kinetic coefficients of the electric conductivity $\sigma(\varepsilon_s, T)$, Hall $R(\varepsilon_s T)$, and the thermopower $\alpha_T(\varepsilon_s, T)$ are expressed through the carrier concentrations by the formulae

$$\sigma(\varepsilon_s, T) = qu_n(n + \gamma_{np}n_p), \quad R(\varepsilon_s, T) = \frac{\gamma_{np}^2 n_p - n}{q(n + \gamma_{np}n_p)^2},$$

$$\alpha_T(\varepsilon_s, T)$$

$$= \frac{k\left[A(n - \gamma_{np}n_p) + \gamma_{np}n_p \ln\dfrac{n_p}{N_p} - n\ln\dfrac{n}{N_c}\right]}{q(n + \gamma_{np}n_p)}.$$

After transition to relative concentrations of the charge carriers $\bar{n}$ and $\bar{n}_p$, as well as after revealing the temperature dependence of the mobility and density of states, these formulae take a form convenient for numerical calculations

$$\frac{\sigma(\varepsilon_s, T)}{\sigma_0} = \left(\frac{T}{293}\right)^3(\bar{n} + \sqrt{\gamma_{pn}}\bar{n}_p), \quad \frac{R(\varepsilon_s, T)}{R_0} = \frac{\sqrt{\gamma_{pn}}\bar{n}_p - \bar{n}}{\left(\dfrac{T}{293}\right)^{\frac{3}{2}}(\bar{n} + \sqrt{\gamma_{pn}}\bar{n}_p)^2},$$

$$\frac{\alpha_T(\varepsilon_s, T)}{\alpha_{T0}} = \frac{A(\bar{n} + \sqrt{\gamma_{pn}}\bar{n}_p) + \sqrt{\gamma_{pn}}\bar{n}_p \ln\bar{\zeta}_V - \bar{n}\ln\bar{\zeta}_c - \dfrac{\varepsilon_F}{kT}(\bar{n} + \sqrt{\gamma_{pn}}\bar{n}_p)}{\bar{n} + \sqrt{\gamma_{pn}}\bar{n}_p},$$

where σ_0, R_0, and α_{T0} are the coefficients of the electric conductivity σ, Hall R, and the thermopower α_T determined at room temperature $T_0 = 293$ K:

$$\sigma_0 = qu_n(T = 293)N_c(T = 293),$$

$$R_0 = q^{-1}N_c^{-1}(T = 293), \quad \alpha_{T0} = q^{-1}k.$$

As a result of computer calculation, the dependences on the temperature and energy of the level of occupation by collectivized electrons are obtained.

COMPUTER CALCULATION

Computer calculation of the substance kinetic characteristics is made for an improvised semimetal with $\Delta = 15.3$ meV and $\varepsilon_G = 25$ meV. The interband ratios of the effective masses in the given calculation are assumed to be constant: $\gamma_{Vc} = 3.33$, $\gamma_{pV} = 1/11$, and $\gamma_{pc} = $ 0.33. Let us note that, for calculation according to the concrete three-band pattern, γ_{Vc}, γ_{pV}, and γ_{pc} are complex temperature functions, since they depend on Fermi level shifts in ranges of nonparabolicity of the band dispersion laws. The numbers λ_1 and κ_1 are equal to one, and $\kappa_2 = 6$ is equal to six extreme points in the Brillouin zone, respectively.

The results of the calculations are shown graphically as dependences on the temperature T and concentration of collectivized electrons through the energy parameter of the distribution ε_s. For identification of the family of curves by the temperature T at various ε_s and the family of curves by the parameter ε_s at various temperature values, the curve numbers are in accordance with parameter values from Tables 1 and 2.

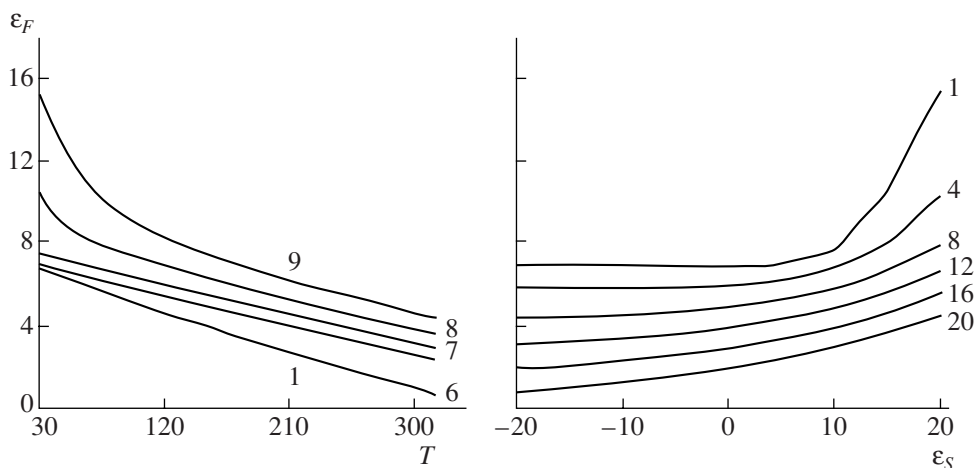Let us note that the requirement of agreement with the experiment cannot be complete, because the calcu-

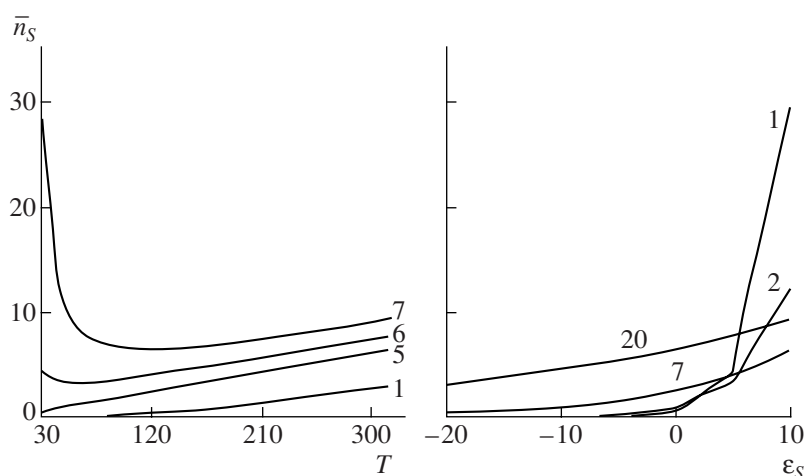**Fig. 3.** Fermi energy expressed in millielectronvolts.

Fig. 4. Concentration of the collectivized electrons in N_{co} units.

lation is made only in the energy range of parabolicity of the band dispersion laws. Thus, neglect of the temperature dependence of the charge carrier effective masses is assumed.

The behavior of the relative characteristics of the substance (semimetal) is shown by 16 graphs. They are arranged into pairs by the temperature T and the parameter ε_s. Each graph contains only the curves selected from complete families of 9 and 20 graphs.

At the given stage of presentation of the results, we will withhold comments explaining the behavior peculiarities and the physical factors of their appearing.

ELECTRIC CONDUCTIVITY OF ELECTROLYTE SOLUTIONS

The electric conductivity of liquids is determined by the possibility of motion of charge carriers under the action of an electric field E determining the current through the electrolyte solution. Free motion of charged particles in solutions is impeded by the polarization friction appearing due to Coulomb interaction of current carriers. Equations of motions of opposite charge carries of equal valence are presented by system of equations (1) in work [10]. These equations, being presented in relative kinetic variables (of the velocity $v = v_+ + v_-$ and the pulse $P = m_- v_- - m_+ v_+$), have the form of reduced equations:

$$\begin{cases} m\dfrac{dv}{dt} = qE - \bar{\mu}v, \\ \dfrac{dP}{dt} = v(\mu_+ - \mu_-), \end{cases}$$

where μ_+ and μ_- are the coefficients of the polarization friction for anions and cations, respectively; and q is the absolute value of the charge of the opposite current carriers. The given values depend on the masses of the car-

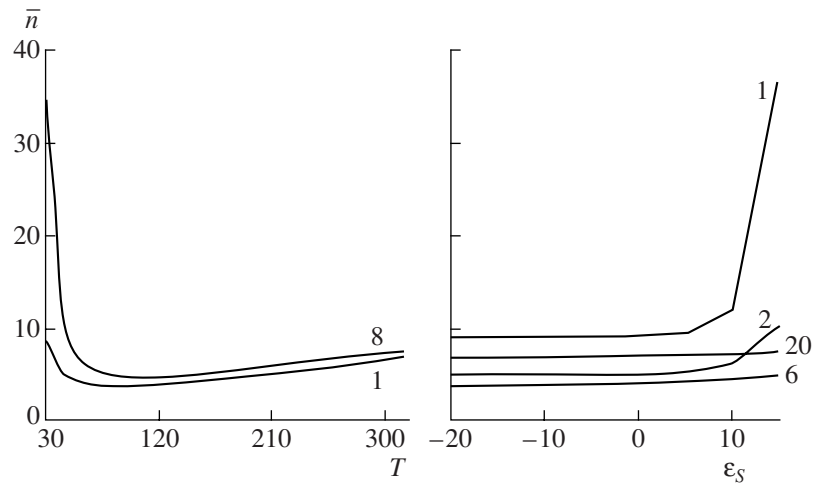**Fig. 5.** Concentration of the conduction electrons in N_{co} units.
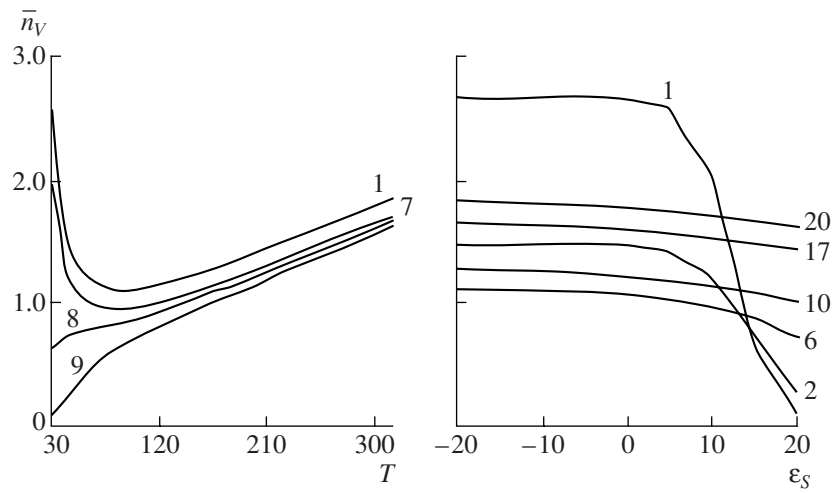

Fig. 6. Concentration of the main valence band holes in N_{vo} units.

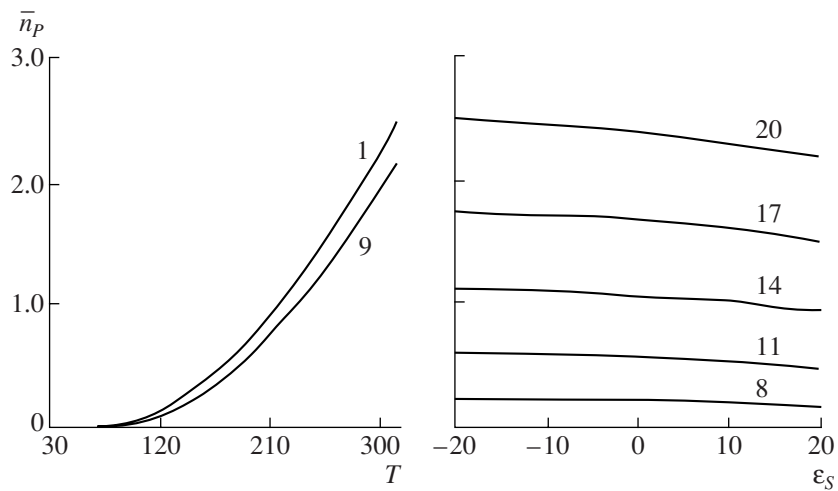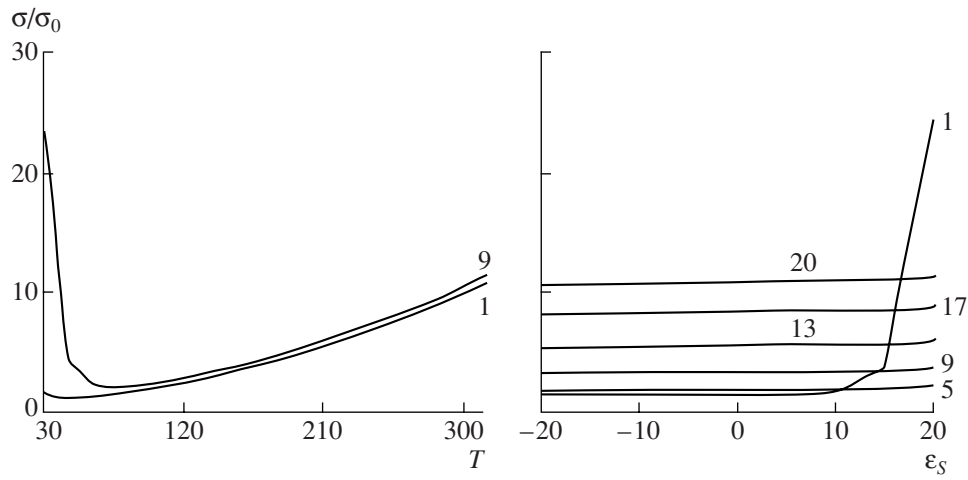**Fig. 7.** Concentration of the second valence band holes in N_{vo} units.
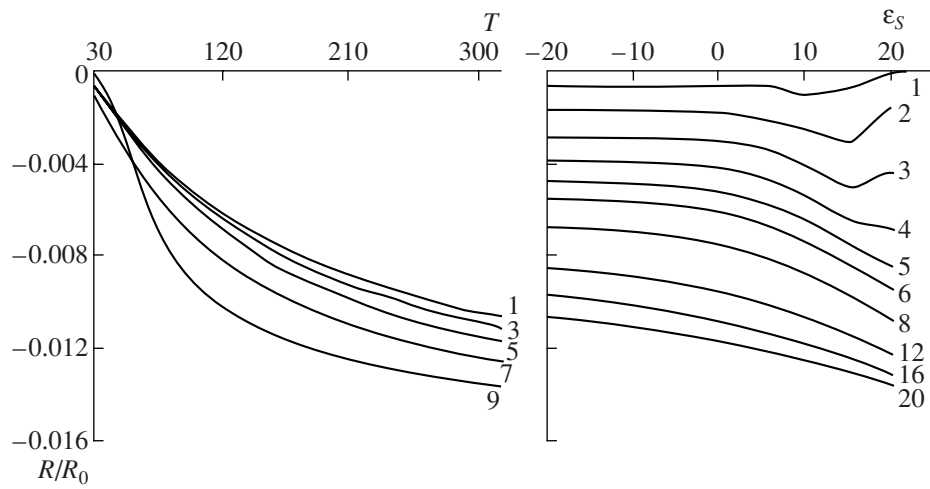
Fig. 8. Electric conductivity in σ_0 units.
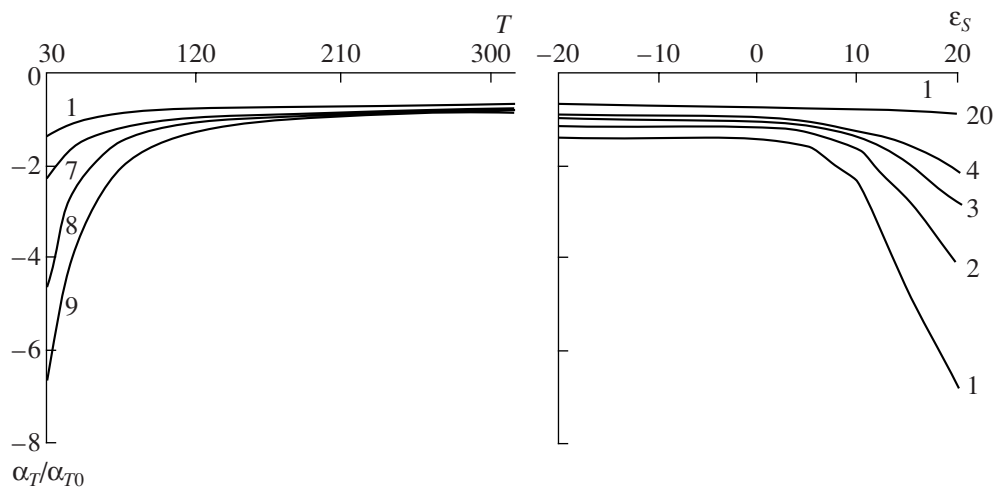

Fig. 9. Hall coefficient in R_0 units.

Fig. 10. Thermopower coefficient ($A = 1$) in α_{T0} units.

Table 3. Values of the charge transference numbers

Electrolyte	AgNO$_3$	NaCl	KCl	HCl
Cation transference number	$\vartheta_{Ag^+} = 0.31$	$\vartheta_{Na^+} = 0.25$	$\vartheta_{K^+} = 0.16$	$\vartheta_{H^+} = 1$
Anion transference number	$\vartheta_{NO_3^-} = -0.18$	$\vartheta_{Cl^-} = -0.38$	$\vartheta_{Cl^-} = -0.14$	$\vartheta_{Cl^-} = -35$
Electrolyte	KBr	KI	KNO$_3$	LiCl
Cation transference number	$\vartheta_{K^+} = 0.14$	$\vartheta_{K^+} = 0.13$	$\vartheta_{K^+} = 0.14$	$\vartheta_{Li^+} = 0.25$
Anion transference number	$\vartheta_{Br^-} = -0.28$	$\vartheta_{I^-} = -0.43$	$\vartheta_{NO_3^-} = 0.22$	$\vartheta_{Cl^-} = -1.26$
Electrolyte	NH$_4$Cl	KOH	LiOH	NaOH
Cation transference number	$\vartheta_{NH_4^+} = 0.08$	$\vartheta_{K^+} = 0.1$	$\vartheta_{Li^+} = 0.31$	$\vartheta_{Na^+} = 0.24$
Anion transference number	$\vartheta_{Cl^-} = -0.16$	$\vartheta_{OH^-} = -0.04$	$\vartheta_{OH^-} = -0.76$	$\vartheta_{OH^-} = -0.18$

riers as follows: the mass $m = \dfrac{m_+ m_-}{m_+ + m_-}$, the friction coefficient $\bar{\mu} = \dfrac{m_+ \mu_- + m_- \mu_+}{m_+ + m_-}$.

According to the theory of Debye–Huckel, the space charge density near certain ions is determined by the distribution function with a certain radius of screening depending on the solution temperature [11]. In other words, in the external field, the charge carriers will obey free motion only with predefinite effective charges, their values being imposed by the charge environment density. Therefore, effectives charges are attributed to free motion of the current carrier particles in the external field E:

$$q_+ = q - \mu_+ u, \quad q_- = q - \mu_- u,$$

where $u = v/E$ is the relative mobility common for both charge types. Hence, new quasiparticles, charge carriers with the charge numbers $\vartheta_+ = q_+/q$ and $\vartheta_- = q_-/q$, are in free motion in the field E freed from friction with the medium.

Stabilization of the current mode occurs for the time $\tau = m/\bar{\mu}$, the mobility being equal to the ratio $\dfrac{q}{\bar{\mu}}$. Thus, the charge numbers determining the charge transfer in the electrolyte are equal to

$$\vartheta_+ = 1 - \frac{\mu_+}{\bar{\mu}}, \quad \vartheta_- = 1 - \frac{\mu_-}{\bar{m}}.$$

In this aspect, the electric conductivity of the electrolyte solution is determined by the generalized formula $\sigma = (q_+ + q_-)nu = (\vartheta_+ + \vartheta_-)\dfrac{nq^2}{\bar{\mu}}$, where n is the electrolyte concentration. The charge transference numbers and electric conductivity of the electrolyte solution may be presented in the form

$$\vartheta_+ = \frac{m_+(\mu_- - \mu_+)}{m_- \mu_+ + m_+ \mu_-},$$

$$\vartheta_- = -\frac{m_-(\mu_- - \mu_+)}{m_- \mu_+ + m_+ \mu_-},$$

$$\sigma = \frac{nq^2(m_+^2 - m_-^2)(\mu_- - \mu_+)}{m_- \mu_+ + m_+ \mu_-}.$$

This presentation of the kinetic characteristics of the electrolyte solution is incomplete; it should be added to by a factor of the force action of the electric field on the medium: $F = \dfrac{dP}{dt} = v(\mu_+ - \mu_-)$, which in the stabilized current mode takes the form $F = \dfrac{qE(\mu_+ - \mu_-)}{\bar{\mu}}$. Let us note that, in the adopted model between the current density $j = \sigma E$ and the force action on the electrolyte, there is the ratio $\dfrac{j}{F} = nq\dfrac{m_- - m_+}{m_+ + m_-}$. Let us note that the disappearance of the force action is possible only under the condition $\mu_+ = \mu_-$, immediately leading to the current disappearance. Thus, the current passing is inevitably interrelated with the electric field force action on the electrolyte. This indicates a destructive action in biological media—electroplasmolysis of raw materials, which is mentioned in [10]. Let us also note that, at realization of the conditions $m_+ \neq m_-$ and $\mu_+ \neq \mu_-$, being almost absolute for the majority of electrolytes, the charge transfer may take place in the stabilized current mode. This means that the current in electrolytes will flow until the processes of dissociation and recombination of carriers in the solution stop. In general, observation of the current saturation condition is not always possible.

Stabilization of the current mode in the electrolytic medium occurs for the time τ.

Current carriers cover the distance between the electrodes d for the time $\tau_d = \dfrac{d}{\nu} = \dfrac{\bar{\mu}d}{qE}$. Thus, stabilization of the current mode is possible under the condition that $\tau < \tau_d$ or at moderate fields $E < \dfrac{\bar{\mu}^2 d}{mq}$.

Besides, a purely physical consideration of the current stabilization in electrolytes is reasonable for limited intervals of the electrolyte solution concentration determined by a balanced level of dissociation–recombination of current carriers in the solution. In other words, the electric conductivity of solutions is the electrochemical medium characteristic rather than kinetic, including both at its analytical description.

Agreement of charge transference numbers by current carriers adopted in electrochemistry can link the dependence of the solution electric conductivity coefficient with chemical transformations under the action of the field of the electrolyte itself. The introduced charge transference numbers, proceeding from the physical description of the process, are analogous to the ones adopted in electrochemistry. Estimation of the transference numbers for various dilute solutions of electrolytes in water [12] is carried out according to the formulae of the two-component system of charge carriers. The friction coefficients are approximated by the Stokes formula [13]. Values of the charge transference numbers are given in Table 3.

Let us note that the transference numbers, in general, depend on the temperature and concentration of the electrolyte. The presented model does not cover revealing of the temperature and concentration dependences. Besides, the model is analytically developed only for univalent carriers in the case of pairwise interaction.

COMMENTS AND CONCLUSIONS

Metallic conductivity based on comprehensive covalent bonds, when, due to overlapping of atomic shells of electron density, a part of all the electrons participating in the crystalline bond is free, is fundamental for crystal conductors. In essence, this is a remarkable property of the covalent bond between atoms, when, in the region of electron shell overlapping, the bond electrons gain excess freedom. The part of free electrons (quasiparticles) is proportional to the relative volume of the region of overlapping of all the atoms participating in the covalent bond. Therefore, even the first group metals have different coefficients of electric conductivity.

The dispersion law for a free quasiparticle is always parabolic, though with an overdetermined mass. One can surely state that substances with electron conductivity in their structure are based on covalent bonds. In metals, the comprehensive covalent bond, termed metallic, is based on overlapping of atomic clouds of electron density with a great number of nearest neighbors of the overlapping. As a result of this bond realization, the bond electrons gain excess freedom. In the best conductors, these electrons constitute deciles of electrons per lattice atom. This characteristic of the quasiparticle freedom is determined by the effective mass.

In semiconductors and semimetals, the metallic bond electrons, realizing the bond between integral crystal structure units (cells), are differentiated from electrons of internal bonds. The covalent bonds inside the unit cells are more rigid, and they determine the prevailing stability of the cell structure. Electrons of these bonds gain their freedom only in the exchange processes inside the cells, since drift from the bond leaves a vacancy for changing the cell's electron density. Thus, the same electrons of the covalent bonds take part in the semiconductor intrinsic conductivity.

According to the adopted ideology, the presence of physical overlapping of atomic clouds of electron density means that the substance is characterized by electron conductivity. It is natural that less dense structures, for which overlapping of atomic clouds of electron density is not typical, are not characterized by electron conductivity. For example, ionic or molecular crystals may possess significant electron conductivity only under pressure sufficient for overlapping of electron shells.

Let us note that the band structure of covalent crystals is an approximate pattern of the cell kinetics of electrons. Model errors of the band pattern may prevail over errors of the model calculation. Therefore, calculations with the parabolic dispersion law in bands are justified by the experimental accounting of the effective masses of quasiparticles.

A large class of ionic conductors does not exclude the presence of electric conductivity in them, though its part in the total conductivity is, apparently, insignificant.

Since this is the last work of our colleague, we consider it appropriate to accompany it with commemorative information.

Nikolai Ivanovich Botoshan was born on August 6, 1941, in the village of Drepkautsy in the Brichany district of the Republic of Moldova. He finished middle school in his home village, and, in 1959, he became a student of the Physical Faculty of Chisinau State University. As one of the best graduates, he was invited to work for the Chair of Theoretical Physics headed by Prof. Yu.E. Perlin (later on a corresponding member of the Academy of Sciences of Moldova).

Since 1978, he worked in the Institute of Applied Physics. In 1980, he successfully defended his dissertation on superconductivity under the scientific supervision of Academician V.A. Moskalenko. In 1985, he began to work in the Laboratory of Electrical Treatment of Plant-Growing Products.

Beyond all doubt, Nikolai Ivanovich was a talented physicist. His scientific interests covered a very wide range of investigations—from elementary particles to problems of earthquakes and astronomy. He was characterized by indefatigable industry; he possessed unique intuition and could explain various phenomena and regularities. Enthusiastically and selflessly he worked with both students and scientific researchers; moreover, he always tried to come to the aid of those who needed it. Our colleague could scarcely be exaggerated as a wonderful collocutor: he was skilled in talk on any problem.

Nikolai Ivanovich died early in the morning on December 11, 2006, when he was going up the stairs of the Institute of Applied Physics to the laboratory that he heartily headed for the sake of revival of its former glory and advancement of electroplasmolysis technologies.

We especially miss Nikolai Ivanovich in the laboratory's research. This is a real confirmation of the fact that, leaving us, our colleagues take parts of our souls with them. It is sad to understand how desperate everlasting irrevocable losses are. At the same time, we calm ourselves imagining that Nikolai Ivanovich is merely not in today.

REFERENCES

1. Suris, P.A. and Frenkel', V.Ya., Investigations of Ya.I. Frenkel' on Theory of Electric Conductivity of Metals, *UFN*, 1994, vol. 164 (4), pp. 379–396.

2. Bush, G., Electron Conductivity of Nonmetals, *UFN*, 1952, vol. 47 (2), pp. 258–317.

3. Gurzhi, R.N. and Kopeliovich, A.I., Low Temperature Electric Conductivity of Pure Metals, *UFN*, 1981, vol. 133 (1), pp. 33–74.

4. Gudden, B., Electric Conductivity of Electron Semiconductors, *UFN*, 1935, vol. 15 (6), pp. 703–738.

5. Poling, L., *Priroda khimicheskoi svyazi* (Nature of Chemical Bond), Moscow, Leningrad, 1947.

6. Mott, N. and Devis, E., *Elektronnye protsessy v nekristallicheskikh veshchestvakh* (Electron Processes in Noncrystalline Substances), Moscow: Mir, 1982, vols. 1 and 2.

7. Blatt, Frank J., *Teoriya podvizhnosti elektronov v tverdykh telakh* (Theory of Electron Mobility in Solids), Moscow, Leningrad: Fizmatgiz, 1963.

8. *Fizika tverdogo tela. Spetspraktikum* (Solid State Physics. Special Practical Course), Strukov, B.A., Ed., Moscow: Izd. Mosk. Univ., 1983.

9. *Polumetally i uzkozonnye poluprovodniki: Sbornik statei* (Semimetals and Narrow Band Semiconductors. Coll. Papers), Chisinau: Shtiintsa, 1979, p. 219.

10. Botoshan, N.I., Bologa, M.K., Berzoi, S.E., and Tsyrdya, I.D., Appearance of Electrohydrodynamic Impact on Boundaries of Inhomogeneities in Heterogeneous Media at Current Passing, *Elektron. Obrab. Mater.*, 2002, no. 1 (213), pp. 52–56.

11. Antropov, L.I., *Teoreticheskaya elektrokhimiya* (Theoretical Electrochemistry), Moscow: Vysshaya Shkola, 1965.

12. *Kratkii spravochnik fiziko-khimicheskikh velichin* (Brief Handbook of Physicochemical Quantities), Leningrad: Khimiya, 1983.

13. *Tablitsy fizicheskikh velichin. Spravochnik* (Tables of Physical Quantities. Handbook), Kikoin, I.K., Ed., Moscow: Atomizdat, 1976.

ELECTRICAL PROCESSES
IN ENGINEERING AND CHEMISTRY

The Role of Cyclic Electric-Thermal Polarization in Formation of Piezoelectric and Electrophysical Properties of Compositions Based on Polyvinylidene Fluoride and PKR3M Piezoceramics

M. A. Ramazanov and Z. E. Mustafaev

Baku State University, ul. Z. Khalilova 23, Baku, AZ-1148 Republic of Azerbaijan

Received June 27, 2007

Abstract—The role of boundary polarization processes in the formation of piezoelectric and electrophysical properties of a composition based on polyvinylidene fluoride and PKR3M piezoceramics is investigated. It is revealed that changes of the strength characteristics of the composition is connected with changes of the physical structure of the boundary layer and interface interactions. An increase in the interface interaction and orderliness of the polymer structure within the interface region is shown, which results in enhancement of the piezoelectric and electrophysical properties of the composition after the cyclic electric-thermal polarization.

INTRODUCTION

A keen interest in composite materials on the basis of polymers and piezoceramics has been observed recently. The application of such materials progressively transfers from the purely theoretic to practical area. The high piezoelectric sensitivity g_{lj}, elasticity, low dielectric capacity ε, and loss tangent $\tan\delta$ are positive characteristics of composites as compared with piezoceramics [1–3, 5, 6]. Polymer-piezoceramic compositions have high piezoelectric and electrophysical properties and are widely applied in various converters, medical apparatuses, and acoustic antennae.

It is well known that polymer-piezoceramic compositions acquire piezoelectric properties after the electric-thermal polarization (ETP). During the ETP process, charges are built up on the interface boundaries of the composition constituents. However, this, above all, causes a change of the phase interaction between the composite constituents, which influences the piezoelectric and electrophysical properties of the composition. That is why a scrupulous analysis of the influence of the interface interactions on the piezoelectric and electrophysical properties is required after cyclic ETP.

EXPERIMENTS

The paper presents results of the investigation of cyclic ETP influence on the piezoelectric and electrophysical properties of a composite based on polar polymer polyvinylidene fluoride (PVDF) and circonate-titanate-plumbum piezoceramics [4] with a rhombohedic structure of the PKR3M band. Piezoceramic particles of size $50 < d < 63$ µm and polymer powder were mechanically mixed in a ball mill. In this case, the volume content of the composition was PVDF + 20% PKR3M.

The compositions were obtained by the method of hot pressing at the polymer matrix mp under a pressure of 15 MPa for 10 min with subsequent cooling at a rate of 2000 K/min by dipping the melt into liquid nitrogen between two aluminum foils. All the specimens of the PVDF + PKR3M composition were made in the form of a film, and their piezoelectric and electrophysical properties were determined at a temperature of 293 K. The specimens were polarized by the ETP method. Each cycle included heating at a temperature of 393 K for an hour and cooling for half an hour between cycles under a constant electric field with a field strength of 3×10^6 V/m. The cycles were brought to five in number. The strength characteristics of the compositions under investigation were determined at a temperature of 293 K in compliance with [2]. The compositions' piezoelectric properties were measured in a static mode. Measurements of the dielectric capacity and loss tangent were conducted with the help of an E8-4 automatic bridge at a frequency of 1 kHz, and the volume resistivity of the specimens was measured by means of an E6-13A teraohmmeter. The charge state of the compositions was examined using the method of thermally stimulated depolarization (TSD) [7]. The value of the charge stored in the process of the composites polarization was calculated using the area under the TSD curve. Each point of the curve was checked five times, and the mean value of the results was obtained.
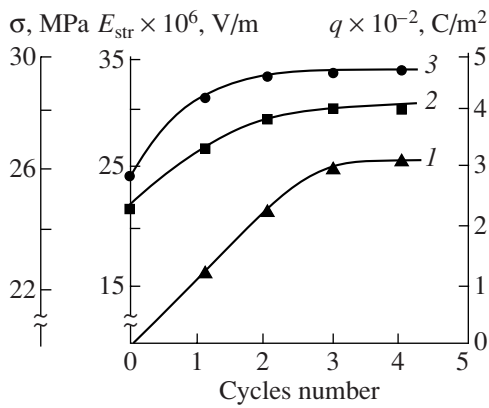
Fig. 1. Dependences of the (*1*) charge density *q*, (*2*) mechanical strength σ, and (*3*) electrical strength E_{str} on the number of ETP cycles for the PVDF + 20% PKR3M composition.

Fig. 2. TSD curves of the composition preliminarily exposed to cyclic ETP at a field strength of 3×10^6 V/m.

RESULTS AND DISCUSSION

Figure 1 shows the mechanical (σ) and electrical (E_{str}) strengths and also the charge density *q* as functions of the number of ETP cycles. As can be seen from Fig. 1, the cyclic ETP significantly influences the value of the stabilized charge and the strength characteristics of the composition.

Indeed, with an increase of the number of polarization cycles, the PVDF + PKR3M composition magnitudes σ, E_{str}, and *q* first grow (up to three cycles) but then tend to saturation. The charge density *q* has been calculated from the TSD curves given in Fig. 2. It is seen from the curves that the cyclic ETP influences not only the charge value determined using the area confined with the TSD curves but also changes the charge deposit spectrum, in connection with which an increase of the number of cycles of the treatment under heating and the effect of the electric field cause a rise of the temperature that corresponds to the TSD curve maximum with the spectrum areas remaining almost unchanged after the third cycle.

The experiments have shown that ETP strongly influences the composition's dielectric properties. The composition's magnitudes of the volume resistivity $\log \rho_v$, the dielectric capacitivity ε, and the loss tangent tag δ were measured under a constant electric field after some various cyclic ETPs.

The resistivity $\log \rho_v$, dielectric capacitivity ε, and loss tangent tag δ are plotted against the number of ETP cycles in Fig. 3. It is seen that ε and tag δ are decreasing with the number of cycles increasing, and, after the third cycle, they remain unchanged. Such character of their dependence is explained by changes of the physical structure of the polymer matrix in the near-boundary layer and of the interface interaction of the composition constituents. The growth of $\log \rho_v$ testifies to a decrease of the volume charges in the composition,
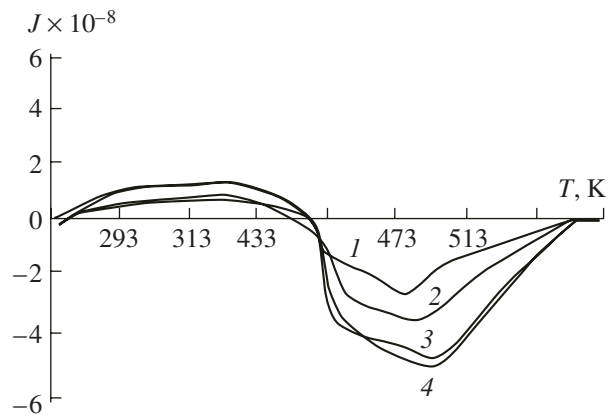
which brings an increase of the strength characteristics of the composite.

It can be assumed that the changes of the above physical characteristics after the cyclic ETP must be followed by changes of the piezoelectric modulus d_{33} and piezoelectric sensitivity g_{33} of the composition under investigation. Figure 4 presents the piezoelectric modulus d_{33}, piezoelectric sensitivity, and a basic parameter of the piezoelectric sensitivity in the reception mode $d_{33}g_{33}$ as functions of the number of ETP cycles.

It is clearly seen that the composite's piezoelectric modulus and piezoelectric sensitivity are notably improved after the ETP. This fact points out that the main role in forming the composite's piezoelectric properties is played by polarization processes that occur inside the piezoceramics' particles and on the polymer–piezoceramics boundary.
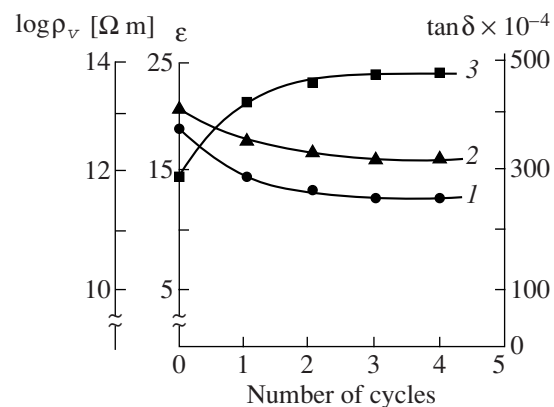
Fig. 3. Dependences of (*1*) the dielectric capacitivity ε, (*2*) loss tangent tag δ, and (*3*) volume resistivity $\log \rho_v$ on the number of ETP cycles.

$d_{33} \times g_{33}$, m²/N $g_{33} \times 10^2$, V m/N d_{33}, nC/N
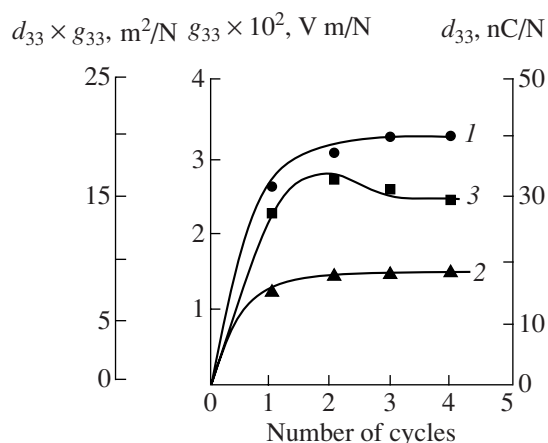
Fig. 4. Dependences of the (*1*) piezoelectric modulus d_{33} and (*2*) piezoelectric sensitivity g_{33} and (*3*) their product $d_{33}g_{33}$ on the number of ETP cycles.

During the ETP of the composite, there occur various polarization processes in it, the most important of which are the orientation polarization of domains in particles of the piezoelectric filler, the injection of charge carriers from electrodes into the composition and their stabilization in traps inside the polymer, and the polarization phenomena on the polymer–filler boundary. These processes cause an increase of the piezoelectric modulus and piezoelectric sensitivity of the composition.

The specimens of polymer piezoelectric composites were investigated before and after the ETP with the use of a scanning electronic microscope (series JSM-6480, JEOL company, Japan) under vacuum at room temperature. The multiangle scanning electronic microscope (JSM-6480) allows one to examine specimens without any preliminary ETP and without spraying a conducting layer and to obtain images of size up to 3 nm.

It is clearly seen from Fig. 5 that, after the cyclic ETP (Fig. 5b), the ordering of the composition structure occurs.

CONCLUSIONS

Analyses of the experimental results testify that the interface interaction of the composite's constituents after the cyclic ETP significantly influences their strength characteristics and electrophysical properties. The observed increase of the composition's magnitudes σ and E_{str} at different cycles after the ETP may be associated with the ordering of the physical structure of the interface boundary layer and the charge storage on the interface of the composition's constituents. The strong internal local electric field (with the strength determined by the formula $E_k = Q/\varepsilon\varepsilon_k$) is created in the composition owing to the charge storage, which, in its turn, reduces the strength of the external electric field, and,

(a)

(b)
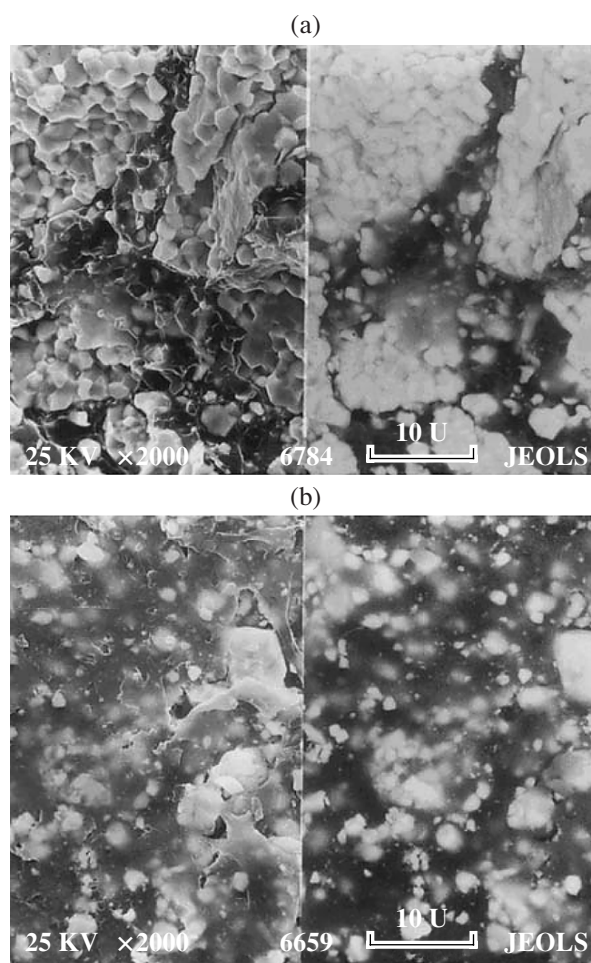
Fig. 5. Microphotos of the composition PVDF + 20% PKR3M before (a) and after (b) processing.

as a result, the breakdown occurs at the higher voltage. The shift of the TSD curves' maximums to the higher temperature region indicates that, after the cyclic ETP, the ordering of the physical structure occurs in the composition. After the preliminary ETP, the shift of the maximums in the TSD spectrum to the high temperature region is explained by the increasing concentration of the localization centers of the charges, which have orientation from the surfaces of the piezoelectric particles, into the depth of the polymer matrix. The decrease of ε testifies to the increase of the composite polarization. If ε becomes less, then the composition polarization becomes more. Furthermore, a decrease of tag δ implies an increase of the strength and interface interaction of the composition. An increase of $\log\rho_v$ predicts a decrease of the volume charges, which reduce the composition strength.

Notice that, during the ETP, most charges accumulate in the interface layer and this, in turn, increases the orientation of the domains; i.e., the polarization process is improved and the value of the maximal reorientation

of the ion polarization is $0.866P_S$. Owing to such polarizations, the piezoelectric modulus and piezoelectric sensitivity of the composition increase.

Thus, from the above experimental data, it follows that there is a correlation of the changes of the dielectric and piezoelectric properties and the strength characteristics of the polymer–piezoceramics compositions. A decrease of the values of the dielectric capacitivity and the loss tangent implies an increase in the resistivity, the electrical and mechanical strength, the piezoelectric modulus, and the piezoelectric sensitivity and charges stored in the ETP process. The observed changes of ε, $\tan\delta$, d_{33}, g_{33}, σ, and E_{str} depending on the number of ETP cycles are connected with the charge actions during the ETP when the interface interaction of the composition's constituents changes.

REFERENCES

1. Ramazanov, M.A., Abasov, S.A., Mustafaev, Z.E., *Vliyanie elektropolyarizatsii na prochnostnye svoistva kompozitsii na osnove polimer-p'ezoelektrik* (The Influence of Electric Polarization on Strength Characteristics of a Polymer-Piezoelectric Composition), *Novye tekhnologii–21-i vek*, 2001, no. 6, pp. 26–29.

2. Abasov, S.A., Ramazanov, M.A., Ibragimova, N.S., Mustafaev, Z.E., The Influence of Preliminary Treatment under the Effect of Electric Field on the Strength Properties of the Composition on the Base of Polyethylene and Piezoceramics, *Fiz. Khim. Obrab. Mater.*, 2003, no. 5, pp. 87–88.

3. Ramazanov, M.A., Ibragimova, Kh.S., Abasov, S.A., Gasanov, A.M., The Influence of Preliminary Electric Treatment on Charge State and Strength Properties of Polyethylene-Piezoceramicss Composition, *Elektron. Obrab. Mater.*, 2005, no. 4, pp. 57–61.

4. Fesenko, E.F., Dantsiger, A.Ya., Razumovskaya, O.N., *Novye p'ezokeramicheskie materialy* (New Piezoceramics Materials), Rostov-on-Don: Rost. Gos. Univ., 1983.

5. Furukawa, T., Fujino, K., Fukada, E., Electromechanical Properties in the Composites of Epoxy, Resin and PZT Ceramics, Jap. *J. Appl. Phys.*, 1976, vol. 15, pp. 2119–2129.

6. Chen, J.T., A Constitutive Equation for Composite Systems, *J. Polym. Sci.,-Poly. Phys.* Ed., 1983, 11, pp. 2013–2026.

7. Gorokhovatskii, Yu.A., *Osnovy termodepolyarizatsionnogo analiza* (Foundations of Thermal Depolarization Analysis), Moscow, 1983.

Statistical Modeling of Electrochemical Reactivation Conditions for Detecting Sensitization to IGC of Austenitic Stainless Steel Type 316L[1]

A. Kriaa[a], N. Hamdi[b], K. Jbali[b], H. Sidhom[c]

[a] Departement de Physique Chimie, Ecole Supérieure des Sciences et Techniques de Tunis, Tunisia
[b] Institut National de Recherche Scientifique de Borj-Cedria, Hammam lif BP 95-2050, Tunis, Tunisia
[c] Laboratoire de Mécanique et Matériaux de l'ESSTT, 5 Avenue Taha Hussein 1008, monfleury, Tunis, Tunisia

Received May 23, 2007

Abstract—The aim of this study was to determine the optimum conditions of the DL EPR test in order to evaluate the highest values of the degree of sensitization (DOS) of a forged austenitic stainless steel type 316L evaluated by the ratio I_r/I_a or Q_r/Q_a in %. The criteria of sensitization to the IGC corresponds to $I_r/I_a > 1\%$ and $Q_r/Q_a > 1\%$. A model using a full factorial design has been established, and the selected factors were the sweep rate (dE/dt), sulphuric acid concentration (H_2SO_4), ammonium thiocyanate concentration (NH_4SCN), and temperature in °C. A first order model is obtained by using a 2^4 full factorial design. An experimental test carried out using a 2^4 factorial design indicated that all the factors and their interactions have a positive effect on the response I_r/I_a. Furthermore, the highest value detected of I_r/I_a was found to be 65.6%. On the other hand, a microstructural study based on an optical microscope and a scanning transmission electron microscope (STEM) has been carried out for annealed and aged samples (550°C–80000 h). The profiles of the chromium, nickel, and molybdenum concentration established by X-ray microanalysis in STEM confirm a decrease of the content of these elements leading to the formation of Cr-depleted zones responsible for the sensitization to the IGC.

DOI: 10.3103/S1068375507060178

1. INTRODUCTION

The austenitic stainless steels are susceptible to intergranular corrosion (IGC) and intergranular stress corrosion craking (IGSCC). The basic cause of both these forms of corrosion is sensitization. Exposure to a temperature range of 500–800°C during welding or service leads to precipitation of chromium rich carbides at the grain boundaries and formation of chromium depletion regions adjacent to these carbides. In 1978, the potentiodynamic reactivation technique was developed into a quantitative, nondestructive test method for measuring sensitization in welded and weldable AISI 304 and 304L stainless steel (SS) piping for use in boiling water nuclear reactors [1, 2]. It has been found that sensitization made the piping subject to intergranular stress corrosion cracking in high temperature (289°C) water. This created the need for a nondestructive method of determining the sensitization at the grain boundaries.

Several investigations [2–21] have contributed to the development of the EPR (Electrokinetic Potentiodynamic Reactivation) method. Different versions of this technique exist today, and the most frequently used, due to its lower sensitivity at the surface state [13, 18, 19], is the double loop reactivation method (DL-EPR) [7, 10]. The high sensitivity of this technique has been proved on numerous grades of austenitic stainless

steels and nickel alloys. The most published experimental data of EPR tests relative to austenitic stainless steels are summarized in Table 1. One can notice that the composition of the electrolyte is usually constituted of sulfuric acid (H_2SO_4) added with a depassivator as KSCN [13–15], NH_4SCN [2, 17] or HCl [14] in the case of the modified EPR method. The scan rate range is between 0.5 and 2.5 mV/s [13–15], and the temperature of the test is often ambient [2, 13, 17, 23] or 30°C [13, 15, 20]. However, the high precision to detect mild degrees of sensitization, i.e., in the range from where no carbide precipitation occurs to the level where one or more grains are completely surrounded by "ditches" in the etch structure, requires (i) a specific study of the electrolyte composition, temperature, potential range, and sweep rate [2, 13–17] and (ii) the selectivity required to detect the sensitization (Table 1).

The double loop EPR test consists of an anodic sweep from the corrosion potential to the peak potential in the passive region followed by a reactivation scan from the peak potential back to the corrosion potential. The degree of sensitization is then determined from the ratio of the maximum current in the reactivation scan divided by the maximum current in the anodic scan, or I_r/I_a. The greater the ratio, the greater the degree of sensitization. In order for the EPR test to be selective, there must be significant increases in the I_r/I_a value corresponding to increases in the level of sensitization in the

---

[1] The text was submitted by the authors in English.

Table 1. Main published experimental data of EPR tests

Specimen designation	Temperature, °C	Electrolyte composition	Limit conditions of the potential, mV/S.C.E	Scan rates, mV/s	Criteria of sensitization to the IGC	References
304-304L	30	H_2SO_4 0.5M KSCN 0.01M	−400 to +300	1.67	–	[13]
316L	30	H_2SO_4 6N KSCN 0.005M	−600 to +200	1.67	$I_r/I_a \gg 0$	[15]
AISI 304	30	H_2SO_4 0.5M KSCN 0.01M	−400 to +300	1.67	$I_r/I_a > 0.005$ Metallographic	[18]
AISI 304L	30	H_2SO_4 0.5M KSCN 0.01M	−500 to +300	–	$I_r/I_p > 0.0182$	[20]
Z2NCDU 25–20.04M Super austenitic	25	H_2SO_4 33% 0.3% HCl	−30 to +560	0.5	$I_r/I_a > 1\%$	[14]
304LN et 316LN	25	H_2SO_4 0.5M NH_4SCN 0.01M	–	1.67	–	[13] [2]
304LN–316LN	25	H_2SO_4 0.5M NH_4SCN 0.01M	+200 to E_{corr}	1.66	$I_r \gg 0$ ou $Q_r \gg 0$ Metallographic	[17]
316L	25–40	H_2SO_4 0.1–4M NH_4SCN 0.01–0.1M	−400 to −300	0.5–5	$I_r/I_a >$ to 1% metallographic	this study

Note: I_a—activation peak current density; I_r—reactivation peak current density; Q_r—reactivation electric charge density; Q_a—activation electric charge density.

Table 2. Chemical composition of austenitic stainless steel type 316L used in this investigation in weight percent (%)

Material	C	S	P	Si	Mn	Ni	Cr	Mo	Ti	Nb	Cu	N
316L	0.022	0.015	0.020	0.35	1.74	13.4	17.3	2.13	<0.005	<0.005	0.04	0.035

material. Therefore, the electrolyte composition and parameters must be examined with utmost care to determine changes that would make the test more selective and thus make better the discriminating capacity of the test [22].

The electrochemical reactivation conditions for detecting sensitization to IGC of austenic stainless steels have not been widely studied in the literature. For this reason, we have conducted experiments to study the main parameters controlling the sensitivity of the EPR technique in order to detect mild intergranular precipitation inducing sensitization of forged austenitic stainless steel to IGC. A 2^n factorial experimental design was used to determine the optimum conditions, and a first-order model that related the degree of sensitization (DOS) to the process factors was obtained.

2. EXPERIMENTAL DESIGN

The experimental design is widely used for controlling the effects of parameters in many processes. Its usage decreases the number of experiments, time, and material resources. Furthermore, the analysis performed on the results is easily realized and experimental errors are minimized. Statistical methods measure the effects of changes in the operating variables and their mutual interactions on process through the experimental design method. Today, the mostly widely used experimental design to estimate the main effects, in addition to interaction effects, is the 2^n factorial design, when each variable is investigated at two levels. According to the 2^n factorial experimental design method, the principal steps of the experiments are designed: determination of the response variables, the choice of the factor levels, and the statistical analysis of the data. Consequently, the final step of the work is to obtain a statistical regression model [24].

3. EXPERIMENTAL METHOD

3.1. Materials and Heat Treatment

Austenitic stainless steel samples of type 316L were used during the course of this investigation, and its chemical composition is given in Table 2. All the specimens were solution heat-treated at 1100°C for 1 h in an argon protective atmosphere followed by water quenching. It was confirmed by microscopic examination that the alloys were in the fully solution annealed form.

The sensitization treatment was carried out at 550°C for 80000 h for the 316L stainless steels [25]. The sensitization heat treatment was selected so as to result in
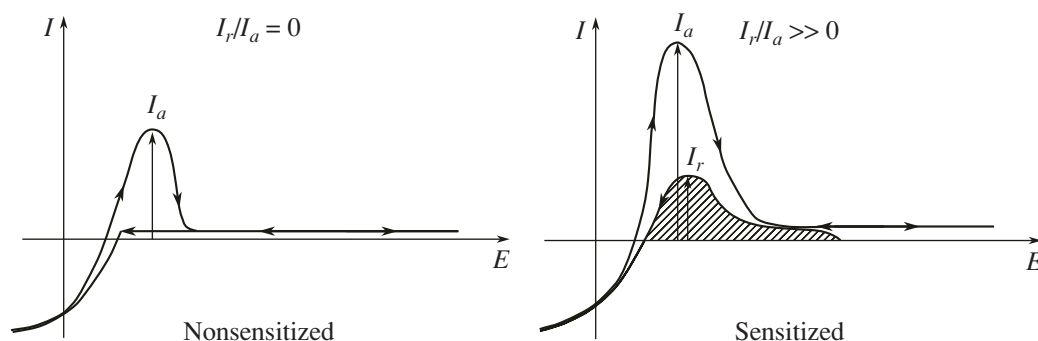
Fig. 1. Methods of the data analysis

full coverage of the grain boundaries by the chromium-depleted regions and, at the same time, not to allow for a very high DOS.

3.2. Microstructural Analysis

The microstructures of the as received and aged states have been examined using a metallographic microscope and a scanning transmission electron microscope (STEM), and the profiles of the chromium, molybdenum, and nickel concentration at the grain boundaries of the aged state 550°C–80000 h have been established by X-ray microanalysis on thin foils at 300 kV. The identification of intergranular carbides was done by electronic diffraction, and their contents in the metallic elements have also been determined by X-ray microanalysis [25].

3.3. Factorial Design and DL EPR Test

3.3.1. Design of the experiments. Factorial design is widely used in statistical planning of experiments to obtain empirical linear models relating process responses to process factors [26–29]. 2^n factorial design, where each variable runs at two levels, is often used to obtain first-order models. If the variance analysis indicates that the overall curvature is significant, auxiliary experiments are carried out to develop second-order models [30]. A full factorial design was selected to study the influence of different factors in order to establish the optimum conditions of the degree of sensitization (I_r/I_a or Q_r/Q_a in %). These factors are the scan rates (dE/dt, mV/s), the concentration of sulphuric acid ($[H_2SO_4]$, mol/l), the concentration of the

Table 3. Evaluation of the test criteria

Criteria of sensitization	Annealed state	Sensitized state
I_r/I_a (%)	<0.03	>1
Q_r/Q_a (%)	<0.05	>1

depassivator ($[NH_4SCN]$, mol/l), and the temperature of the electrolyte (°C).

3.3.2. DL-EPR test. The EPR test equipment consisted of a Tacussel-type PGT 24-1 potentiostat/galvanostat, a servovit generator, and a millivoltmeter. The platinum sheet and saturated calomel electrode (SCE) were used as counter and reference electrodes, respectively. The curves were plotted on an SE-790 x–y recorder. The series of DL-EPR tests were conducted as mentioned by some authors [4, 17, 22, 18]. After establishing of the E_{corr}, the specimen was polarized from the initial potential $E_{corr} = -450$ mV in the cathodic region to an anodic potential of +250 mV/SCE in the passivity region. As soon as this potential was reached, the scanning direction was reversed and the potential was decreased to the cathodic region (Fig. 1). The peak reactivation current (I_r) and the peak activation current (I_a) were measured during the backward and the forward scans, respectively. The degree of sensitization (DOS) is measured by determining the ratio of the maximum current generated by the reactivation scan to that of the anodic scan: (I_r/I_a%), or by the ratio of the electric charges (Q_r/Q_a%), where Q_r is the reactivation surface charge density and Q_a is the activation passivation surface charge density. The criteria of sensitization indicated in Table 3 are in agreement with Y. Cètres et al. [14].

For the DL-EPR test, a 30 μm SiC paper was usually used for the final polishing; a finer finish of 1 μm was used to enhance the quality of the photographs. The specimens of the section equal to 1 cm^2 aged under the above mentioned conditions were polished mechanically and mounted in an epoxy resin. The freshly polished specimen was immersed in the electrolyte for 120 s to determine the corrosion potential.

3.3.3. Microstructural examination. After each DL-EPR test, the microstructure was observed and the mode of attack was determined using an optical microscope. The extent of the attack is compared with the ratio I_r/I_a% value.
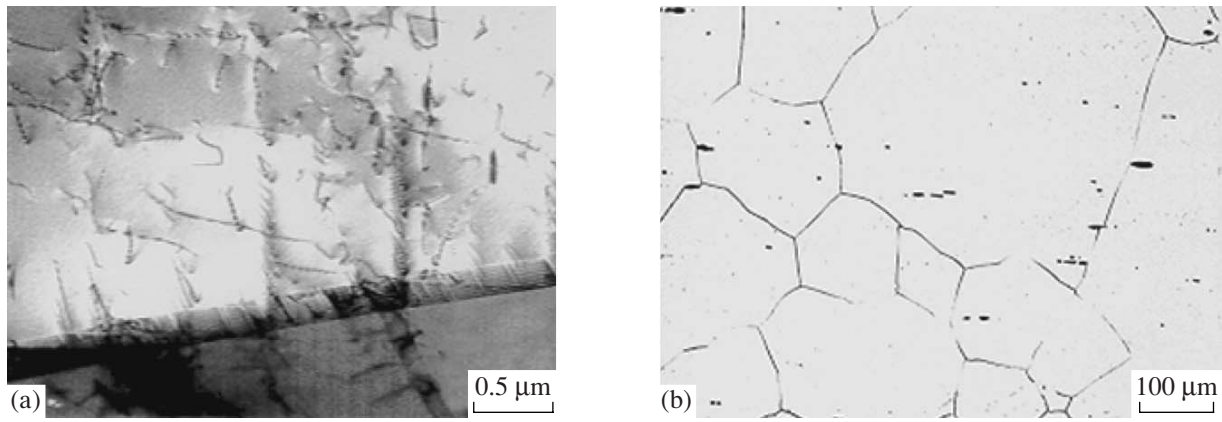
Fig. 2. Perfectly homogenized austenitic structures obtained after annealing. Structure of a sample on an optical microscope (a) and the structure on thin foil using STEM (b).
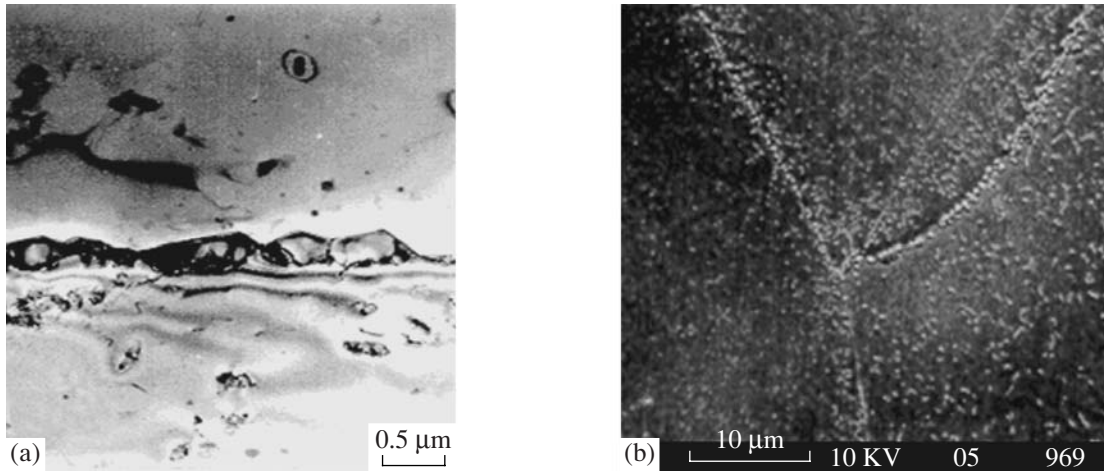
Fig. 3. Precipitations of M23C6 carbides after heat-treatment at 550°C for 80000 h. M23C6 carbide precipitations using MES (a); intergranular precipitation of M23C6 carbides using MET (b).

The Test selectivity is a qualitative evaluation of the sample attack with the optical microscope. It refers to grain boundary attack without causing other forms of corrosion during the DL-EPR test.

The test sensitivity is the absolute value of the test criterion, as indicated in Table 3.

4. RESULTS AND DISCUSSION

4.1. Microstructural Analysis

The microstructural examination of the annealed samples was performed by optical microscope and scanning transmission electron microscope (STEM). The results reveal an austenitic structure perfectly homogenized and without intergranular precipitation (Fig. 2).

On the other hand, the aged state at 550°C for 80000 h shows a discontinuous precipitation of $M_{23}C_6$ carbides at grain boundaries and abundant intragranular precipitation (Fig. 3). At this point, the chromium depletion consecutive with the intergranular precipitation shows denuded zones of intragranular carbides at grains boundaries (Fig. 3a).

The X-ray microanalysis on thin foils in STEM performed on $M_{23}C_6$ carbides permits one to determine the

Table 4. Concentration of metallic elements of the determined carbides M23C6 by X-ray microanalysis on thin foils using STEM

Weight %	Si	Cr	Mn	Fe	Ni	Mo
$M_{23}C_6$	0.3	68.7	1.8	14.1	3.3	11.8
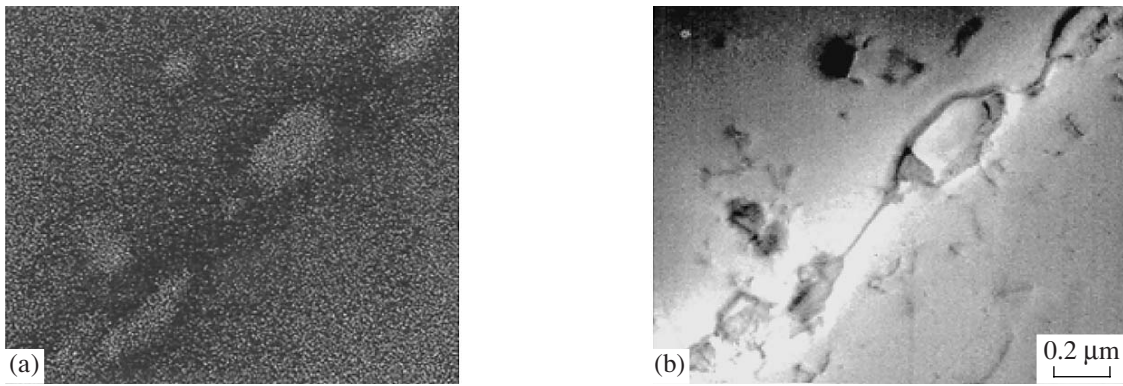
Fig. 4. Cr-depleted zones obtained after intergranular precipitation of M23C6 carbides (Aged state 550°C for 80000 h). Cr-depleted zones obtained after electrolytic polishing (a); qualitative distribution of the chromium in depleted zones (b).
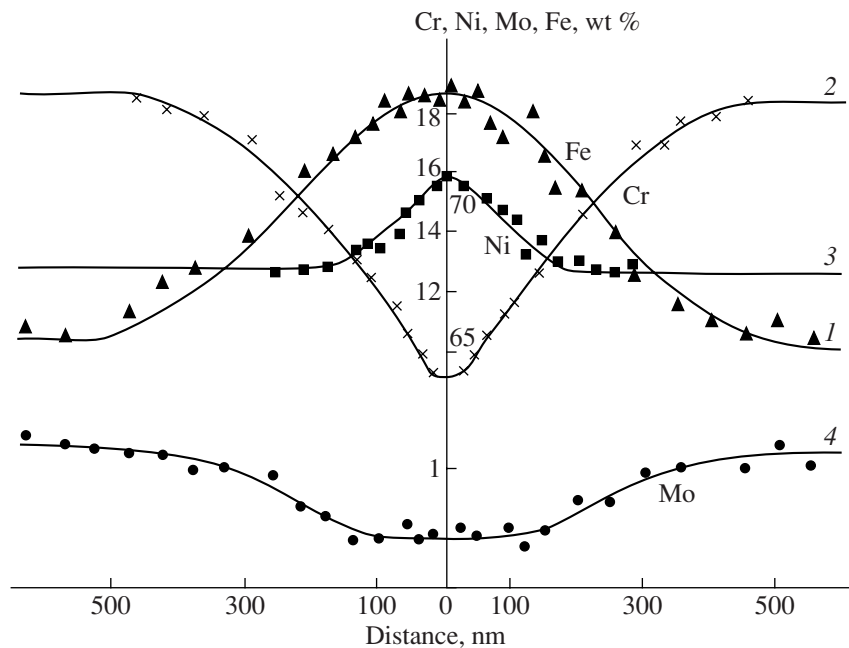
Fig. 5. Profiles of iron, chromium, and nickel and molybdenum concentrations associated with the Cr-depleted zone shown in Fig. 4 (aged state 550°C for 80000 h). Nominal content: *1*—[Fe] 65.2; *2*—[Cr] 18.6; *3*—[Ni] 12.7; *4*—[Mo] 1.2 wt %.

average concentration of metallic elements of these carbides without taking into account the carbon. Table 4 shows that these carbides, which are rich in chromium (68.7%), contain other significant metallic elements such as iron, nickel, and molybdenum.

The involvement of elements such as chromium and molybdenum in the intergranular carbides' composition appreciably decreases their content in the vicinity of the grain boundaries and contributes to the formation of Cr-depleted zones responsible for sensitization to IGC (Fig. 4). The profiles of the concentration associ-

ated with these zones confirm the depletion of elements of the M23C6 carbides' composition, which is compensated for by an increase of the Fe and Ni content (Fig. 5).

4.2. DL-EPR Test Results

It is well known that, during the EPR test, an oxide layer is electrochemically built up at the passivation potential. This layer protects the underlying matrix from corrosion during subsequent reactivation. Assum-
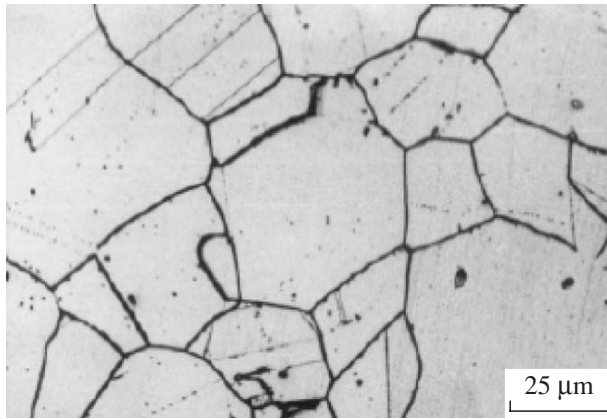
Fig. 6. Microstructure produced on a nonsensitized sample after DL-EPR testing in an electrolyte at 25°C (no intergranular attack is observed).

Fig. 7. Microstructure produced on a sensitized sample (550°C–80000 h) after DL-EPR testing at 25°C. The electrolyte was 4M H_2SO_4 + 0.01 M NH_4SCN, and the scan rate was 0.5 mV/s (severe grain boundary attack and general corrosion was produced on this sample).

ing a chromium depletion mechanism, the zones adjacent to the grain boundaries are deficient in free chromium once they become sensitized. At these sites, the passivation layer preferentially breaks down during reactivat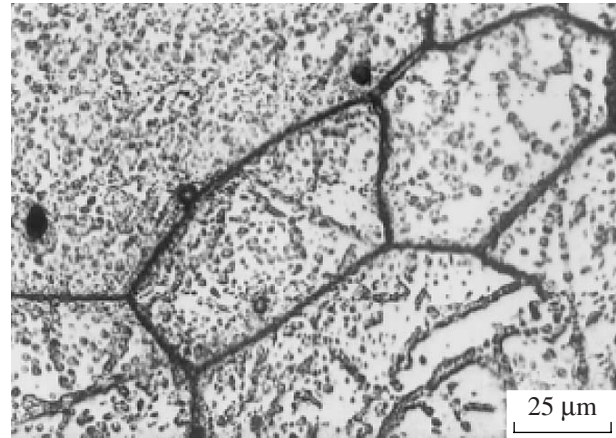ion, thus allowing active dissolution to occur. The inside of the grain, where no chromium depletion has occurred, remains unattacked [22, see references therein]. The quality of the oxide layer depends primarily on the passivation circumstances, on the one hand, and the local composition of the underlying matrix, on the other hand. The extent of the grain boundary attack depends on the reactivation circumstances and the local quality of the built up oxide layer [22].

The assessment of the sensitization to the IGC of austenitic stainless steel type 316L by DL EPR testing was investigated. The ratios I_r/I_a in % and the charge density Q_r/Q_a% determined for the annealed and aged samples at 550°C for 80000 h are reported in Table 5. Experimentally, for the reproducibility, all the tests were at least repeated twice in order to reduce the scatter of the test results. As is seen in Table 6, the annealed samples show low DOS in the DL-EPR testing (I_r/I_a% = 0). A laboratory solutionizing heat treatment [1100°C WQ (water quenching)] shows no IGC with DL EPR testing (Fig. 6). On the other hand, the aged

samples show different levels of sensitization depending on the parametric values of the DL-EPR test (Fig. 7).

The collected data were analyzed by a PC using the NEMRODW computer software package for the evaluation of the effect of each parameter on the optimization criteria. In order to determine the optimum conditions and derive a model for the criteria I_r/I_a, a full factorial of the 2^4 type was used. The sweep rate (X_1), sulphuric acid concentration (X_2), ammonium thiocyanate concentration (X_3), and temperature (X_4) were chosen as independent variables for the model. The factors level is shown in Table 6. The matrix for four variables is varied at two levels (+1 and –1). The higher level of the variable was designated as "+" and the lower level was designated as "–."

The 2^4 full factorial design was used to obtain a first-order model with interaction terms. As usual, the experiments were performed in random order to avoid systematic error. In addition, three central replicates were also added to the experimental design to calculate the pure experimental error. The results are given in Table 6. In order to confirm the predictability of the obtained model, two tests were performed on both sides of the

Table 5. Factor levels used in the full factorial design

Symbols of factors	Factors	High level (+)	Medium level (0)	Low level (–)	Increment
X1	Sweep rate, mV/s	5	2.25	0.5	2.75
X2	H_2SO_4 concentration, mol/l	4	2.05	0.1	1.95
X3	NH_4SCN concentration, mol/l	0.1	0.055	0.01	0.045
X4	Temperature, °C	40	32.5	25	17.5

Table 6. Experimental design matrix and response value

Exp. no.	X_1 dE/dt	X_2 [H_2SO_4]	X_3 [NH_3SCN]	X_4 Temperature	Annealed state I_r/I_a, %	Annealed state Q_r/Q_a, %	Aged state I_a, mA/cm²	Aged state I_r, mA/cm²	Aged state I_r/I_a, %	Aged state Q_r/Q_a, %
6	−1	−1	−1	−1	0	0	32.0	2.54	7.93	7.19
7	+1	−1	−1	−1	0	0	11.49	1.05	9.1	15
12	−1	+1	−1	−1	0	0	5.237	3.435	65.6	53.65
9	+1	+1	−1	−1	0	0	8.033	1.267	15.8	28.57
1	−1	−1	+1	−1	0	0	42.28	10.17	24.07	21.68
8	+1	−1	+1	−1	0	0	32.14	4.432	13.78	31.98
13	−1	+1	+1	−1	0	0	162.4	56.89	35.03	34.65
4	+1	+1	+1	−1	0	0	250.2	45.82	18.31	18.70
5	−1	−1	−1	+1	0	0	2.02	0.340	16.83	23.33
10	+1	−1	−1	+1	0	0	0.558	0.186	33.33	33.33
16	−1	+1	−1	+1	0.04	0	2.892	1.071	37.03	45.45
2	+1	+1	−1	+1	0	0	6.145	1.584	25.77	30
11	−1	−1	+1	+1	0	0	69.88	8.68	12.42	9.89
14	+1	−1	+1	+1	0	0	73.63	6.832	9.27	8.81
3	−1	+1	+1	+1	0.02	0	143.6	21.66	15.08	20.04
15	+1	+1	+1	+1	0	0	157.0	14.44	9.19	14.04
1*	0	0	0	0	0	0	16.73	3.67	21.93	17.85
2*	0	0	0	0	0	0	31.14	6.52	20.94	15.65
3*	0	0	0	0	0	0	21.61	4.82	22.30	18.75

* Central point replicates

Table 7. Tests carried out on both sides of the experimental central domain

Exp. no.	dE/dt	[H_2SO_4]	[NH_3SCN]	Temperature	Y_{exp}	Y_{cal}
1	1 mV/s	1 M	0.03 M	30°C	21.75	20.67
2	2.5 mV/s	3 M	0.06 M	40°C	19.84	20.06

Table 8. Optimal conditions of the sensitization to IGC by the DL EPR test

dE/dt, mV/s	[H_2SO_4], mol/l	[NH_4SCN], mol/l	Temperature, °C	EPR DL response Aged state I_r/I_a	Aged state Q_r/Q_a	Annealed state I_r/I_a	Annealed state Q_r/Q_a
0.5	4	0.01	25	65.6	53.65	0	0

central experimental domain (Table 7). A first order model with interaction terms was chosen to fit the experimental data:

$$\tilde{Y} = b_0 + b_1X_1 + b_2X_2 + b_3X_3 + b_4X_4 +$$
$$+ b_{12}X_1X_2 + b_{23}X_2X_3 + b_{14}X_1X_4 + b_{24}X_2X_4 +$$
$$+ b_{34}X_3X_4 + b_{123}X_1X_2X_3 + b_{124}X_1X_2X_4 +$$
$$+ b_{134}X_1X_3X_4 + b_{234}X_2X_3X_4 + b_{1234}X_1X_2X_3X_4,$$

where $\tilde{Y}$ is the degree of sensitization expressed by the ratio I_r/I_a%, b_0–b_{1234} are the interaction coefficients, and X1–X4 are dimensionless coded factors for the variables. The first order model obtained by variance analysis conducted at a 95% confidence interval is as follows:

$$\tilde{Y}_{Ir/Ia} = 21.784 - 4.965X_1 + 5.942X_2 - 4.640X_3 -$$

$$- 1.919X_4 - 5.494X_1X_2 - 3.684X_2X_3 + 4.490X_1X_4 -$$
$$- 4.04X_2X_4 - 3.735X_3X_4 + 4.348X_1X_2X_3 +$$
$$+ 1.681X_1X_2X_4 - 2.224X_1X_3X_4 +$$
$$+ 2.426X_2X_3X_4 - 1.220X_1X_2X_3X_4.$$

Table 8 gives the optimal conditions of the sensitization to IGC of austenitic stainless steel type 316L (annealed and aged states) by DL EPR testing. The results are shown in Table 9. The highest I_r/I_a value for AISI 316L steel (aged state 550°C–80000 h) was obtained at a 0.5 mV/s sweep rate, 4M H_2SO_4 concentration, 0.01 M NH_4SCN concentration, and a temperature of 25°C. In contrast, the lowest I_r/I_a value was obtained for AISI 316L steel (aged state 550°C–80000 h) at a 0.5 mV/s sweep rate, 0.1M H_2SO_4 concentration, 0.01 M NH_4SCN concentration, and temperature of 25°C.

To test the significance of the factor effects, an analysis of the variance was conducted at a 95% confidence interval. The significant main and interaction terms are shown in Fig. 8. From the statistical analysis described in Table 9, the sweep rate, sulfuric acid concentration, ammonium thiocyanate concentration, and temperature have positive effects on the DOS of austenic stainless steel of type 316L evaluated by the ratio I_r/I_a%. Also, the second order interaction effects given in Fig. 9 were an important factor in the DL-EPR tests. In fact, the
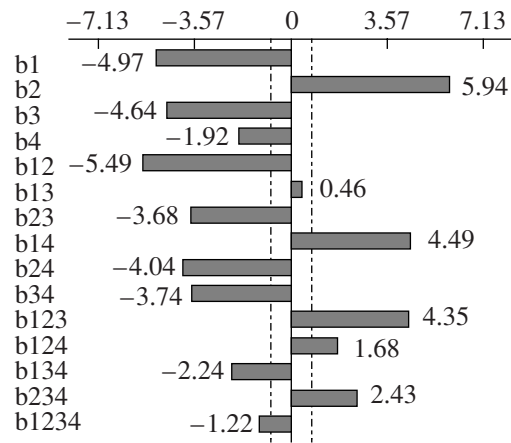

Fig. 8. Significant main, second order, and interaction terms on the DOS of AISI 316L steel using DL-EPR tests (aged state: 550°C–80 000 h).

interactions study reveals five significant second-order interactions (X_1X_2, X_1X_4, X_2X_3, X_2X_4, and X_3X_4). On the other side, in order to validate this model, our approach is as follows: (i) the analysis of the residuals ($\tilde{Y}_{exp} - \tilde{Y}_{cal}$) shown in Table 10 is consistent with the experimental and calculated values of I_r/I_a in %, and (ii) the analysis of the variance shown in Table 11 and also established at the 95% confidence interval substan-

Table 9. Effect of factors and their interactions

Factors and interactions	Coefficient	degree of freedom (d.o.f)	standard error	t^*_{exp}	Significance or Decision ($\alpha = 0.05$)
X_1	−4.97	2	0.175	28.4	effective
X_2	5.94	–	–	33.94	effective
X_3	−4.64	–	–	26.51	effective
X_4	−1.92	–	–	10.97	effective
X_1X_2	−5.49	–	–	31.37	effective
X_1X_3	0.46	–	–	2.63	ineffective
X_2X_3	−3.68	–	–	21.03	effective
X_1X_4	4.49	–	–	25.67	effective
X_2X_4	−4.04	–	–	23.08	effective
X_3X_4	−3.74	–	–	21.37	effective
$X_1X_2X_3$	4.35	–	–	24.86	effective
$X_1X_2X_4$	1.68	–	–	9.6	effective
$X_1X_3X_4$	−2.24	–	–	12.8	effective
$X_2X_3X_4$	2.43	–	–	13.89	effective
$X_1X_2X_3X_4$	−1.22	–	–	6.97	effective

Note: $*t_{exp}$ is t—Student [28, 29], $t_2^{0.05} = 4.303$ (from a statistic table, where $\alpha = 0.05$ and d.o.f = 2. If $t_{exp} < t_2^{0.05}$, the factor is ineffective).
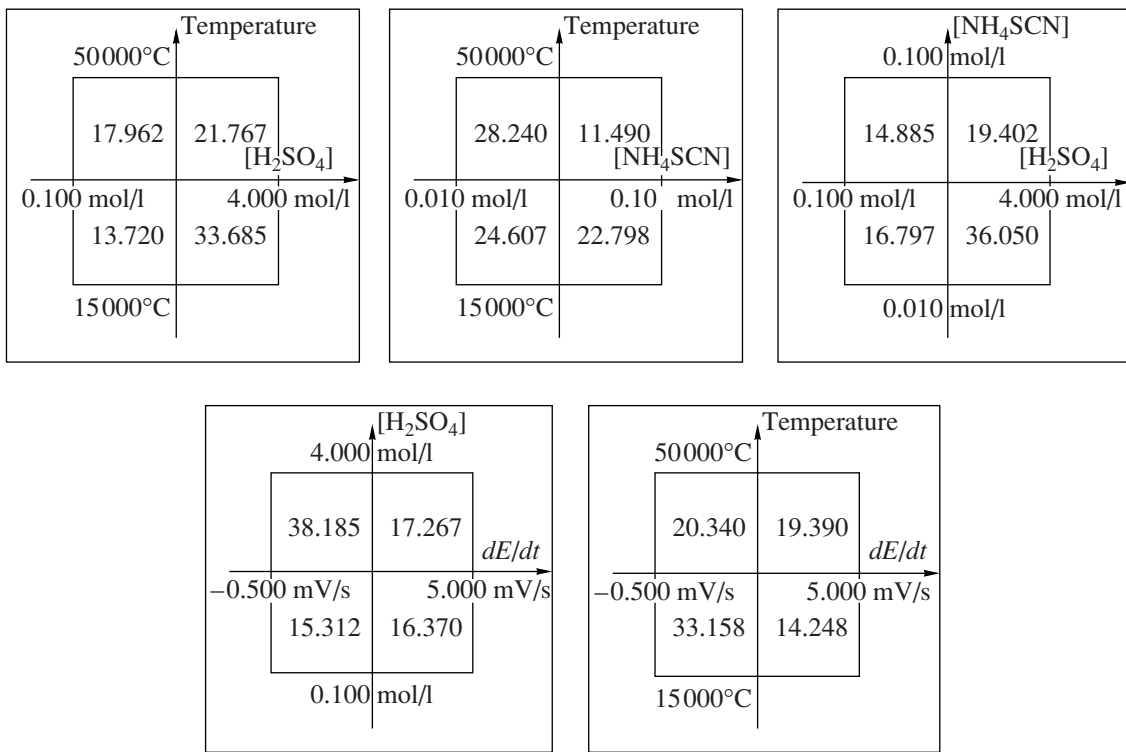
Fig. 9. Significant second order interactions on the DOS of AISI 316L steel using DL-EPR tests (aged state: 550°C–80 000 h).

tiates that the overall effective factors retained for the first-order model have a significant effect on the response $I_r/I_a\%$. Moreover, the analysis of the variance indicates that the first-order model can be satisfactorily used in such multiple linear regression analysis ($F_{0.05(12.4)} > F_{0.05(14.4)} > F_{0.05(24.4)}$). The correlation coefficient, r^2, was found to be 99.427%, indicating the pertinence of the model. Based on these results, it was obviously not necessary to conduct auxiliary experiments using an orthogonal central composite design to obtain a second-order model. The NEMRODW of the obtained results shows that all of the variables studied and their combinations affect the degree of sensitization of the austenitic stainless steel evaluated by the ratio I_r/I_a in %.

The significant factors deducted from the experimental design that have a direct influence on the quality of the DL-EPR test results will be discussed in the next paper. This parametric study is needed in order to further improve the selectivity of the test.

Table 10. Residuals

I_r/I_a exp, %	7.93	9.1	65.6	15.8	24.07	13.78	35.03	18.31	16.83	33.33	37.03	25.77	12.42	9.27	15.08	9.19
I_r/I_a cal, %	7.47	9.56	65.14	16.26	24.53	13.32	35.49	17.85	16.37	33.79	36.57	26.23	12.88	8.81	15.54	8.73
residuals	−0.46	0.46	−0.46	0.46	0.46	−0.46	0.46	−0.46	−0.46	0.46	−0.46	0.46	0.46	−0.46	0.46	−0.46

Table 11. Analysis of variance

Source of variation	Sum of squares	D.o.f	Mean squares	F ratio	Significance
regression	3415.9815	14	243.998679	223.989424	<0.01***
residual	4.357325	4	1.08933125		
total	3420.29046	18	190.016137		

Note: $F_{0.05(12.4)} = 5.91$ and $F_{0.05(24.4)} = 5.77$ (statistical table).

5. CONCLUSIONS

The optimum conditions of the criteria of the sensitization to IGC of austenitic stainless steels of type 316L were investigated. The ratio $I_r/I_a\%$ was determined with respect to the temperature, sweep rate, and concentration of H_2SO_4 and NH_4SCN by means of a factorial design. The 2^4 full factorial design was used to obtain a first-order model with interaction terms. From the experimental results, the optimal conditions were obtained as the sweep rate 0.5 mV/s, the $[H_2SO_4]$ 4 M, the $[NH_4SCN]$ 0.01 M, and the temperature 25°C. In this study, the highest degree of sensitization for AISI 316L obtained was 65.6%. The correlation coefficient calculated for the first-order model at the 95% confidence level has a high value of 99.427%. The model has nearly fitted the full first-order model. Thus, the model supports the experimental data very well. It is very efficient, pertinent, and has no systematic errors. All the parameters studied affect the $I_r/I_a\%$ response. It is believed that the model obtained for the DOS to IGC of AISI 316L may provide a background for pilot and industrial scale applications.

REFERENCES

1. Clarke, W.L., Romero, V.M., and Danko, J.C., Detection of Sensitization in Stainless Steels Using Electrochemical Techniques, *CORROSION/77, Preprint of National Association of Corrosion Engineers*, Houston, Texas, 1977, no. 180.

2. Clarke, W.L., Cowan, R.L., and Walker, W.L., *Comparative Methods for Measuring Degree of Sensitization in Stainless Steel. Intergranular Corrosion of Stainless Alloys,* ASTM STP 656, R.F. Steigerwald, Ed., Philadelphia, Pennsylvania: ASTM, 1978, p. 99–132.

3. Wasnik, D.N., Kain, V., Samajdar, I., and Verlinden, B., Resistance to Sensitization and Intergranular Corrosion through Extreme Randomisation of Grain Boundaries, *Acta Materialia*, 2002, vol. 50, pp. 4587–4601.

4. Matula, M., Hyspecka, L., Svoboda, M., Vodarek, V., Dagbert, C., Galland, J., Stonawzka, Z., and Tuma, L., Intergranular Corrosion of AISI 316L Steel, *Materials Characterization,* 2001, vol. 46, pp. 203–210.

5. Cihal, V. and Stefec, R., On the Development of the Electrochemical Potentiokinetic Method, *Electrochim. Acta*, 2001, vol. 46, pp. 3867–3877.

6. Cihal, V., Desestret, A., and Wagner, G.H., *Test d'étude et d'évaluation de la sensibilité des aciers inoxydables a la corrosion intergranulaire* (5ème Congrès Européen de la Corrosion), Paris, mars 1973, pp. 249–254.

7. Verneau, M., Charles, J., and Dupoiron, F., *Application of Accelerated Corrosion Tests to Service Life Prediction of Materials,* Cragnolino, G. and Sridhar, N., Eds., Philadelphia: ASTM, STP1194, 1993.

8. Cihal, V., *Progrès récents de la méthode potentiocinétique par réactivation de mesure de la sensibilité des aciers inoxydables à la corrosion intergranulaire* (30ème Cercle d'étude des Métaux), Lyon, mai 1991.

9. Cihal, V., A Potentiokinetic Reactivation Method for Predicting the I.C.C and I.G.S.C.C Sensitivity of Stainless Steels and Alloys, *Corros. Sci.*, 1980, vol. 20, p. 737.

10. Verneau, M. and Scarabello, J.M., *EPR (Electrochemical Potentiodynamic Reactivation)-une Technique pour Réceptionner les Matériels en Aciers Inoxydables Corroyés et Moulés* (206ème Manifestation de la Fédération Européenne de la Corrosion, Corrosion Dans les Usines Chimiques et Para Chimiques), Grenoble, Octobre 1994.

11. Sibaud, G., Développement de la Méthode EPR (Electrochemical Potentiokinetic Reactivation) pour le Contrôle de Structure de Matériaux Moulés en Acier Inoxydable et Alliage Base Nickel, *Mémoire C.N.A.M., Métallurgie*, Septembre 1995.

12. Lopez, N., Cid, M., Puiggali, M, Azkarate, I., and Pelayo, A., Application of Double Loop Electrochemical Potentiodynamic Reactivation Test to Austenitic and Duplex Stainless Steels, *Mater. Sci. Eng.*, 1997, vol. A 229, p. 123.

13. Mazaudier, D., Sanchez, G., and Fauvet, P., *Application de la Méthode EPR au Contrôle des Aciers Inoxydables de Type 304L,* 3ème Colloque Européen, Lyon, Oct. 14–15, 1997, pp. C4-1–C4-12.

14. Cètre, Y., Eichner, P., Sibaud, G., and Scarabello, J.M., *Développement de la Technique EPR pour le Contrôle de la Structure des Matériaux Moulés,* 3ème Colloque Européen, Lyon, Oct. 14–15, 1997, pp. C4-1–C4-12.

15. Verneau, M. and Bonnefois, B., *Corrosion Dans les Usines Chimiques et para Chimiques,* 3ème Colloque Européen, Lyon, Oct. 14–15, 1997, pp. C4-1–C4-12.

16. Lopez, N., Mesure de la sensibilite a la C.S.C. Intergranulaire, d'un Acier Inoxydable Duplex a l'aide D'essais Electrochimiques (Technique EPR), *Matériaux et Techniques*, 1995, no. XII, pp. 50–52.

17. Mudali, U.K., Dayal, R.K., Gnanamoorthy, J.B., and Rodriguez, P., Influence of Thermal Aging on the Intergranular Corrosion Resistance of Types 304LN and 316LN Stainless Steels, *Metall. Mater. Trans.,* October 1996, vol. A 27, pp. 2881–2887.

18. Majidi, A.P. and Stretcher, M.A., The Double Loop Reactivation Method for Detecting Sensitization in AISI 304 Stainless Steels, *Corrosion–NACE*, November 1984, vol. 40, no. 11, p. 584.

19. Majidi, A.P. and Stretcher, M.A., Potentiodynamic Reactivation Method for Detecting Sensitisation in AISI 304 and 304L Stainless Steels, *Corrosion,* 1984, vol. 40, no. 8, pp. 393.

20. Goodwin, S.J., Quayle, B., and Noble, F.W., Polarization Behaviour of Austenitic and Duplex Steels in the Double Loop Reactivation Test, *Corrosion-NACE*, December, 1987, vol. 43, no. 12, p. 743.

21. Charbonnier, J.C. and Jossic, T., An Electrochemical Study of Intergranular Corrosion Related to the Chromium Depletion Mechanism in the Case of 18–10 Austenitic Stainless Steels, *Corros. Sci.,* 1983, vol. 23, no. 11, p. 1191.

22. Roelandt, A. and Vereecken, J., A Modified Electrochemical Technique (Electrochemical Potentiokinetic Reactivation) for Evaluating the Susceptibility of Inconel 600 to Intergranular Corrosion, *Corrosion–NACE*, 1986, vol. 42, no. 5, pp. 289–298.

23. Edgemon, G.L., Marek, M., Wilson, D.F., and Bell, G.E.C., Sensitisation Behaviour of Alloy 800 H as Characterised by the Electrochemical Potentiokinetic Reactivation (EPR) Technique, *Corrosion-NACE*, 1994, vol. 50, no. 12, pp. 912–918.

24. Montgomery, B.C., *Design and Analysis of Experiments*, 6th ed., USA: John Wiley and Sons, 2005.

25. Sidhom, H., *Etude de l'évolution Structural au Cours du Vieillissement de deux Aciers Inoxydables Austénitiques, et de Son Influence sur les Propriétés Mécaniques et de Corrosion Intergranulaire*, Thèse d'état, à l'université de Paris-Sud centre d'ORSAY, 1990.

26. Pradymna, K., Nail, L.B.S., and Das, S.C., Aqueous SO2 Leaching Studies on Nishikhal Manganese ore through Factorial Experiment, *Hydrometallurgy*, 2000, vol. 54, pp. 217–228.

27. Şayan, E. and Bayramoğlu, M., Statistical Modeling and Optimization of Ultrasound–Assisted Sulfuric Acid Leaching of TiO_2 from Red Mud, *Hydrometallurgy*, 2004, vol. 71, pp. 397–401.

28. Sado, G. and Sado, M., *Les Plans d'Experience. De l'Expérimentation à l'Assurance Qualité*, AFNOR 1991, pp. 2–3, 69–83, 87–108, 125–130, 139–144, 183–185, 189–190.

29. Goupy J. Dunod, *La Méthode des Plans d'Expérience*, Paris, 1988, Code 042962.

30. Myers R.H. *Response Surface Methodology*, New York: Allyn and Bacon, 1971, p. 126.

EQUIPMENT
AND INSTRUMENTS

Sensitive Thermosensors on the Basis
of Highly Compensated Silicon

M. K. Bakhadyrkhanov, S. A. Valiev, S. S. Nasriddinov, and S. A. Tachilin

Tashkent State Technical University, ul. Universitetskaya 2, Tashkent, 700095 Republic of Uzbekistan

Received May 4, 2007

Abstract—The results of studies and working out and creation of a thermosensor on the basis of highly compensated silicon doped with Mn and S are presented in this work. It is stated that the thermosensitivity and the stability of the parameters of the worked out thermosensor are higher than those of the existing sensitive thermosensor. It is stated that the thermosensor on the basis of highly compensated silicon doped with manganese Si⟨B,Mn⟩ more effectively functions in the region of temperatures $T = 100$–400 K, and the thermosensor on the basis of Si⟨B,S⟩ can be successfully used in the region of more high temperatures $T = 200$–450°C.

DOI: 10.3103/S106837550706018X

It is difficult to conceive a successful solution of modern technical and ecological problems without sensitive and quick-acting thermosensors. The elaboration of thermosensors permitting one to control the object temperature remotely is of particular interest. The potentialities (sensitiveness and quick action) of the existing thermosensors on the basis of semiconductive materials have practically been exhausted [1]. Therefore, new materials and new physical phenomena should be used to create an up-to-date generation of sensitive sensors. From this standpoint, the functional potentialities of a highly-compensated semiconductor are very important. Unlike ordinary semiconductors, it possesses the same concentration of charge carriers as an intrinsic semiconductor (at $T = 300$ K). In such a semiconductor lattice, there exists nonlocal screening of impurity atom ions (including twice and more ionized ones) whose concentration are hundreds and millions times more than the concentration of equilibrium charge carriers ($N_a^- \gg p_0$, $N_d^{++} \gg n_0$). This difference substantially increases the decreasing of the temperature. In such materials, the local electrical neutrality is absent and the system itself is in an extremely nonequilibrium state. The electrophysical and photoelectric properties of such materials essentially differ from weakly-compensated materials in which there are observed some new physical phenomena [2, 3].

The procedure of obtaining highly-compensated silicon with reproducible parameters is a rather fine and complicated problem demanding an individual approach to every doping impurity and the initial material parameters, because, under the conditions of a high compensation, not only the distribution of charge carriers on energy states and the electron structure of defects changes but the diffusion coefficient, the dissolution, and the impurity atom energy levels as well.

Highly compensated silicon was obtained with the help of multistage diffusion doping of monocrystalline silicon of *p*-type with the specific resistance $c = 1 \times 10$ Ω/cm by impurities of sulfur and manganese. Diffusion of these impurities was performed from the gas phase on the basis of the procedure we have worked out, thus allowing one to completely exclude the silicon surface erosion during the process of diffusion of these impurities, as well as obtain highly-compensated silicon with reproducible parameters. These impurities are chosen because, unlike other impurity atoms generating deep levels, they possess a greater concentration of electroactive atoms and stable states in the lattice under the conditions of high compensation. Five samples were used in every lot at diffusion. The main parameters of the highly compensated silicon doped by sulfur and manganese are presented in Table 1.

The obtained material was exposed to mechanical and chemical processing to manufacture thermosensors. Metal nickel was chemically settled on its surface with a thickness of $d = 1$ μm with the following thermal annealing in vacuum at $T = 450$–470°C for $t = 12$–15 min.

Then, the obtained silicon plates were cut on a special installation into squares with dimensions of $1 \times 1 \times 0.5$ mm³. After tinning and soldering of the external contacts, the pressurization of the thermosensors was performed.

The most important features of a sealer are its strength, watertightness, and resistance to various acids and alkalis. The thermal stability and heat conduction of a sealer provide high quick-acting and operating parameters of the finished thermosensors. The examination of the current–voltage characteristics showed that the contacts were ohmic ones everywhere over the studied temperature region.

Table 1. Parameters of highly compensated silicon Si⟨S, Mn⟩

Before diffusion		After diffusion				
specific resistance, Ω cm	conductivity type	samples	specific resistance, Ω cm	concentration of charge carriers, cm^{-3}	concentration of boron ions, cm^{-3}	concentration of ions Mn^{++}, S^{++}, cm^{-3}
1	P	Si⟨B, S⟩	$(1.5–1.7) \times 10^5$	$(2–3.5) \times 10^{10}$	2×10^{16}	10^{16}
1	P	Si⟨B, S⟩	$(2–2.5) \times 10^5$	$(2.5–3) \times 10^{10}$	2×10^{16}	10^{16}
5	P	Si⟨B, S⟩	$(1.3–1.6) \times 10^5$	$(3–3.5) \times 10^{10}$	4×10^{15}	2×10^{15}
5	P	Si⟨B, S⟩	$(1.9–2.5) \times 10^5$	$(2.5–3.5) \times 10^{10}$	4×10^{15}	2×10^{15}
2	P	Si⟨B, Mn⟩	$(1.4–1.7) \times 10^5$	$(3–3.5) \times 10^{10}$	10^{16}	5×10^{15}
2	P	Si⟨B, Mn⟩	$(2–2.4) \times 10^5$	$(2.5–3) \times 10^{10}$	10^{16}	5×10^{15}
10	P	Si⟨B, Mn⟩	$(1.5–1.7) \times 10^5$	$(3–3.5) \times 10^{10}$	2×10^{15}	10^{15}
10	P	Si⟨B, Mn⟩	$(2–2.3) \times 10^5$	$(2.5–3) \times 10^{10}$	2×10^{15}	10^{15}

Table 2. Parameters of thermosensors on the basis of highly compensated Si⟨B, S⟩

Lot	Nominal resistance, Ω cm	Sensitivity index, V, K	Temperature range, K	Time lag, s		Dimensions, mm
				τ_1	τ_2	
1	$(3–5) \times 10^5$	6900–7000	200–450	12–15	20–25	$1 \times 1 \times 0.5$
2	$(8–10)^5$	7100–7200	200–450	12–15	20–25	$1 \times 1 \times 0.5$
3	$(3–5) \times 10^5$	7000–7100	200–450	12–15	20–25	$1 \times 1 \times 0.5$
4	$(8–5) \times 10^5$	7200–7400	200–450	12–15	20–25	$1 \times 1 \times 0.5$

Note: Sulfur concentration: lots 1 and 2, $N_S = 10^{15}$ cm^{-3}; lots 3 and 4, $N_S = 10^{16}$ cm^{-3}; τ_1, establishment time at $T = 25–100$ K; τ_2, recovery time at $T = 100–25$ K in the air.

Table 3. Parameters of thermosensors on the basis of highly compensated Si⟨B, Mn⟩

Lot	Nominal resistance, Ω cm	Sensitivity index, V, K	Temperature range, K	Time lag, s		Dimensions, mm
				τ_1	τ_2	
1	$(4–5) \times 10^5$	6700–6950	200–450	13–15	25–30	$1 \times 1 \times 0.5$
2	$(7–8) \times 10^5$	6900–7100	200–450	13–15	25–30	$1 \times 1 \times 0.5$
3	$(4–5) \times 10^5$	7100–7200	200–450	13–15	25–30	$1 \times 1 \times 0.5$
4	$(7–8) \times 10^5$	7200–7300	200–450	13–15	25–30	$1 \times 1 \times 0.5$

Note: Manganese concentration: lots 1 and 2, $N_{Mn} = 10^{15}$ cm^{-3}; lots 3 and 4, $N_{Mn} = 5 \times 10^{15}$ cm^{-3}; τ_1, establishment time at $T = 25–100$ K; τ_2, recovery time at $T = 100–25$ K in the air.

The main parameters of the finished thermosensors were determined under equal thermodynamic conditions. In Tables 2 and 3, there are displayed the parameters of thermosensors produced on the basis of highly compensated materials, which are presented in Table 1.

It is seen that the thermosensitivity of the presented thermosensors is very high; it is 25–50 times more than that of the most sensitive ones. As a result of theoretical calculations and analysis of the parameters of the thermosensors produced on the basis of noncompensated silicon with the intrinsic conductivity obtained by noncrucible zone melting with $\rho \sim 2 \times 10^4$ Ω cm, it was

established that the sensitivity of these sensors is also 50–70% less than that of the sensors we had elaborated.

Rather high quick acting both at establishment and restoration of the object temperature is the next peculiarity of the thermosensors. Under operating conditions, the thermosensor consumes very little energy. It should also be noted that the sensitivity of the same thermosensors with different concentrations of doping impurities is substantially more in the case of the high-ohmic compensated silicon. These data indicate the peculiarities of the properties of the thermosensors manufactured on the basis of high-compensated silicon

and their great functional potentialities. The principle advantage of these thermosensors is their usage with the aim of remote control of the object temperature.

The stability of the elaborated thermosensor parameters has been examined under various extreme conditions and for a long time (for 3 years). As the results show, there are no noticeable changes.

It is also established that the thermosensors on the basis of highly-compensated silicon doped by manganese work more validly in the temperature region $T = 100$–$400°C$, and thermosensors on the basis of $Si\langle B,S\rangle$ can be used successively in the region of higher temperatures $T = 200$–$450°C$.

The stability of the parameters, the low energy consumption under operating conditions, the high sensitiveness, the quick acting, and the possibility to use the thermosensors for remote control of the object temperature, as well as in various media and objects, determine the great functional potentialities of the thermosensors on the basis of highly-compensated silicon.

REFERENCES

1. http://www.w3.org/TR/html4/loose.dtd.
2. Bakhadyrkhanov, M.K., Zikrillaev, N.F., and Ayupov, K.S., JTF, 2006, vol. 76, no 9, pp. 128-129.
3. Bakhadyrkhanov, M.K., Ayupov, K.S., and Sattarov, A., JTF, 2005, vol 39, no 7, pp. 823–825.

OPERATING EXPERIENCE

Study of Polymer–Piezoceramic Composites by the Radio-Thermo-Luminescence Method

M. M. Kuliev

Institute of Radiation Problems, National Academy of Sciences of Azerbaijan,
F. Agaeva 9, Baku, AZ-1143 Republic of Azerbaijan

Received June 4, 2007

Abstract—In this work, the features of the dependence of radiothermoluminescence (RTL), charge stabilization, change of the temperature of structural β- and γ-transitions on the dose of γ-irradiation and degree of filling Φ of composites based on high-density polyethylene (HDPE) and piezoceramic fillers of the PKR-3M type are investigated. It is shown that the dependences of thermoluminescence intensity of the filling degree $J(\Phi)$ are characterized by extrema at the filler content as high as 5 vol % and a dose $D = 20$–30 kGy. It is shown that γadiation at defined doses leads to inhibition of the process of β-relaxation of HDPE in the composition, which can be associated with the formation of new trapping centers of excess charges of electrets.

INTRODUCTION

The electroactive (electret, piezo-, and pyroelectric) properties of multiphase (two and more) systems based on polymers and piezoceramic fillers are determined by the type of cohesion and the nature of the filler as well as by the particularities of the electron–ion and polarization processes within the phases and on their boundaries [1, 2]. The kinetics of these properties formation are also known [2, 3] to depend essentially on the character of the relaxation processes in these materials. Furthermore, the effectiveness of the electroactive properties of polymer composites (PC) formation is also influenced by interphase phenomena, volume charge generation, etc. [4, 5]. In particular, the polarized state is shown to lead to recapture of charges stabilized on the traps, which results in a decrease of the dielectric losses in PE and PP electric films [2–5]. At the same time, the role of the structural and nonequilibrium processes in the formation of the electroactive properties of composites has not been studied sufficiently well. Note that radiation-technological issues related to the production of radioelectrets and photoelectrets of PC, as well as related to the radiation and structural modification of their electroactive properties, are becoming of special importance. Study of PC relaxation properties by the method of radio-thermo-luminescence (RTL) will allow one to reveal some particularities of the electroactive properties acquisition by polymer materials [3–8] and to determine points of excess charges localization on traps of various nature. The RTL method was used in [8] to study the existence of structural transition temperatures in polymer composites based on BaTiO₃. The shift of the β-transition locations of the polymer matrix into the region of low temperatures with an increase of the piezofiller content was discovered.

Furthermore, the authors of [9] believe that, in the temperature region of 4.2–500 K, in solid composite materials, there is a set of characteristic temperatures. Testing and investigation of the operating abilities of electroactive composite materials at these characteristic temperatures seem to be important. So far, there is no agreement about the molecular mechanism of formation of radiation-modified PC electroactive properties. The RTL method is widely used in the study of the components compatibility and a number of other properties of PCs and their modifications [7–10].

The purpose of this paper is the application of the RTL method to study the temperature change of the structural transitions, the particularities of the charge stabilization depending on the γ-radiation dose D, and to measure the polymer composites filling.

EXPERIMENTAL

The study objects were composites based on high-density polyethylene 20806-024 (HDPE) with PKR-3M piezoceramic filler of the zirconate-titanate–lead family (CTL). Composites samples in the form of discs were obtained from a homogenous mixture of polymer–piezoceramic powders with piezoparticles 63 to 100 μm in size. The samples used for the RTL analysis were placed on the bottom of stainless cups 8 mm in diameter and covered by a stainless mesh for the light output. Before being irradiated, the samples in the cups were vacuumed in a glass ampoule to a pressure of 1.33×10^{-3} Pa and cooled down to a temperature of 77 K by immersing into a container with liquid nitrogen. The vacuuming time t needed to get rid of the gases dissolved in a sample was determined as a function of the films' thickness by the formula

$$T = h^2/4K,$$

where h is the films' thickness, and K is coefficient of the diffusion of air in the polymer $\approx 10^{-3}$ m^2/s [2].

The irradiation was performed with γ-radiation from ^{60}Co using an RKh-γ-30 apparatus at a temperature of 77 K, and the dose rate was 3.3×10^3 Gy/h.

The RTL spectrums described in [6] were measured using a TLG-69M apparatus at a heating rate of 12 K/min in the temperature range from 77 to 300 K. The reproducibility of the RTL maximum location, as a rule, was 2–3 K. The sample luminescence was registered in the 300–820 nm range with help of a PEM-51 photoelectret multiplier. The sample temperature was registered by a copper-constantan thermocouple.

The effective energy of activation E_a corresponding to the γ-process was determined by the method of the RTL peaks half-width. Individual values of E_a were compared to the results obtained by the method of initial velocities. The calculations were performed by the formula

$$E_a = \frac{E_- + E_+}{2}, \text{ where } E_- = \frac{0.98 k T_m T_+}{T_m - T_-}, \text{ but}$$

$$E_+ = \frac{1.42 T_m T}{T_+ - T_m}.$$

Here, T_m is the temperature of the intensity maximum on the RTL curve, T_- and T_+ are the temperatures of the low-temperature and high-temperature sides of the luminescence maximum at the point where the intensity is equal to half of the maximum, and K is the Boltzmann constant.

RESULTS AND DISCUSSION

Figure 1 shows RTL curves of the original HDPE (curve *1*) and composites based on it (curves *2–5*) after γ-irradiation at 77 K with a dose of 3×10^4 Gy. The same picture is observed at absorbed doses of 0.5×10^4 and 1.5×10^4 Gy. As one can see from the figure, the RTL curve for pure HDPE basically has two luminescence maximums: a low-temperature first maximum at 169 K and a relatively high-temperature second peak at 239 K.

The presence of structural transitions in the PC registered from the RTL curves relates to variation of the molecular mobility of kinetic units in the regions of α-, β-, and γ-transitions.

An RTL curve represents a number of luminescence peaks appearing as a result of recombination of charges stabilized in the process of irradiation at low temperatures. The luminescence peaks' intensity is increased due to an increase of the charges' recombination rate $\left(J \sim \Psi \dfrac{dn}{dt} \right.$, where ψ is the portion of the electrons caus-
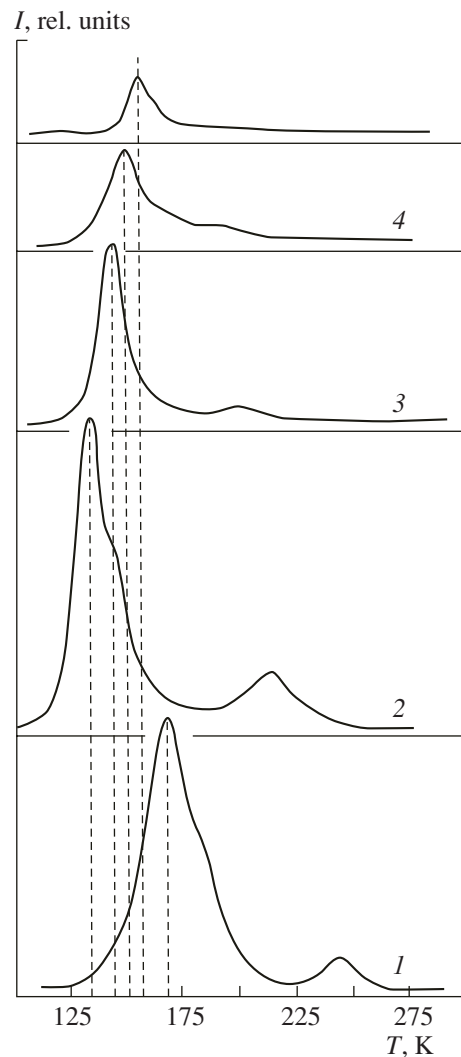

Fig. 1. Radio-thermo-luminescence of HDPE and its composites: *1*, HDPE; *2*, HDPE + 5 vol % PKR-3M; *3*, HDPE + 10 vol % PKR-3M; *4*, HDPE + 20 vol % PKR-3M; *5*, HDPE + 50 vol % PKR-3M. Absorbed dose—3×10^4 Gy.

ing the light emission $\Big)$ in the interval of the relaxation or phase transition; hence, their temperature location (RTL peaks) is closely connected with the phase-aggregative state, the presence of admixtures, etc., in particular, with peculiarities of the relaxation or phase transition passing [6].

After modification of HDPE by introduction of PKR-3M, the following changes appear in the RTL curves: introduction of 5% PKR-3M in HDPE increases the intensity of both the peaks' luminescence and shifts the temperature T_m of their maximums in the direction of lower temperatures. A subsequent increase of the filling measure leads to a decrease of these peaks' intensity; at 30 vol %, the second peak corresponding to
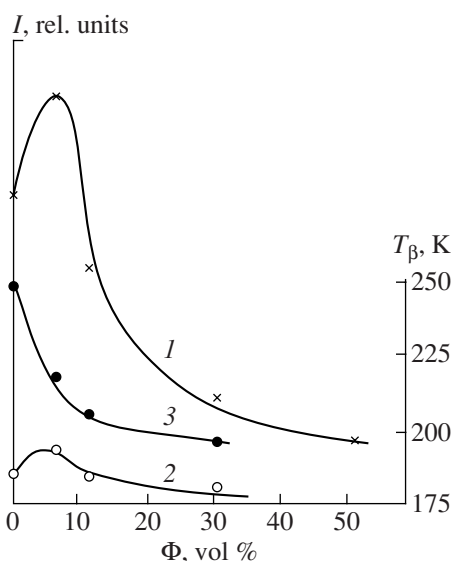
Fig. 2. Dependences of the γ- (*1*) and β-maximum (*2*) intensities and of the β-transition temperature location (*3*) on the content of the filler. Absorbed dose—3×10^4 Gy.
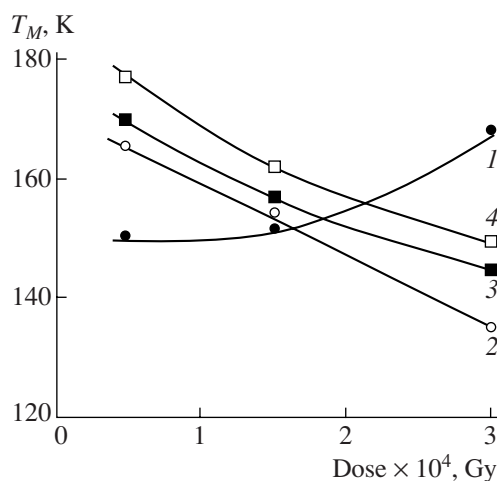

Fig. 3. Dependences of the temperature of the γ-transition maximum for HDPE and its composites on the absorbed dose: *1*, HDPE; *2*, HDPE + 5 vol % PKR-3M; *3*, HDPE + 10 vol % PKR-3M; *4*, HDPE + 30 vol % PKR-3M.

the β-relaxation process almost disappears. At that, the T_m value of the first peak for HDPE remains higher than T_m for the composites.

Based on the temperature location of the luminescence peaks, the latter can be related to γ- and β-transitions in HDPE [6, 9]. Usually, the γ-transition is determined by oscillations of several carbon atoms of the polymer main chain or the movement of separate segments on the surface of polymer crystals. The second peak at 239 K characterizes the process of HDPE devitrification, which is called β-transition. Between the γ- and β-transitions on the RTL curves, a γ-peak (Fig. 1) in the shape of a shoulder can be observed. It follows from the figure that, by introduction of a filler, extremal variation of its intensity depending on the filling measure Φ is connected with variation of the molecular mobility of the macromolecules' segments. At values of Φ > 5 vol % PKR-3M in HDPE, the β-relaxation process is suppressed (hampered). A similar effect is also observed on the dependencies of the β-peak intensity on the dose of γ-irradiation for epoxy composites [10].

Variation of E_a (eV) of the γ-transition as a function of the absorbed dose for HDPE + PKR-3M composites

D, kGy	5	15	30
Φ, vol %			
0	0.196	0.247	0.289
5	0.113	0.170	0.153
10	0.125	0.180	0.190
30	0.145	0.195	0.213
50	0.163	0.215	0.241

The increase of the luminescence intensity at Φ = 5 vol % PKR-3M shows that the structural changes taking place in the polymer phase lead to the emergence of new centers (traps) for the charges' stabilization, while the decrease of the amplitude maximum of the composites RTL with an increase of the volume content can be explained by the decrease of the portion of small-scale segmental mobility. The temperature of the β-transition maximum shifts in the direction of low temperatures, which shows that, with introduction of the filler, the β-relaxation process in HDPE is suppressed. These conclusions are supported by the results shown in Fig. 2.

The dependences of the γ- and β-maximums on the content of the piezofiller (curves *1* and *2*, respectively) are shown here. One can see that, at the values of Φ ≈ 3–6 vol %, the luminescence intensity is maximal, and, at that, T_β shifts in the direction of low temperatures. These changes can relate to the polymer structurization. Apparently, the fillers play the role of nucleating centers observed with growth of the HDPE crystallization measure.

Figure 3 shows T_m dependences of the γ-peak maximum on the absorbed dose for HDPE (curve *1*) and its composites (curves *2–4*) with volume contents of the piezophase of 5, 10, and 30 vol %, respectively. One can see that, with an increase of the absorbed dose D, the temperature of the γ-peak maximum for HDPE grows from 150 to 169 K. Such a change for HDPE can be explained by the process of functional groups crosslinking under the irradiation effect. This process hampers the movement of methylene groups (CH_2) in the amorphous region, while, for the HDPE composites, a monotonous decrease of the T_m values is observed. This can be related to the shallow admixture centers determined by the filler particles. In fact, as one can see from the table, the effective energy of the low-temperature γ-process activation for the composites with an increase
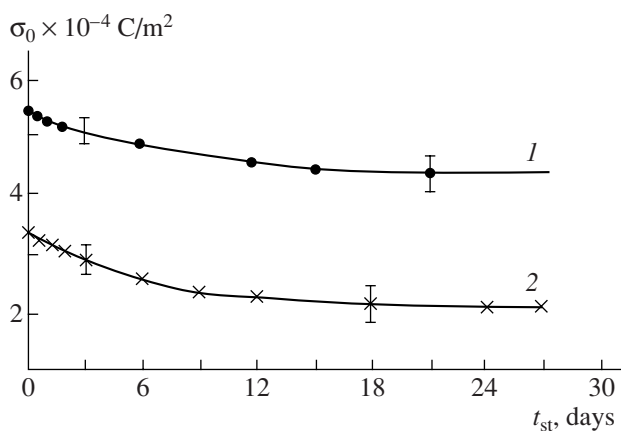
Fig. 4. Dependences of the electret charge density on the storage time t_{st} before (curve *1*) and after (curve *2*) the preliminary γ-irradiation.

Thus, the RTL method allows one to reveal new particularities of excess charges stabilization in HDPE/PKR-3M polymer composites. The correlation between the variations of the RTL maximums' intensities and the electret properties of the composite as a function of the filling measure and the dose of γ-irradiation is shown, which leads to the β-relaxation process.

of the filling measure always remains lower than for HDPE.

The dependence $T_β$ – (Φ) (Fig. 2, curve *3*) is of big practical interest. Variations of $T_β$, i.e., the temperature of the polymer vitrifying with introduction of other fillers, were observed in the past [6, 10]. In this case, the decrease of $T_β$ of HDPE at filling by PKR-3M can also relate to relaxation of internal stresses appearing at the polymer crystallization. Samples with a volume content of the filler Φ = 5 vol % (Fig. 2, curve *1*) are characterized by a high output of thermoluminescence, which indicates the emergence of multiple centers of excess charges localization at radiolysis. This assumption can be confirmed by data on the electret properties of such composites.

Figure 4 shows results on variation of the electret charges' surface density $σ_e$ as a function of the storage time t_{st} of corona electrets made of a composite with a content of 95 : 5 vol % HDPE and PKR-3M, respectively, before (curve *1*) and after (curve *2*) preliminary γ-irradiation of D = 30 kGy. Polarization was performed by the effect of a unipolar corona discharge (7 kV, 5 min). One can see that the preliminarily γ-modified HDPE/PKR-3M samples possess a higher electret charge and stability. These data fit the results from [2], where an increase of $σ_e$ was demonstrated for an HDPE/CTS-19 system with a content of 90 : 10 vol %. Data in Fig. 2 show that, indeed, filled HDPE radiation modification leads to emergence of new charges' stabilization centers and, at the same time, suppresses the β-relaxation processes in the polymer. These statements are confirmed by data on the measurement of the dose dependences of the RTL intensity for individual as well as for mixed polymer composites. The RTL intensity for pure polymers is known to linearly increase up to a dose of 30–50 kGy followed by saturation when the traps are filled. At doses of more than 50 kGy, the RTL intensity starts decreasing [7, 11].

REFERENCES

1. Kuliev, M.M., Niftiev, S.N., Musaeva, S.N., Faradzhade, I.A., Shakhtaktinsky, M.G., and Kurbanov, M.A. On Mechanism of the Electrets Effect in the Polymers, Dispersed by the Particles of the Piezoelectric Materials, *Fizika* (Azerb.), 2000, vol. 6, no. 4, pp. 3–5.
2. Magerramov, A.M., *Strukturnoe i radiatsionnoe modifitsirovanie elektretnykh, p'ezoelektricheskikh svoistv polimernykh kompozitov* (Structural and Radiation Modification of Electret, Piezoelectric Properties of Polymer Composites), Baku, 2001.
3. Magerramov, A.M., Nuriev, M.A., and Safarov, N.Yu., Particularities of Radiothermoluminescence in Nonuniformly Polarized Piezocomposites, *Trudy V mezhdunarodnoy konferentsii "Optika, optoelektronika i tekhnologii"* (Proc. V Int. Conf. "Optics, Optoelectronics, and Technologies), Ul'yanovsk, 2003, 135 p.
4. Shakhtakhtinskii, M.G., Sadykhov, Kh.A., Maggeramov, A.M., *O roli mezhfaznykh yavlenii pri formirovanii p'ezosvoistva polimernykh kompozitov* (On Role of Interphase Phenomena at Formation of Piezoproperty of Polymer Composites), *Uch. Zap. AzTU*, 1994, no. 2, pp.165–170.
5. Magerramov, A.M. and Dashdamirov, M.K., On Structural Aspects of Radiation Modification of Dielectric Properties of Polyolefines, *Khim. Vysokikh Energii*, 2005, vol. 39, no. 2, pp. 1–7.
6. Kuleshov, I.V. and Nikol'skii, V.G., *Radiotermolyuminestsentsiya polimerov* (Radiothermoluminescence of Polymers), Moscow: Khimiya, 1991, 128 p.
7. Kuliev, M.M., Radiothermoluminescence of Polymer-Piezoceramic Composites, *Elektron. Obrab. Mater.*, 2005, no. 6, pp. 79–82.
8. Bogatko, V.V., Aulov, V.A., and Venevtsev, Yu.N., *Radiotermolyuminestsentsiya soedinenii SrTiO₃, KtaO₃ i BaTiO₃ (Radiothermoluminescence of Compounds SrTiO₃, KtaO₃, and BaTiO₃), Sistemy osobykh temperaturnykh tochek v tverdykh telakh* (Systems of Special Temperature Points in Solid Bodies), Venevtsev, Yu.N., Ed., Moscow, 1986, pp. 90–94.
9. Aulov, V.A. and Lednev, I.K., Relation between RTL Maximums and Relaxation Transitions in Polymers, *Sistemy osobykh temperaturnykh tochek v tverdykh telakh* (Systems of Special Temperature Points in Solid Bodies), Venevtsev, Yu.N., Ed., Moscow, 1986, pp. 82–87.
10. Aulov, V.A., Kuchkina, I.O., Makarov, S.V., Pantyukhin, A.A., Ozerin, A.N., and Bakeev, N.F., Particularities of Radiothermoluminescence in Reactor Powders of Supermolecular Polyethylene, *Vysokomolekulyarnye Soedineniya*, 2003, ser. 45, no. 4, pp. 588–596.
11. Partridzh, P., Radiothermoluminescence of Polymers, *Radiatsionnaya Khimiya Makromolekul* (Radiation Chemistry of Macromolecules), Moscow: Atomizdat, 1978, pp. 176–204.

OPERATING
EXPERIENCE

Sensitivity of Composites Based on Gelatin and Nanoparticles Cu$_2$S and CdS to Vapors of Some Organic Compounds

M. B. Muradov[a], M. A. Nuriev[b], G. M. Eivazova[a]

[a] *Baku State University, ul. Khalilova 23, Baku, AZ-1073 Azerbaijan*
[b] *Institute of Radiation Problems, Academy of Sciences of Azerbaijan,*
F. Agaeva 9, Baku, 1143 Azerbaijan
Received June 29, 2007

Abstract—The gas-sensitivity of gelatin/Cu$_2$S and gelatin/CdS samples under the effect of vapors of different solvents and ethyl alcohol has been investigated. It is shown that composites on the basis of polymers with Cu$_2$S and CdS nanoparticles are sensitive to vapors of different solvents. The gas sensitivity of the nanocomposites depends on the rate of matrix filling and the chemical data of the testing gas. These materials could be used as a sensitive element in different gas sensors and detectors.

DOI: 10.3103/S1068375507060208

INTRODUCTION

The demands for the control of the environment and ecology always give impetus to the research in order to elaborate gas sensors. These sensors are necessary for technological control of chemicometallurgical interactions and gas and oil manufactures. There exist various gas-sensitive sensors characterized by different operating principles and manufacturing processes. Solid-state sensors are distinct from other ones thanks to their portability and simplicity of design. Electric signals produced by such portable sensors permit one to get information on the composition and physical parameters of the surrounding medium. The results obtained in this sphere allowed creation of various multifunctional devices [1]. Different semiconducting materials serve as sensitive elements in gas sensors [2].

Nanocomposites are very interesting from the point of view of creation of gas sensors. The processes of interaction of nanocomposites with gaseous phase molecules are the determining factors. At present, resistive type sensors [3, 4] based on polymers with metal fillers are widely used. Polymeric composites with semiconducting nanoparticles are of special interest. Nanoheterogeneous polymeric composites consist of a polymer matrix with ultradispersed particles with dimensions of 20–100 nm with the distances between them on the same order [5]. Such systems possess unusual photo- and gas-sensitive properties, which are determined by the process of the charge redistribution at the expense of the external effects. These systems' electric conductivity grossly changes even at room temperature as a result of adsorption of various vapors and gases [6, 7]. The changes of the nanocomposite electric conductivity at the sorption of various gases depends on a lot of factors: the level of filling of the polymeric matrix with semiconducting nanoparticles, the interparticle dis-

tance, and the interphase interaction between the matrix and semiconducting particles. In this connection, the technology of chalcogenide semiconductor nanoparticle formation in the polymeric matrix volume with the help of ion layer-by-layer chemisorption [8] permits purposefully changing the particle concentration and interparticle distance in nanocomposites.

The study is of the gas sensibility of composites on the basis of a gelatin polymeric matrix and nanoparticles of copper sulphide (gelatin/Cu$_2$S) and cadmium sulphide (gelatin/CdS) under the effect of vapors of different solvents and ethyl alcohol.

EXPERIMENTAL

Gelatin/CdS and gelatin/Cu$_2$S nanocomposites were obtained with the help of ion layer-by-layer chemisorption in the volume of the polymeric matrix, which was described in works [9–12]. Gelatin thin films were used as a substrate. Solutions of Cd(NO$_3$)$_2$ · 4H$_2$O, CuSO$_4$ · 5H$_2$O, and Na$_2$S · 9H$_2$O with a concentration of 0.2 mol were the source of anions and cations. The sorption time was 30 s. Threefold washing of the samples was carried out after the sorption of every type of ions to remove the remains of the electrolytes. This permitted preventing the possibility of spontaneous nucleous generation in the volume of the polymeric matrix.

Representations of samples of gelatin/3 cycles CdS (a) and gelatin/15 cycles CdS (b), which were obtained with the help of an atom-force microscope (NTEGRA, NT-MDT), are displayed in Fig. 1. The dimensions of the nanoparticles and the distance between them can be estimated according to the pictures. The estimation for the sample with three cycles of generation shows that the average size of the nanoparticles is about 3.2 nm. The figure depicts that the density of the nanoparticles
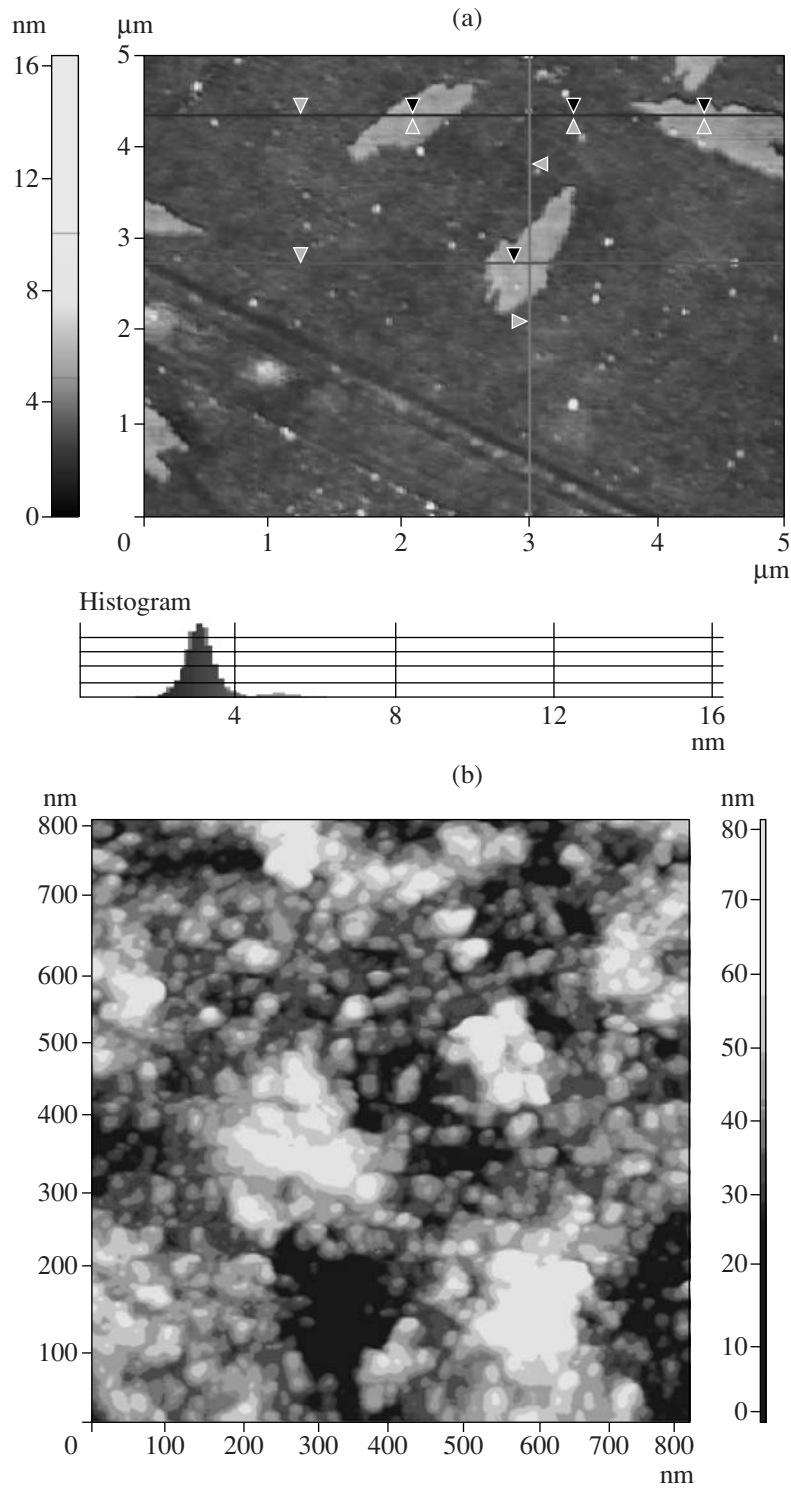
Fig. 1. Surface morphology of samples: gelatin/3 cycles CdS(a) and gelatin/15 cycles CdS (b).

along the defects of the polymeric matrix is more than on the remaining part. This evidently is connected with the higher density of sorption centers. For the gelatin/30 cycles CdS samples, the average dimensions of the particles are 19 nm. It is seen that, with the increase of the cycle number, the particle sizes grows and the interparticle distance reduces. The variation of the interparticle distance should result in a change of the
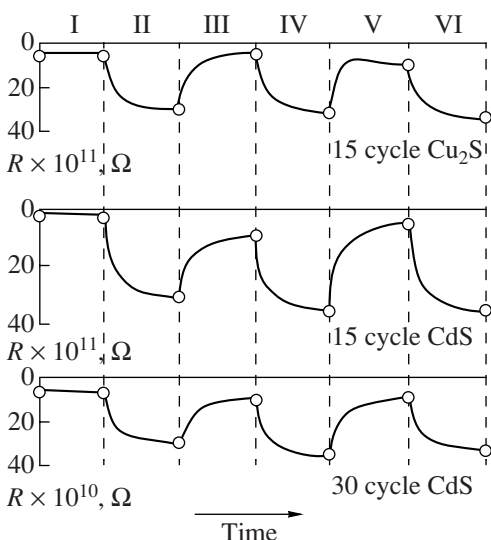
Fig. 2. Kinetics of changes of the surface specific resistance with time for nanocomposites: gelatin/15 cycles Cu₂S, gelatin/15 cycles CdS, and gelatin/30 cycles CdS.
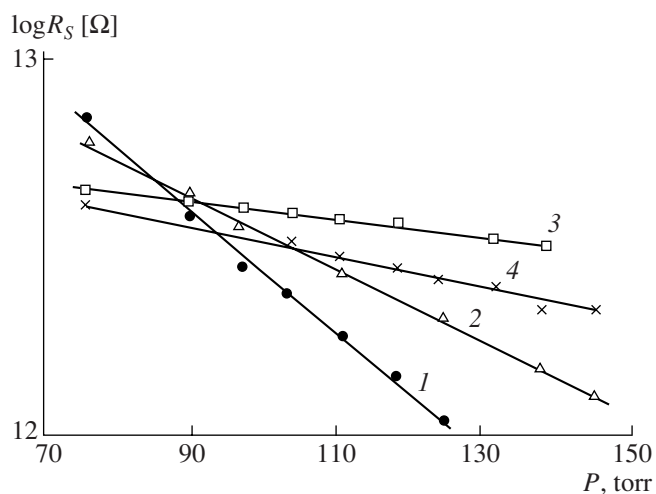

Fig. 3. Resistance dependence on the variation of the alcohol vapor pressure for samples of gelatin/15 cycles CdS: *1*, alcohol, *2*, acetone, *3*, dichloroethane, *4*, methylethylketone.

conductance mechanism and influence the composite gas sensitivity.

To test the gas sensitivity, a sample with electrodes placed parallel on its surface was seated in the measuring cell. The alteration of the resistance with time at a certain pressure in different gas media was registered by a self-recorder through an E6-13A teraohmmeter. The measurements were conducted in two manners: (1) The volume was exhausted up to a vacuum of 10^{-1} atm (76 torr) and, after the test gas or vapor was introduced, the sample's sensitivity to the given gas was determined according to the change of the resistance value (the sample's gas sensitivity to the vapors of ethyl alcohol and acetone was estimated). (2) The vessel with the test substance (alcohol or solvent) was placed into a Dewar flask and was cooled preliminary with the help of liquid nitrogen. After freezing, the vacuum system with the measuring cell and the vessel was exhausted up to a vacuum of 10^{-2} atm. Then, the vessel with the test substance was heated under different conditions. The pressure in the measuring cell grew up to the pressure of the saturated vapors of a certain liquid at the given temperature and the change of resistance with the pressure alteration was recorded. The gas sensitivity was determined by the following formula:

$$\gamma = (R_1 - R_0)/(P_1 - P_0) = \Delta R/\Delta P, \qquad (1)$$

where P_0 and R_0 are the initial values of the pressure and resistance, P_1 and R_1 are the final values of the pressure and resistance, and ΔP and ΔR are the changes of the pressure and resistance.

DISCUSSION OF THE RESULTS

In Fig. 2, there is shown the time dependence of the change of resistance of gelatin/15 cycles Cu₂S, gelatin/15 cycles CdS, and gelatin/30 cycles CdS nanocomposites in the air at a standard pressure of 1 atm (760 torr) (section I), after exhausting up to 10^{-1} atm (76 torr) (section II); after admission of air (section III); after the repeat exhausting up to 10^{-1} atm (section IV); and after admission of ethyl alcohol vapors (section V), when the pressure in the cell varies from 76 up to 117 torr.

It is seen that the values of the initial resistance and the resistance corresponding to a pressure of 10^{-1} atm (76 torr) don't change with time; i.e., they are relatively stable. However, the resistance change at admission of ethanol after exhausting up to 10^{-1} atm has different values for different compositions. The best gas sensitivity at the admission of ethyl alcohol vapors is observed for the gelatin/15 cycles CdS nanocomposites (9.5×10^{10} Ω/torr).

To determine the gas sensitivity of the gelatin/15 cycles CdS samples, the second method was used.

In Fig. 3, there is depicted the run of the dependence of the resistance of the gelatin/15 cycles CdS samples on the pressure of the saturated vapors of the ethyl alcohol (curve *1*), acetone (curve *2*), dichloroethane (curve *3*), and methylethylketone (curve 4). According to the slope of the characteristics, it can be said that a high gas sensitivity is observed at the admission of the vapors of ethyl alcohol. Such changes of the sensitivity will be clear if we compare the chemical data of these solvents.

In the table, there are presented the chemical structure, boiling temperature, and molecular weight of the solvents

Vapors of	Ethyl alcohol	Acetone	Methyl-ethylke-tone	Dichloro-ethane
Structure	C_2H_6O	C_3H_6O	C_4H_8O	$Cl_2C_2H_4$
Molecular weight	46	58	72	99
Boiling temperature, °C	78	56	83	79.6
P_0, torr	76	76	76	76
P_1, torr	125	146	146	139
R_0, 10^{12} Ω	1	2	3.5	5.3
R_1, 10^{12} Ω	8.5	8	6.5	6.8
R, 10^{12} Ω	7.5	6	3	1.5
ΔP, 10^{12} torr	49	70	70	63
γ, 10^{10} Ω torr	15.3	8.6	4.3	2.38

used and the gas sensitivity for the gelatin/15 cycles CdS sample calculated by formula (1) from the dependence displayed in Fig. 3. It is seen from the comparison that ethyl alcohol has the least molecular weight of all these materials and the highest gas sensitivity of the samples is observed under the effect of its vapors. The sequence of the sample gas sensitivity to the vapors of these solvents should coincide with the sequence of their molecular weight decrease. We can say that the sample, when in contact with the vapors of these solvents, exhibits the best adsorption, and, accordingly, high gas sensitivity is observed in vapors and gases with a relatively less molecular weight.

At the adsorption of the gas and vapors of various materials, the absorbent molecules, penetrating into the interparticle space, cause the reduction of the potential barrier and correspondingly the change of the nanoparticle yield work. It, in turn, is accompanied by the growth of the resistance because of the tunneling between nanoparticles. When nanocomposite structures are compared with the model of the dynamic lattice of accidental resistances, then the reduction of the yield work of the nanoparticles at adsorption causes the formation of conductive bonds between them and the increase of the effective conducting lattice in the nanocomposite. The growth of the molecule dimensions, worsening the penetration into the interparticle space, should lead to the worsening of the gas sensitivity, which is observed experimentally.

Consequently, the investigation carried out shows that composites on the basis of a polymer with nanopar-

ticles of copper sulphide and cadmium sulphide are sensitive to vapors of various solvents. The nanocomposite sensitivity depends on the level of the matrix filling and the chemical data of the gas being tested. These materials can be used as a measuring element of different gas sensors and pick ups.

REFERENCES

1. Moriizumi, T., *Thin Solid Films*, 1988, no. 160, p. 413.
2. Temofonte, T.A. and Schoch, K.E., *J.Appl. Phys.*, 1989, vol. 65, no. 3, p. 1350.
3. Trakhtenberg, L.I., Gerasimov, G.N., Potapov, I.K., Rostovshchikova, T.N., Smirnov, V.V., and Zufman, V.Yu., Nanocompositional Metal–Polymer Films: Sensor, Catalytic, and Electrical Properties, *Vestn. Mosk. Univ., Ser. 2:Khim.*, 2001, vol. 42, no. 5, pp. 325–331.
4. Grigor'ev, E.I., Vorontsov, P.S., Zav'yalov, S.A., and Chvalun, S.N., Adsorption Effect on Conductivity of Self-Organized Metal–Polyparaxylelene Nanocomposites, *Pis'ma Zh. Tekh. Fiz.*, 2003, vol. 28, no. 20, pp. 15–21.
5. Vorontsov, P.S., Gerasimov, G.N., Golubeva, E.N., Grigor'ev, E.I., Zav'yalov, S.A. Zav'yalova, L.M., and Trakhtenberg, L.I., Gas-Sensitive and Catalytic Properties of the Ensemble of Interacting Palladium Nanoparticles, *Zh. Fiz. Khim.*, 1998, vol. 72, no. 10, pp. 1912–1914.
6. Udaratin, A.V. and Fedorov, M.I., Measurer of the Methane Concentration, *Sensor*, 2003, no. 1, pp. 50–51.
7. Anisimov, O.V., Maksimova, N.K., Filonov, N.G., Khludkova, L.S., and Chernikov, E.V., Peculiarities of Electric and Gas-Sensitive Characteristics of Thin Films of Tin Dioxide Obtained by Cathode Spraying, *Sensor*, 2003, no. 1, pp. 40–47.
8. Klechkovskaya, V.V., Maslov, V.N., and Muradov, M.B., *Kristallografiya*, 1989, vol. 34, no. 1, p. 182.
9. Nicolau, Y.F. and Menard, J.C., *J. Crystal Growth*, 1988, vol. 92, p. 128.
10. Lindroos, S., Kanniainen, T., and Leskela, M., *Thin Solid Films*, 1995, no. 263, p. 79.
11. Agasiev, A.A. and Muradov, M.B., *Pis'ma Zh. Tekh. Fiz.*, 1997, vol. 17, p. 54.
12. Kalandaragh Yashar Azizian, Muradov, M.B., and Mamedov, R.K., *J. Crystal Growth*, 2007 (submitted).